

QUANTITATIVE DETECTION OF FLUID DISTRIBUTION  
USING TIME-LAPSE SEISMIC

A DISSERTATION

SUBMITTED TO THE DEPARTMENT OF GEOPHYSICS

AND THE COMMITTEE ON GRADUATE STUDIES

OF STANFORD UNIVERSITY

IN PARTIAL FULFILLMENT OF THE REQUIREMENTS

FOR THE DEGREE OF

DOCTOR OF PHILOSOPHY

Futoshi Tsuneyama

July 2005

© Copyright by Futoshi Tsuneyama 2005  
All Rights Reserved

I certify that I have read this dissertation and that, in my opinion, it is fully adequate in scope and quality as a dissertation for the degree of Doctor of Philosophy.

---

Gary Mavko (Principal Adviser)

I certify that I have read this dissertation and that, in my opinion, it is fully adequate in scope and quality as a dissertation for the degree of Doctor of Philosophy.

---

Biondo Biondi

I certify that I have read this dissertation and that, in my opinion, it is fully adequate in scope and quality as a dissertation for the degree of Doctor of Philosophy.

---

Tapan Mukerji

Approved for the University Committee on Graduate Studies.

# Abstract

The quantitative evaluation of time-lapse seismic data remains a challenge. In most cases of time-lapse seismic analysis, fluid displacement and pressure changes are detected by changes in amplitude strength, travel time, and/or Poisson's ratio. However, the result is still qualitative, due to poor match between the model predictions and the actual seismic data.

Velocity anisotropy is one important reason for the mismatch. Especially for deviated wells in offshore fields, we must correct for velocity-anisotropy effects to obtain realistic sonic-log responses that are equivalent to seismic data. I compile experimental velocity-anisotropy data from cores in the literature to explore the empirical relationships between anisotropy parameters and general well-log information. Then, I develop a method to estimate Thomsen's anisotropy parameters  $\varepsilon$  and  $\gamma$  using a regression of the data in the crossplot domain between velocity and porosity. I present the result of an application of the method to demonstrate the significance of the correction.

Next, using the corrected velocity information, I present a method of impedance decomposition using three elastic impedance data derived from the seismic inversion of angle stacks. By applying seismic inversion, we can derive rock impedance from seismic data. However, if it is possible to decompose the impedance into two fundamental properties, namely velocity and density, we can determine the rock trend in the  $Vp$ - $\rho$  plane, and to derive quantitative rock properties, such as shale volume. I discuss the effect of noise on the analysis as the most important reason that decomposition is difficult. Then, I show an innovative method incorporating rock-physics bounds as constraints for the analysis. The method is applied to an actual dataset from an offshore oil field; I demonstrate the result of analysis for sand-body detection.

Based on the estimated  $Vp$ ,  $Vs$ ,  $\rho$  and shale volume from the elastic impedances, I develop a workflow to determine the saturation of formation-water, oil and gas from seismic data through a sequence of analyses and calculations. I present the subsequent steps, considering the pressure effect and the saturation scale of fluids for time-lapse seismic analysis. Then, I demonstrate a deterministic approach to computing the fluid

saturation to evaluate time-lapse seismic data. In this approach, I derive the physical properties of the water-saturated sandstone reservoir, based on the inputs. Next, by comparing the in-situ-fluid-saturated properties with the 100% formation-water-saturated reservoir properties, I determine the bulk modulus and the density of the fluid phase in the reservoir. Solving three equations simultaneously (relating the saturations of water, oil and gas in terms of the bulk modulus, density and the total saturation), I compute the saturation of each fluid. I use a real time-lapse seismic dataset to demonstrate the process and the result. In the result, I emphasize the validity of the workflow for quantitatively detecting the fluid displacement and for delineating a remaining oil accumulation.

In addition, I present a theoretical approach for understanding rock  $V_p$ - $V_s$  relations using the Hashin-Shtrikman bounds and several effective-medium theories. I discuss the upper Hashin-Shtrikman bound as the lowest  $V_p/V_s$  bound and the lower Hashin-Shtrikman bound as the highest  $V_p/V_s$  bound. I explore  $V_p$ - $V_s$  relations by effective-medium theories in the crossplot domain among  $V_p$ ,  $V_s$  and porosity. Then, I show that the location in the crossplots is an indicator of the pore shape. The stiffest pore shape, a sphere, gives us the upper Hashin-Shtrikman bound, and the softest pore shape, a flat film, gives us the lower Hashin-Shtrikman bound, or the Reuss bound. Based on this observation, I explain why a linear  $V_p$ - $V_s$  relation, which I use in the workflow to derive fluid saturation, represents the general trend of sandstone very well.

# Acknowledgments

First of all, I am deeply indebted to the Snorre unit partners--Statoil, Petoro, Norsk Hydro, ExxonMobil, Idemitsu, RWE Dea, TOTAL, Amerada Hess, and Shell--for allowing me to utilize the dataset of the Snorre field and publish the result. I thank the Stanford Rock Physics and Borehole Geophysics project for supporting this research.

On my first visit to Stanford, I bumped into Margaret Muir in the Mitchell building. I was looking for Gary, but he was out of his office. In a moment, she decided to drive me to the place where he was, even though she didn't know who I was. Since then, she has kept providing all the necessary support for my academic life with the best timing, the best form, and in the best location. It will never be sufficient to send my sincere appreciation to Margaret.

Gary Mavko is an excellent advisor as well as an outstanding entertainer. He often gave me small but critical pieces of advice that allowed me to break through individual difficulties I had been facing in my research. His handwritten figures for explaining his ideas are my lifetime collection. Tapan Mukerji provided me extremely important advice and consultations. All my research results were refined by taking his advices every time. Jack Dvorkin showed me how we should evoke scientific curiosity about nature. I was impressed with his way of talking, asking and answering. Of course, Amos Nur is the one who inspired me to study rock physics and join the SRB group. Whenever I saw him, I always felt good for no reason, just like seeing clear blue sky.

In addition, I would like to express my special thanks to Steve Graham for his kind acceptance to use the Landmark system in his group, and for his warm friendship. I appreciate Jef Caers, Biondo Biondi and Simon Klemperer. They served as the members of my defense committee.

I thank all SRB staff and students: first year room mates, Juan-Mauricio Florez-Nino and Ayako Kameda; co-TAs for rock physics classes, Kyle Spikes and Kevin Wolf; course selection and computer consultants, Ezequiel Gonzalez and Youngseuk Keehm; all old friends and new friends. An alumna of the SRB, Dawn Burgess, proofread all of my manuscripts. I thank for her patience.

When I proposed my plan for this research to my company in October, 2001, Mr. Kenzo Kurihara, the president of Idemitsu Oil & Gas Co. at that time, endorsed the plan without precondition in a short minute. My appreciation for his belief in my potential kept me going forward every day. All my colleagues in Idemitsu Tokyo and Idemitsu Petroleum Norge helped me by providing the field data for the case study, and they have given me many useful comments for my research and assistance for my life. All the financial support for my research was provided by Idemitsu Kosan Co., Ltd. in Japan.

I thank my parents. They gave me two different talents from each of them, extreme prudence and meticulousness from my mother, intrepidity but temerity from my father. All four traits were very useful, case by case, in the last three years. One of my sisters has been surviving a serious illness. She has kept pretending to be as usual, hiding her illness by constantly calling us from a hospital, until we noticed it. I was so happy to see her after two years.

Finally, I deeply appreciate my wife and sons, Machiko, Koh and Aoi. They were always together with me and shared all difficulties and happiness every day. We had some family ceremonies every month in the first year to endure the most difficult time for everyone. A hamster, Moh Moh, joined us in our second month, and helped us relieve our stress until the end of this winter. She will be alive in our memory of Stanford.

# Contents

## Abstract

|                  |   |           |
|------------------|---|-----------|
| <b>Chapter 1</b> | <b>Introduction</b>   | <b>1</b>  |
| 1.1              | Chapter description   | 1         |
| 1.2              | Geologic outline of the field for a case study                                | 4         |
|                  | REFERENCES  | 8         |
| <b>Chapter 2</b> | <b>Velocity anisotropy estimation for brine-saturated sandstone and shale</b> | <b>12</b> |
| 2.1              | Abstract  | 12        |
| 2.2              | Introduction  | 13        |
| 2.3              | Application result  | 14        |
| 2.4              | Estimation method of velocity anisotropy                                      | 17        |
| 2.5              | Alternative methods   | 30        |
| 2.6              | Conclusions   | 32        |
|                  | REFERENCES  | 34        |
| <b>Chapter 3</b> | <b>Elastic-impedance analysis constrained by rock-physics bounds</b>          | <b>36</b> |
| 3.1              | Abstract  | 36        |
| 3.2              | Introduction  | 37        |
| 3.3              | Noise effect in elastic-impedance analysis                                    | 38        |
| 3.4              | Theoretical assessment of noise effect  | 43        |
| 3.5              | Possible sources of noise   | 48        |
| 3.6              | Constraints for elastic-impedance analysis                                    | 50        |
| 3.7              | Validation of the method with a case study                                    | 56        |
| 3.8              | Comparison with unprocessed data  | 68        |
| 3.9              | Conclusion  | 71        |
|                  | REFERENCES  | 73        |

|                  |   |            |
|------------------|---|------------|
| <b>Chapter 4</b> | <b>Quantitative detection of fluid distribution using time-lapse seismic</b>                          | <b>75</b>  |
| 4.1              | Abstract  | 75         |
| 4.2              | Introduction  | 76         |
| 4.3              | Pressure effect   | 78         |
| 4.4              | Fluid-saturation scale  | 81         |
| 4.5              | Representative properties of the solid phase  | 84         |
| 4.6              | Workflow to determine fluid saturation  | 86         |
| 4.7              | Sensitivity analysis  | 96         |
| 4.7.1            | Fluid-saturation scale  | 97         |
| 4.7.2            | Velocity and bulk density   | 99         |
| 4.7.3            | Porosity and shale volume   | 102        |
| 4.7.4            | Fluid and solid properties  | 103        |
| 4.8              | Implementation of the workflow on time-lapse seismic  | 105        |
| 4.9              | Conclusions   | 115        |
|                  | REFERENCES  | 117        |
| <br>             |   |            |
| <b>Chapter 5</b> | <b>Exploring <math>V_p</math>-<math>V_s</math> relations: Approach from effective medium theories</b> | <b>120</b> |
| 5.1              | Abstract  | 120        |
| 5.2              | Introduction  | 121        |
| 5.3              | The Hashin-Shtrikman bounds   | 122        |
| 5.4              | $V_p$ - $V_s$ relation of sandstone   | 126        |
| 5.4.1            | Stiff-sand and soft-sand models   | 126        |
| 5.4.2            | Effective elastic moduli of a rock with tubular pores   | 133        |
| 5.4.3            | Self-consistent inclusion model of spheroid pores   | 136        |
| 5.4.4            | Comparison of the theoretical trends with laboratory measurements                                     | 140        |
| 5.4.5            | Modified Reuss bound  | 143        |
| 5.5              | $V_p$ - $V_s$ relation of carbonates  | 147        |
| 5.6              | Conclusions   | 151        |
|                  | REFERENCES  | 154        |

|                   |  |     |
|-------------------|--|-----|
| <b>Appendix A</b> | MATLAB code for the grid preparation of velocity-anisotropy analysis                                 | 156 |
| <b>Appendix B</b> | MATLAB code for the estimation of velocity anisotropy  | 158 |
| <b>Appendix C</b> | HRS code for elastic-impedance analysis constrained by rock-physics bounds                           | 159 |
| <b>Appendix D</b> | HRS code for the computation of fluid saturation:<br>(1) calculation of common rock-frame properties | 160 |
| <b>Appendix E</b> | HRS code for the computation of fluid saturation:<br>(2) calculation of fluid saturation             | 163 |

# List of Tables

|            |  |     |
|------------|--|-----|
| Table 3.1: | Summary of possible source and the category of noise.                                  | 49  |
| Table 3.2: | Summary of the parameters used to calculate the Hashin-Shtrikman bounds of sandstone.  | 51  |
| Table 4.1: | The parameters of the solids and fluids.   | 88  |
| Table 4.2: | The parameters to generate a model for sensitivity analysis.                           | 96  |
| Table 5.1: | Summary of the parameters used to calculate the Hashin-Shtrikman bounds of sandstone.  | 124 |
| Table 5.2: | Summary of the parameters used to calculate the Hashin-Shtrikman bounds of carbonates. | 147 |

# List of Figures

- Figure 1.1: The oil field for a case study. The three red lines illustrate deviated wells in the study area; the green line represents a vertical well in the area. The surface is the seismic horizon corresponding to a near top target reservoir. The color code is the two-way travel time from sea level to the horizon. The horizon dips northwest, to the left in this figure, with interruption of normal faults. 7
- Figure 2.1: An application result of my anisotropy correction method. The top left chart exhibits data from a deviated-well before the anisotropy correction, whereas the bottom left chart exhibits the deviated-well data after the correction. The top right chart shows data from a nearby vertical well, an ideal distribution after the correction. Note that the shale trend, along the fixed blue arrow in this figure, becomes concordant between the deviated-well and the vertical well after the correction. The well trajectories of the two wells are shown in the bottom right panel 15
- Figure 2.2: Well logs of a deviated-well. The fifth column from the left shows the estimated epsilon by my method. The blue dashed trace in the  $V_p$  column is a sonic log before the correction; the red trace in the same column is the sonic log after the anisotropy correction. 16
- Figure 2.3: The AVO modeling result of an interface between shale and oil sandstone. The blue curve corresponds to the reflectivity response derived from a sonic-log before the anisotropy correction. The red curve indicates the reflectivity response calculated from the sonic-log after the anisotropy correction. Note (1) the difference between the zero incident angle reflectivities and (2) the different trends of reflectivities as the incident angle increases. I used the anisotropic AVO equation in Thomsen (2002). The symbol  $\phi$  is fractional porosity,  $S_w$  is fractional water saturation, and oil saturation is  $1-S_w$ . 17

- Figure 2.4: The crossplot of  $Vp(0)$  vs. porosity for the compiled database of laboratory experiments. The database includes both dry samples and brine-saturated samples. Left: the data points are color-coded by Thomsen's anisotropy parameter  $\varepsilon$ . Right: the data points are color-coded by lithology. The red curve is the upper Hashin-Shtrikman bound of a quartz-water mixture with a critical porosity of 0.4. The blue curve is the Reuss bound of a clay-water mixture. 18
- Figure 2.5: Iso- $\varepsilon$  contours and the data points of brine-saturated sandstone and shale. The contours correspond to modified Reuss curves based on Equation 2.1, with two arbitrary P-wave moduli at the end points:  $M_1$  for zero porosity and  $M_2$  for fractional porosity 1. 20
- Figure 2.6: An empirically derived regression curve between  $M_1$  and  $M_2$ . The red points are plotted according to the result of fitting iso- $\varepsilon$  contours to the database. 20
- Figure 2.7: The estimation result of the anisotropy parameter  $\varepsilon$  in the  $Vp(0)$  vs. porosity domain for brine-saturated sand and shale. Right: actual  $\varepsilon$  vs. estimated  $\varepsilon$ . The red line is the 1:1 trend. 22
- Figure 2.8: Estimation result of the anisotropy parameter  $\gamma$  in the  $Vs(0)$  vs. porosity domain for brine-saturated sand and shale. Right: actual  $\gamma$  vs. the estimated  $\gamma$ . The red line is the 1:1 trend. 24
- Figure 2.9: Regressions between epsilon and the  $M_2$  calculated for epsilon; also between gamma and the  $M_2$  calculated for gamma. The color indicates lithology: yellow represents sand, red is siliceous shale, and brown is shale. The blue lines indicate the employed regression lines to generate Figures 2.7 and 2.8. 26
- Figure 2.10: The estimation result of the anisotropy parameter  $\delta$  for brine-saturated sand and shale. The red line is the 1:1 trend. 27
- Figure 2.11: Histograms of velocity differences. From the left, first column: actual velocity at the angle, minus  $Vp(0)$ ; second column: actual velocity at the

angle, minus estimated velocity by Thomsen's exact equation with estimated  $\varepsilon$  and  $\delta$ ; third column: actual velocity minus estimated velocity by Thomsen's approximation equation with estimated  $\varepsilon$  and  $\delta$ ; fourth column: actual velocity minus estimated velocity by Thomsen's approximation equation without the  $\delta$  term. 28

Figure 2.12: Quantitative comparison of the histograms in Figure 2.11. The left chart exhibits the mean of the  $V_p$  difference, and the right chart shows the standard deviation of the  $V_p$  difference. The blue dots correspond to the first column from the left in Figure 2.11, black dots represent the second column, green dots represent the third column, and the red dots indicate the data from the fourth column. 29

Figure 2.13: Estimation result of the anisotropy parameter  $\varepsilon$  by a neural network. Right: Actual  $\varepsilon$  vs. the estimated  $\varepsilon$ . The red line is the 1:1 trend. 31

Figure 2.14: Comparison of estimation results of the anisotropy parameter  $\varepsilon$  in the  $V_p(0)$ -porosity domain. Left: the proposed method in this paper. Right: the method by Li (2002). The upper curve is the upper Hashin-Shtrikman bound of a quartz-water mixture with a critical porosity of 0.4. The lower curve is the Reuss bound of a clay-water mixture. 32

Figure 3.1: The result of inverse calculation for  $V_p$  and  $\rho$  from three  $EIs$ . The left three columns show exact  $EIs$  in blue and data with 1% random noise added in the dashed red line. The 4<sup>th</sup> and 6<sup>th</sup> columns from the left are actual  $V_p$  and  $\rho$ . The 5<sup>th</sup> and 7<sup>th</sup> columns are comparisons between the actual data in blue and the back-calculated result in the dashed red line for  $V_p$  and  $\rho$  respectively. The right-most column exhibits acoustic impedance in the same color scheme. 40

Figure 3.2: The result of the inverse calculation for  $V_p$ ,  $V_s$  and  $\rho$  from three  $EIs$  with 10% offset-consistent noise. The column allocation and color code are the same as in Figure 3.1. The right-most column exhibits the  $V_s$  comparison. Note the separation between the actual data in blue and the calculation result in red is minimal in  $V_p$  and the largest in  $\rho$ . 42

- Figure 3.3: The result of inverse calculation for  $V_p$ ,  $V_s$  and  $\rho$  from three  $EIs$  with 25% offset-consistent noise. The column allocation and color code are the same as in Figure 3.1. Note that despite the high noise level,  $V_p$  does not exhibit any estimation errors, whereas I observe the highest error in  $\rho$  and much smaller miscalculations in  $V_s$ . 42
- Figure 3.4: Scanning result for the optimal mid-stack angle of seismic data in terms of minimizing the effect of random noise on elastic-impedance analysis. I assumed a near-stack angle of  $5^\circ$  and a far-stack angle of  $45^\circ$  for this case. 46
- Figure 3.5: The calculation result of noise enhancement factor varying  $K=(V_s/V_p)^2$ .  $V_p/V_s$  changes from 3.0 to 1.0 by 0.2 increment from the top to the bottom. A near-stack angle of  $5^\circ$  and a far-stack angle of  $45^\circ$  are assumed. Note that the minimum value of  $1/A$  is obtained at  $33^\circ$  for all cases. 47
- Figure 3.6: The first step of an  $EI$  analysis method. I apply a least-squares linear fitting to  $EIs$  in the  $\ln EI - \sin^2 \theta$  plane to obtain the general trend. Three points and the linear trend are extracted from an application for the actual data set. 52
- Figure 3.7: Comparison between the modified Hashin-Shtrikman bounds of several schemes and the distribution of actual data. The green lines represent a quartz-water mixture; the red lines indicate a mixture of water and the average solid of the target field; the blue lines represent a clay-water mixture. The dashed lines in the  $V_s$ -porosity plane are the transformed Hashin-Shtrikman bounds from the  $V_p$ -porosity plane using Equation 3.10 for black lines;  $V_p/V_s=1.6$  for magenta lines;  $V_p/V_s=2.0$  for cyan lines. All bounds have 0.4 as the critical porosity. 52
- Figure 3.8: Comparison between the modified Hashin-Shtrikman bounds of several schemes and a distribution of actual data. The representation scheme is same as Figure 3.7. All modified bounds assume 0.4 for the critical porosity. 54

- Figure 3.9: The modified Hashin-Shtrikman bounds of the schemes described in Figure 3.7 in the crossplot between the  $Vp/Vs$  ratio and density. The dashed lines correspond to the lower Hashin-Strikman bounds in the velocity-porosity plane; the solid lines are equivalent to the upper Hashin-Strikman bounds. Note that the upper and lower Hashin-Strikman bounds are coincident when  $Vp/Vs$  is a constant value. 55
- Figure 3.10: Comparison between the modified Hashin-Shtrikman bounds in the schemes described in Figure 3.7 and the actual data distribution calculated from well-log data. The dashed lines correspond to the lower Hashin-Strikman bounds; the solid lines are equivalent to the upper Hashin-Strikman bounds in the velocity-porosity plane. 55
- Figure 3.11: The inverse-matrix calculation results at a vertical well location from the unprocessed seismically derived  $EIs$ , in red, in the left three columns. The three right columns exhibit the calculation result from least-squares-fitted  $EIs$  in red. The blue lines are the actual well-log data. Note that the horizontal axes are logarithmic scale, but the range is one order smaller in the right half. 57
- Figure 3.12: The crossplot of the seismically derived  $EI$  data between  $EI_{far}$  and  $EI_{near}$  before constraining with rock-physics bounds (after least-squares fit). The red lines are the employed rock-physics bounds; the blue lines are lines parallel to the bounds, which will coincide with the red lines after the second step. The color code is the two-way time of the seismic data point in millisecond. 58
- Figure 3.13: The results of the inverse matrix calculation from our method fully applied to  $EIs$  in red at a well location. The blue lines are the actual well-log data. Note the significantly improved match between the seismic-analysis result and the well data compared to Figure 3.11. 60
- Figure 3.14: The crossplot of  $Vp-\rho$  on the left and  $Vs-\rho$  on the right. The dashed lines indicate the gradient used to determine shale volume in these plots. The large circles are points derived from the  $EI$  analysis of seismic data; the points color-coded in shale volume are well-log data. 61

- Figure 3.15: The shift of data location due to fluid saturation for a well-log data in the  $Vp$ - $\rho$  plane. The open circles represent the data location with in-situ fluid. The solid markers correspond to the data location after fluid-substituting to a water-saturated condition. Both are color-coded by the initial water saturation. Note the direction of data shift is parallel to the iso-shale-volume contours in the solid straight lines. 62
- Figure 3.16: The comparison between the shale volume from the data location with in-situ fluid and that with 100% water. The rock with in-situ fluid gives us higher shale volume than the rock with 100% water. However, the differences between two results are less than 10% in shale volume as shown in a histogram. 62
- Figure 3.17: The comparison of shale volumes. The yellow trace is the shale volume from well-log analysis; the green line represents a mean filtered version of the yellow trace. The magenta line exhibits the shale volume determined in the crossplot between  $Vp$  and  $\rho$ , based on the  $EI$  analysis of the seismic data. In addition, the red dashed line exhibits the shale volume estimated in the crossplot for  $Vs$  and  $\rho$  from the  $EI$  analysis. 63
- Figure 3.18: Shale-volume section obtained by the elastic-impedance analysis constrained by rock-physics bounds at the top. The bottom is the near-stack seismic section at the same location. The well log in red indicates the shale volume from well-log analysis, 0 on the left end and 1 for the right-end. Note that the top section demonstrates good agreement with the well log. The wiggle traces in the top section are the same seismic data as the bottom section. The color code in the top section is shale volume clipped in the range from 15% to 65%. 64
- Figure 3.19: The shale-volume section obtained by the elastic-impedance analysis constrained by rock-physics bounds at the top. The elastic-impedance section of the near-stack seismic data is at the bottom. This elastic-impedance data is one of the input data for the analysis. There is a tendency for higher impedances to correspond to higher shale. However, the lithology distribution is not clear in the impedance section at the bottom. 66

- Figure 3.20: The 3-D visualization of the resultant sand-body distribution. The color code is sand volume, where 127 corresponds to 55%, and -128 indicates 85% averaged sand volume within the seismic resolution. I set the transparency to illuminate the portion with more than 60% sand volume. The total width of the area is about 5km. 67
- Figure 3.21: The 3-D visualization of the resultant sand-body distribution. I set the transparency to illuminate the portion with more than 80% sand volume. Note that there are sand bodies which exhibit shapes similar to longitudinal bars and/or meandering channels. 67
- Figure 3.22: The 3-D visualization of the sand body distribution derived from unprocessed *EIs*. The color code is sand volume, but 127 corresponds to  $-10^{10}$  due to the abnormal calculation results from the unprocessed inputs; the scale is logarithmic. 69
- Figure 3.23: The 3-D visualization of the sand-body distribution derived from unprocessed *EIs*. This shows the result of extracting the portions of high sand content. Note that we cannot observe any clear sediment bodies. 69
- Figure 3.24: The strong amplitude reflectors in the near-stack seismic data. A pair of strong parallel reflectors at the bottom left are correlatable to the channels in Figure 3.21. However, the extension in the northeast direction is not as clear as in Figure 3.21. 70
- Figure 3.25: The strong amplitude reflectors in the far-stack seismic data. There are channel-like features around the center, but the reflectors are dimming out to the edge of the figure. 70
- Figure 4.1: The ratio of  $V_p$  at specific effective pressures to  $V_p$  at 30MPa effective pressure. I observe a very clear trend in the  $V_p$  ratio with effective pressure. 80
- Figure 4.2: Pressure change between two seismic acquisitions. The solid markers represent the first seismic survey. The empty markers correspond to the

second survey. Effective pressure, the difference between the overburden pressure and the formation pressure, increases during production, since the formation pressure of the reservoir declines due to oil production. Note that the differences of effective pressure are almost identical, except for the green data. 80

Figure 4.3: The velocity changes corresponding to the pressure changes in Figure 4.2. The degree of the velocity change is less than the 1% change in the velocity in the first survey. I convert the increase of effective pressure to the increase in velocity using Equations 4.1 and 4.2. Solid markers represent  $V_p$ , and empty markers denote  $V_s$ . 81

Figure 4.4: The generated fluid-saturation log of Well A for two seismic surveys in the two left columns. The green line indicates formation-water saturation; the interval between the green line and the red line (or to the right end) corresponds to oil saturation. The red line to the right end represents gas saturation. The two right columns show calculated elastic impedances. The color code is as follows: blue for the near stack; red for the mid stack; green for the far stack. 83

Figure 4.5: The mineral composition of the target sandstone reservoir. The sandstone is comprised of 40-60% quartz; 10-20% feldspar; and a small number of lithic fragments. 85

Figure 4.6: The crossplot of the calculated shear and bulk moduli of the sandstone in Figure 4.5. I use the Hill average for multi-mineral compositions. Clay is excluded from this calculation. Then, I use the shale volume from the elastic-impedance analysis to vary the solid-phase properties by mixing the representative properties of sandstone and clay, based on the shale volume. The color differences indicate different subunits in the reservoir. The shapes of the markers correspond to different wells. 86

Figure 4.7: The workflow to derive the density and bulk modulus of in-situ fluid. The input data at the top right is described in this paper. The sequence of computations to determine the final targets is explained step by step in this section. The input data in the top left box is discussed in Chapter 3. 87

Figure 4.8: Average trend between porosity and bulk density from the well-log data of the target reservoir. The red line represents the employed linear regression. The cyan line corresponds to the trend for 100% water saturated condition and the green line corresponds to 100% oil saturated trend. The histogram on the right exhibits the estimation errors of porosity induced by an averaged trend. 89

Figure 4.9: The calculated results of fluid saturation using different fractions of the saturation scale: homogeneous saturation represented in Equation 4.15 and patchy saturation given in Equation 4.16. For all columns, the thin lines represent the fluid saturation by well-log analysis, whereas the thick lines with open circles correspond to the results derived from seismic-data analysis. 94

Figure 4.10: The resultant fluid saturation for Well A obtained by solving the simultaneous equations. For all columns, the thin lines represent the fluid saturation by well-log analysis, whereas the thick lines with open circles correspond to the results derived from seismic-data analysis. The dashed orange lines show 0.15 deviations from the seismically derived saturation. The erroneous spikes at 2465m and 2540m are induced by the skewed density input derived from the miscalculations in the elastic-impedance analysis. 95

Figure 4.11: The sensitivity analysis of the fluid-saturation scale to the result of the workflow. The solid lines are the fluid saturation of the initial model. The left three columns represent the calculation results for the initial model of 100% patchy saturation. I used the following schemes of saturation scale in the inverse calculation: 100% patchy saturation for the triangles; 99% patchy saturation for the circles; 98% patchy saturation for the crosses. The right three columns show the calculation results for the initial model of the equally mixed saturation-scale schemes. I employed the following schemes in the inverse calculation: 100% patchy saturation for the triangles; 50% patchy saturation and 50% homogenous saturation for the circles; 100% homogenous saturation for the crosses. 97

Figure 4.12: The analysis of sensitivity of the velocity and bulk density to the result of the workflow. The solid lines are the fluid saturation of the initial model. The left three columns show the sensitivity analysis for velocity. The circles represent the base case; the triangles present the resultant saturation calculated from the workflow with 5% lower  $V_p$  and  $V_s$  as inputs; the crosses represent the saturation calculated from the workflow with 5% higher  $V_p$  and  $V_s$ . The right three columns show the sensitivity analysis of density. The circles correspond to the base case; the triangles present the saturation calculated using the workflow with 1% lower density; the crosses represent the calculation result from the workflow with 1% higher density. 100

Figure 4.13: The estimated  $V_p$ ,  $\rho$  and  $V_s$  by the elastic-impedance analysis discussed in Chapter 3. The blue lines represent the actual well logs; the dashed red lines show the results of the seismic-data analysis. Note that most points on the red lines are within the local perturbations of the well logs. 101

Figure 4.14: The analysis of porosity and shale-volume sensitivity to the result of the workflow. The left half shows the sensitivity analysis of porosity: the triangles are the result of 3% smaller porosity; the crosses are the result of 3% higher porosity. The right half shows the sensitivity analysis of shale volume: the triangles represent the result of 100% reduced shale volume; the crosses represent the result of 100% higher shale volume. 103

Figure 4.15: The sensitivity analysis of the fluid and solid properties to the result of the workflow. The left half shows the sensitivity analysis of fluid properties: the asterisks represent the fluid properties in Table 4.2 after rounding to the first decimal point in the workflow. The right half shows the sensitivity analysis of solid properties: the triangles represent the pure quartz assumption for the grains; the asterisks represent Castagna's regression of  $V_p$ - $V_s$  instead of using Han's regression. 105

Figure 4.16: A comparison of the time-lapse seismic data for a case study. The thin red horizon represents the near top reservoir. The black trace indicates the sonic log of Well A. We observe a slight change in seismic amplitude

along the horizon at the down flank, but it is impossible to quantitatively discuss the fluid displacement from the change. 106

Figure 4.17: A comparison of the time-lapse seismic data in the amplitude difference between the near and far stacks. We observe a subtle change in the amplitude difference along the horizon at the down flank, but there is no way to discuss the fluid displacement quantitatively. 107

Figure 4.18: A comparison of the oil-saturation sections calculated from time-lapse seismic data: the top represents 1997; the bottom represents 2001. We observe (1) the clear reduction of oil saturation near the top reservoir at the down flank and (2) a big body of bypassed oil in green in the middle of the reservoir. The color code is fractional oil saturation calculated according to my workflow. 108

Figure 4.19: A comparison of the gas-saturation sections calculated from time-lapse seismic data: the top represents 1997; the bottom represents 2001. We observe the reduction of gas saturation near the top reservoir at the down flank. The color code is fractional gas saturation from 0 to 0.2. 109

Figure 4.20: A comparison of the water-saturation sections calculated from time-lapse seismic data: the top represents 1997; the bottom represents 2001. The image is almost identical to Figure 4.18, since the gas saturation is almost negligible, and I use the inverse of the color code from Figure 4.18. 110

Figure 4.21: The distribution of oil saturation derived from the seismic data acquired in 1997. The color code is in fractional saturation from 1.0 at 127 to 0.0 at -128. 112

Figure 4.22: The distribution of oil saturation derived from the seismic data acquired in 2001. The color code is in fractional saturation from 1.0 at 127 to 0.0 at -128. Note that some higher-oil-saturation bodies in red in Figure 4.21 disappeared after 4 years of production. 112

- Figure 4.23: The distribution of gas saturation derived from the seismic data acquired in 1997. The color code is in fractional saturation from 1.0 at 127 to 0.0 at -128. 113
- Figure 4.24: The distribution of gas saturation derived from the seismic data acquired in 2001. The color code is in fractional saturation from 1.0 at 127 to 0.0 at -128. 113
- Figure 4.25: The distribution of water saturation derived from the seismic data acquired in 1997. The color code is in fractional saturation from 1.0 at 127 to 0.0 at -128. 114
- Figure 4.26: The distribution of water saturation derived from the seismic data acquired in 2001. The color code is in fractional saturation from 1.0 at 127 to 0.0 at -128. 114
- Figure 5.1: The upper and lower Hashin-Shtrikman bounds in the  $V_p$ -porosity plane on the left and the same bounds in the  $V_s$ -porosity plane on the right. The green lines represent a quartz-brine mixture, and the blue lines correspond to a clay-brine mixture. The solid lines correspond to the upper Hashin-Shtrikman bounds, and the dashed lines correspond to the lower Hashin-Shtrikman bound. 125
- Figure 5.2: The upper and lower Hashin-Shtrikman bounds in  $V_p$ - $V_s$  plane. The green and blue lines are equivalent to those in Figure 5.1. The black lines indicate constant  $V_p/V_s$ : the dashed line is  $V_p/V_s=1.5$ ; the solid line corresponds to  $V_p/V_s=2$ . The yellow circles represent the regression line for brine-saturated sandstones by Castagna *et al.* (1993). Note that Castagna's regression is located between the solid green line and the solid blue line. 125
- Figure 5.3: Stiff-sand models in the solid red lines and the dashed magenta lines; soft-sand models in the solid black lines and the dashed cyan lines, based on the Hertz-Mindlin contact stiffness. The red solid lines and the black solid lines are calculated with a fudge factor=0.2, whereas the dashed magenta lines and the cyan lines are calculated with a fudge factor=1. Each set has

five lines, ranging from 100% quartz at the top to 100% clay at the bottom. I applied a porosity-dependent velocity scale. 129

Figure 5.4:  $V_p$ - $V_s$  plot of the stiff-sand and soft-sand models in Figure 5.3. The black lines indicate constant  $V_p/V_s$ : the dashed line for  $V_p/V_s=1.5$  and the solid line for  $V_p/V_s=2$ . The yellow circles represent the regression line for brine-saturated sandstones by Castagna *et al.* (1993). 129

Figure 5.5: The calculation results of the upper Hashin-Shtrikman bound for the mixtures with different quartz contents. I use Hill's average to calculate the dry-rock elastic moduli, ranging from 100% quartz to 100% clay in 10% intervals. All data are brine-saturated using Gassmann's equation. 132

Figure 5.6:  $V_p$ - $V_s$  plot of the data in Figure 5.5, color-coded by porosity. Note that I adopt critical porosity at 0.4. We recognize iso-porosity trends. 132

Figure 5.7: The trends of a rock with tubular pores by a modified Mavko's equation in the velocity-porosity plane. The red circles represents tubes with perfectly circular cross sections, and the purple triangles represents tubes with three-sided hypotrochoid cross sections. 135

Figure 5.8: The trends of a rock with tubular pores by a modified Mavko's equation in the  $V_p$ - $V_s$  plane. The red circles represent tubes with perfectly circular cross sections, and the purple triangles represent tubes with three-sided hypotrochoid cross sections. Note that the trend of the red circles is very close to Castagna's regression for sandstone in the yellow circles. 135

Figure 5.9: The calculation results of a self-consistent inclusion model in the red lines. The numbers indicate the aspect ratios of the pores used in the calculation. 139

Figure 5.10: The same data as in Figure 5.9 in the  $V_p$ - $V_s$  plane. Note that relative position to the Hashin-Shtrikman bounds correlates to that in Figure 5.9. However, the trends of  $\alpha$  higher than 0.06 are not separable in the  $V_p$ - $V_s$  plane. 139

- Figure 5.11: Comparison of the trends from effective-medium models with the laboratory measurement by Han (1986) with a confining pressure of 5MPa. The measurement data are color-coded by the shale volume. 141
- Figure 5.12: The same data as in Figure 5.11 in the  $V_p$ - $V_s$  plane. Note that the data in reddish colors are located in between the solid and dashed black lines, as in Figure 5.11. 141
- Figure 5.13: Comparison of the trends from effective medium models with the laboratory measurement by Han (1986) at a confining pressure of 40MPa. The measurement data are color-coded by the shale volume. 142
- Figure 5.14: The same data as in Figure 5.11 in the  $V_p$ - $V_s$  plane. Note that the data in reddish colors are located between the solid and dashed black lines, although the data exhibit velocities around the solid black line in Figure 5.13. 142
- Figure 5.15: Comparison of the trends of modified Reuss bounds with the laboratory measurement by Han (1986): the solid circles represent the data at 5MPa confining pressure; the open circles are for 40MPa. The measurement data are color-coded by the shale volume. 144
- Figure 5.16: The same data as in Figure 5.15 in the  $V_p$ - $V_s$  plane. Note that the locations of measurement data relative to the modified Reuss bounds are consistent with the relative locations in Figure 5.15 for most of the data. The measurement data are color-coded by the shale volume. 144
- Figure 5.17: Comparison of the modified Reuss bounds in red with known  $V_p$ - $V_s$  relations. The yellow circles represent Castagna's regression for sandstone; the cyan circles represent Castagna's mudrock trend; the purple asterisks correspond to Han's regression for sandstone. 146
- Figure 5.18: The upper and lower Hashin-Shtrikman bounds of carbonates in the  $V_p$ -porosity plane on the left, and the same bounds in the  $V_s$ -porosity plane on

the right. The red lines represent a limestone-brine mixture and the purple lines a dolomite-brine mixture. The solid lines indicate the upper Hashin-Shtrikman bounds and the dashed lines correspond to the lower Hashin-Shtrikman bounds. 148

Figure 5.19: The upper and lower Hashin-Shtrikman bounds of carbonate-brine mixtures in the  $V_p$ - $V_s$  plane. The red lines represent a limestone-brine mixture and the purple lines a dolomite-brine mixture. The red circles and purple squares represent Castagna's regressions for these lithologies. Note that Castagna's regressions agree with the upper Hashin-Shtrikman bound for the lithology. 148

Figure 5.20: A trend of the  $V_p$ - $V_s$  relation for grainstone facies of limestone (dotted red line). The photo on the lower right shows the grainstone; the photo on the left above shows typical limestone. Note that the axes are the reverse of the convention in previous figures. 151

# Chapter 1

## Introduction

### 1.1 Chapter description

As expected by Nur (1997), time-lapse seismic has begun to play an important role in improving oil recovery, since seismic monitoring provides us the information relating to the changes in reservoir fluid and pressure during production. The Norwegian North Sea is an area where time-lapse seismic is commonly used to evaluate producing oil fields.

Several time-lapse seismic studies were published on the North Sea during the last decade. These include studies of the Oseberg field (Johnstad et al., 1995, Rutledal et al., 2003), the Magnus field (Watts et al., 1996), the Gullfaks field (Sonneland et al., 1997, Veire et al., 1998), the Draugen field (Gabriels et al., 1999), the Statfjord field (Al-Najjar et al., 1999) and the Snorre field (Smith et al., 2001).

An impressive example of quantitative analysis of time-lapse seismic was recently demonstrated by Lumley et al. (2003). They determined the axes representing the changes in pressure and water saturation in the crossplot between the P-wave information content ( $A_p$ ) and the S-wave information content ( $A_s$ ) to derive the quantitative indicators of the changing properties.

Johnston et al. (2003) discussed the integration of time-lapse seismic with production logging data for the quantitative analysis of the seismic. A case study of the method is summarized in Gouveia et al. (2004) for the Jotun field in the North Sea. According to their discussions, a key to reducing the artifacts induced during analysis is the coupling of seismic-inversion analysis of different vintages using a common initial model.

Despite the efforts described above, the quantitative analysis of time-lapse seismic to detect the change in fluid saturation remains a challenge, because the match between the model predictions and the actual seismic data is typically poor.

In Chapter 2, I discuss velocity anisotropy, one of the issues for improving the agreement between the model and the actual seismic data. Rowbotham et al. (2003) showed that the correction of velocity anisotropy significantly improves the result of seismic inversion, when deviated wells are used as the control data. Indeed, it is common to use deviated wells as the control data for analyzing offshore seismic data. However, the anisotropy correction of sonic logs for deviation angles is not a standard process. In this chapter, I develop a new method to estimate velocity anisotropy parameters from the well-log information of a single well. To obtain the relationships among velocity, porosity, and anisotropy parameters, I use a regression method in the velocity-porosity domain for the compiled database of laboratory measurements. I present the result of an

application of the method to demonstrate the significance of the correction. In the following chapters, the seismic data analyses are performed based on the anisotropy-corrected velocities.

In Chapter 3, I explore the effect of random and consistent noise as the source of miscalculation in deriving  $V_p$ ,  $V_s$  and  $\rho$  from the elastic-impedance ( $EI$ ) analysis of seismic data.  $EI$  is the apparent seismic impedance at specific incident angles, which was derived by Connolly (1998, 1999) and Mukerji (1998). Just as the contrast in acoustic impedance across a boundary determines normal incidence reflectivity, the contrast in  $EI$  determines the reflectivity at the corresponding angle of incidence. When we have  $EIs$  for three different stack angles of the same seismic data, it is possible in principle to back-calculate  $V_p$ ,  $V_s$ , and  $\rho$ . However, in general, the maximum stack angle of seismic data is limited to be less than  $30^\circ$ , which is not wide enough to obtain stable calculation results. In this chapter, I develop a method to minimize the calculation error by applying constraints based on rock-physics bounds. I validate the method by analyzing 3-D seismic data of an actual oil field; I demonstrate the result of delineating sand-body distribution by implementing the method.

In Chapter 4, based on the  $V_p$ ,  $V_s$ ,  $\rho$ , and shale volume calculated in Chapter 3, I develop a deterministic workflow to derive fluid saturation from seismic and well-log data; velocities, density and fluids saturation are calibrated to the time of seismic acquisition. The workflow is a tower of the carefully stacked building blocks of rock-physics knowledge: the Voigt-Reuss-Hill average (Hill, 1952) for solid properties; the Batzle-Wang method (Batzle and Wang, 1992) to determine fluid properties; a method to consider fluid-saturation scale for seismic analysis (Sengupta et al., 2003); the Gassmann

equation of fluid substitution (Gassmann, 1951); the  $V_p$ - $V_s$  relations for brine-saturated sandstone (Castagna et al., 1993 and Han, 1986); and coupling time-lapse seismic analysis using common rock-frame properties (Johnston et al., 2003). Then, I apply the workflow to the time-lapse seismic data of an offshore oil field. In the results, finally, I show a clear image of the fluid displacement in the reservoir after 4 years of oil production and delineate a remaining oil body.

In Chapter 5, I discuss  $V_p$ - $V_s$  relations of reservoir rocks. The most widely used empirical  $V_p$ - $V_s$  relations have been published by Castagna et al. (1993), for rock types including sandstone, mudrock, limestone and dolomite. Xu and White (1995) demonstrated a method to determine the  $V_p$ - $V_s$  relation of shaly sandstone by mixing two inclusion models with different aspect ratios, which represent the sandstone and shale portions. However, there is no systematic explanation of why a linear regression works well in most cases. I adopt the Hashin-Shtrikman bounds (Hashin and Shtrikman, 1963) to explore  $V_p$ - $V_s$  relations for rock-fluid mixtures. Then, I compare the  $V_p$ - $V_s$  relations calculated by the stiff-sand and soft-sand sand models by Dvorkin and Nur (1996), a model with tubular pores by Mavko (1980) and a self-consistent inclusion model of skewed-spheroid pores by Berryman (1995). This chapter explains why I use a simple  $V_p$ - $V_s$  relation in the workflow discussed in Chapter 4.

## **1.2 Geologic outline of the field for a case study**

The target field is situated in a major late Jurassic to early Cretaceous structural high at the western margin of a north Viking Graben Permo-Triassic rift in the North Sea. There is a series of large westward- to northwestward-tilted fault blocks. The field has

reservoirs in the Triassic “L” Formation and Triassic to Early-Jurassic “S” Formation. The structure contains a series of major faults, which follow a NNE-SSW structural trend. Most of these faults exhibit dip slip to the east.

The reservoir section was deposited as post-rift fill sediments. The main depositional environment of the target horizon, the “S” Formation, is a braided-river fluvial system with some interactions of a meandering-river system. The top of the “S” Formation is overlain by marine shale. The “S” Formation is divided into 5 zones: “S1” to “S5”, numbered from the top. The upper zones show coarser grains in sandstone and have significantly better reservoir properties than the lower parts. The “S” Formation demonstrates the repeated cycles of upward-fining and blocky sandstone sequences in the well logs. Especially for the upper part, the sequences are interpreted as the sheet sands of low-sinuosity braided-stream complexes.

Therefore, to understand the fluid behavior in the subsurface, it is important to map the distribution of the sand bodies with good reservoir properties and to detect fluid saturation using the seismic data.

The production of this field is undertaken by applying water-alternating-gas injection scheme to enhance oil production and maintain the reservoir pressure.

The database for the case study includes the following:

1. Time-lapse seismic: 3-D coverage, vintages 1997 and 2001, with 3 angle stacks (9°, 15°, 23.5°) for each vintage, matching filter applied;
2. Well logs of 4 wells (1 vertical well and 3 deviated wells (deviation around 60° in the reservoir) ): gamma ray, density, neutron, resistivity, dipole sonic, caliper, deviation angle;

3. Well-log interpretation: CPI log including porosity, fluid saturation, shale volume, and permeability in some wells;
4. Well-completion report: geologic description, horizon tops, and well trajectory;
5. Core data: lithology description, microscope image, and core-velocity measurements;
6. Geologic model: classification of reservoir units and fault distribution;
7. Reservoir-simulator output: reservoir-flow units and time-lapse outputs of the history-matched data (porosity, permeability, pressure, fluid saturation) at well locations.

Figure 1.1 shows an image of the case-study field. The three wells in red are deviated wells with maximum deviation angles exceeding 70°; Well A is a vertical well located very close to Well H. The surface is the seismic horizon near the top “S” Formation, which dips to the northwest—to the left in Figure 1.1—with interrupting normal faults. The color code is the interpreted two-way travel time in milliseconds from sea level.

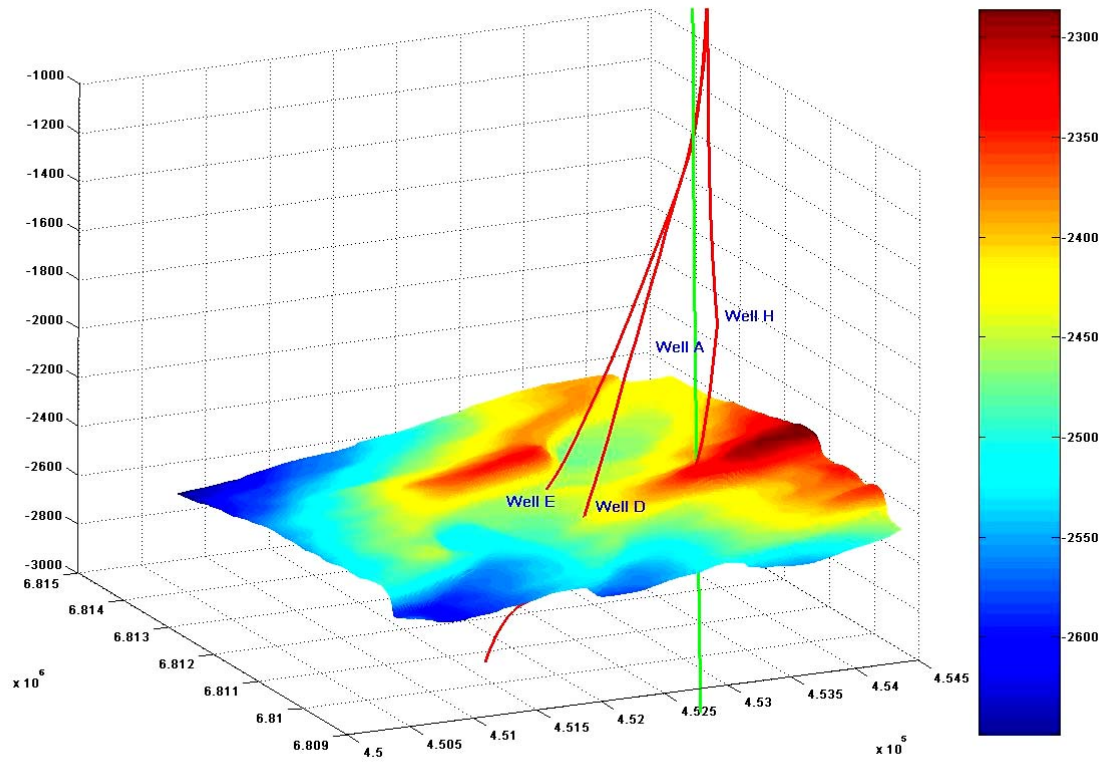


Figure 1.1: The oil field for a case study. The three red lines illustrate deviated wells in the study area; the green line represents a vertical well in the area. The surface is the seismic horizon corresponding to a near top target reservoir. The color code is the two-way travel time from the sea level to the horizon. The horizon dips northwest, to the left in this figure, with interruption of normal faults.

## REFERENCES

- Al-Najjar, N., Doyen, P., Brevik, I., Kvamme, L. and Psaila, D., 1999, Stattjord field -- time-lapse seismic interpretation using a 4-D earth model. Expanded Abstracts, 69th Annual International Meeting, Society of Exploration Geophysicists, 1620-1623.
- Batzle, M., and Wang, Z., 1992, Seismic properties of pore fluids, *Geophysics*, **57**, 1396-1408.
- Berryman, J.G., 1995, Mixture theories for rock properties, in “*Handbook of Physical Constants*”, T.J. Ahrens, eds. American Geophysical Union, Washington D.C., 205-228.
- Castagna, J., Batzle, M. and Kan, T., 1993, Rock Physics – The link between rock properties and AVO response, in *Offset Dependent Reflectivity – Theory and Practice of AVO Analysis*, J.P. Castagna and M. Backus, eds. Investigations in Geophysics, No. 8, Society of Exploration Geophysicists, Tulsa, Oklahoma, 135-171.
- Connolly, P., 1998, Calibration and inversion of non-zero offset seismic. Expanded Abstracts, 68th Annual International Meeting, Society of Exploration Geophysicists, 182-184.
- Connolly, P., 1999, Elastic impedance. *The Leading Edge*, **18**, 438-452.
- Dvorkin, J. and Nur, A., 1996, Elasticity of high-porosity sandstones: Theory for two North Sea datasets. *Geophysics*, **61**, 1363-1370.
- Gabriels, P. W., Horvei, N. A., Koster, J K., Onstein, A., Geo, A. and Staples, R., 1999, Time Lapse Seismic Monitoring of the Draugen Field. Expanded Abstracts, 69th Annual International Meeting, Society of Exploration Geophysicists, 2035-2037.

- Gassmann, F., 1951, Über die elastizität poroser medien. *Verteljahrsschrift der Naturforschenden Gesellschaft in Zurich*, **96**, 1-23.
- Gouveia, W. P., Johnston, D. H. and Solberg, A., 2004, Remarks on the estimation of time-lapse elastic properties: the case study for the Jotun field, Norway, Expanded Abstracts, 74th Annual International Meeting, Society of Exploration Geophysicists, 2212-2215
- Han, D-H., 1986, *Effects of Porosity and Clay Content on Acoustic Properties of Sandstones and Unconsolidated Sediments*. Ph.D. dissertation, Stanford University.
- Hashin, Z. and Shtrikman, S., 1963, A variational approach to the theory of elastic behavior of multiphase materials, *Journal of Mechanics and Physics Solids*, **11**, 127-140.
- Hill, R., 1952, The elastic behavior of a crystalline aggregate. *Proc. Phys. Soc. London Ser. A*, **65**, 349-354.
- Johnstad, S., Seymour, R., and Smith, P., 1995, Seismic reservoir monitoring over the Oseberg field during the period 1989-1992. *First Break*, **13**, May, 169-183.
- Johnston, D. H., Gouveia, W. P., Solberg, A. and Lauritzen, M., 2003, Integration of time-lapse seismic and production logging data: Jotun Field, Norway, Expanded Abstracts, 73rd Annual International Meeting, Society of Exploration Geophysicists, 1346-1349.
- Lumley, D., Meadows, M., Cole, S. and Adams, D., 2003, Estimation of reservoir pressure and saturations by crossplot inversion of 4D seismic attributes. 73rd Annual International Meeting, Society of Exploration Geophysicists, 1513-1516.

- Mavko, G., 1980, Velocity and attenuation in partially molten rocks, *Journal of Geophysical Research*, **85**, 5173-5189.
- Mukerji, T., Jørstad, A., Mavko, G., and Granli, J., 1998, Near and far offset impedances: Seismic attributes for identifying lithofacies and pore fluids. *Geophysical Research Letter*, **25**, 4557-4560.
- Nur, A., 1997, Rock physics and 4-D seismic for improved oil recovery, Expanded Abstracts, 67th Annual International Meeting, Society of Exploration Geophysicists, 1009-1011.
- Rowbotham, P., Marion, D., Eden, R., Williamson, P., Lamy, P. and Swaby, P., 2003, The implication of anisotropy for seismic impedance inversion. *First Break*, **21**, 53-57.
- Rutledal, H., Helgesen, J. and Buran, H., 2003, 4D elastic inversion helps locate in-fill wells at Oseberg field. *First Break*, **21**, 39-43.
- Sengupta, M., Mavko, G. and Mukerji, T., 2003, Quantifying subresolution saturation scales from time-lapse seismic data: A reservoir monitoring case study. *Geophysics*, **68**, 803-814.
- Smith, P., Berg, J., Eidsvig, S., Magnus, I. and Verhelst, F., 2001, 4-D Seismic in a complex fluvial reservoir: The Snorre feasibility study. *The Leading Edge*, **20**, 270-277.
- Sonneland, L., Veire, H. H., Raymond, B., Signer, C., Pedersen, L., Ryan, S., and Sayers, C., 1997, Seismic reservoir monitoring on Gullfaks. *The Leading Edge*, **16**, 1247-1252.

- Veire, H. H., Reymond, S. B., Signer, C., Tennebo, P. O. and Sonneland, L., 1998, Estimation of reservoir fluid volume through 4-D seismic analysis on Gullfaks. Expanded Abstracts, 68th Annual. International Meeting: Society of Exploration Geophysicists, 27-30
- Watts, G., Jizba, D., Gawith, D., and Gutteridge, P., 1996, Reservoir monitoring of the Magnus field through 4-D time-lapse seismic analysis. *Petroleum Geoscience*, **2**, 361-372.
- Xu, S. and White, R.E., 1995, A new velocity model for clay-sand mixtures. *Geophysical Prospecting*, **43**, 91-118.

# Chapter 2

## Velocity anisotropy estimation for brine-saturated sandstone and shale

### 2.1 Abstract

Velocity anisotropy is one of the important parameters to consider in seismic analyses. Especially for deviated-wells in offshore fields, we must correct for velocity anisotropy effects to obtain realistic sonic-log responses that are equivalent to seismic data for small incident angles. However, there is no appropriate method for anisotropy correction using well-log information from a single well, which is often the only information available. I compiled experimental velocity anisotropy data from cores in the literatures to explore the empirical relationships between anisotropy parameters and general well-log information. Eventually, I found that there is a clear trend of velocity anisotropy in the crossplot domain between velocity and porosity. Consequently, I

developed a method to estimate Thomsen's (1986) anisotropy parameters  $\varepsilon$  and  $\gamma$  using a regression in that domain. The advantage of this method is that one can estimate  $\varepsilon$  and  $\gamma$  from well-log curves of  $V_p$  and total porosity. In this chapter, I first present the result of an application of the method to demonstrate the significance of the correction. Then, I show how I developed the method. In addition, I discuss an alternative approach incorporating a neural network, and compare my method with the method proposed by Li (2002).

## **2.2 Introduction**

Rowbotham et al. (2003) showed that the correction of velocity anisotropy significantly improves the result of seismic inversion, when deviated wells are used as the control data. Indeed, it is common to use deviated wells as the control data for analyzing offshore seismic data. However, the anisotropy correction of sonic-logs for deviation angles is not a standard process. Therefore, in the real world, well control is often distorted when the correction for sonic-logs is not applied, especially for geologic sequences with many interbedded shaly layers, where we expect larger anisotropy effects. Hornby et al. (2003) proposed a method to estimate anisotropy parameters from the sonic logs of differently deviated-wells, including a vertical well. This method, as well as the simplified version of this method in Rowbotham et al. (2003), is based on the assumption that the shale layer is perfectly homogeneous in the area where the wells are deviated, so the velocity variation depends only on the deviation angles of the wells. Then, the optimum anisotropy parameters are determined to obtain a sonic-log velocity consistent

with a nearby vertical well. Obviously, this method is not applicable for laterally heterogeneous lithofacies sequences, such as fluvial deposits. Furthermore, we may not have a nearby vertical well in some cases. Therefore, an alternative method for estimating anisotropy parameters is necessary to correct the sonic log in heterogeneous geologic sequences and/or to perform anisotropy correction with single-well information. I developed a new method to estimate velocity anisotropy parameters from the well-log information of a single well.

### **2.3 Application result**

Before explaining the analysis procedure, I preview the results. Figure 2.1 shows the result of my correction for an example well. In the top left chart, the circle markers are sample points from a deviated well (deviation angles in a reservoir are  $57^{\circ}$ - $62^{\circ}$ ) before an anisotropy correction, color-coded by shale volume. The bottom left chart shows the sample points from the same deviated well, but after the anisotropy correction using my method. The chart on the top right exhibits data points from a nearby vertical well, which show the ideal data distribution that would be expected after an anisotropy correction. The arrows in the charts indicate lithology trends of increasing shaliness, which are obtained from the chart of the nearby vertical well, then overlaid on the charts for the deviated well. I emphasize that the shale trend (data points along the blue arrow in the figure) becomes concordant between the deviated well and the vertical well after the new correction method is applied. Figure 2.2 shows well logs from the deviated well, including estimated Thomsen's (1986) epsilon and sonic logs both before and after the

anisotropy correction. This correction magnifies the velocity contrast between the shale and sand; as a result, the seismic modeling of the data is modified as well after the correction. I calculated the AVO responses at an interface between shale and reservoir sand, as presented in Figure 2.3. In this figure, two significant effects of the anisotropy correction are clear. First, the magnitude of zero offset reflectivity after the correction is less than half of that before the correction.

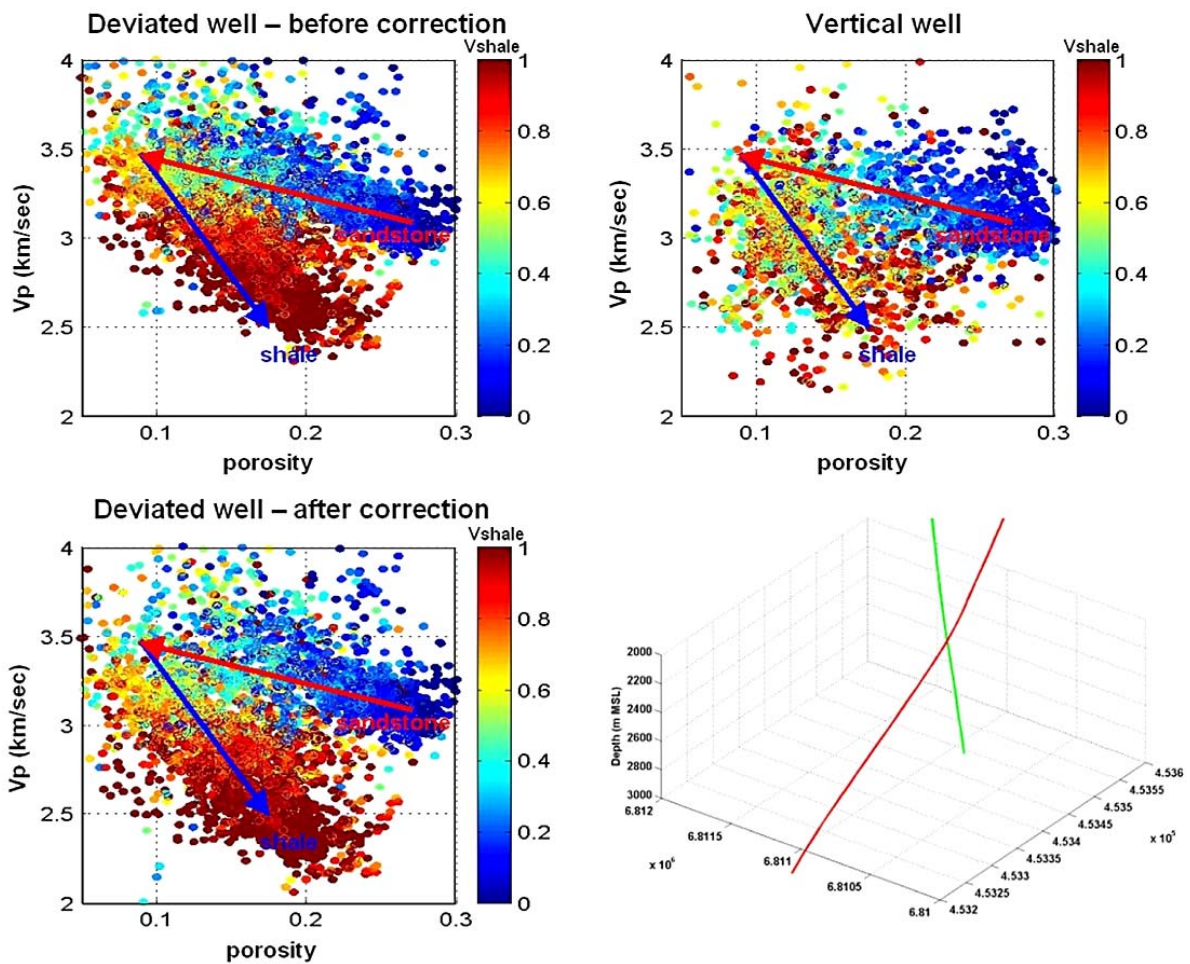


Figure 2.1: An application result of my anisotropy correction method. The top left chart exhibits data from a deviated-well before the anisotropy correction, whereas the bottom left chart exhibits the deviated-well data after the correction. The top right chart shows data from a nearby vertical well, an ideal distribution after the correction. Note that the shale trend, along the fixed blue arrow in this figure, becomes concordant between the deviated-well and the vertical well after the correction. The well trajectories of the two wells are shown in the bottom right panel.

Second, the AVO response before the correction is almost flat, but after the correction the response shows decreasing reflectivity with increasing incident angle in this light oil reservoir case. This example shows that using velocity data without an anisotropy correction may induce significant errors in seismic analyses.

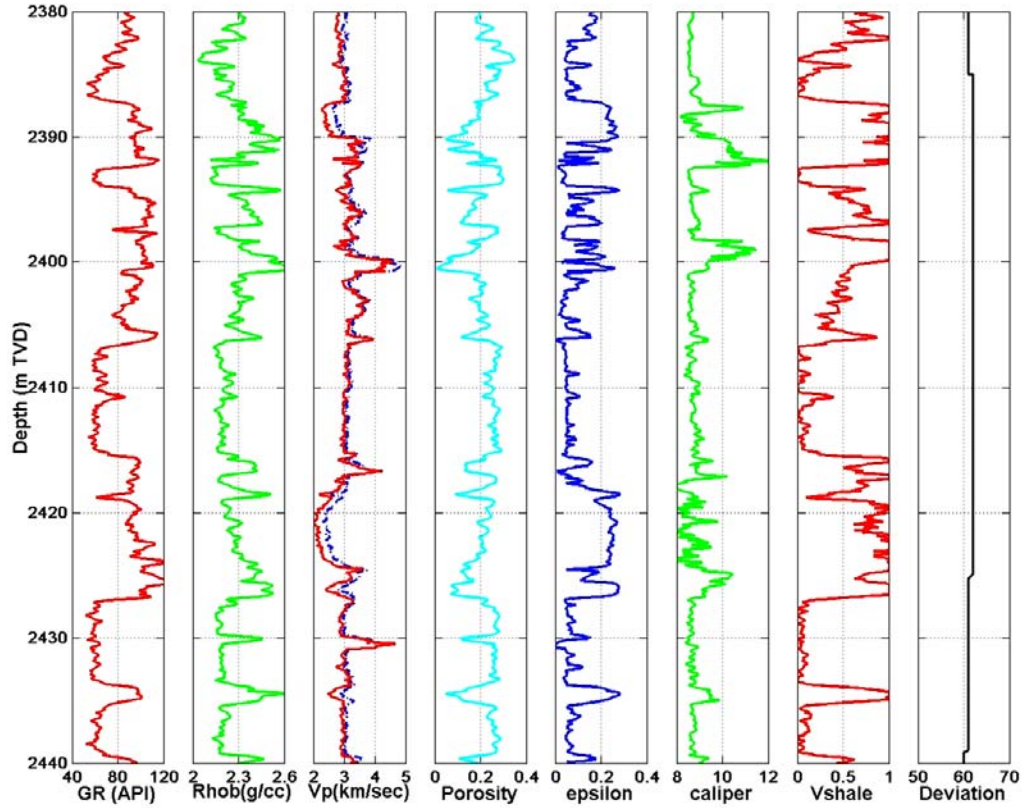


Figure 2.2: Well logs of a deviated-well. The fifth column from the left shows the estimated epsilon by my method. The blue dashed trace in the Vp column is a sonic log before the correction; the red trace in the same column is the sonic log after the anisotropy correction.

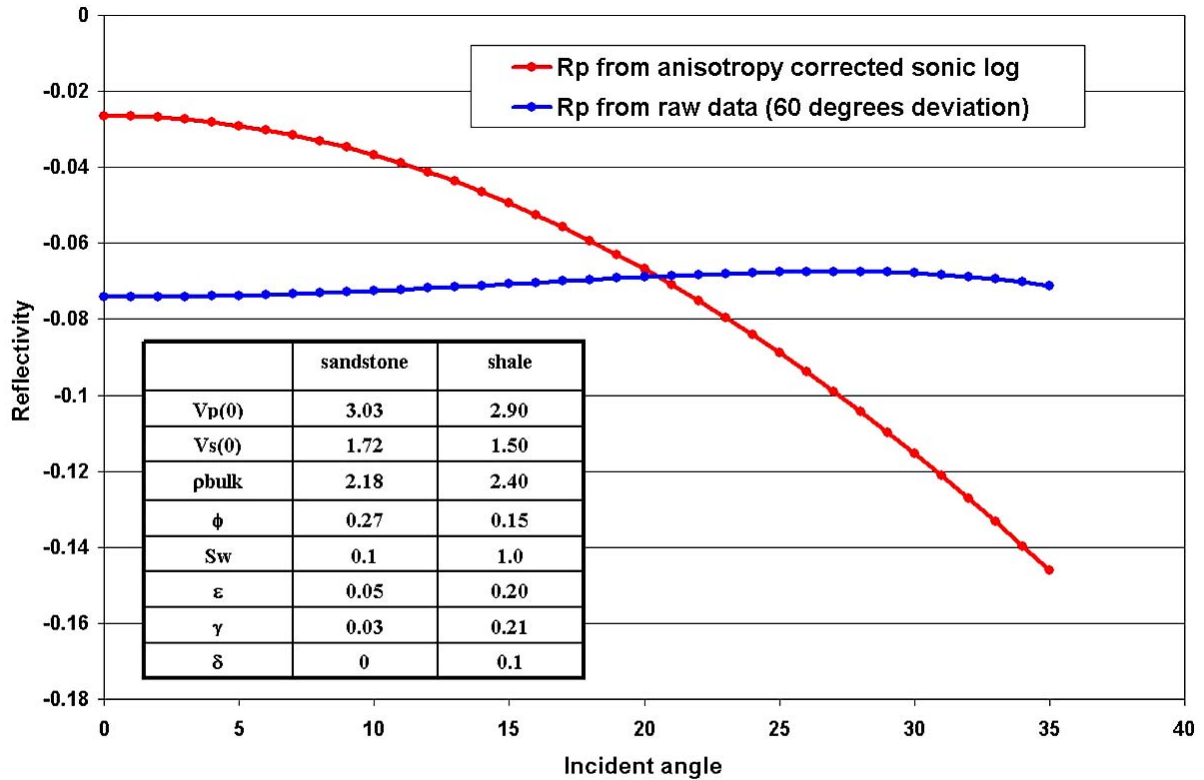


Figure 2.3: The AVO modeling result of an interface between shale and oil sandstone. The blue curve corresponds to the reflectivity response derived from a sonic-log before the anisotropy correction. The red curve indicates the reflectivity response calculated from the sonic-log after the anisotropy correction. Note (1) the difference between the zero incident angle reflectivities and (2) the different trends of reflectivities as the incident angle increases. I used the anisotropic AVO equation in Thomsen (2002). The symbol  $\phi$  is fractional porosity.  $S_w$  is fractional water saturation and oil saturation is  $1-S_w$ .

## 2.4 Estimation method of velocity anisotropy

I compiled laboratory measurements by Lo et al. (1986), Vernik & Liu (1997), and Wang (2002). Assuming that most subsurface rocks are transversely isotropic with vertical symmetry axis, I examined the compiled data to explore relationships between common well-log information ( $V_p$ ,  $V_s$ , density, porosity, effective pressure) and Thomsen's anisotropy parameters ( $\varepsilon$ ,  $\gamma$ ,  $\delta$ ).

After generating a series of crossplots, I found a clear trend of  $\varepsilon$  in the domain of normal incident  $V_p$  ( $=V_p(0)$ ) and bulk porosity as shown in Figure 2.4. To eliminate

effects of saturation, I extracted only the measurements for brine-saturated sandstone and shale from the database. I scrutinized the extracted dataset to obtain an appropriate regression method to estimate  $\varepsilon$  from  $V_p(0)$  and porosity  $\phi$ . In this investigation, modified Reuss average curves, as a function of arbitrary P-wave moduli and porosity, are found to yield a good functional form for iso- $\varepsilon$  contours in the crossplot domain between  $V_p(0)$  and porosity  $\phi$ . The Reuss bound is the isostress average of two materials, so that the mental image of the Reuss scheme is alternating layers of two materials. This fact suggests that as  $V_p(0)$  for the fixed porosity approaches the minimum velocity on the Reuss bound, a rock tends to have more horizontally layered internal texture; for that reason, the rock demonstrates larger velocity anisotropy.

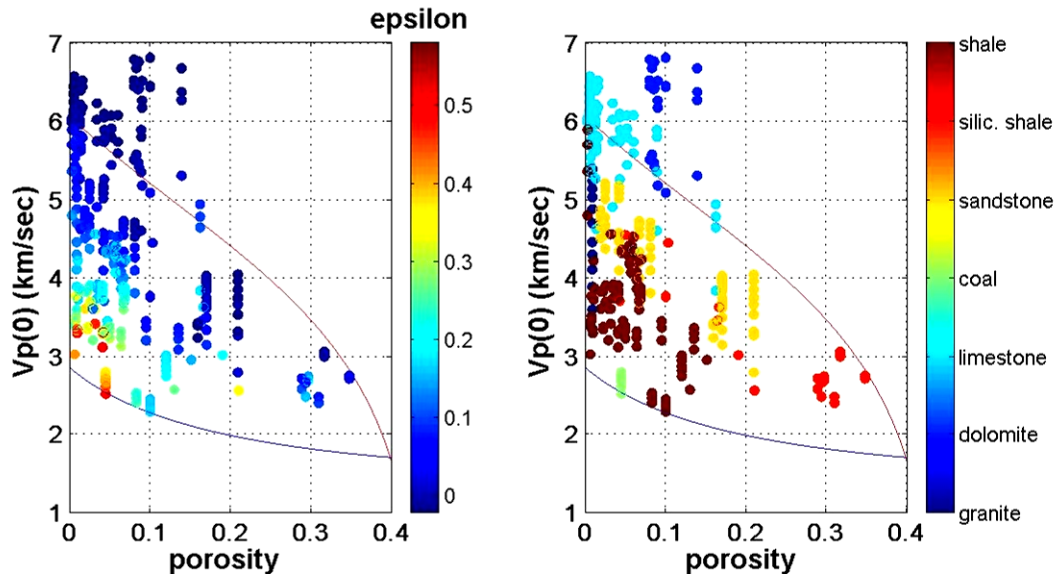


Figure 2.4: The crossplot of  $V_p(0)$  vs. porosity for the compiled database of laboratory experiments. The database includes both dry samples and brine-saturated samples. Left: the data points are color-coded by Thomsen's anisotropy parameter  $\varepsilon$ . Right: the data points are color-coded by lithology. The red curve is the upper Hashin-Shtrikman bound of a quartz-water mixture with a critical porosity of 0.4. The blue curve is the Reuss bound of a clay-water mixture.

The equation for modified Reuss curves is given in Equation 2.1, where  $M_1$  and  $M_2$  are two arbitrary P-wave moduli of the end points  $\phi=0$  and  $\phi=1$ , respectively. Taking  $\phi$

as the material fraction of  $M_2$ , to simplify the calculation, I set densities 2.65 g/cm<sup>3</sup> for  $M_1$ ; 1.00 g/cm<sup>3</sup> for  $M_2$ . Choosing  $\phi$  as the fraction of  $M_2$  might seem counterintuitive. However, this empirical exercise leads to a useful description of the anisotropic data. Here, P-wave modulus  $M$  is the product of the density and the square of the P-wave velocity for each material. Then the P-wave velocity of the mixture is expressed as below:

$$Vp(0) = [ ((1 - \phi) / M_1 + \phi / M_2 )^{-1} / ( \phi + 2.65(1 - \phi) ) ]^{1/2}. \quad (2.1)$$

To optimize the fitting of iso- $\varepsilon$  contours to the data points for small  $\varepsilon$  values, where we have sufficient data coverage, I calculate iso- $\varepsilon$  contours using least squares. Next, I extrapolate the resultant contours for larger  $\varepsilon$  values. The obtained iso- $\varepsilon$  contours are almost parallel to the Reuss bound, as shown in Figure 2.5. For this process, I use only the laboratory data with effective pressure greater than 30MPa, since the data with lower effective pressure is highly scattered.

In addition, we find the relationship between  $M_1$  and  $M_2$  based on their values derived during the generation of iso- $\varepsilon$  contours. Figure 2.6 shows the data points and the regression curve given by

$$M_1 = -2.3095 M_2^2 + 35.525 M_2 - 37.403 \quad . \quad (2.2)$$

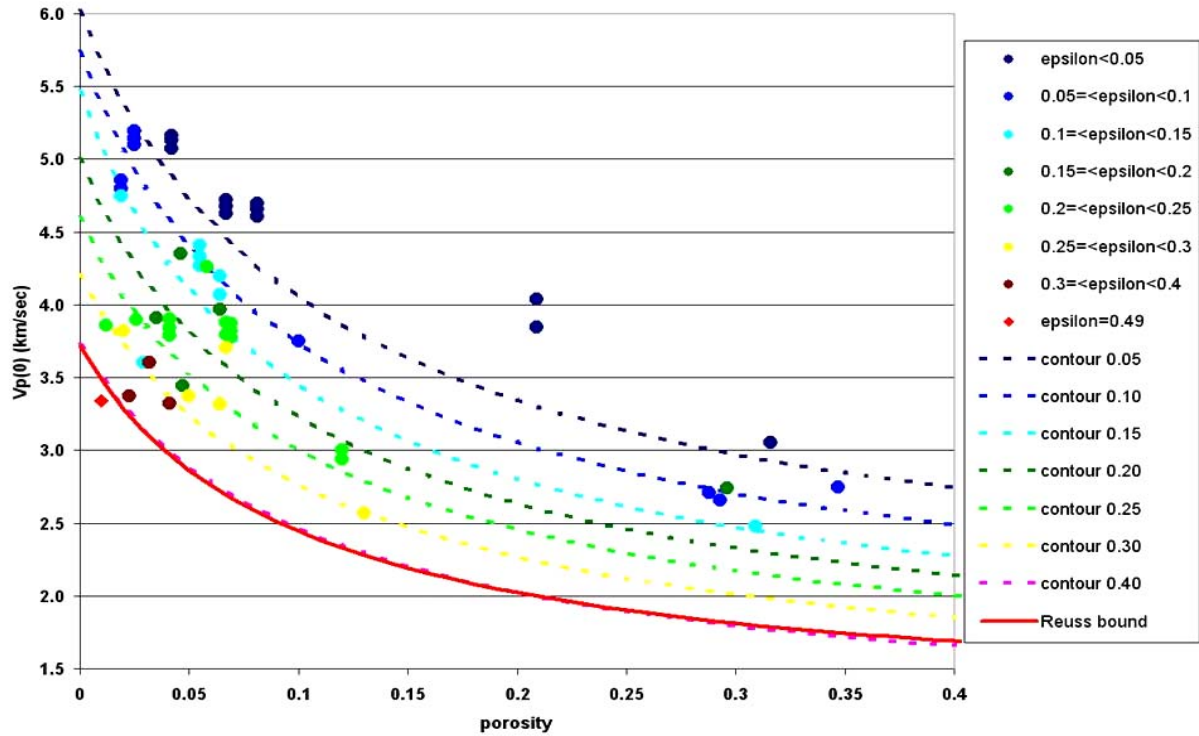


Figure 2.5: Iso- $\epsilon$  contours and the data points of brine-saturated sandstone and shale. The contours correspond to modified Reuss curves based on Equation 2.1 with two arbitrary P-wave moduli at the end points:  $M_1$  for zero porosity and  $M_2$  for fractional porosity 1.

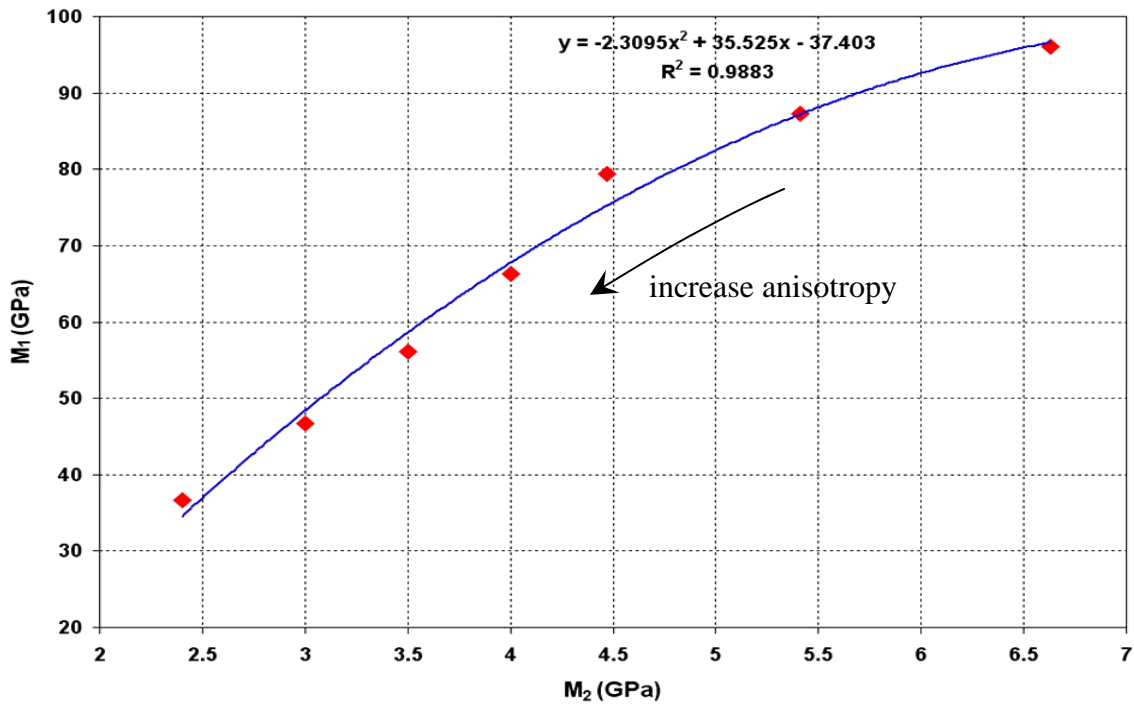


Figure 2.6: An empirically derived regression curve between  $M_1$  and  $M_2$ . The red points are plotted according to the result of fitting iso- $\epsilon$  contours to the database.

Here, I solve Equations (2.1) and (2.2) simultaneously to determine  $M_1$  and  $M_2$  from  $V_p(0)$  and  $\phi$ . First I rearrange Equation (2.1) to obtain

$$M_1M_2/(M_2(1-\phi)+\phi M_1) = 2.65V_p(0)^2 - 1.65\phi V_p(0)^2 = A . \quad (2.3)$$

Now, I express the relationship between  $M_1$  and  $M_2$  using  $A$ :

$$M_1 = (A - A\phi)M_2 / (M_2 - A\phi). \quad (2.4)$$

I plug this relationship into Equation (2) to obtain the following equation:

$$-2.3095M_2^3 + (35.525 + 2.3095A\phi)M_2^2 - (37.403 + 35.525A\phi - A\phi + A)M_2 + 37.403A\phi = 0. \quad (2.5)$$

Next, I rearrange this equation in the form of  $x^3 + ax^2 + bx + c = 0$  and solve it as shown below, where  $p$ ,  $q$ ,  $m$ , and  $n$  are intermediate products.

$$a = (35.525 + 2.3095A\phi) / (-2.3095) \quad (2.6)$$

$$b = -(37.403 + 35.525A\phi - A\phi + A) / (-2.3095)$$

$$c = (37.403A\phi) / (-2.3095)$$

$$p = b - (a^2/3)$$

$$q = 2(a^3/27) - (ab)/3 + c$$

$$m = (-q/2 + \sqrt{q^2/4 - p^3/27})^{1/3}$$

$$n = -1(\text{abs}(-q/2 - \sqrt{q^2/4 - p^3/27}))^{1/3}$$

$$M_2 = -(m+n) - a/3$$

Finally, I use regressions between  $M_2$  and  $\varepsilon$  to determine the  $\varepsilon$  value, assuming the minimum  $\varepsilon$  is zero. These regressions are derived from the compiled database of brine-saturated sandstone and shale as well. Figure 2.9 exhibits these regressions for  $\varepsilon$  and  $\gamma$ .

$$\begin{aligned} \varepsilon &= -1.0428M_2 + 3.621, & M_2 < 3.2048, & (2.7) \\ &= -0.0809M_2 + 0.5383, & 3.2048 \leq M_2 < 5.9924, & \\ &= -0.0152M_2 + 0.1446, & M_2 \geq 5.9924. & \end{aligned}$$

Using Equations 2.3, 2.6 and 2.7, now we can determine  $\varepsilon$  from  $Vp(0)$  and  $\phi$ .

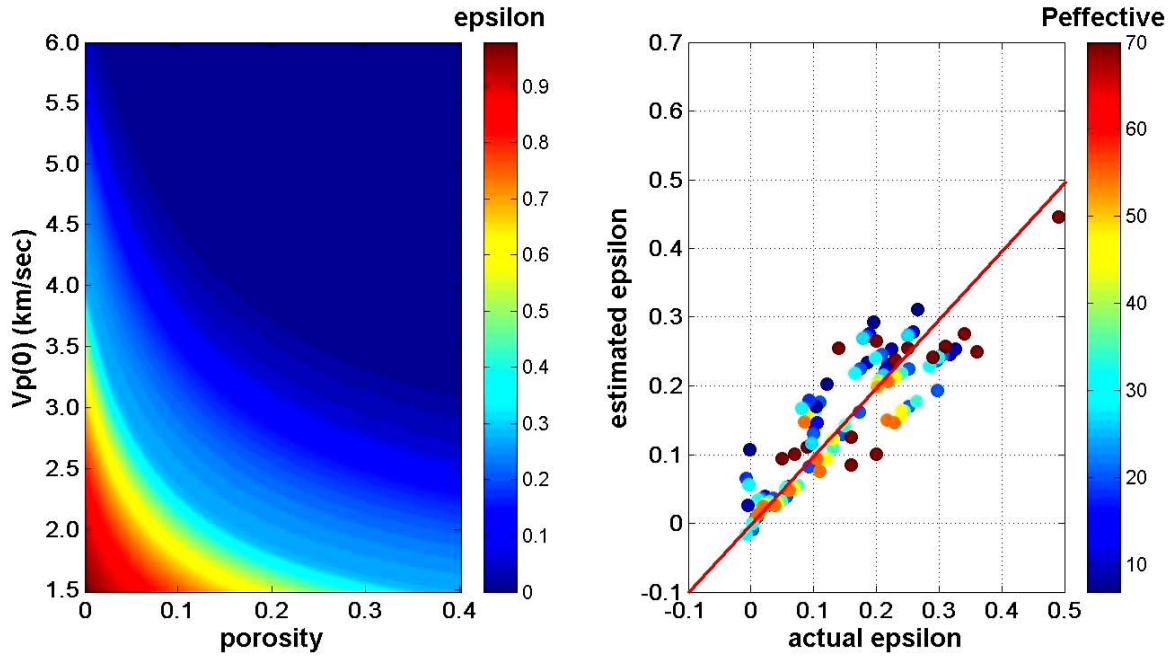


Figure 2.7: The estimation result of the anisotropy parameter  $\varepsilon$  in the  $Vp(0)$  vs. porosity domain for brine-saturated sand and shale. Right: actual  $\varepsilon$  vs. estimated  $\varepsilon$ . The red line is the 1:1 trend.

The left chart of Figure 2.7 presents the calculated  $\varepsilon$  value for  $Vp(0)$ , ranging from 1.5 to 6 km/sec, and fractional porosity, between 0 and 0.4; the chart on the right exhibits the correlation between the actual  $\varepsilon$  and the estimated value. In the right-hand side chart, the markers are color-coded by the effective pressure of their laboratory measurements in MPa. Note that three to four linearly aligned markers with changing color in the chart are data measured on the same core sample but in different pressure conditions. These data indicate that the influence of effective pressure is more or less parallel to the 1:1 line in the chart. This shows that the pressure effect on  $\varepsilon$  is independent of this estimation method.

I apply the same approach to estimate Thomsen's anisotropy parameter  $\gamma$  from  $Vs(0)$  and porosity as displayed in Figure 2.8. I derive the equation below from a regression for iso- $\gamma$  contours:

$$A = 2.65Vs(0)^2 - 1.65\phi Vs(0)^2. \quad (2.8)$$

$$-5.6031M_2^3 + (24.278 + 5.6031A\phi)M_2^2 + (18.778 - 24.278A\phi + A\phi - A)M_2 - 18.778A\phi = 0. \quad (2.9)$$

Then I solve the equation for  $M_2$ , where  $p$ ,  $q$ ,  $m$ , and  $n$  are intermediate products.

$$a = (24.278 + 5.6031A\phi) / (-5.6031), \quad (2.10)$$

$$b = (18.778 - 24.278A\phi + A\phi - A) / (-5.6031),$$

$$c = (-18.778A\phi) / (-5.6031),$$

$$p = b - (a^2/3),$$

$$q=2(a^3/27)-(ab)/3+c,$$

$$m=(-q/2+\text{sqrt}(q^2/4-p^3/27))^{1/3},$$

$$n=-1(\text{abs}(-q/2-\text{sqrt}(q^2/4-p^3/27)))^{1/3},$$

$$M_2=-(m+n)-a/3.$$

I find regressions between  $M_2$  and  $\gamma$  to determine the  $\gamma$  value, assuming the minimum  $\gamma$  is zero.

$$\begin{aligned} \gamma &= -1.3598M_2+1.3284, & M_2 < 0.8549, \\ &= -0.1286M_2+0.2759, & 0.8549 < M_2 < 1.8711, \\ &= -0.0316M_2+0.0944, & M_2 \geq 1.8711. \end{aligned} \tag{2.11}$$

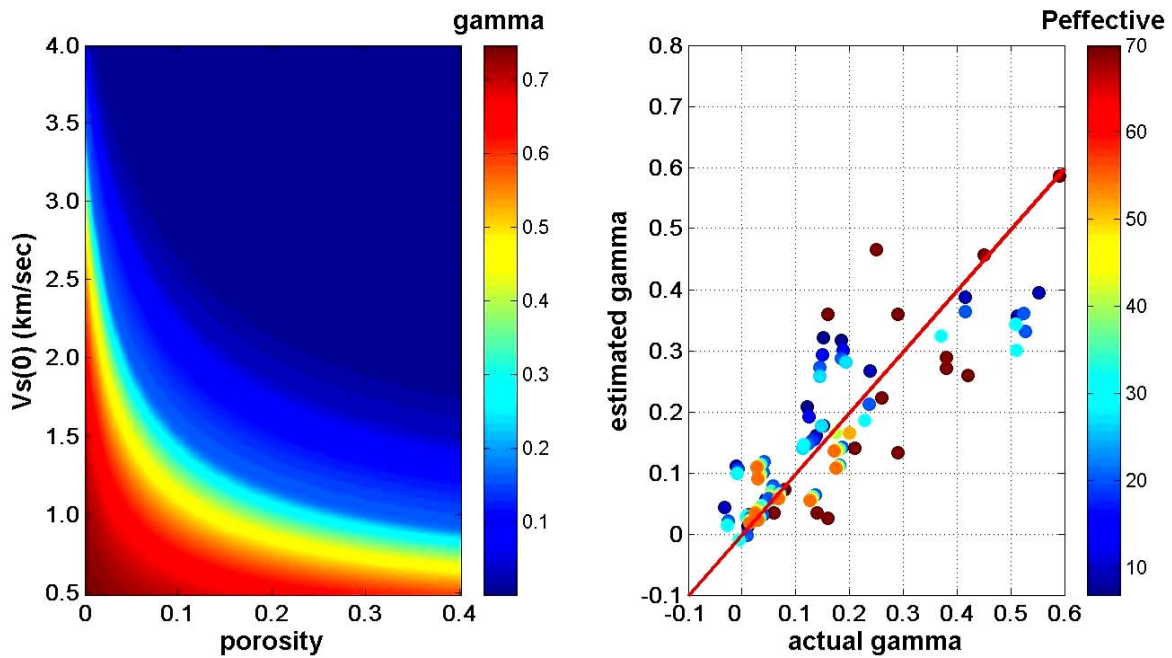


Figure 2.8: Estimation result of the anisotropy parameter  $\gamma$  in the  $V_s(0)$  vs. porosity domain for brine-saturated sand and shale. Right: actual  $\gamma$  vs. the estimated  $\gamma$ . The red line is the 1:1 trend.

An alternative way to determine  $\gamma$  is direct regression from  $\varepsilon$ . Wang (2002) provided a linear regression for his whole dataset as shown below:

$$\gamma = -0.01049 + 0.9560\varepsilon. \quad (2.12)$$

I derive a slightly different regression from the compiled dataset for brine-saturated sandstone and shale as follows:

$$\gamma = -0.0282 + 1.2006\varepsilon. \quad (2.13)$$

When sonic-log velocities are very low, around the lowest limit of the distribution of compiled data in Figure 2.4, it is better to use a direct regression to estimate  $\gamma$ , since the compiled dataset does not contain many data points in the low-velocity range; the data are broadly scattered in that range. Figure 2.9 presents regressions between  $M_2$  and  $\varepsilon$  on the left, as well as  $M_2$  and  $\gamma$  on the right. In this figure, sandstone is color-coded in yellow, siliceous shale in red, and shale in brown.

At this point, we have  $Vp(0)$ ,  $Vs(0)$ ,  $\varepsilon$ , and  $\gamma$ , so that we can calculate the four stiffness constants of a TI medium,  $C_{11}$ ,  $C_{33}$ ,  $C_{44}$ , and  $C_{66}$ , by adding density information. Furthermore, to determine  $C_{13}$ , I adopt a linear regression between  $C_{12}$  and  $C_{13}$  in the database for brine-saturated sandstone and shale. Given this regression, we compute  $\delta$  as follows:

$$C_{33} = Vp(0)^2 \rho, \quad (2.14)$$

$$C_{44}=Vs(0)^2\rho,$$

$$C_{11}=2\varepsilon C_{33}+C_{33},$$

$$C_{66}=2\gamma C_{44}+C_{44},$$

$$C_{12}=C_{11}-2C_{66},$$

$$C_{13}=0.9749C_{12}-2.3471,$$

$$\delta=\{(C_{13}+C_{44})^2-(C_{33}-C_{44})^2\}/2C_{33}(C_{33}-C_{44}).$$

However, the result shows the highly scattered distribution of  $\delta$  as displayed in Figure 2.10. The large estimation errors may induce significant miscalculation of velocity during anisotropy correction when the estimated  $\delta$  is used.

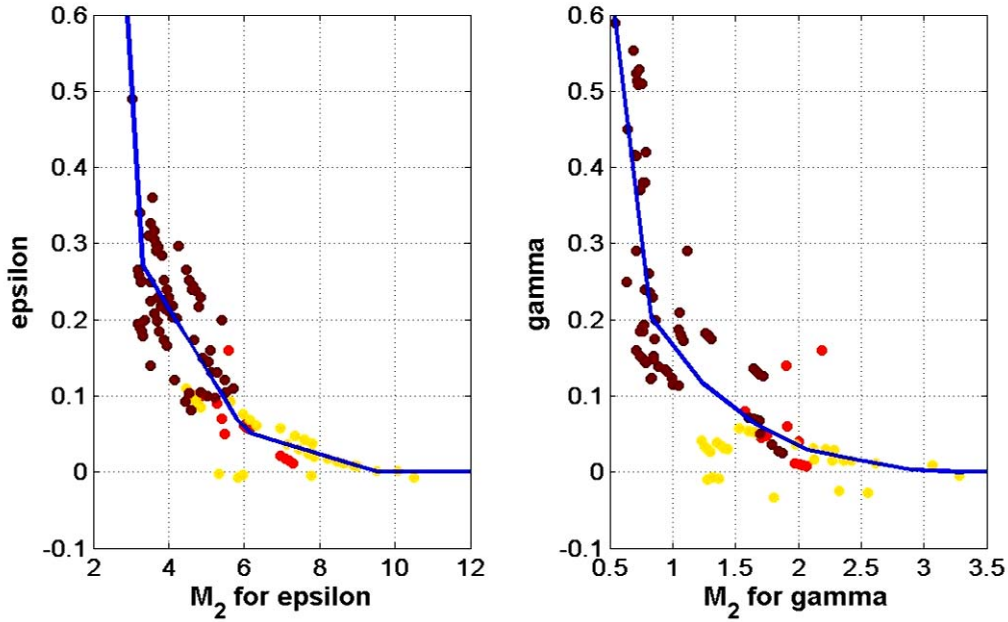


Figure 2.9: Regressions between epsilon and the  $M_2$  calculated for epsilon; also between gamma and the  $M_2$  calculated for gamma. The color indicates lithology: yellow represents sand, red is siliceous shale, and brown is shale. The blue lines indicate the employed regression lines to generate Figures 2.7 and 2.8.

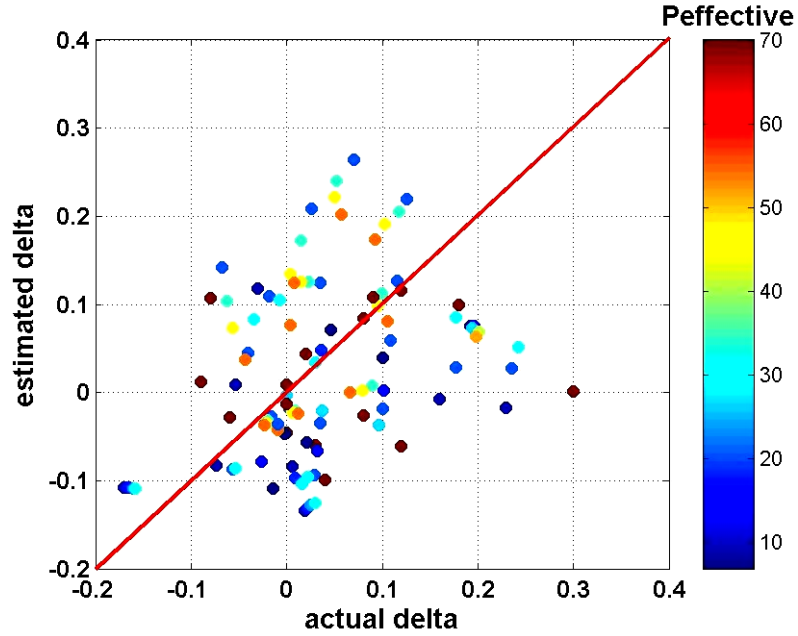


Figure 2.10: The estimation result of the anisotropy parameter  $\delta$  for brine-saturated sand and shale. The red line is the 1:1 trend.

To clarify the contribution of the  $\delta$  term, I compare the results of the velocity anisotropy correction for  $V_p$  with and without the  $\delta$  term. First, I determine the angle velocities for the dataset using Thomsen's exact equation. The first column of Figure 2.11 shows the difference between the actual  $V_p$  at the given propagation angle and the  $V_p(0)$ . The horizontal axis of the histograms represents velocity difference in km/sec. At higher angles, actual  $V_p$  is always higher than  $V_p(0)$ . Nevertheless, the velocity difference depends on the degree of velocity anisotropy of each rock sample. The second column from the left corresponds to the difference between the actual  $V_p$  and the result of the anisotropy correction by Thomsen's exact equation, using my estimated  $\varepsilon$  and  $\delta$ . Most data are corrected into appropriate ranges, yet we observe slight miscorrection due to the estimation error of  $\delta$  value for smaller angles. The third and fourth column shows the differences between the actual  $V_p$  and the corrected results using Thomsen's

approximation. For the third column, I adopt the estimated  $\varepsilon$  and  $\delta$  in the computation, whereas I omit the  $\delta$  term of the equation for the fourth column.

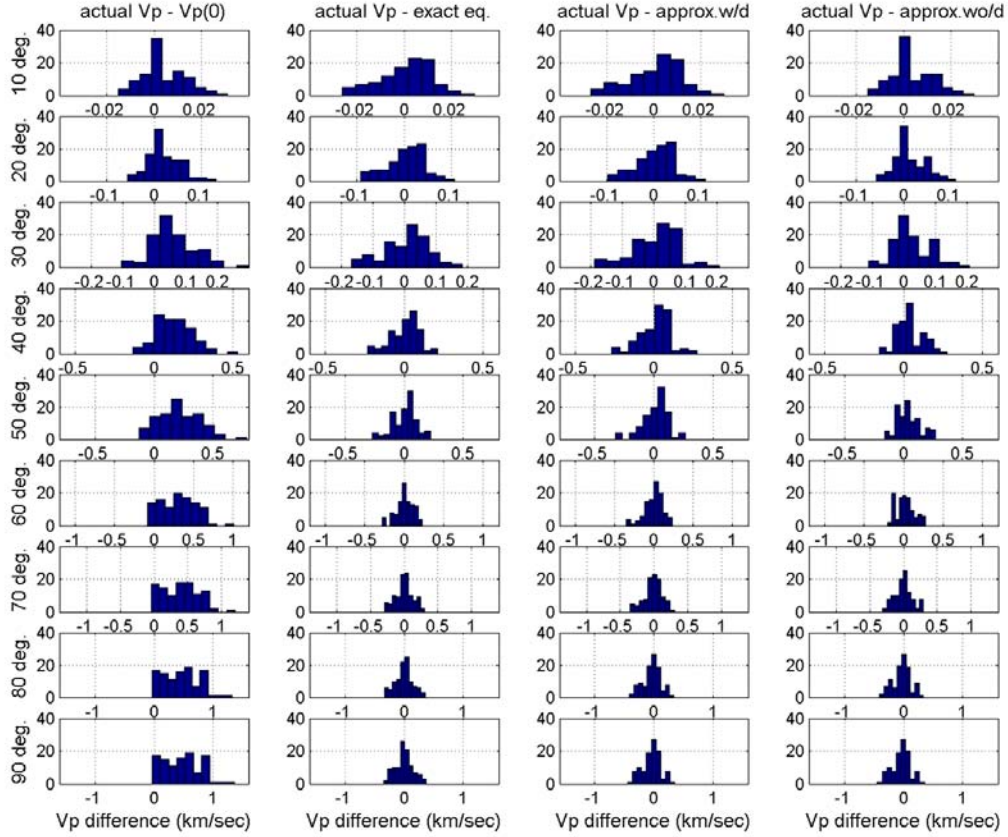


Figure 2.11: Histograms of velocity differences. From the left, first column: actual velocity at the angle, minus  $V_p(0)$ ; second column: actual velocity at the angle, minus estimated velocity by Thomsen's exact equation with estimated  $\varepsilon$  and  $\delta$ , third column: actual velocity minus estimated velocity by Thomsen's approximation equation with estimated  $\varepsilon$  and  $\delta$ ; fourth column: actual velocity minus estimated velocity by Thomsen's approximation equation without the  $\delta$  term.

Note that even though I omit the  $\delta$  term of Thomsen's approximation, the effect of the anisotropy correction remains almost the same. Figure 2.12 shows the quantitative comparison of the histograms of  $V_p$  difference in terms of the mean and standard deviation of the distribution.

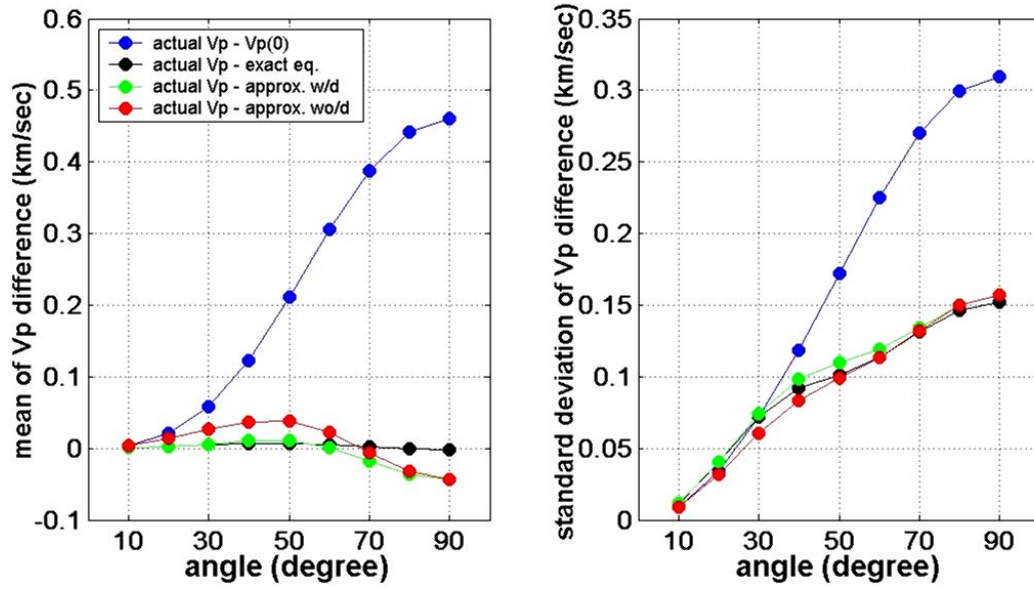


Figure 2.12: Quantitative comparison of the histograms in Figure 2.11. The left chart exhibits the mean of the  $V_p$  difference and the right chart shows standard deviation of the  $V_p$  difference. The blue dots correspond to the first column from the left in Figure 2.11, black dots represent the second column, green dots represent the third column, and the red dots indicate the data from the fourth column.

From these investigations, I conclude that the simple equation below corrects velocity anisotropy for  $V_p$  sufficiently well:

$$V_p(\theta) = V_p(0)[1 + \varepsilon \sin^4 \theta]. \quad (2.15)$$

For S-waves, in case of well deviation exceeding around  $50^\circ$ , I assume the logging device measures  $V_{S_{horizontal}}$ , which is the fast  $V_s$  in this angle range. Then, I employ Thomsen's approximation equation for the correction of  $V_{S_{horizontal}}$  as follows:

$$V_s(\theta) = V_s(0)[1 + \gamma \sin^2 \theta]. \quad (2.16)$$

Since I define a method for calculating anisotropy parameters from velocity and porosity as illustrated in Figures 2.7 and 2.8, we can derive a relationship among  $V_p(\theta)$ , porosity, and  $\varepsilon$ , or a relationship among  $V_s(\theta)$ , porosity, and  $\gamma$ , for any arbitrary deviation angles. For an example of the P-wave case, I convert the vertical axis of the left chart in

Figure 2.7 from  $Vp(0)$  to  $Vp(\theta)$ , based on a well deviation angle  $\theta$ , using the Equation (2.15). Then, I determine  $\varepsilon$  corresponding to the sonic-log velocity,  $Vp(\theta)$ , and porosity from a well-log analysis. In this way, I can determine the anisotropy parameters and calculate the normal incident velocities from the well-log information of any single well, as demonstrated in Figure 2.2. I demonstrated the application of my method in the first section. This method is empirical, so we may need to calibrate the trends when the laboratory measurements of velocities, porosity, and anisotropy parameters are available in a target area. However, the method is robust and suitable for any practical use. One important point of this method is that well-log velocities should be fluid-substituted to a brine-saturated condition before applying the anisotropy correction.

## 2.5 Alternative methods

Besides the approximation method discussed above, I examined several alternative methods, including different regression curves in the  $Vp(0)$ -porosity domain, utilizing density instead of porosity, and a neural-network approach. Figure 2.13 exhibits the result from a neural network: it is trained with  $Vp$  and porosity from my database. The correlation between actual  $\varepsilon$  and the estimated  $\varepsilon$  exhibits a better match than my method, as shown in the right chart of Figure 2.13. However, when we simulate the distribution of  $\varepsilon$  in  $Vp(0)$ -porosity domain, we observe an irregular distribution of  $\varepsilon$ , due to an over-fitting by the neural network, as shown in the left chart of Figure 2.13. This roughness of the distribution causes unstable calculations of  $\varepsilon$  in the application of this neural network to actual data.

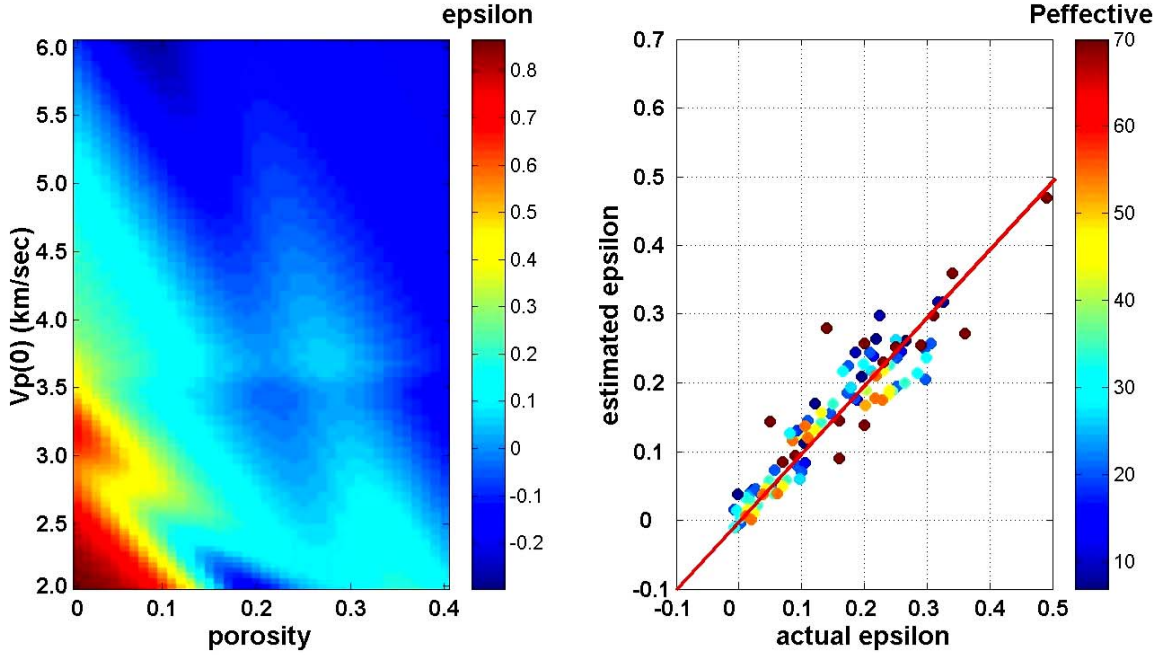


Figure 2.13: Estimation result of the anisotropy parameter  $\varepsilon$  by a neural network. Right: Actual  $\varepsilon$  vs. the estimated  $\varepsilon$ . The red line is the 1:1 trend.

Li (2002) proposed a method to estimate the velocity anisotropy  $\varepsilon$  from  $Vp(0)$  and clay volume in the equation below:

$$\varepsilon = (0.7V_{clay}(Vp(0) - Vp_{water})) / (Vp_{quartz} - Vp_{water} - 2.29V_{clay}). \quad (2.17)$$

I examine this equation for well data in comparison with my method. Figure 2.14 demonstrates the result. The resultant range of  $\varepsilon$  by Li's method often extends to high values. This fact suggests that the equation by Li needs scale adjustment. Furthermore, higher-velocity samples correspond to higher  $\varepsilon$  at the same clay volume in his method. This is because he used  $Vp(0)$  in the numerator in his equation. The resultant trend of  $\varepsilon$  in the  $Vp(0)$ -porosity domain does not agree with observations from the experimental

dataset. In the laboratory measurements, we recognized that lower  $Vp(\theta)$  corresponds to higher  $\varepsilon$  in the same porosity range.

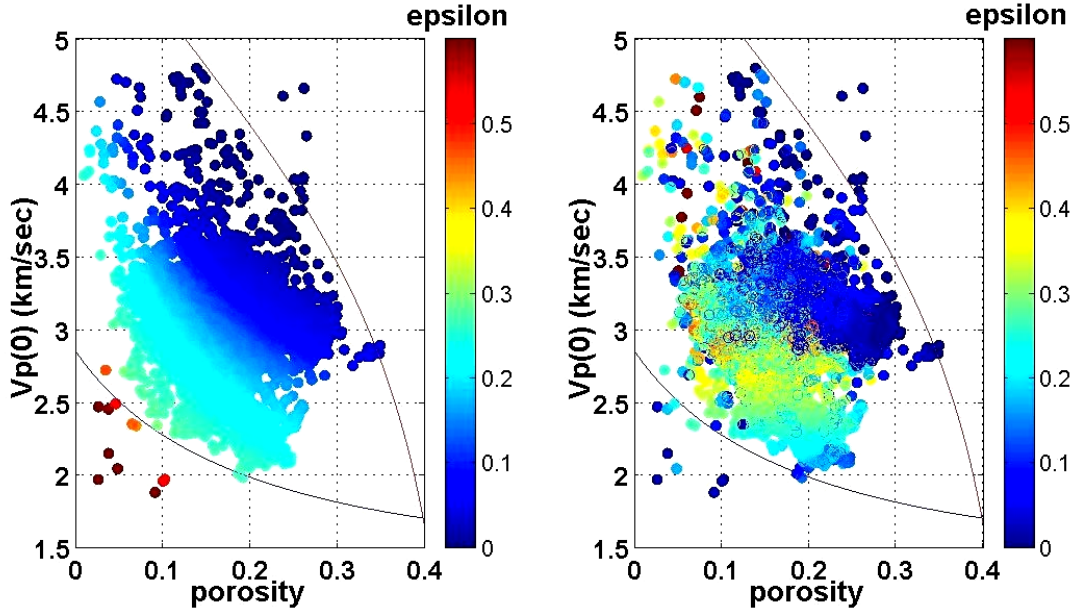


Figure 2.14: Comparison of estimation results of the anisotropy parameter  $\varepsilon$  in the  $Vp(\theta)$ -porosity domain. Left: the proposed method in this paper. Right: the method by Li (2002). The upper curve is the upper Hashin-Shtrikman bound of a quartz-water mixture with a critical porosity of 0.4. The lower curve is the Reuss bound of a clay-water mixture.

## 2.6 Conclusions

I developed estimation methods for velocity anisotropy parameters  $\varepsilon$  and  $\gamma$  from well-log information of a single well. To obtain the relationship between velocity, porosity, and anisotropy parameters, I used a regression method in the velocity-porosity domain for the compiled database of laboratory measurements, which consists of only brine-saturated sandstone and shale. The proposed methods estimate  $\varepsilon$  and  $\gamma$  within reasonable ranges, but I could not estimate  $\delta$  properly. I examined Thomsen's approximation equation for  $Vp(\theta)$  without the  $\delta$  term and validated it for computing  $\varepsilon$  and  $Vp(\theta)$  from

$V_p(\theta)$ , porosity, and well-deviation angle from well logs. I showed an application result, demonstrating its impact on AVO modeling. The new method is most suitable when the deviation angle exceed about  $50^\circ$ , where  $V_p(\theta)$  depends strongly on  $\varepsilon$  but not  $\delta$ ; in addition,  $V_s(\theta)$  corresponds to horizontal  $V_s$ .

It is inappropriate to extend this method to very low velocity ranges, such as below the Reuss bound of a clay-water mixture. The compiled dataset does not include enough control points in such low velocity ranges.

In the following chapters, I apply this correction method for velocity anisotropy to all the control wells in a case study dataset. Therefore, the seismic data analyses in the following chapters are based on the anisotropy-corrected velocities.

## REFERENCES

- Castagna, J., Batzle, M. and Kan, T., 1993, Rock Physics – The link between rock properties and AVO response, in *Offset Dependent Reflectivity – Theory and Practice of AVO Analysis*, J.P. Castagna and M. Backus, eds. Investigations in Geophysics, No. 8, Society of Exploration Geophysicists, Tulsa, Oklahoma, 135-171.
- Hornby, B., Howie, J. and Ince, D., 2003, Anisotropy correction for deviated-well sonic logs: Application to seismic well tie. *Geophysics*, **68**, 464-471.
- Li, Y., 2002, Anisotropic well logs and their applications in seismic analysis. SEG Expanded abstract 72nd Annual Meeting, 2459-2462.
- Lo, T. W., Coyner, K. B. and Toksoz, M. N., 1986, Experimental determination of elastic anisotropy of Berea Sandstone Chicopee Shale and Chelmsford Granite. *Geophysics*, **51**, 164-171.
- Mavko, G., Mukerji, T. and Dvorkin, J., 1998, *The Rock Physics Handbook, Tools for Seismic Analysis in Porous Media*, Cambridge University Press.
- Rowbotham, P., Marion, D., Eden, R., Williamson, P., Lamy, P. and Swaby, P., 2003, The implication of anisotropy for seismic impedance inversion. *First Break*, **21**, 53-57.
- Thomsen, L., 1986, Weak elastic anisotropy. *Geophysics*, **51**, 1954-1966.
- Thomsen, L., 2002, Understanding seismic anisotropy in exploration and exploitation: Distinguished Instructor Series, 5, Society of Exploration Geophysicists.
- Vernik, L. and Liu, X., 1997, Velocity anisotropy in shales: A petrophysical study. *Geophysics*, **62**, 521-532.

Wang, Z., 2002, Seismic anisotropy in sedimentary rocks, part 1: A single-plug laboratory method. *Geophysics*, **67**, 1415-1422.

Wang, Z., 2002, Seismic anisotropy in sedimentary rocks, part 2. Laboratory data: *Geophysics*, **67**, 1423-1440.

# Chapter 3

## Elastic-impedance analysis constrained by rock-physics bounds

### 3.1 Abstract

The reflection coefficient of seismic data is a function of the impedance contrast at a subsurface interface. Hence, by applying seismic inversion, I can derive rock impedance from seismic data. Impedance is more useful for reservoir characterization than interface responses such as seismic amplitude, since it is an interval property. However, if it is possible to decompose the impedance into two fundamental properties, namely velocities and density, I can utilize the currently available rock-physics applications both to determine the rock trend in the  $V_p$ - $\rho$  plane, and to derive quantitative rock properties, such as shale volume. In this chapter, I present a method of impedance decomposition using three elastic impedance data derived from the seismic inversion of angle stacks. I

discuss the effect of noise on the analysis as the most important reason that decomposition is difficult. Then, I show an innovative method incorporating rock-physics bounds as constraints for the analysis. The method is applied to an actual dataset from an offshore oil field; I demonstrate the result of analysis for sand-body detection.

### 3.2 Introduction

Elastic impedance ( $EI$ ) is the apparent seismic impedance at specific incident angles, which was derived by Connolly (1998, 1999) and Mukerji et al. (1998). This elastic impedance is a function of P-wave velocity ( $V_p$ ), S-wave velocity ( $V_s$ ), density ( $\rho$ ), and the incident angle ( $\theta$ ), based on the approximations of Zoeppritz's equations (1919) by Aki and Richards (1980), and Shuey (1985). Therefore, when we have elastic impedances for three different stack angles of the same seismic data, it is possible in principle to back-calculate  $V_p$ ,  $V_s$ , and  $\rho$  from the three elastic impedances. Very often, the maximum stack angle of seismic data is limited to be less than  $30^\circ$ , which is not wide enough to obtain stable calculation results. Hence, except when we have long-offset seismic data with the offset angles beyond around  $60^\circ$ , it is generally impractical to calculate  $V_p$ ,  $V_s$ , and  $\rho$  separately from the seismic data.

Instead of calculating  $V_p$ ,  $V_s$ , and  $\rho$  directly from elastic impedances, desired properties are most often estimated by establishing empirical relationships between the impedance and the rock properties at well locations using well-log data. Whitcomb et al. (2002) introduced extended elastic impedance ( $EEI$ ) in a modified form of elastic impedance using  $\tan\chi$  as an alternative for  $\sin^2\theta$  of the incident angle. Then, they

extended the linear trend of the impedance change as a function of  $\sin^2 \theta$  of the incident angle, from negative infinity at  $\chi = -\pi/2$  to positive infinity at  $\chi = \pi/2$ , in place of a limited extension of the horizontal axis from 0 at  $\theta = 0$  to 1 at  $\theta = \pi/2$ . In the same paper they demonstrated the lithology impedance and the fluid impedance for specific  $\chi$  values. However, all indicators still represent impedance. With this approach one cannot take advantage of well-known rock physics trends in the velocity-density or  $V_p$ - $V_s$  domains.

In this chapter, I explore the effect of random and offset-consistent noise as the source of miscalculation for deriving  $V_p$ ,  $V_s$  and  $\rho$ . Next, I develop a method to stabilize and improve the calculation, by applying constraints based on rock-physics bounds. I validate the method by analyzing 3-D seismic data of an actual oil field; I demonstrate the result of delineating sand-body distribution by implementing the method.

### 3.3 Noise effect in elastic-impedance analysis

Elastic impedance is expressed in the formula below:

$$EI(\theta) = V_p^a V_s^b \rho^c, \quad (3.1)$$

where

$$\begin{aligned} a &= 1 + \tan^2 \theta, \\ b &= -8K \sin^2 \theta, \\ c &= 1 - 4K \sin^2 \theta, \\ K &= (V_s / V_p)^2. \end{aligned}$$

One way to think of elastic impedance is that contrast of  $EI(\theta)$  at a layer boundary determines the reflectivity at that angle, analogous to the way that normal incidence reflectivity is determined by the contrast of acoustic impedance.

Therefore, when I have three different elastic impedances corresponding to three seismic stack angles of  $\theta_n$ ,  $\theta_m$ , and  $\theta_f$ , the relation can be expressed in a matrix form:

$$\begin{pmatrix} \ln EI(\theta_n) \\ \ln EI(\theta_m) \\ \ln EI(\theta_f) \end{pmatrix} = \begin{pmatrix} 1 + \tan^2 \theta_n & -8K \sin^2 \theta_n & 1 - 4K \sin^2 \theta_n \\ 1 + \tan^2 \theta_m & -8K \sin^2 \theta_m & 1 - 4K \sin^2 \theta_m \\ 1 + \tan^2 \theta_f & -8K \sin^2 \theta_f & 1 - 4K \sin^2 \theta_f \end{pmatrix} \begin{pmatrix} \ln Vp \\ \ln Vs \\ \ln \rho \end{pmatrix}. \quad (3.2)$$

Equation 3.2 is a general matrix form to relate three unknowns ( $\ln Vp$ ,  $\ln Vs$ ,  $\rho$ ) to three measurements ( $\ln EI(\theta_n)$ ,  $\ln EI(\theta_m)$ ,  $\ln EI(\theta_f)$ ), when all angles and  $K$  are known. Consequently, when three  $EI$ s are available from elastic impedance inversions of seismic data, it is possible in principle to calculate  $Vp$ ,  $Vs$ , and  $\rho$  by multiplying the inverse matrix of the first matrix on the right-hand side in Equation 3.2 to both sides of the equation from the left; I obtain Equation 3.3:

$$\begin{pmatrix} 1 + \tan^2 \theta_n & -8K \sin^2 \theta_n & 1 - 4K \sin^2 \theta_n \\ 1 + \tan^2 \theta_m & -8K \sin^2 \theta_m & 1 - 4K \sin^2 \theta_m \\ 1 + \tan^2 \theta_f & -8K \sin^2 \theta_f & 1 - 4K \sin^2 \theta_f \end{pmatrix}^{-1} \begin{pmatrix} \ln EI(\theta_n) \\ \ln EI(\theta_m) \\ \ln EI(\theta_f) \end{pmatrix} = \begin{pmatrix} \ln Vp \\ \ln Vs \\ \ln \rho \end{pmatrix}. \quad (3.3)$$

The practical problem is that the matrix is poorly conditioned unless  $\theta_n \ll \theta_m \ll \theta_f$ .

As an example, I use a portion of the actual well-log data to calculate the exact  $EI$ s of three different angles (  $9^\circ$ ,  $15^\circ$  and  $23.5^\circ$ ) according to the stack angles of the seismic data of the target oil field.

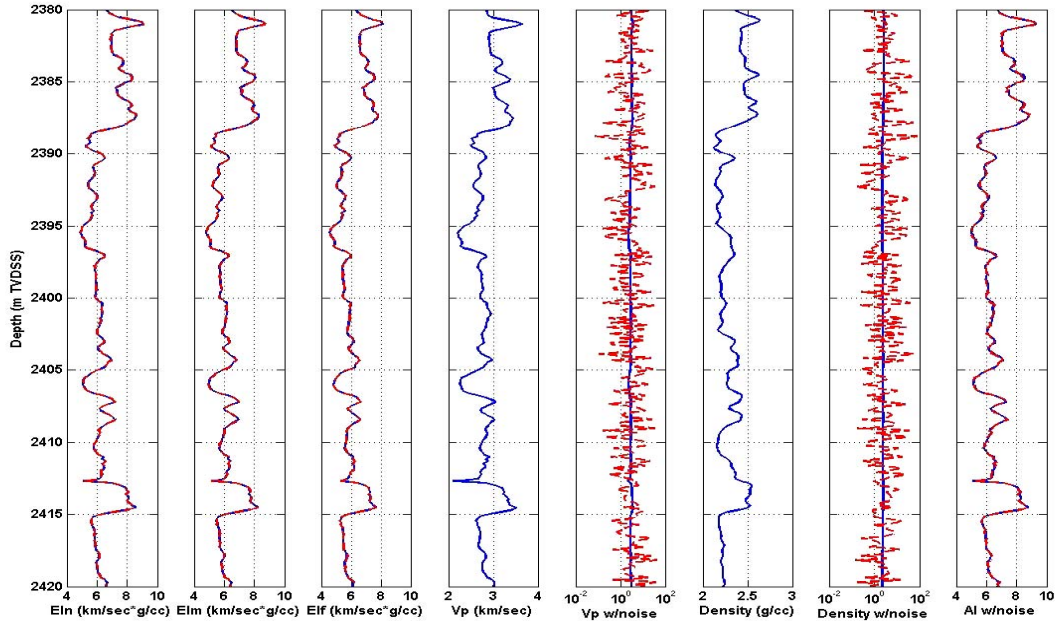


Figure 3.1: The result of inverse calculation for  $V_p$  and  $\rho$  from three  $EI$ s. The left three columns show exact  $EI$ s in blue and data with 1% random noise added in the dashed red line. The 4<sup>th</sup> and 6<sup>th</sup> columns from the left are actual  $V_p$  and  $\rho$ . The 5<sup>th</sup> and 7<sup>th</sup> columns are comparisons between the actual data in blue and the back-calculated result in the dashed red line for  $V_p$  and  $\rho$  respectively. The right-most column exhibits acoustic impedance in the same color scheme.

After adding 1% random noise for all  $EI$ s, but different noise profiles for each  $EI$ , I back-calculate  $V_p$ ,  $V_s$ , and  $\rho$  from the  $EI$ s by the inverse matrix method of Equation 3.3, Figure 3.1 shows the result. In this figure the three columns on the left show  $EI$ s of the near, mid and far angles in blue for the original data, and as a dashed red line for the 1% noise-added data. Since the noise level is so small, we do not see a distinct separation between the two data sets. The 4<sup>th</sup> and 6<sup>th</sup> columns are the actual logs of  $V_p$  and  $\rho$ , respectively. The 5<sup>th</sup> and 7<sup>th</sup> columns present comparisons between the actual logs in blue and the inverse calculation results with noise-added data in dashed-red lines. Note that the horizontal scale is logarithmic in these comparisons. The results demonstrate that the miscalculations are very high, more than 0.1 to 10 times of the original data. Since the calculations were performed on the three  $EI$ s, the errors in  $V_p$  and  $\rho$  are anti-

correlated; where we calculate very high  $V_p$ , we have very low  $\rho$ , and vice versa. The product of  $V_p$  and  $\rho$ , acoustic impedance, exhibits only small errors, as shown in the right-hand column of the same figure.

This simple calculation illustrates that it is extremely difficult to reliably derive  $V_p$ ,  $V_s$  and  $\rho$  from  $EIs$  spanning a narrow range of angles. Even 1% random noise may totally invalidate the calculation result. This problem is the main reason why researchers prefer to use impedance data directly to estimate rock properties rather than decomposing the impedance into velocity and density.

Next, let us change the noise scheme to offset-consistent noise. In other words, I add exactly the same noise to each of three  $EIs$  at the same depth point. Figure 3.2 summarizes the calculation result of this scheme with a noise level of 10% of the original data. The column allocation and the color code are the same as shown in Figure 3.1, except that I display the comparison of  $V_s$  in the right-most column instead of the acoustic impedance. Since the noise level is 10 times higher than in the previous case, the separation between the original  $EI$  in blue and the noise-added  $EI$  in red is distinguishable in the left three columns. However, the most remarkable difference from the previous result is in comparisons of  $V_p$ ,  $V_s$  and  $\rho$ . I observe an almost perfect match for  $V_p$  and  $V_s$ , with only small miscalculation for  $\rho$ . This result suggests that the inverse calculation is not sensitive to noise consistent across the  $EIs$ . Figure 3.3 demonstrates the calculation result for a higher level of offset-consistent noise. In this case, the noise level is 25% of the original  $EI$  data. Even at this high noise level, the calculated  $V_p$  does not exhibit any error, whereas I observe the highest errors in  $\rho$  and small errors in  $V_s$ .

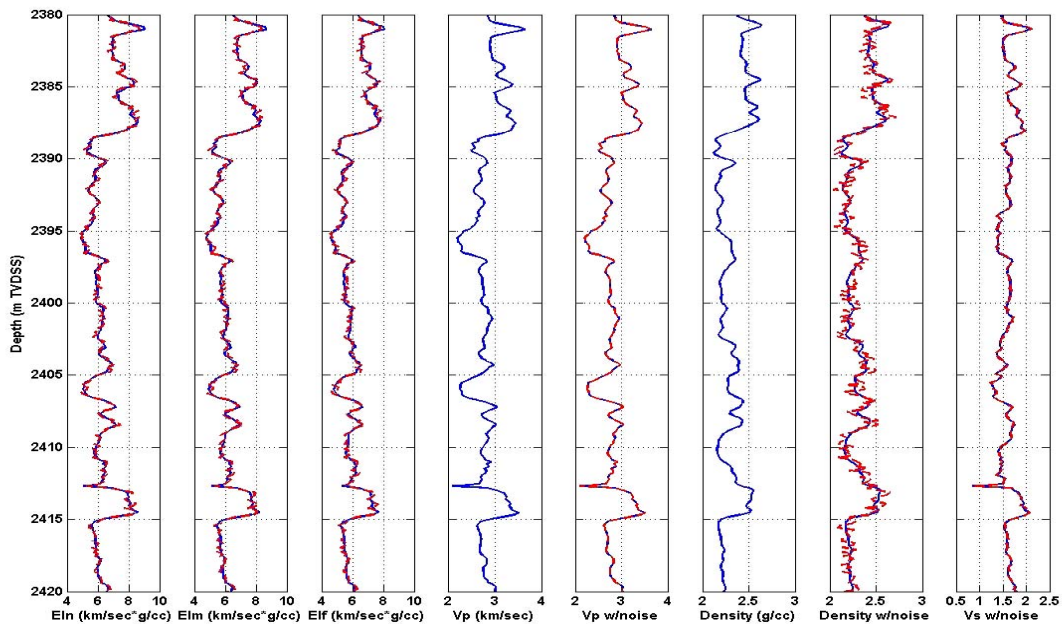


Figure 3.2: The result of the inverse calculation for  $V_p$ ,  $V_s$  and  $\rho$  from three  $EI$ s with 10% offset-consistent noise. The column allocation and color code are the same as in Figure 3.1. The right-most column exhibits the  $V_s$  comparison. Note the separation between the actual data in blue and the calculation result in red is minimal in  $V_p$  and the largest in  $\rho$ .

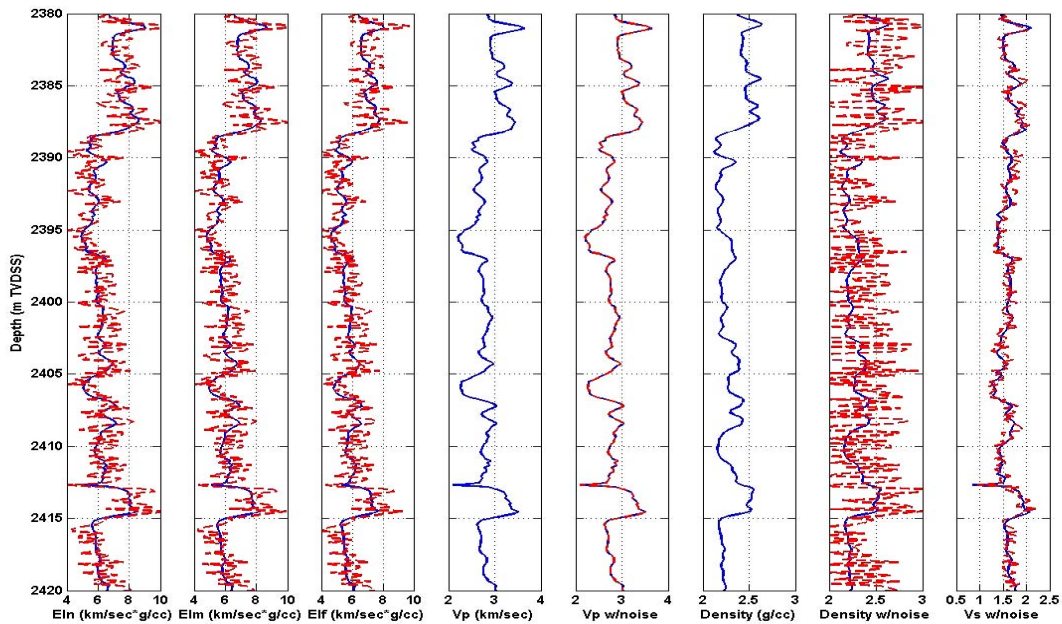


Figure 3.3: The result of inverse calculation for  $V_p$ ,  $V_s$  and  $\rho$  from three  $EI$ s with 25% offset-consistent noise. The column allocation and color code are the same as in Figure 3.1. Note that despite the high noise level,  $V_p$  does not exhibit any estimation errors, whereas I observe the highest error in  $\rho$  and much smaller miscalculations in  $V_s$ .

### 3.4 Theoretical assessment of noise effect

I investigated the inverse matrix calculation in general form to obtain a clear explanation for the observations discussed in the previous section. First, I set  $K=0.25$ , which is equivalent to a  $Vp/Vs$  ratio equal to 2, to simplify the matrix form, which results in the following:

$$\begin{pmatrix} \ln Vp \\ \ln Vs \\ \ln \rho \end{pmatrix} = \begin{pmatrix} 1/\cos^2 \theta_n & -2\sin^2 \theta_n & \cos^2 \theta_n \\ 1/\cos^2 \theta_m & -2\sin^2 \theta_m & \cos^2 \theta_m \\ 1/\cos^2 \theta_f & -2\sin^2 \theta_f & \cos^2 \theta_f \end{pmatrix}^{-1} \begin{pmatrix} \ln EI(\theta_n) \\ \ln EI(\theta_m) \\ \ln EI(\theta_f) \end{pmatrix}. \quad (3.4)$$

Then, using algebra to derive the inverse matrix in a 3 x 3 matrix form, eventually I obtain the inverse matrix with a scale factor of  $1/A$ , as described in Equation 3.5:

$$\frac{1}{A} \begin{pmatrix} 2(\cos^2 \theta_m - \cos^2 \theta_f) & 2(\cos^2 \theta_f - \cos^2 \theta_n) & 2(\cos^2 \theta_n - \cos^2 \theta_m) \\ \frac{\cos^2 \theta_m}{\cos^2 \theta_f} - \frac{\cos^2 \theta_f}{\cos^2 \theta_m} & \frac{\cos^2 \theta_f}{\cos^2 \theta_n} - \frac{\cos^2 \theta_n}{\cos^2 \theta_f} & \frac{\cos^2 \theta_n}{\cos^2 \theta_m} - \frac{\cos^2 \theta_m}{\cos^2 \theta_n} \\ 2\left(\frac{\sin^2 \theta_m}{\cos^2 \theta_f} - \frac{\sin^2 \theta_f}{\cos^2 \theta_m}\right) & 2\left(\frac{\sin^2 \theta_f}{\cos^2 \theta_n} - \frac{\sin^2 \theta_n}{\cos^2 \theta_f}\right) & 2\left(\frac{\sin^2 \theta_n}{\cos^2 \theta_m} - \frac{\sin^2 \theta_m}{\cos^2 \theta_n}\right) \end{pmatrix}, \quad (3.5)$$

where,

$$A = 2 \left( -\frac{\cos^2 \theta_n}{\cos^2 \theta_m} + \frac{\cos^2 \theta_m}{\cos^2 \theta_n} - \frac{\cos^2 \theta_m}{\cos^2 \theta_f} + \frac{\cos^2 \theta_f}{\cos^2 \theta_m} - \frac{\cos^2 \theta_f}{\cos^2 \theta_n} + \frac{\cos^2 \theta_n}{\cos^2 \theta_f} \right).$$

The most significant finding related to this inverse matrix is the sum of each row. The sums end up with 0 for the first row, -0.5 for the second row and 1 for the third row,

respectively independent of the selection of stack angles. Equation 3.6 summarizes the relationship in a simple form below:

$$\begin{pmatrix} \ln Vp \\ \ln Vs \\ \ln \rho \end{pmatrix} = \frac{1}{A} \begin{pmatrix} d_{11} & d_{12} & d_{13} \\ d_{21} & d_{22} & d_{23} \\ d_{31} & d_{32} & d_{33} \end{pmatrix} \begin{pmatrix} \ln EI_n \\ \ln EI_m \\ \ln EI_f \end{pmatrix}, \quad (3.6)$$

where,

$$\begin{aligned} \frac{1}{A} \sum_{j=1}^3 d_{1j} &= 0, \\ \frac{1}{A} \sum_{j=1}^3 d_{2j} &= -0.5, \\ \frac{1}{A} \sum_{j=1}^3 d_{3j} &= 1. \end{aligned}$$

Then, I express the inverse matrix calculation of noise-added  $EI$ s with the noise level  $\delta_N$  as follows:

$$\begin{aligned} \ln Vp &= \frac{1}{A} (d_{11} \ln EI_n + d_{12} \ln EI_m + d_{13} \ln EI_f) \\ &+ \frac{1}{A} (d_{11} \ln(1 + \delta_{Nn}) + d_{12} \ln(1 + \delta_{Nm}) + d_{13} \ln(1 + \delta_{Nf})), \\ \ln Vs &= \frac{1}{A} (d_{21} \ln EI_n + d_{22} \ln EI_m + d_{23} \ln EI_f) \\ &+ \frac{1}{A} (d_{21} \ln(1 + \delta_{Nn}) + d_{22} \ln(1 + \delta_{Nm}) + d_{23} \ln(1 + \delta_{Nf})), \\ \ln \rho &= \frac{1}{A} (d_{31} \ln EI_n + d_{32} \ln EI_m + d_{33} \ln EI_f) \\ &+ \frac{1}{A} (d_{31} \ln(1 + \delta_{Nn}) + d_{32} \ln(1 + \delta_{Nm}) + d_{33} \ln(1 + \delta_{Nf})). \end{aligned} \quad (3.7)$$

Therefore, when the noise is offset-consistent for all  $EI$ s, I notice that the noise effect of such offset-consistent noise is given in the following form by taking the relationship described in Equation 3.6 into account:

$$\begin{aligned}
noise\_effect\_for\_ln\ Vp &= \frac{1}{A}(d_{11} + d_{12} + d_{13})\ln(1 + \delta_N) = 0, \\
noise\_effect\_for\_ln\ Vs &= \frac{1}{A}(d_{21} + d_{22} + d_{23})\ln(1 + \delta_N) = -0.5\ln(1 + \delta_N), \quad (3.8) \\
noise\_effect\_for\_ln\ \rho &= \frac{1}{A}(d_{31} + d_{32} + d_{33})\ln(1 + \delta_N) = \ln(1 + \delta_N).
\end{aligned}$$

This result explains exactly what I observed in Figure 3.3, where  $Vp$  was not influenced by 25% offset-consistent noise on  $EIs$ , but the maximum noise effect is demonstrated in the determination of  $\rho$  and a small noise effect exists in  $Vs$ . In the actual application, the noise effect follows an exponential, so that when  $\rho$  has  $e^1=2.72$  noise effect,  $Vs$  will exhibit  $e^{-0.5}=0.61$  noise influence. In other words, the effect of offset-consistent noise on  $Vs$  is about 22% of that for  $\rho$ .

On the other hand, in the case of random noise, I expect all determinations of  $Vp$ ,  $Vs$  and  $\rho$  to be influenced by noise as expressed below:

$$noise\_effect_i = \frac{1}{A}(d_{i1} \ln(1 + \delta_{Nn}) + d_{i2} \ln(1 + \delta_{Nm}) + d_{i3} \ln(1 + \delta_{Nf})). \quad (3.9)$$

In Equation 3.9 the most important point is the factor  $1/A$ , which is given formulated in Equation 3.5. This scale factor is a function of the three stack angles of seismic data. The value varies widely, depending on the selection of stack angles. For example, assuming the seismic data with a near-stack angle of  $5^\circ$  and a far-stack angle of  $45^\circ$ , what is the optimal mid-stack angle to eliminate the influence of random noise for elastic-

impedance analysis? Figure 3.4 shows the scanning result of  $1/A$ ; I call it a noise enhancement factor, as a function of the middle-stack angle.

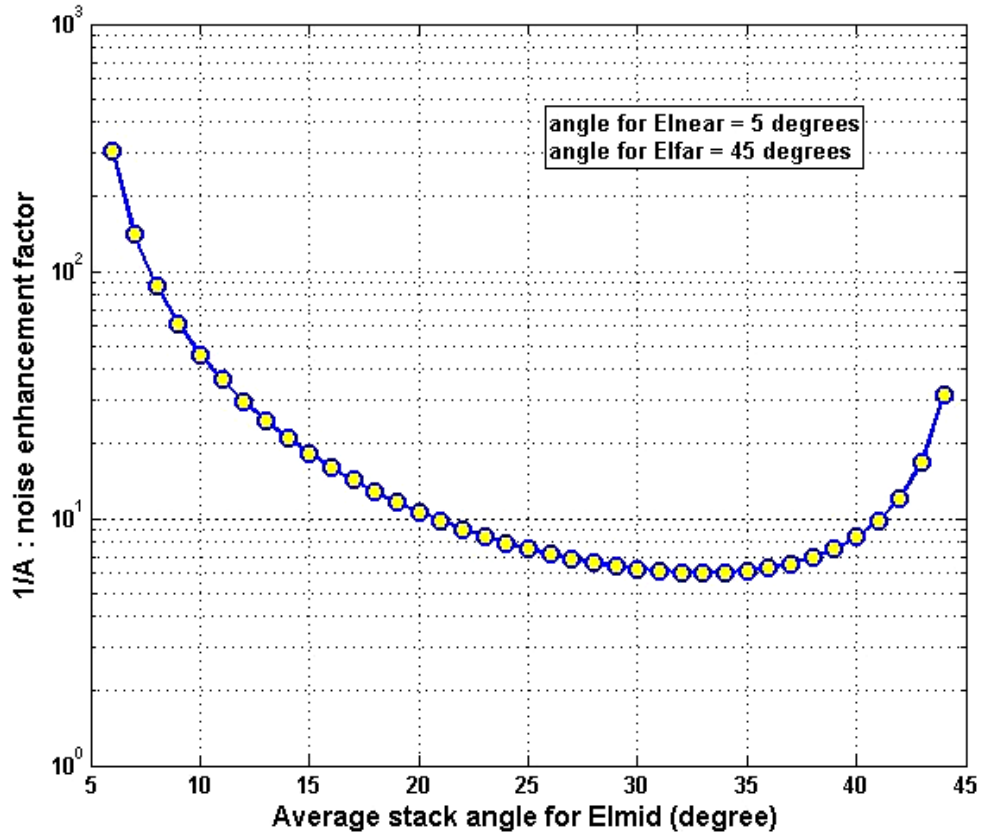


Figure 3.4: Scanning result for the optimal mid-stack angle of seismic data in terms of minimizing the effect of random noise on elastic-impedance analysis. I assumed a near-stack angle of  $5^\circ$  and a far-stack angle of  $45^\circ$  for this case.

Based on this scan result, we can determine that the optimal angle to minimize the random noise effect is about  $33^\circ$  for this case. Note that the answer is not just the midpoint of near-offset angle and far-offset angle. Another parameter affecting the calculation of  $1/A$  is  $K=(V_s/V_p)^2$ . Figure 3.5 shows the results of the calculation for  $1/A$  with varying  $V_p/V_s$ : 1.0, 1.2, 1.4, 1.6, 1.8, 2.0, 2.2, 2.4, 2.6, 2.8, 3.0, from the bottom to

the top. Although the resultant curves shift the locations as increasing  $Vp/Vs$ , the angle for the minimum  $1/A$  stays the same at  $33^\circ$ .

Likewise, it is possible to quantitatively evaluate the design of long-offset seismic acquisition to reduce the effect of random noise. When we have enough separation for the three stack angles,  $1/A$  can be less than 1, which means that we can dilute the random noise effect by taking sufficiently long offset for seismic data. In contrast to long-offset acquisition,  $1/A$  will be greater than 100, when the three angles are very close together.

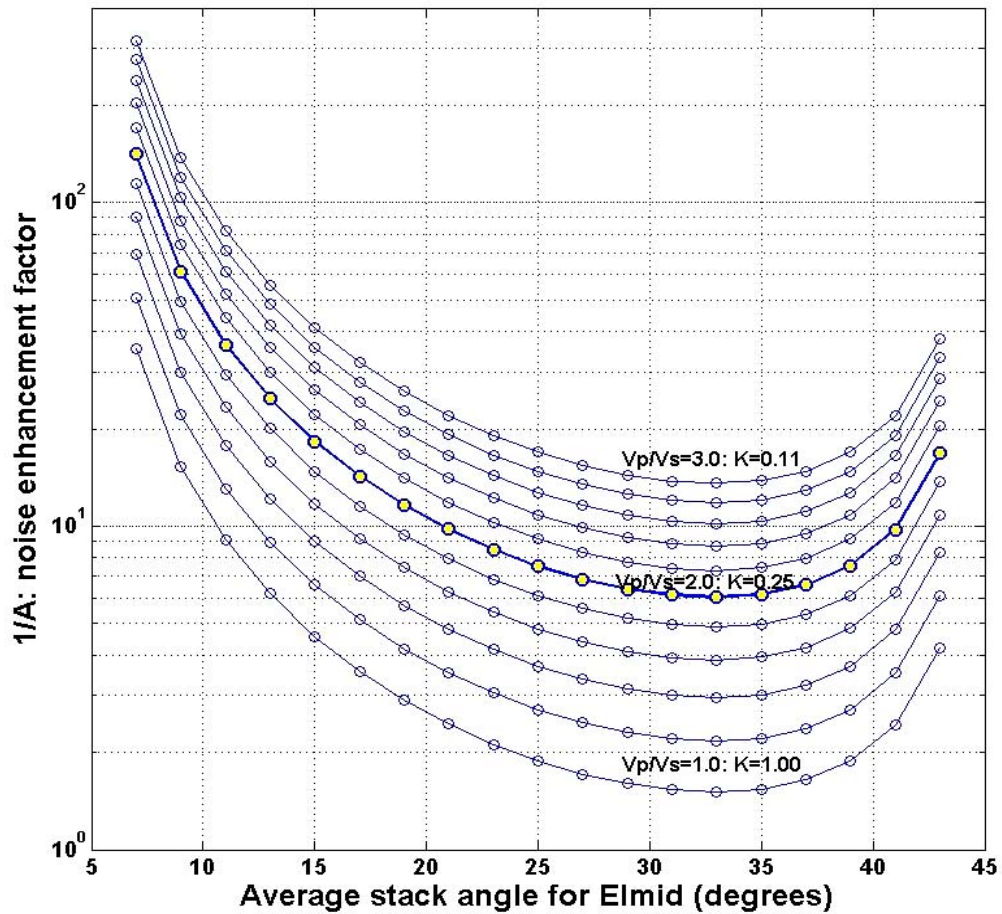


Figure 3.5: The calculation result of noise enhancement factor varying  $K=(Vs/Vp)^2$ .  $Vp/Vs$  changes from 3.0 to 1.0 by 0.2 increment from the top to the bottom. A near-stack angle of  $5^\circ$  and a far-stack angle of  $45^\circ$  are assumed. Note that the minimum value of  $1/A$  is obtained at  $33^\circ$  for all cases.

### 3.5 Possible sources of noise

In the consideration of noise, there are many possible sources of noise in seismic data acquisition, data processing and inversion analysis. Table 3.1 summarizes several sources and the category of noise.

Acquisition system can induce noise at the same level for all offsets, in such case the wavelet of seismic source is distorted from the ideal shape for entire survey. On the other hand, low energy shots and/or bad receiver responses happening occasionally are appeared to be random noise after the binning of 3-D data. Likewise, noise derived from acquisition conditions, such as swelling or feathering, is added trace by trace inconsistent to incident angles. This type of noise is categorized in random noise.

In data processing, first consideration is the remaining influence of multiple. For the case study dataset, the radon transform was used for suppressing multiple. Consequently, amplitudes along hyperbolic events are preserved. This means the energy of multiple remains only where the multiple signal across the hyperbolic events: the influence of remaining multiple is not offset-consistent. Another important source of errors in data processing is velocity analysis. When an inappropriate velocity model is assigned to some depth ranges, the velocity curve move-out the seismic data by inappropriate amounts, which depend on offset. If the estimation error of velocity is small, the move-out errors may occur in one direction, the resultant angle stack seismic data include both offset-consistent noise and random noise. In contrast, if the estimation error of velocity is large, each angle stack exhibits different influence from the inappropriate velocity model. In this case, the influence is categorized in random noise.

The possible main sources of offset-consistent noise are in seismic inversion analysis. First one is low frequency model generated by the well-log data of control. Low frequency model is indispensable to perform seismic inversion to provide a background trend of impedance change. However, when the well-log data include distorted values of velocity and/or density, the unreasonable values affect the low frequency models for all stack angles since the all models are derived from the same well-log data. In addition, in my case, I use a same wavelet to invert all seismic angle stacks since the angles are close enough ( $9^\circ$ ,  $15^\circ$ ,  $23.5^\circ$ ) and there is no significant difference among extracted wavelets for the three angles. By this application, the errors in wavelet estimation uniformly affect the inversion results of all offset angles. Note that using a common wavelet may induce offset-consistent noise but it reduces the risk of inducing random noise caused by employing different wavelets for different offset angles. When different wavelets are used for different angle stacks, the mismatches between the estimated wavelets and the seismic data are fully random, which are appeared as random noise in the inversion results.

Table 3.1: Summary of possible source and the category of noise.

|             | Possible source of noise                      | Offset-consistent noise | Random noise |
|-------------|---|-------------------------|--------------|
| Acquisition | Acquisition system (source, receiver)         | X                       | X            |
|             | Acquisition conditions (swelling, feathering) |                         | X            |
| Processing  | Remaining multiple influence                  |                         | X            |
|             | Inappropriate velocity model                  | X                       | X            |
| Inversion   | Errors in low frequency model                 | X                       |              |
|             | Insufficient wavelet matching                 | X                       | X            |

### 3.6 Constraints for elastic-impedance analysis

Based on the discussion about the effect of noise on elastic-impedance analysis, I notice that the precise balance among the three *EIs*, which is equivalent to eliminating the effect of random noise on the inverse-matrix calculation, is the key to deriving reasonable values of  $V_p$ ,  $V_s$  and  $\rho$ . I develop a method to restore balance among *EIs* from the noise-distorted *EIs* of the seismic-inversion results.

The first step is to find the least-squares linear fit in the  $\ln EI - \sin^2 \theta$  plane. Assuming the thickness of reservoir layer is thick enough relative to the seismic resolution, in smaller angles of seismic offset, up to around  $30^\circ$ , the reflection coefficient is expected to have a linear trend in the amplitude- $\sin^2 \theta$  plane; in other words, the reflection coefficient is half of the logarithmically scaled impedance response. At each seismic data point, I apply least-squares fitting to the *EIs* in the  $\ln EI - \sin^2 \theta$  plane to obtain the general trend as shown in Figure 3.6. Deviations of the data from the straight line are considered to indicate random errors in the *EIs*. The fit *EI* values are used in the subsequent interpretation.

The second step is to apply rock-physics bounds to constrain the distribution of *EIs* within a theoretically reasonable range. I examined well-log data in the target area to determine the constraining bounds for the actual dataset. Figure 3.7 shows the rock-physics bounds in the velocity-porosity planes. The left chart shows the upper and lower modified Hashin-Shtrikman bounds computed for a mixture of mineral at  $\phi=0$  (zero porosity) with soft sediment at  $\phi_c=0.4$  (a critical porosity). The green lines represent modified bounds for a quartz-water mixture; the red lines represent a mixture between the

average solid of the target field (Hill's average of felspathic arenite) and water; the blue lines are for a clay-water mixture in the  $V_p$ -porosity plane. I emphasize that these are modified bounds representing the soft sediment at  $\phi_c=0.4$  with mineral at  $\phi=0$ . The parameters used to calculate the bounds are summarized in Table 3.2.

Table 3.2: Summary of the parameters used to calculate the Hashin-Shtrikman bounds of sandstone.

| Material                                    | Bulk modulus (GPa) | Shear modulus (GPa) | Density (g/cm <sup>3</sup> )                      |
|---|--------------------|---------------------|---|
| quartz                                      | 37                 | 44.73               | 2.65  |
| average solid of the target field           | 35.64              | 28.17               | 2.66  |
| clay  | 23                 | 8                   | 2.58  |
| water                                       | 2.7416             | 0                   | 1.0038  |
| mixture at critical porosity ( $\phi=0.4$ ) | 4.3575             | 0.09                | $0.6\rho_{\text{solid}} + 0.4\rho_{\text{brine}}$ |

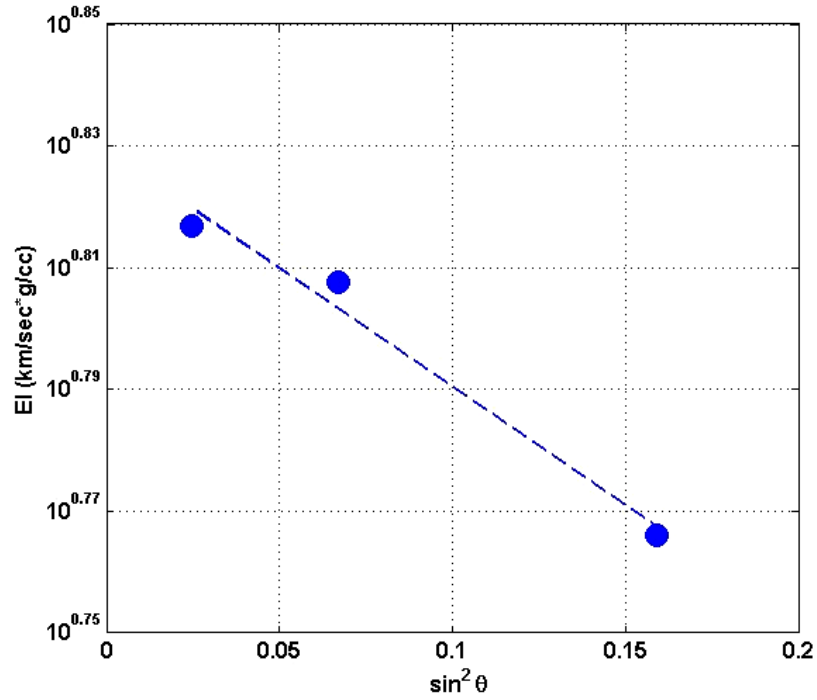


Figure 3.6: The first step of an  $EI$  analysis method. I apply a least-squares linear fitting to  $EI$ s in the  $\ln EI - \sin^2 \theta$  plane to obtain the general trend. Three points and the linear trend are extracted from an application for the actual data set.

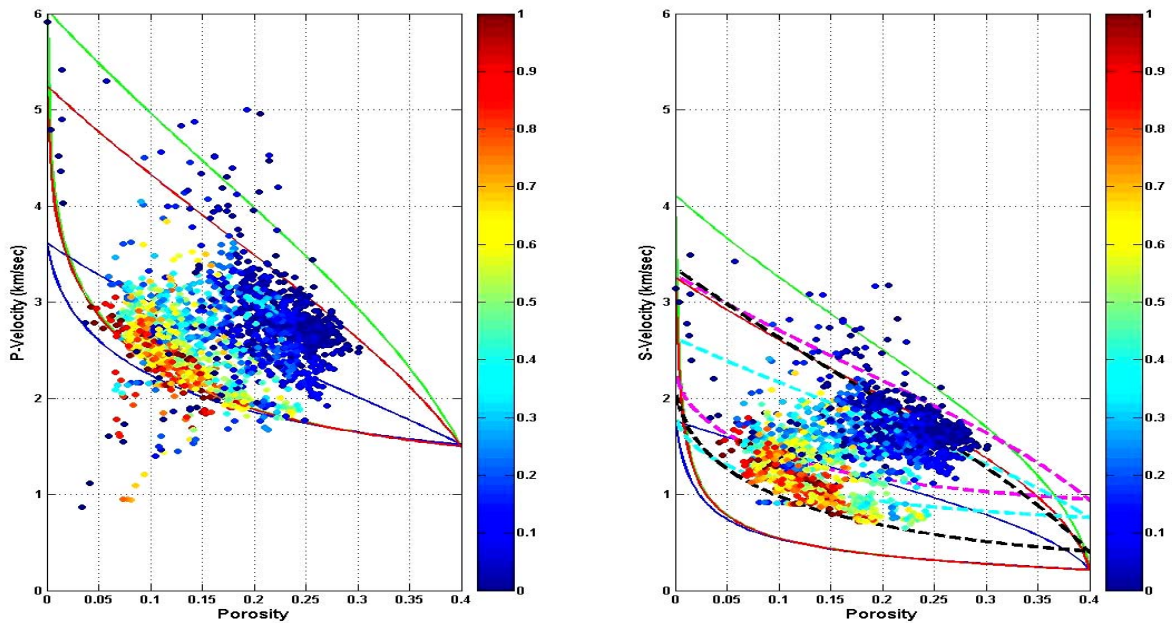


Figure 3.7: Comparison between the modified Hashin-Shtrikman bounds of several schemes and the distribution of actual data. The green lines represent a quartz-water mixture; the red lines indicate a mixture of water and the average solid of the target field; the blue lines represent a clay-water mixture. The dashed lines in the  $V_s$ -porosity plane are the transformed Hashin-Shtrikman bounds from the  $V_p$ -porosity plane using Equation 3.10 for black lines;  $V_p/V_s=1.6$  for magenta lines;  $V_p/V_s=2.0$  for cyan lines. All bounds have 0.4 as the critical porosity.

The data points in Figure 3.7 demonstrate well log data in the target area, color-coded by the shale volume in fractions.

The right chart in Figure 3.7 exhibits the same modified bounds and data in the  $V_s$ -porosity plane with three additional bound sets. The black dashed lines indicate the  $V_s$ -porosity bounds calculated from the Hashin-Shtrikman bounds in the  $V_p$ -porosity plane using modified Han's equation for the  $V_p$ - $V_s$  relation shown below, which gives us a good fit to the actual measurements in the study area:

$$V_s = 0.79V_p - 0.79. \quad (3.10)$$

The dashed magenta lines represent the transformed Hashin-Shtrikman bounds from the  $V_p$ -porosity plane, assuming that the  $V_p/V_s$  ratio is 1.6. The dashed lines in cyan are the transformed Hashin-Shtrikman bounds from the  $V_p$ -porosity plane, assuming that  $V_p/V_s$  is equal to 2.0. I used 0.09 GPa as the shear modulus at the critical porosity of water-saturated sandstone, which is compiled from the measurements of unconsolidated sandstone by Zimmer (2003).

Next, given a porosity- $\rho$  relation in the field, I converted the horizontal axis to density and generated Figure 3.8. In addition, I show the  $V_p/V_s$  trend in terms of density change in Figure 3.9. Since  $EI$  is a function of  $V_p$ ,  $V_s$  and  $\rho$  with an incident angle of  $\theta$ , the  $V_p/V_s$  trend is an important factor in selecting adequate rock-physics bounds to constrain the  $EI$  distribution. Figure 3.10 shows several bounds and the actual well-log data distribution, color-coded by the shale volume, in the  $EI(23.5^\circ)$ - $EI(9^\circ)$  plane. Considering all the plots described above, the appropriate bounds I selected to limit distribution of  $EIs$  are the dashed black bound for the upper limit and the dashed magenta line for the lower

limit in the  $EI(23.5^\circ)$ - $EI(9^\circ)$  plane. Since the variation of  $EI$ s is mainly controlled by  $V_p/V_s$ , the selection of appropriate rock-physics bounds for constraints is equivalent to the selection of the relevant  $V_p$ - $V_s$  relations.

Once I choose the bounds, the seismic inversion results are crossplotted in the  $EI_{far}$ - $EI_{near}$  plane, and all points in the plot are squeezed to lie between the upper and lower bounds in the direction orthogonal to the bound lines, keeping relative positions. The details of this process is explained in the next. Then I determine exactly the same relative locations between the bounds in  $EI_{mid}$ - $EI_{near}$  plane to obtain corrected  $EI_{mid}$ . By doing this, I correct the three  $EI$  values to fall within the expected bounds, while preserving the relative difference of  $EI$  responses derived from seismic impedance inversion.

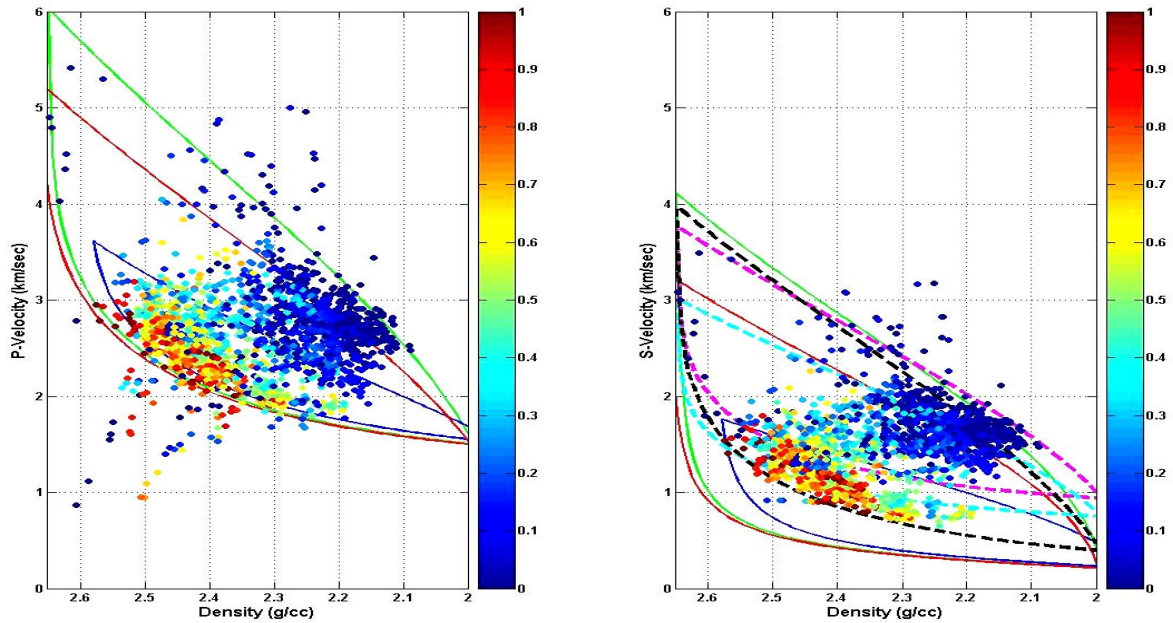


Figure 3.8: Comparison between the modified Hashin-Shtrikman bounds of several schemes and a distribution of actual data. The representation scheme is same as Figure 3.7. All modified bounds assume 0.4 for the critical porosity.

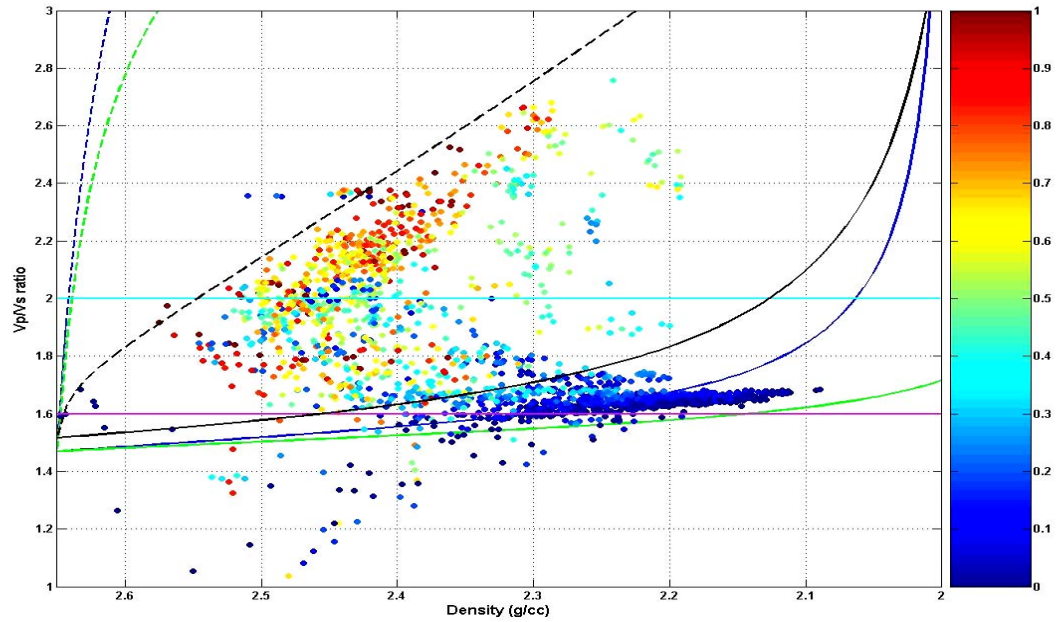


Figure 3.9: The modified Hashin-Shtrikman bounds of the schemes described in Figure 3.7 in the crossplot between the  $Vp/Vs$  ratio and density. The dashed lines correspond to the lower Hashin-Shtrikman bounds in the velocity-porosity plane; the solid lines are equivalent to the upper Hashin-Shtrikman bounds. Note that the upper and lower Hashin-Shtrikman bounds are coincident when  $Vp/Vs$  is a constant value.

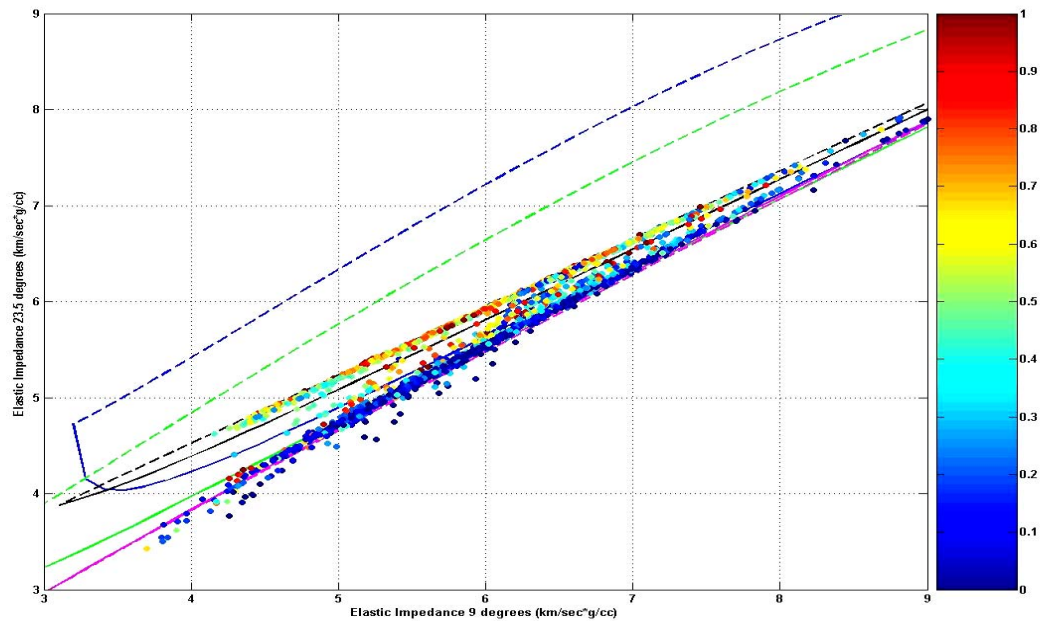


Figure 3.10: Comparison between the modified Hashin-Shtrikman bounds in the schemes described in Figure 3.7 and the actual data distribution calculated from well-log data. The dashed lines correspond to the lower Hashin-Shtrikman bounds; the solid lines are equivalent to the upper Hashin-Shtrikman bounds in the velocity-porosity plane.

### 3.7 Validation of the method with a case study

I applied the method described in the previous section to a dataset from an offshore oil field with four control wells, plus three angle stack seismic cubes with  $9^\circ$ ,  $15^\circ$  and  $23.5^\circ$  average offset angles. The target reservoir is interpreted as blanket sandstone sheets in the depositional environment of braided river channel stacks in the early Jurassic age. The well-log database includes all the standard logs from one vertical well and three deviated wells. The velocity logs for the deviated wells are corrected in terms of velocity anisotropy by the method discussed in Chapter 2. The  $V_s$  log is not available for all the wells, but I generate the  $V_s$  logs for necessary wells using Equation 3.10, since that equation gives us a good fit to the actual data of available  $V_p$  and  $V_s$  in this area, in a brine-saturated condition.

Figure 3.11 compares the results of the inverse-matrix calculation applied to the seismic cubes without the rock physics constraints. I compute  $V_p$ ,  $\rho$  and  $V_s$  from the  $EIs$  derived from the seismic data at the location of a vertical well, with and without a least-squares fit in the  $\ln EI - \sin^2 \theta$  plane. In the three columns on the left side, the red dashed lines display the resultant  $V_p$ ,  $\rho$  and  $V_s$  computed from the  $EIs$  without any processing. The right three columns demonstrate the  $V_p$ ,  $\rho$  and  $V_s$  calculated from the  $EIs$  extracted from a least-squares fit in the  $\ln EI - \sin^2 \theta$  plane as illustrated in Figure 3.6. In both cases, I show the actual  $V_p$ ,  $\rho$  and  $V_s$  in blue lines. The horizontal axes are in logarithmic scale. Note that the disagreement of the inverted  $V_p$ ,  $\rho$  and  $V_s$  relative to the actual well-log data subsequent to the least-squares fit are one order of magnitude less than for the original  $EIs$  without the least-squares correction. Furthermore, the shapes of the resultant

logs on the right are different from those on the left, suggesting that simply scaling the original results will never be equivalent to the least-squares processed results.

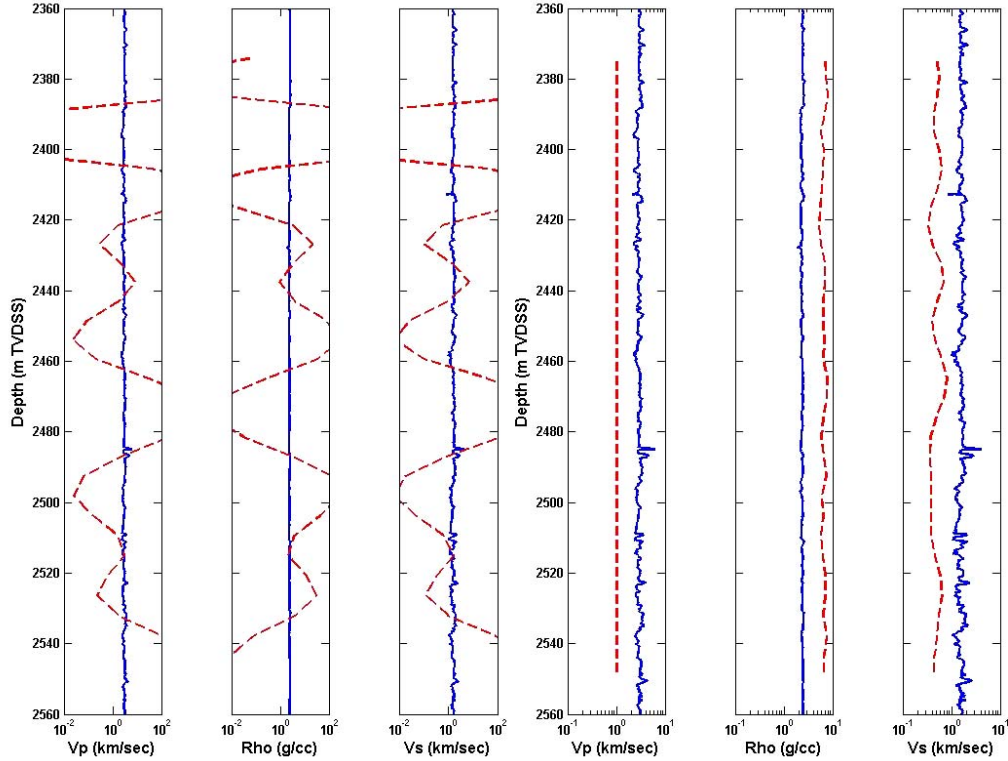


Figure 3.11: The inverse-matrix calculation results at a vertical well location from the unprocessed seismically derived  $EI$ s, in red, in the left three columns. The three right columns exhibit the calculation result from least-squares-fitted  $EI$ s in red. The blue lines are the actual well-log data. Note that the horizontal axes are logarithmic scale, but the range is one order smaller in the right half.

The second step is performed in  $EI_{far}-EI_{near}$  plane as in Figure 3.12. First, I fix the  $EI_{near}$  value, vertically compress the data variation of  $EI_{far}$  into the range of the-rock-physics bounds, and find vertical displacements ( $dY$ ). Next, I fix the  $EI_{far}$  and horizontally compress the data scattering of  $EI_{near}$  into the rock-physics bounds, to find horizontal displacements ( $dX$ ). Eventually, I employ trigonometric calculations to determine the diagonal shift ( $dx, dy$ ) from the horizontal displacement ( $dX$ ) and the vertical displacement ( $dY$ ) in Equation 3.11.

$$\begin{aligned} dx &= dXdY^2 / (dX^2 + dY^2) \\ dy &= dX^2 dY / (dX^2 + dY^2) \end{aligned} \quad (3.11)$$

The crossplot of  $EI_{far}$  and  $EI_{near}$  is displayed in Figure 3.12; red lines represent the employed rock-physics bounds; the blue lines are drawn to be parallel to the bounds whereas containing almost of the raw data. After corrections are applied, the blue lines coincide with the red lines together with all the data points.

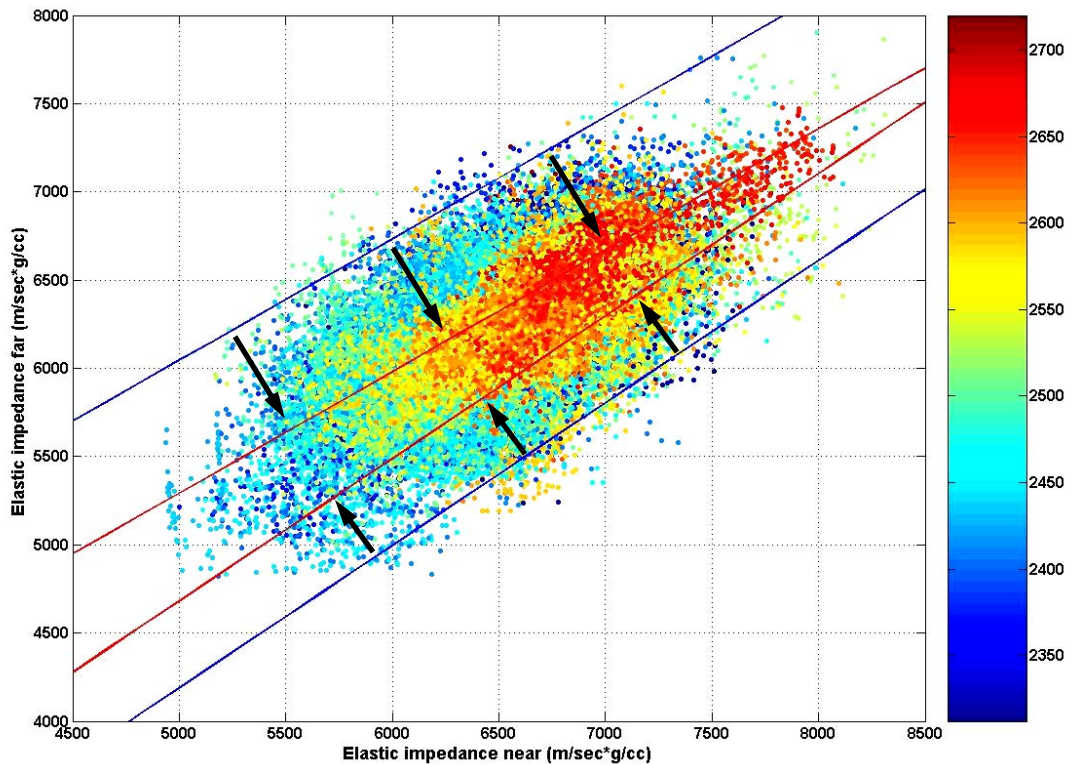


Figure 3.12: The crossplot of the seismically derived  $EI$  data between  $EI_{far}$  and  $EI_{near}$  before constraining with rock-physics bounds (after least-squares fit). The red lines are the employed rock-physics bounds; the blue lines are lines parallel to the bounds, which will coincide with the red lines after the second step. The color code is the two-way time of the seismic data point in millisecond.

After applying the second step, I extracted the corrected  $EI$ s from the seismic along the vertical well and computed  $Vp$ ,  $Vs$  and  $\rho$  by the inverse matrix method. Figure 3.13

shows the results in red, with the actual well-log data in blue. Since the analysis results are derived from the seismic inversion, I cannot obtain high resolution response at the top of the reservoir at an approximate depth of 2350m, due to the shoulder effect. In addition, I observe a spiky miscalculation in  $\rho$  at 2500m and a small drift in  $V_s$  in the range from 2460m to 2500m. However, the overall results are a significant improvement relative to the well data, so that we can grasp the trends of these three fundamental rock properties.

The rock-physics constraints discussed above correct the random-noise-distorted  $EI$  values: random noise expands the data scattering in a direction perpendicular to the rock physics bounds in Figure 3.12. On the other hand, offset-consistent noise alters the data location in a direction parallel to the rock physics bounds in Figure 3.12. Therefore the effect of offset-consistent noise is not eliminated by my method. It is suggested that the spiky miscalculations in  $\rho$  and  $V_s$  in Figure 3.13 are derived from offset-consistent noise. The level of the offset-consistent noise is not significant in this case since the red dashed lines capture the background trends of the well-log data in blue.

In addition, the residual between actual seismic trace and synthetic seismogram increases by applying my method. Any seismic-inversion algorithms minimize an objective function to find the best fit between the actual seismic and the inverted impedance using a wavelet. However, my method re-expands the residual to restore a better balance among the three  $EI$ s.

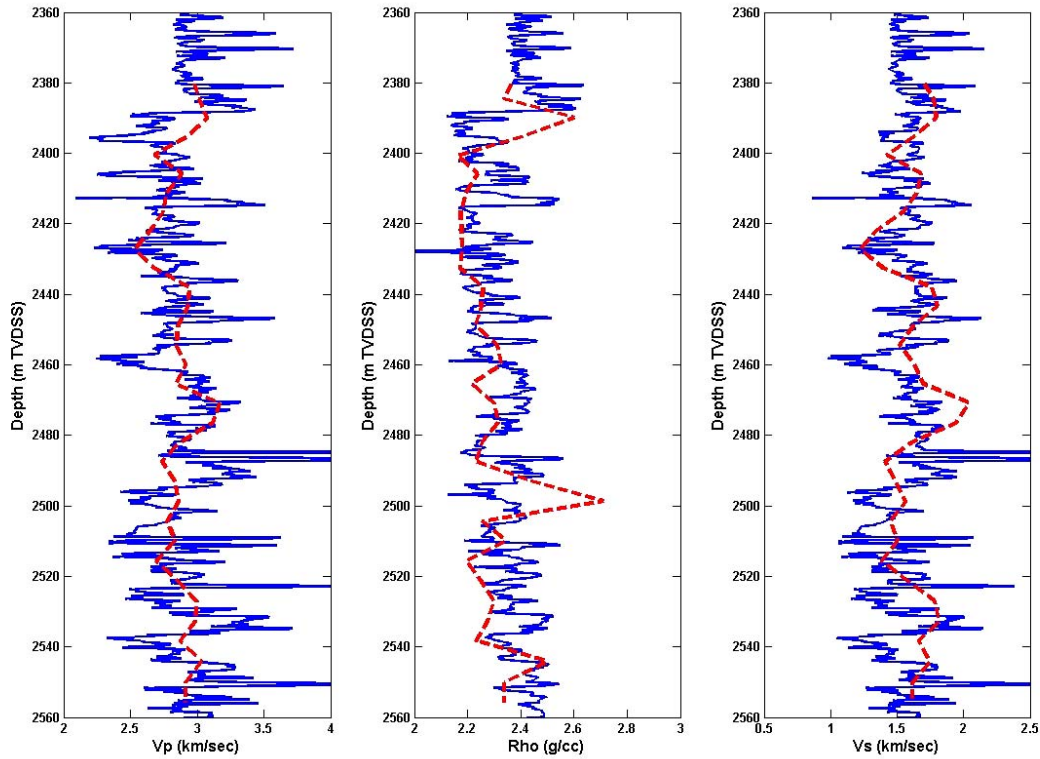


Figure 3.13: The results of the inverse matrix calculation from our method fully applied to *EI*s in red at a well location. The blue lines are the actual well-log data. Note that the significantly improved good match between the seismic-analysis result and the well data compared to Figure 3.11.

Once I obtain  $V_p$ ,  $V_s$  and  $\rho$  separately, I can take advantage of numerous rock-physics tools. One of the benefits of using these tools is to evaluate shale volume quantitatively from velocities and  $\rho$ , in order to detect the distribution of sand bodies from 3-D seismic data. I generate the crossplots of  $V_p$ - $\rho$  as well as  $V_s$ - $\rho$  in Figure 3.14. The larger circles in the figure are the points of resultant velocity- $\rho$  derived from *EI* analysis of the seismic data at a well location. I also plot well-log data color-coded by shale volume in small dots in the same figure. Using the constant gradient indicated by the dashed line in the plots, I determine the shale volume from the intercept of the same gradient line through each data point. I use the  $V_p$ - $\rho$  plane since the  $V_s$  exhibits more errors in Figure 3.13.

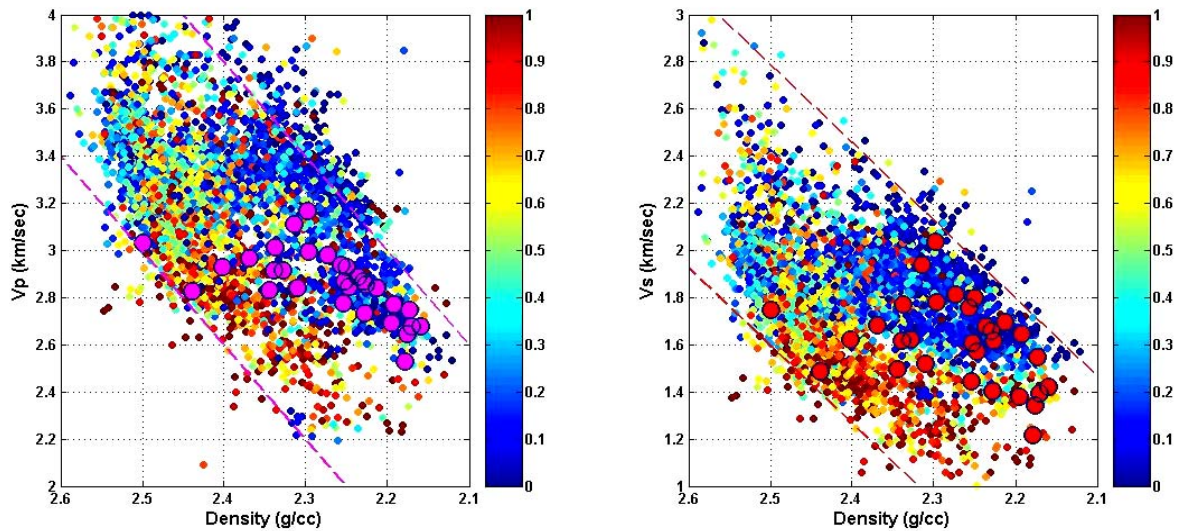


Figure 3.14: The crossplot of  $V_p$ - $\rho$  on the left and  $V_s$ - $\rho$  on the right. The dashed lines indicate the gradient used to determine shale volume in these plots. The large circles are points derived from the  $EI$  analysis of seismic data; the points color-coded in shale volume are well-log data.

In this process, the data location in the velocity- $\rho$  plane is different depend on the fluid component in a rock. Figure 3.15 shows an example of the location shift due to the fluid saturation determined for a well-log data. The open circles represent the data location with in-situ fluid in the reservoir color-coded by water saturation ( $S_w$ ), where the remaining fluid is 39.4°API oil ( $S_o=1-S_w$ ). Then, the solid markers correspond to the data location after fluid-substituted to 100% water-saturated condition by the Gassmann equation. The solid lines are iso-shale-volume contours. Note that the direction of the data shift by oil saturation is almost parallel to the iso-shale-contours, since oil saturation decreases both velocity and density. Figure 3.16 compares the shale volume from the data location with in-situ fluid and that from the data location with 100% water. As observed in the left chart, the data location with in-situ fluid gives us higher shale volume than that with 100% water. However, the differences between the two results are mostly less than 10% in the shale volume as shown in the histogram in Figure 3.16.

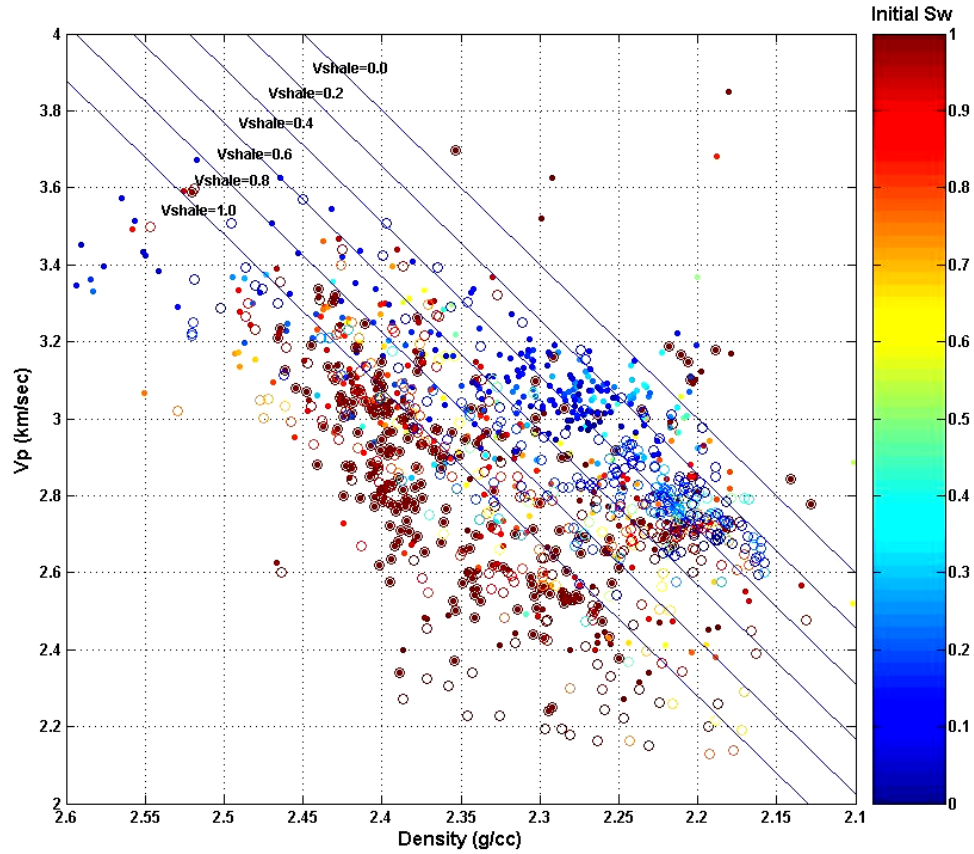


Figure 3.15: The shift of data location due to fluid saturation for a well-log data in the  $V_p$ - $\rho$  plane. The open circles represent the data location with in-situ fluid. The solid markers correspond to the data location after fluid-substituting to a water-saturated condition. Both are color-coded by the initial water saturation. Note the direction of data shift is parallel to the iso-shale-volume contours in the solid straight lines.

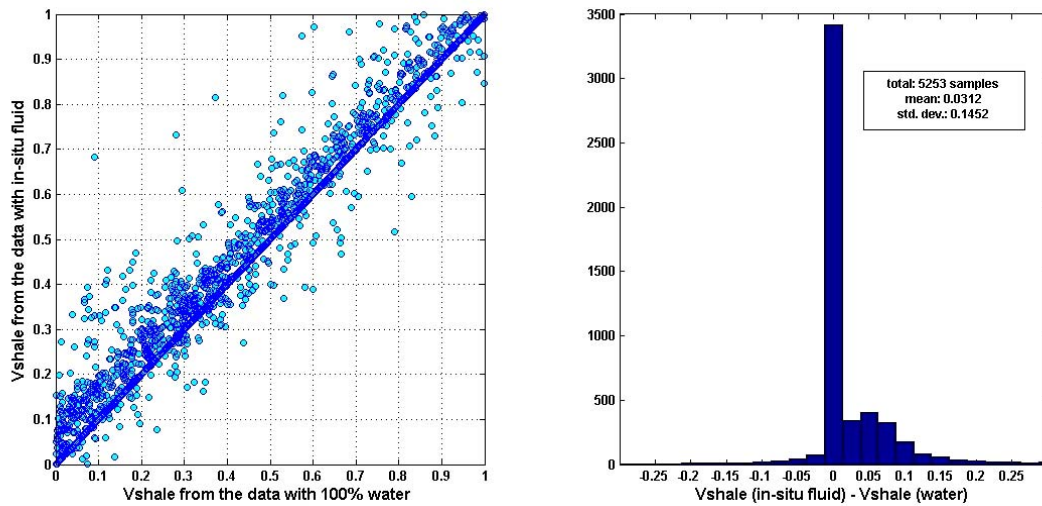


Figure 3.16: The comparison between the shale volume from the data location with in-situ fluid and that with 100% water. The rock with in-situ fluid gives us higher shale volume than the rock with 100% water. However, the differences between two results are less than 10% in shale volume as shown in a histogram.

Figure 3.17 compares the estimated shale volume with the shale volume from the CPI (computer processed interpretation) well-log analysis of the well. In this figure, the yellow trace is the shale volume by well-log analysis, whereas the green line is a mean filtered trace of the yellow data. The magenta trace is the shale volume based on the  $V_p$ - $\rho$  plot in Figure 3.14; the red dashed trace is the resultant shale volume from the crossplot of  $V_s$ - $\rho$ . I capture the basic trend of the shale volume profile, although I miss the sharp boundary at the top of the reservoir around 2350m again; moreover there seem to be time shifts or phase rotation around 2460-2480m. Eventually, the complete computation sequence is applied to the 3-D seismic dataset. In Figure 3.18, I compare the original seismic data of the near stack and the shale volume section derived from the  $EI$  analysis through the vertical well displayed in Figure 3.17. The section is an east-west seismic line extracted from the 3-D seismic data. The well-log data in red indicates the shale volume by log analysis, which is the same trace as the yellow trace shown in Figure 3.17. We cannot resolve the lithology in the amplitude section at the bottom of Figure 3.18.

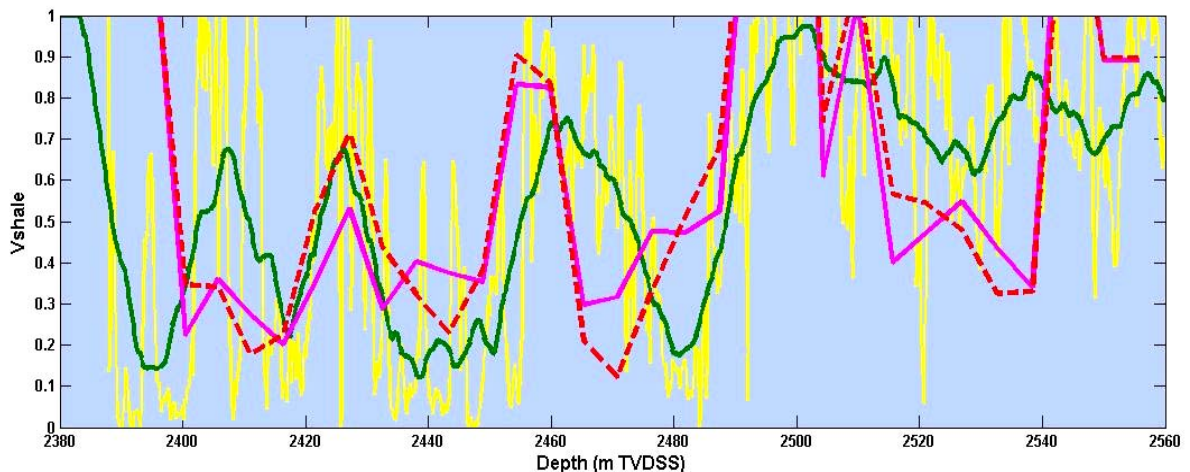


Figure 3.17: The comparison of shale volumes. The yellow trace is the shale volume from well-log analysis; the green line represents a mean filtered version of the yellow trace. The magenta line exhibits the shale volume determined in the crossplot between  $V_p$  and  $\rho$ , based on the  $EI$  analysis of the seismic data. In addition, the red dashed line exhibits the shale volume estimated in the crossplot for  $V_s$  and  $\rho$  from the  $EI$  analysis.

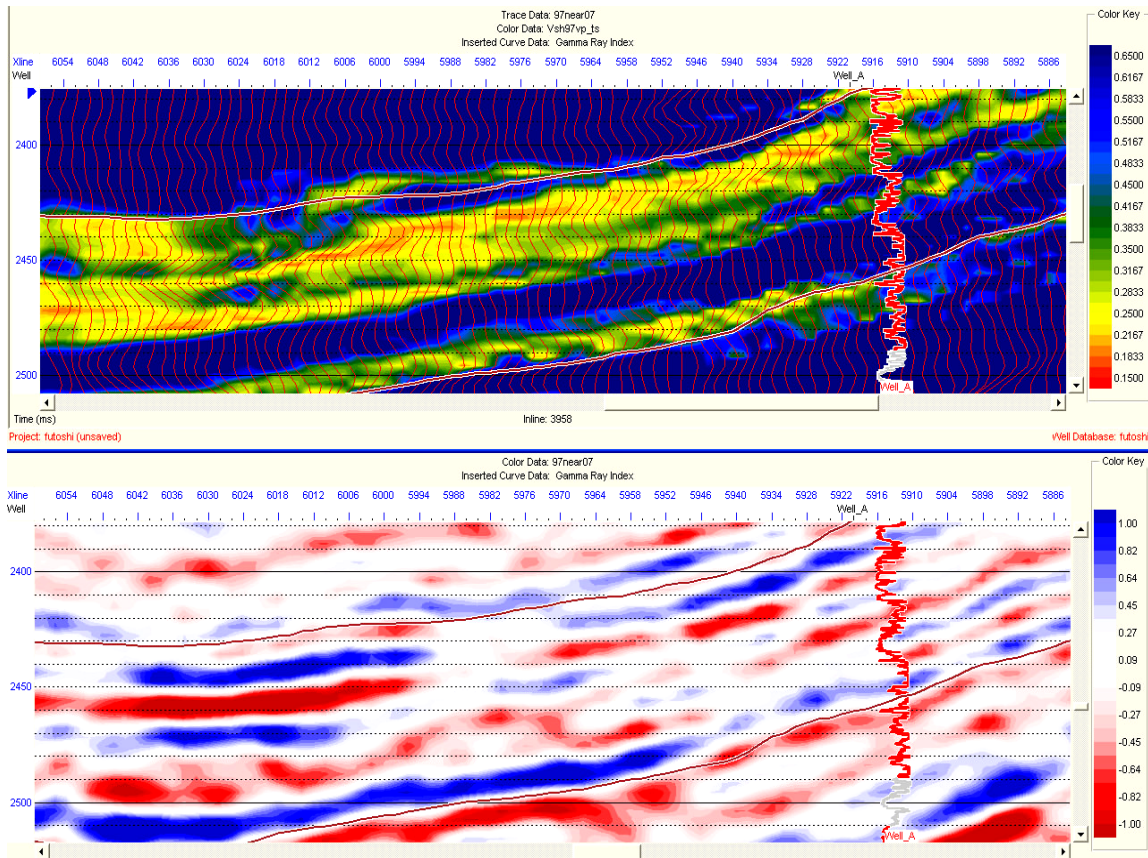


Figure 3.18: Shale-volume section obtained by the elastic-impedance analysis constrained by rock-physics bounds at the top. The bottom is the near-stack seismic section at the same location. The well log in red indicates the shale volume from well-log analysis, 0 on the left end and 1 for the right-end. Note that the top section demonstrates good agreement with the well log. The wiggle traces in the top section are the same seismic data as the bottom section. The color code in the top section is shale volume clipped in the range from 15% to 65%.

In contrast to the bottom section, we recognize the sandstone layers clearly in the shale volume section at the top. Moreover, the shale volume agrees well with the well-log analysis in red at the location of Well A, where the shale volume is 0 at the left end and 1 at the right end. For comparison, I superimposed the red wiggle traces in the top section, which are the same seismic traces as those in the bottom section. The color code for the top section is clipped from 15% to 65% of the shale volume to emphasize the variation of lithology in the section.

Likewise, I present the comparison of the shale-volume section to the elastic-impedance section derived from the seismic inversion in Figure 3.19. In this comparison, we notice that the impedance section does not manifest the lithology distribution. We only recognize a subtle indication of the fact that higher impedances correspond to higher shale volume.

I export the result of the elastic-impedance analysis constrained by rock-physics bounds into 3-D visualization software to understand the distribution of sand bodies. Figures 3.20 and 3.21 display the sand-body distribution. Based only on geologic data, geologists in charge of this field interpreted that the reservoir is blanket sandstone of braided river channel stacks. In Figures 3.20 and 3.21, we distinguish the sandstone distribution derived from the seismic data; the image agrees with the depositional environment given by the geologists. Furthermore, I confirmed that the sand-volume profiles are consistent to the well log analysis results at all well locations of available wells. I set the color code from 55% sand volume at the 127 side of the legend to 85% sand volume at the -128 end of the legend for these figures. Then, I tune the transparency to illuminate the sandstone bodies which have more than 60% sand volume in Figure 3.20. The advantage of this approach is that we can assess the result in quantitative ways. In Figure 3.21, I change the transparency setting to highlight the sand bodies with more than 80% sand volume. I detect the core parts of the channel stacks in this figure. In fact, now we can recognize sand bodies, which exhibit similar shapes to longitudinal bars and/or meandering channels. I observe several sets of parallel channels with crossing channels between those in Figure 3.21. Also small streams seem to join the main channels from the side in the direction from NNE to SSW, which indicates the flow

direction of this braided-river system in Jurassic age. The wide spread sandstone bodies are surrounding the core parts of the channel stacks as shown in Figure 3.20.

Based on the observations in these figures, the channel stacks extend in a NNE-SSW direction. Thus, I expect a higher rate of fluid flow in that direction, which is also suggested by reservoir engineering data of this producing oil field.

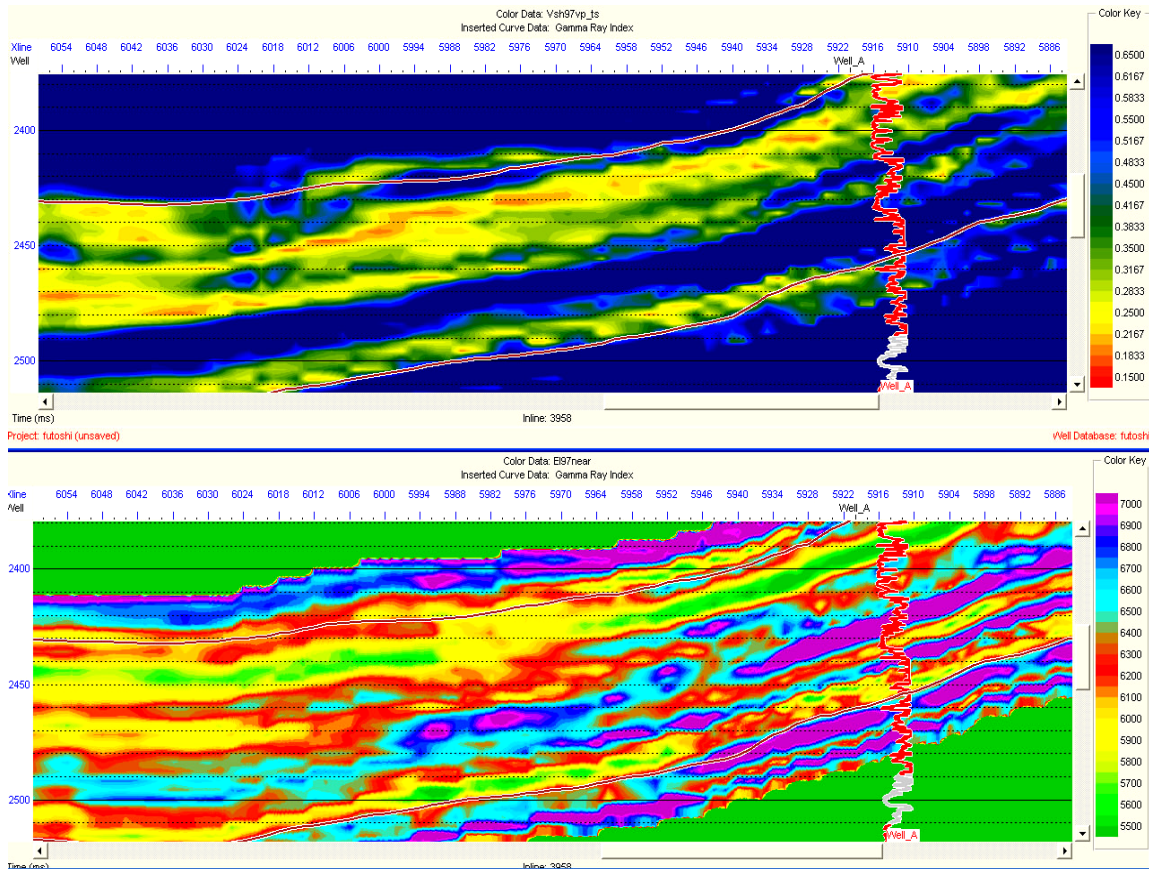


Figure 3.19: The shale-volume section obtained by the elastic-impedance analysis constrained by rock-physics bounds at the top. The elastic-impedance section of the near- stack seismic data is at the bottom. This elastic-impedance data is one of the input data for the analysis. There is tendency for higher impedances to correspond to higher shale. However, the lithology distribution is not clear in the impedance section at the bottom.

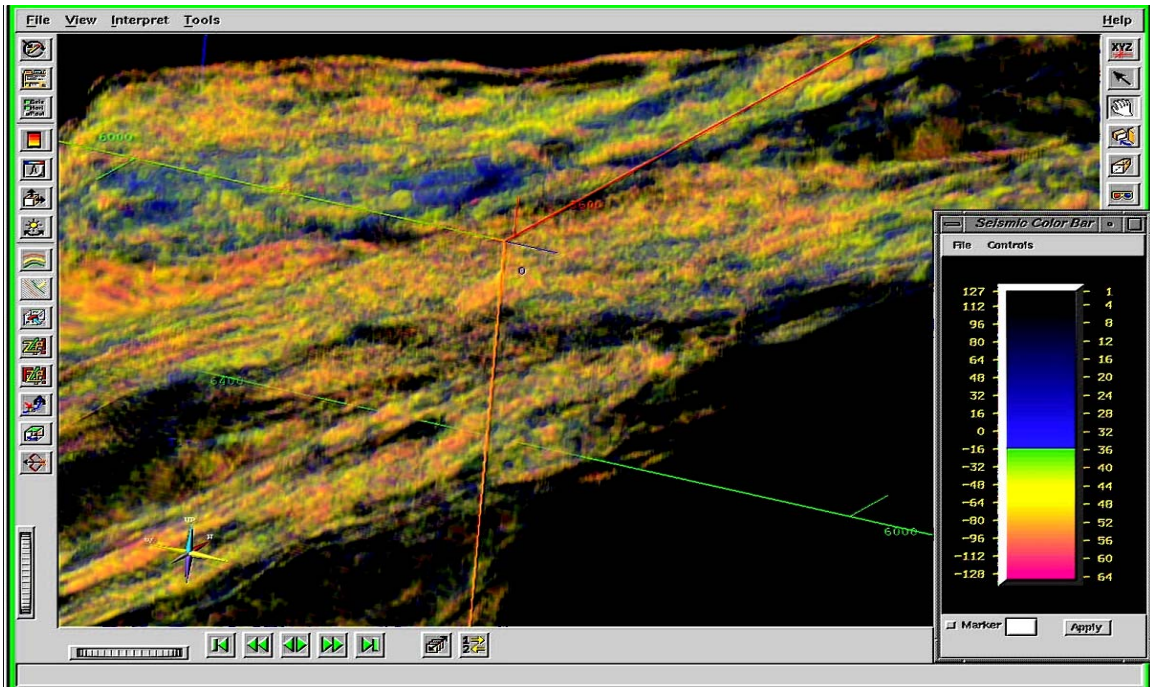


Figure 3.20: The 3-D visualization of the resultant sand-body distribution. The color code is sand volume, where 127 corresponds to 55%, and -128 indicates 85% averaged sand volume within the seismic resolution. I set the transparency to illuminate the portion with more than 60% sand volume. The total width of the area is about 5km

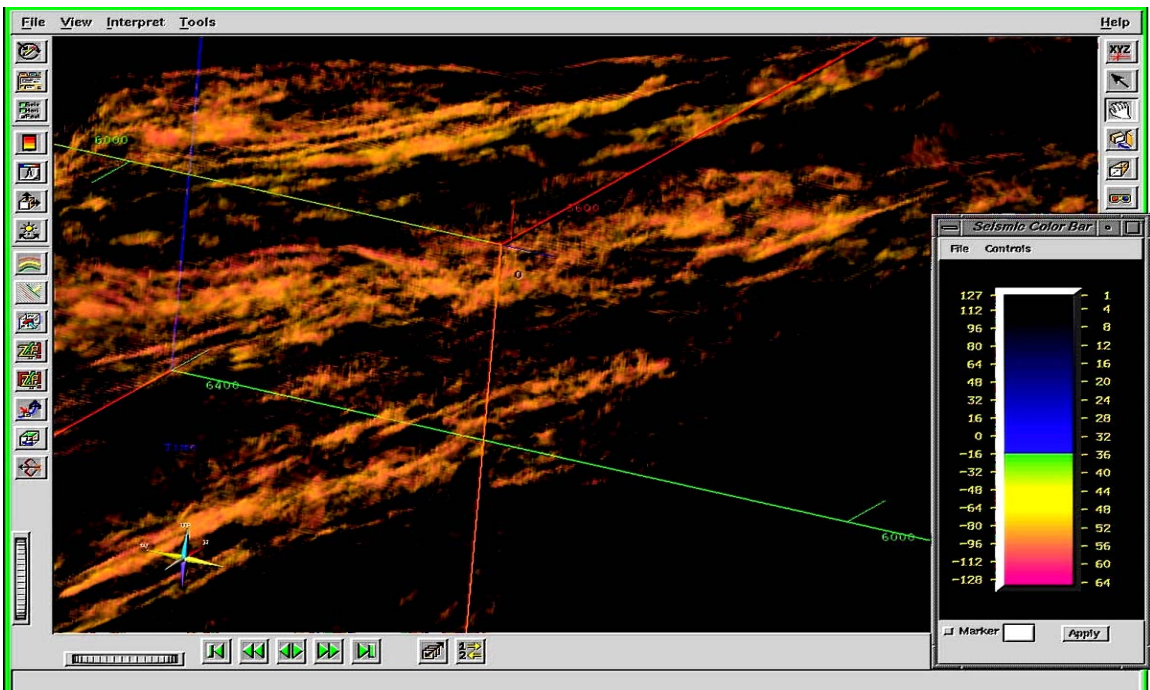


Figure 3.21: The 3-D visualization of the resultant sand-body distribution. I set the transparency to illuminate the portion with more than 80% sand volume. Note that there are sand bodies which exhibit shapes similar to longitudinal bars and/or meandering channels.

### 3.8 Comparison with unprocessed data

What if we do not apply the rock-physics constraints to control the data scatter? Figures 3.22 and 3.23 give the answer to this question. Figure 3.22 shows the sandstone distribution derived from the *EIs* without any correction processes, but I just applied the exactly same inverse matrix calculation to determine  $V_p$ ,  $V_s$ ,  $\rho$ , then determine the shale volume using the data location in the  $V_p$ - $\rho$  plane. Note that the color code is still the fractional sand volume (1 - shale volume). However, the minimum value at 127 on the dark blue end corresponds to  $-10^{10}$ , and the scale is logarithmic due to the abnormal calculation results from the unprocessed *EIs*. In this figure, which is equivalent to Figure 3.20, we cannot observe any patterns to be considered fluvial deposits. Likewise, even when we extract very sandy portions as shown in Figure 3.23, no pattern of sand bodies is mapped out. This result indicates that the constraints based on the rock-physics bounds are indispensable for deriving appropriate results as shown in Figures 3.20 and 3.21.

In many cases, simple seismic attributes--amplitude strength, wavelet form, instantaneous phase, instantaneous frequency, and so on--work well to determine the lithology distribution. Figure 3.24 shows the amplitude of the near-stack seismic of the case-study dataset. I arrange the transparency of the display to highlight the reflectors of strong amplitude, both in the positive and negative directions. We observe a pair of strong parallel reflectors near the compass symbol at the bottom left; these are correlatable to the sand bodies in Figure 3.21. However, the extension of these channels to the northeast direction is not as clear as in Figure 3.21.

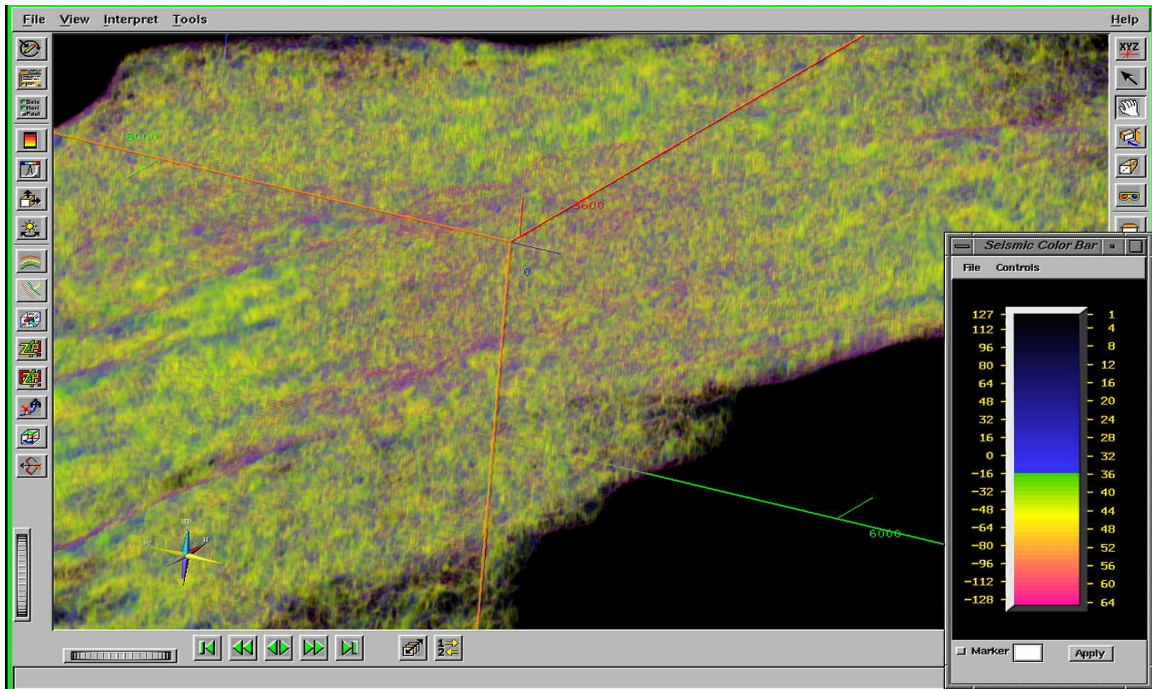


Figure 3.22: The 3-D visualization of the sand body distribution derived from unprocessed *EIs*. The color code is sand volume, but 127 corresponds to  $-10^{10}$  due to the abnormal calculation results from the unprocessed inputs; the scale is logarithmic.

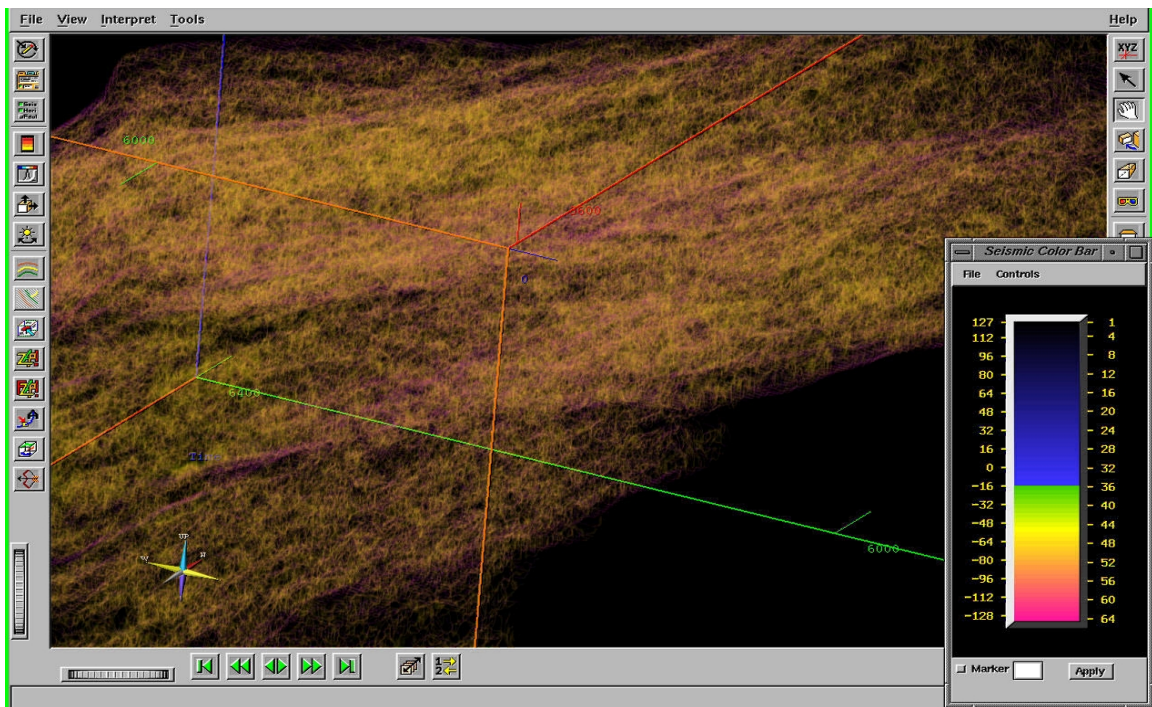


Figure 3.23: The 3-D visualization of the sand-body distribution derived from unprocessed *EIs*. This shows the result of extracting the portions of high sand content. Note that we cannot observe any clear sediment bodies.

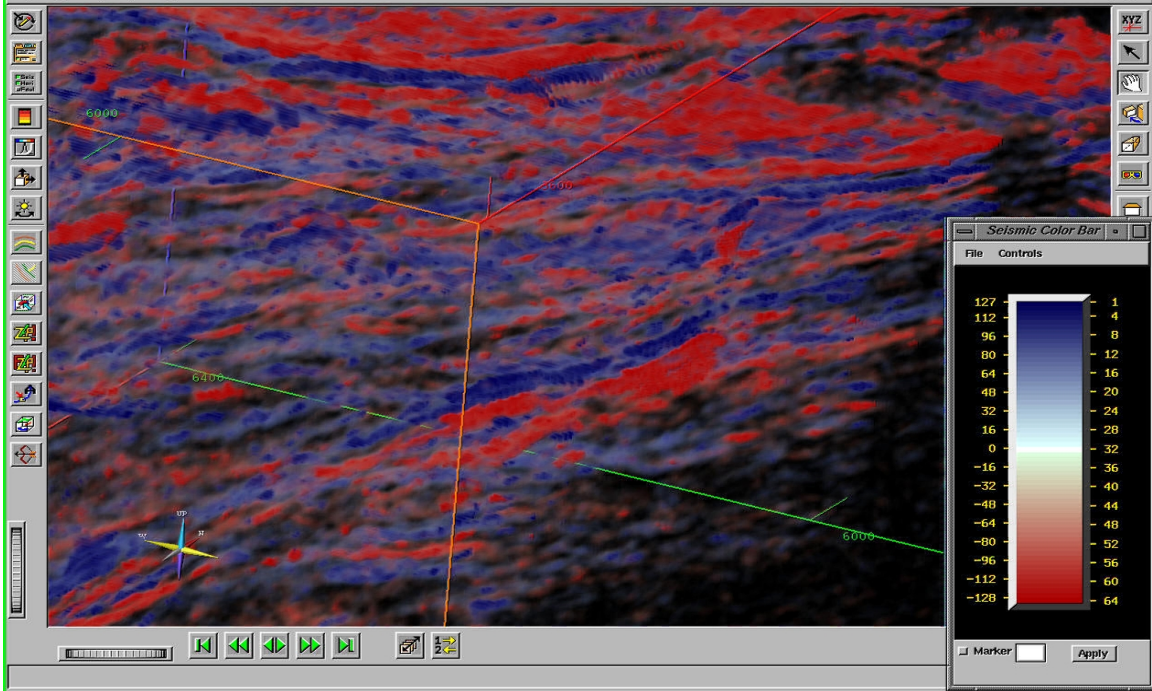


Figure 3.24: The strong amplitude reflectors in the near-stack seismic data. A pair of strong parallel reflectors at the bottom left are correlatable to the channels in Figure 3.21. However, the extension in the northeast direction is not as clear as in Figure 3.21.

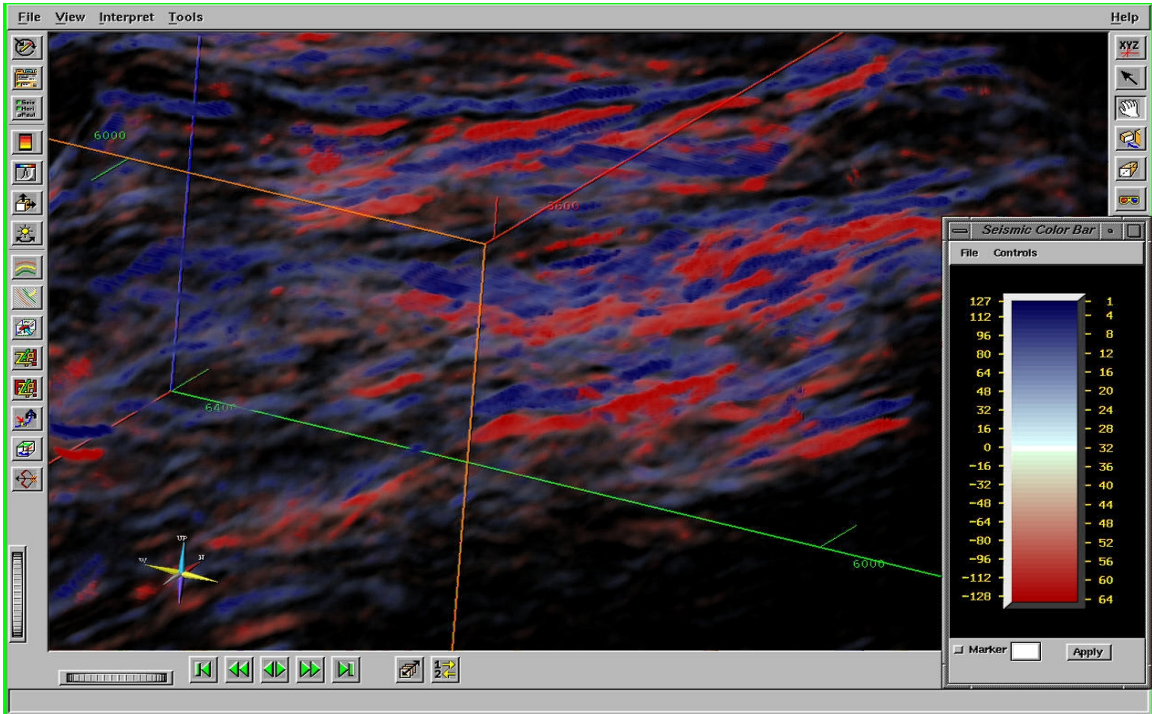


Figure 3.25: The strong amplitude reflectors in the far-stack seismic data. There are channel-like features around the center, but the reflectors are dimming out to the edge of the figure.

Furthermore, in the extended area, the locations of strong amplitude in Figure 3.24 deviate from the channel distribution in Figure 3.21.

Figure 3.25 exhibits the strong reflectors in the seismic data of the far stack. We observe channel-like features around the center of the figure, but the strong reflectors are not clear in the remaining area.

These facts suggest that it is difficult to obtain the total picture of lithology distribution from the original seismic data, although each angle stack has some qualitative information about the lithology distribution. We need to apply a processing sequence, such as the one I discussed in this chapter, to determine the lithology distribution in a quantitative manner.

### **3.9 Conclusions**

I discussed the role of noise on the inverse-matrix calculation in Equation 3.3, when we derive  $V_p$ ,  $V_s$  and  $\rho$  from the elastic impedances by the seismic inversion of angle-stack data. The effect of offset-consistent noise is different from that of random noise. In the case of offset-consistent noise, the noise effect appears most prominent in the calculation of  $\rho$ , but the effect on the computation of  $V_s$  is about 22% of the effect on  $\rho$ . Moreover, there is no effect on  $V_p$  determination. However, if the noise occurs randomly, the effect occurs equally in the determinations of all three properties,  $V_p$ ,  $V_s$  and  $\rho$ . In addition, I observe the noise enhancement factor  $1/A$ , as described in Equation 3.5 for the effect of random noise. Since the  $1/A$  is a function of the three stack angles, if the angles have only small separations such as that of the far-stack angle which is less

than  $30^\circ$ , the effect of random noise will be enhanced on an exponential scale. But the scale is less than 1 when the separations of stack angles are large enough, so that the far-stack angle exceeds  $60^\circ$ . Therefore, in this case, the effect of random noise is reduced by the inverse-matrix calculation. To minimize the random-noise effect for elastic-impedance analysis, the noise-enhancement factor  $1/A$  is practical for finding the optimal combination of stack angles quantitatively.

Based on the outcomes of noise effects, I developed a method to analyze elastic impedances to derive  $V_p$ ,  $V_s$  and  $\rho$ , by eliminating the influence of noise. This new method consists of two steps. In the first step, to obtain the general trend of  $EIs$ , I perform least-squares linear fitting of  $EIs$  in the  $\ln EI - \sin^2 \theta$  plane. Next, I apply rock-physics bounds to constrain the data distribution of the  $EIs$  in the  $EI_{far} - EI_{near}$  plane. This process restores the strict balance of the three  $EIs$  within the constraint of the applied rock-physics bounds. Given the resultant  $EIs$ , I calculate  $V_p$ ,  $V_s$  and  $\rho$  by applying the inverse matrix in Equation 3.5.

Using the dataset of an actual oil field, I demonstrate the result of a case study. The computed  $V_p$ ,  $V_s$  and  $\rho$  are processed one step further to detect subsurface sand bodies. I successfully map out the distribution of fluvial sand bodies at a depth of 2400m; buried fluvial channels in Jurassic age.

In the next chapter, I will discuss a sequence of calculations and analyses to derive the fluid saturation in a subsurface formation based on  $V_p$ ,  $V_s$ ,  $\rho$  and the shale volume determined in this chapter.

## REFERENCES

- Aki, K. and Richards, P. G., 2002, *Quantitative seismology second edition*, University Science Books.
- Connolly, P., 1998, Calibration and inversion of non-zero offset seismic. 68th Ann. Internat. Mtg: Soc. of Expl. Geophys., 182-184.
- Connolly, P., 1999, Elastic impedance. *The Leading Edge*, **18**, 438-452.
- Han, D-H., 1986, *Effects of Porosity and Clay Content on Acoustic Properties of Sandstones and Unconsolidated Sediments*. Ph.D. dissertation, Stanford University.
- Mavko, G., Mukerji, T. and Dvorkin, J., 1998, *The Rock Physics Handbook, Tools for Seismic Analysis in Porous Media*, Cambridge University Press.
- Mukerji, T., Jørstad, A., Mavko, G., and Granli, J., 1998, Near and far offset impedances: Seismic attributes for identifying lithofacies and pore fluids. *Geophysical Research Letter*, **25**, 4557-4560.
- Shuey, R. T., 1985, A simplification of the Zoeppritz equations, *Geophysics*, **50**, 609-614.
- Tsuneyama, F. and Mavko, G., 2005, Velocity anisotropy estimation for brine-saturated sandstone and shale. *The Leading Edge*, in press.
- Whitcombe, D., 2002, Elastic impedance normalization. *Geophysics*, **67**, 60-62.
- Whitcombe, D., Connolly, P., Reagan, R. and Redshaw, T., 2002, Extended elastic impedance for fluid and lithology prediction. *Geophysics*, **67**, 63-67.
- Zimmer, M, 2003, *Seismic Velocities in Unconsolidated Sands: Measurements of Pressure, Sorting, and Compaction Effects*. Ph.D. dissertation, Stanford University.

Zoeppritz, K., 1919, Erdbebenwellen VIII B, On the reflection and propagation of seismic waves, *Göttinger Nachrichten*, **I**, 66-84.

# Chapter 4

## Quantitative detection of fluid distribution using time-lapse seismic

### 4.1 Abstract

Although previous seismic monitoring studies have revealed several relationships between seismic responses and changes in reservoir rock properties, the quantitative evaluation of time-lapse seismic data remains a challenge. In most cases of time-lapse seismic analysis, fluid changes are qualitatively detected by changes in amplitude strength, travel time, and/or Poisson's ratio. Reservoir pressure, another important target of time-lapse analysis, tends to induce time-lapse responses that are different from those of the fluid changes.

I develop a workflow to determine the saturations of formation water, oil and gas from seismic data through a sequence of analyses and calculations, based on the three

elastic impedances at different angles derived from seismic inversion. In Chapter 3, I discussed the preparation of this analysis in terms of determining  $V_p$ ,  $V_s$ ,  $\rho$  and the shale volume from the elastic impedances. In this chapter, I present the subsequent steps, considering the pressure effect and the saturation scale of fluids for time-lapse seismic analysis. Then, I demonstrate a deterministic approach to computing the fluid saturation to evaluate time-lapse seismic data. In this approach, I derive the physical properties of the water-saturated sandstone reservoir, based on several inputs:  $V_p$ ,  $V_s$ ,  $\rho$  and the shale volume from seismic analysis; the average properties of sand grains; and formation water properties. Next, by comparing the in-situ-fluid-saturated properties with the 100% formation-water-saturated reservoir properties, I determine the bulk modulus and the density of the fluid phase in the reservoir. Solving three equations simultaneously (relating the saturations of water, oil and gas in terms of the bulk modulus, density and the total saturation) I compute the saturation of each fluid. I use a real time-lapse seismic dataset from an offshore oil field in the Norwegian North Sea for this study.

## **4.2 Introduction**

The Norwegian North Sea is an area where time-lapse seismic is commonly used to evaluate producing oil fields. Several time-lapse seismic studies were published on the North Sea during the last decade. These include studies of the Oseberg field (Johnstad et al., 1995, Rutledal et al., 2003), the Magnus field (Watts et al., 1996), the Gullfaks field (Sonneland et al., 1997, Veire et al., 1998), the Draugen field (Gabriels et al., 1999), the Statfjord field (Al-Najjar et al., 1999) and the Snorre field (Smith et al., 2001). In the

latest case study of the Oseberg field (Rutledal et al., 2003), the authors state that the Poisson ratio generated from acoustic and elastic impedance inversions is the best qualitative indicator of the changes in subsurface fluid saturation relating to production; and the acoustic impedance is an appropriate parameter for discriminating lithologies in this field. On the other hand, in the cases of the Draugen, Statfjord, and Snorre fields, the authors have confirmed that the time-lapse change of amplitude strength, rather than Poisson's ratio (i.e., brightening or dimming) is the key response indicating the replacement of fluid by the production and injection activities in the fields.

Despite the efforts described above, the quantitative analysis of time-lapse seismic to detect the change of fluid saturation remains a challenge because of the typically poor match between the model predictions and the actual seismic data. There is uncertainty about which parameter most affects the seismic response. For example, in the report of the Magnus field by Watts et al. (1996), reservoir pressure, rather than fluid replacement, was identified as the dominant cause of the amplitude change, whereas the opposite was found to be the case in the Oseberg field (Rutledal et al., 2003).

An impressive example of quantitative analysis of time-lapse seismic was recently demonstrated by Lumley et al. (2003) and Lumley (2004). They adopt two seismic attributes, the P-wave information content ( $A_p$ ) and the S-wave information content ( $A_s$ ), to generate a crossplot between the time-lapse differences of both attributes. Then they find the axes representing the changes in pressure and water saturation in the crossplot to derive the quantitative indicators of the changing properties. The method worked well in the Schienhallion and Gullfaks fields, yet the physical background of the method is not clearly illustrated.

I develop a deterministic process to derive fluid saturation from seismic and well log data; velocities, density and fluids saturation are calibrated to the time of seismic acquisition. Therefore, I avoid confusion regarding the causes for the time-lapse changes in seismic responses.

### 4.3 Pressure effect

The two main causes of the time-lapse change in seismic responses are the changes in fluid saturation and/or effective pressure, due to the production of hydrocarbons. First, using the result of core velocity measurements for the target oil field, I examine the effect of pressure change. All the measurements are carried out on dry rock samples. The velocity is measured under different effective pressures. Figure 4.1 illustrates the pressure dependence of ratio between  $V_p$  measured at a specific effective pressure and  $V_p$  at the effective pressure of 30MPa. The red line represents the approximated overall trend for  $V_p$ , which is given below:

$$V_p(P_{effectiveMPa})/V_p(30MPa) = 1 - 0.38 \exp(-P_{effectiveMPa}/6). \quad (4.1)$$

Likewise, I obtain an equation for the overall trend for  $V_s$  as follows:

$$V_s(P_{effectiveMPa})/V_s(30MPa) = 1 - 0.32 \exp(-P_{effectiveMPa}/7). \quad (4.2)$$

Given the equations above, I calculate the velocity change during time-lapse seismic acquisitions according to the pressure change in the field. I use the formation pressure derived from the reservoir simulation for this analysis; and effective pressure (confining

pressure minus formation pressure) is calculated, assuming that the confining pressure from overburden formations remains constant.

Figure 4.2 demonstrates the change in effective pressure during two seismic surveys. The solid markers represent the first survey; the empty markers denote the second survey. The effective pressure increases during production, since the formation pressure of the reservoir is reduced due to oil production. Note that the different wells demonstrate different pressure ranges, but the pressure difference between the two seismic surveys at each well is almost identical, as shown in Figure 4.2.

Next, I compute the velocity change corresponding to the pressure variation; I plot the calculation result in Figure 4.3. In this field, the first time-lapse seismic data was acquired several years after the start of production, so the effective pressure was already high--more than 19 MPa--as shown in Figure 4.3. This range of pressure corresponds very closely to the ceiling of the highest effective pressure in Figure 4.2. As a result, the increase in effective pressure due to oil production does not significantly affect the velocity change. Based on the result of this analysis, I conclude that the velocity changes due to pressure variation are less than 1% of the velocities observed in the first seismic survey. Consequently, the effect of pressure change on velocity is negligible in this case, so we will not attempt to infer pressure change from the seismic data.

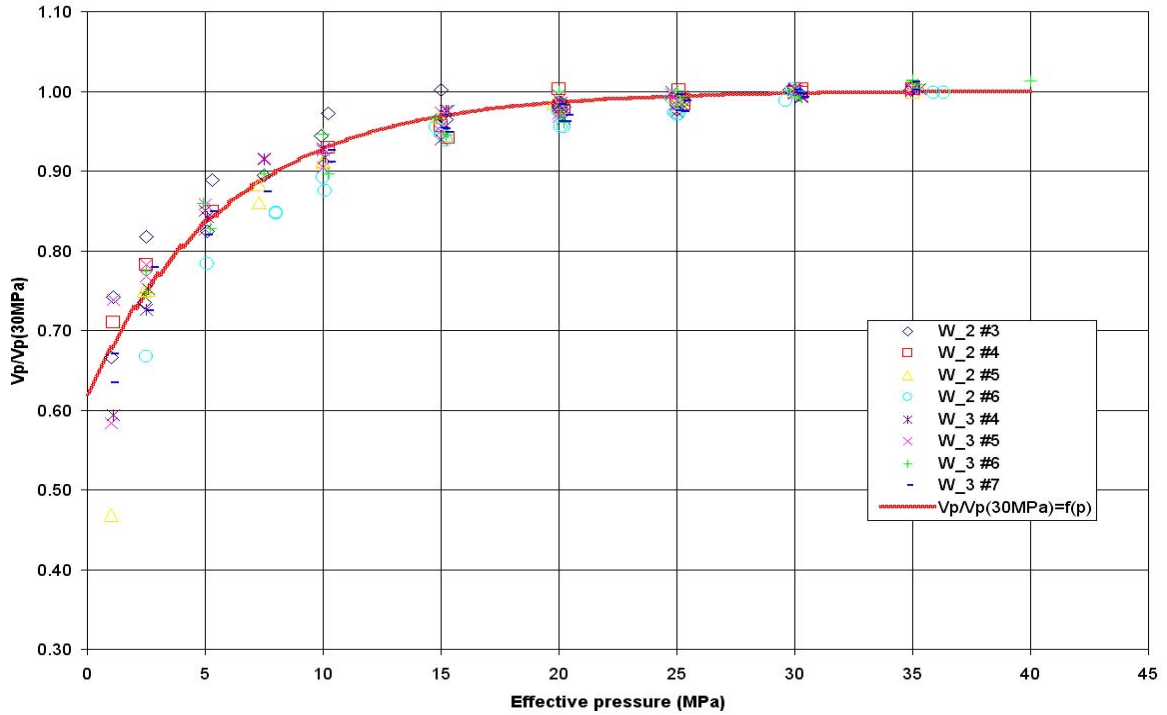


Figure 4.1: The ratio of  $V_p$  at specific effective pressures to  $V_p$  at 30MPa effective pressure. I observe a very clear trend in the  $V_p$  ratio with effective pressure.

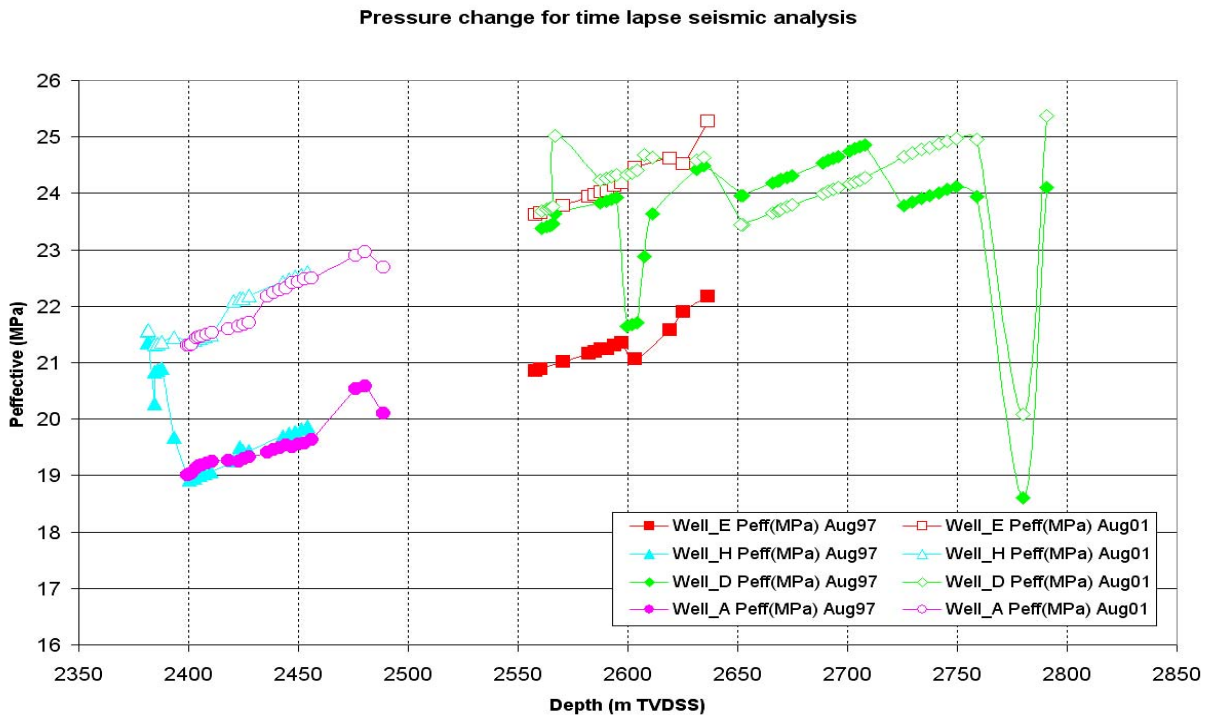


Figure 4.2: Pressure change between two seismic acquisitions. The solid markers represent the first seismic survey. The empty markers correspond to the second survey. Effective pressure, the difference between the overburden pressure and the formation pressure, increases during production, since the formation pressure of the reservoir declines due to oil production. Note that the differences of effective pressure are almost identical, except for the green data.

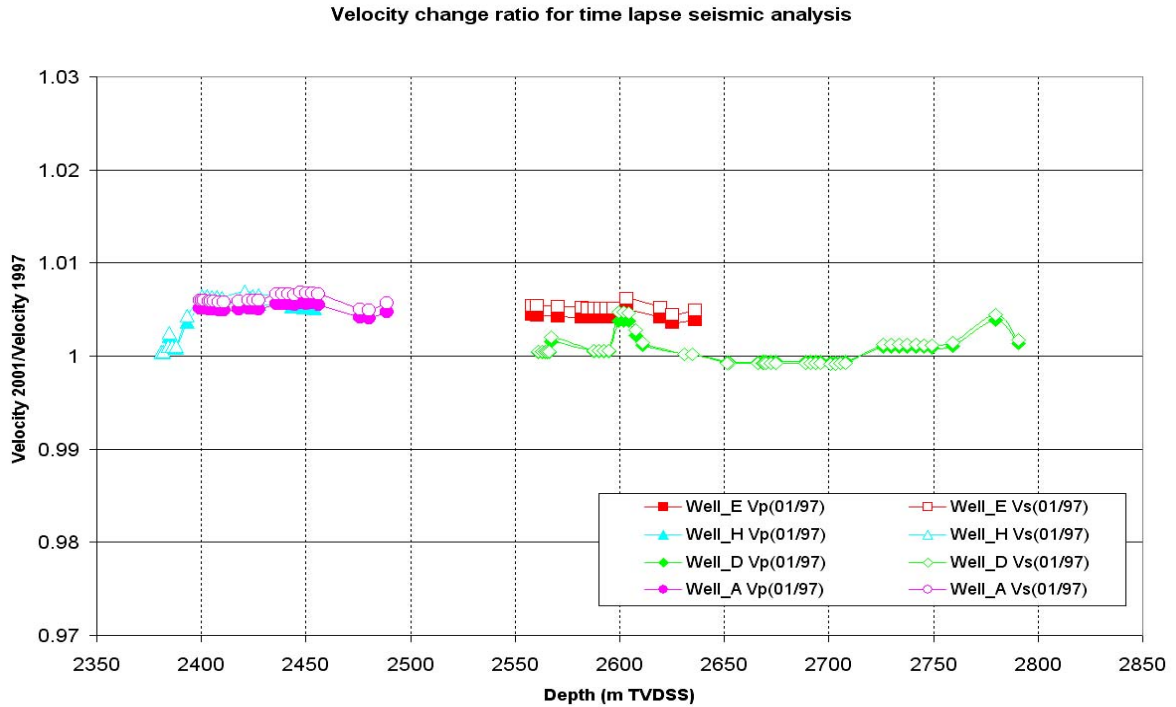


Figure 4.3: The velocity changes corresponding to the pressure changes in Figure 4.2. The degree of the velocity change is less than the 1% change in the velocity in the first survey. I convert the increase of effective pressure to the increase in velocity using Equations 4.1 and 4.2. Solid markers represent  $V_p$ , and empty markers denote  $V_s$ .

#### 4.4 Fluid-saturation scale

The effect of the saturation scale of formation fluids on seismic responses was extensively discussed in Sengupta et al. (2003). We usually adopt the fluid saturation, which is the output from the flow-simulator of a target field, to control seismic analysis. However, in general, the grid size of flow simulators extends several tens of meters, while seismic responses vary depending on the fluid saturation profile on a much smaller scale. Consequently, unless we apply an appropriate downscaling technique, the seismic model based on the output of flow simulators may encounter significant errors. Sengupta et al. (2003) presented a method for restoring the fine-scale profile of fluid saturation, using porosity as a guide for re-allocating gas saturation, the fluid that controlled the

seismic response in their case. They constrained the total volume of free gas as a constant. Then, they accumulated the gas into the intervals in which well-log analysis had identified high-porosity sandstone. The corrected saturation profile was used to model seismic responses, and when the saturation profile was downscaled by an appropriate factor, the resultant amplitude strength in root mean squares matched the actual seismic data well. I employ a similar approach; however, instead of using porosity as a guide for concentrating hydrocarbons, I adopt the original oil saturation before the production as an indicator of highly permeable zones as below:

$$S_{fluid\_downscaled-profile} \propto S_{fluid\_original-profile} \cdot \quad (4.3)$$

I assume that the original oil saturation reflects the permeability of the each fine layer of sandstone better than porosity; since any fine layer with good permeability must have had the potential to accumulate more oil than the surrounding formations in the initial condition.

For the downscaling, I keep the average saturation of the downscaled profile same as the saturation of a corresponding grid of the flow simulator as follows:

$$S_{fluid\_simulator\_grid} = \frac{1}{N} \sum_{i=1}^{N(grid\_top)} S_{fluid\_downscaled-profile} \cdot \quad (4.4)$$

Therefore, assuming an identical porosity distribution between the flow simulator and the downscaled saturation profile, I preserve the volume of fluid for any given intervals.

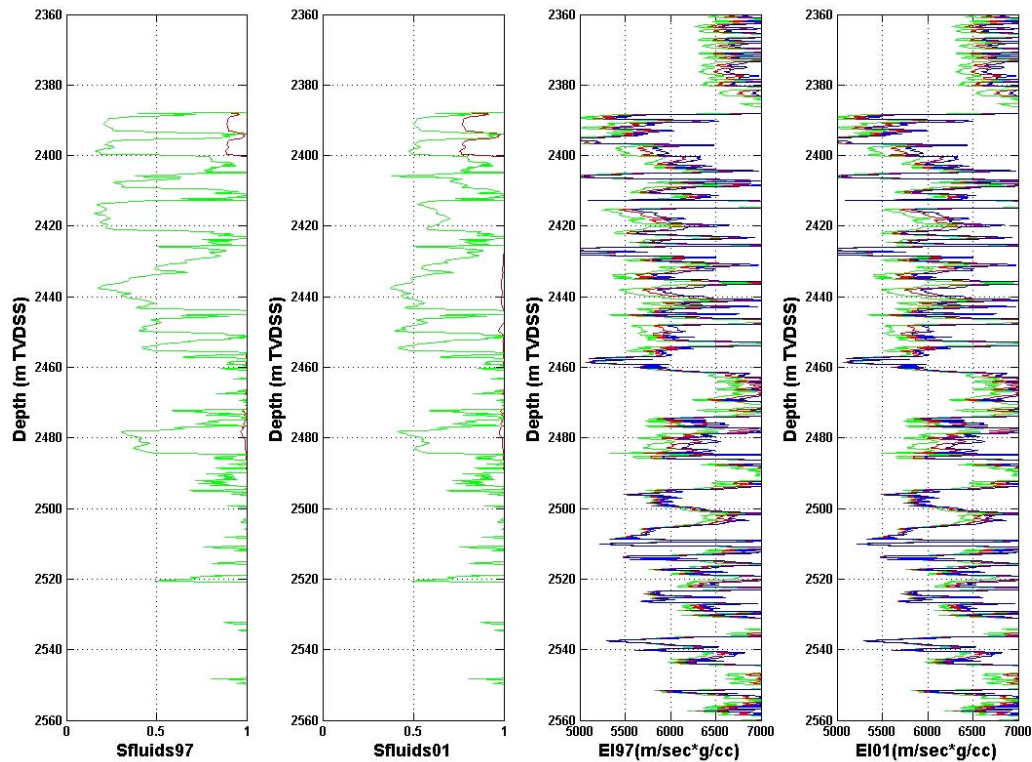


Figure 4.4: The generated fluid-saturation log of Well A for two seismic surveys in the two left columns. The green line indicates formation-water saturation; the interval between the green line and the red line (or to the right end) corresponds to oil saturation. The red line to the right end represents gas saturation. The two right columns show calculated elastic impedances. The color code is as follows: blue for the near stack; red for the mid stack; green for the far stack.

The left two columns of Figure 4.4 illustrate the downscaled profile of fluid saturation for Well A. The green lines indicate the saturation of formation-water, whereas the area to the right of the green line corresponds to hydrocarbon saturations. In the hydrocarbon region, the interval to the right of the red line represents gas saturation, while the interval between the green and red lines, (or to the right of the green line when no red line exists) represents oil saturation. The left-most column shows the fluid saturation profile for seismic acquisition in 1997, and the next column shows that of seismic survey in 2001. The right two columns show calculated elastic impedances ( $EI$ ) of the two seismic acquisitions, where the blue lines are the  $EI$  of the near stack, red are the  $EI$  for the middle stack and green are the  $EI$  of the far stack. I calculate all  $EI$ s based on the well-

log velocities and density after correction for fluids saturation. Note that despite the approximately 25% difference in oil saturation between 1997 and 2001 in the upper half of the reservoir, the *EIs* are not significantly different. This result suggests that fluid substitution from oil to formation-water for saturation changes less than about 25 %, at around 2420 m in Figure 4.4, may be difficult to detect by seismic impedance analysis.

#### **4.5 Representative properties of the solid phase**

I use the Gassmann equations (Gassmann, 1951) to obtain the bulk modulus of the in-situ formation fluid. For this process, I need to determine the physical properties of the solid phase of the reservoir. Figure 4.5 shows the mineral composition of more than one hundred samples from the reservoir, based on laboratory measurements. As shown in the same figure, the reservoir sandstone is comprised of about 40-60% of quartz grains; 10-20% of feldspar; and a small number of lithic fragments. The sandstone is categorized as subarkose arenite to felspathic graywacke.

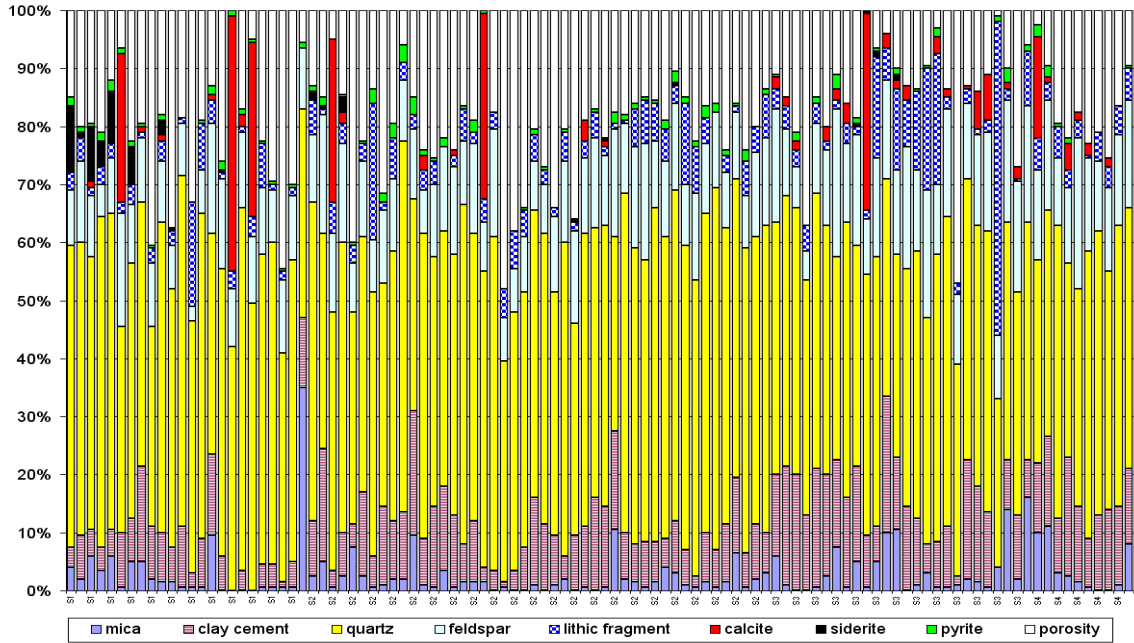


Figure 4.5: The mineral composition of the target sandstone reservoir. The sandstone is comprised of 40-60% quartz; 10-20% feldspar; and a small number of lithic fragments.

Figure 4.6 illustrates the crossplot of the calculated shear moduli and the bulk moduli of the core samples. I use the Voigt-Reuss-Hill (VRH) average (Hill, 1952) to compute the two elastic moduli for multi-mineral composition. Equation 4.5 shows VRH averaging, where “ $f_i$ ” indicates the volume fraction of material (mineral or lithic fragment) “ $i$ ”, and “ $M_i$ ” corresponds to a modulus of material “ $i$ ”.

$$M_{VRH} = 0.5 \sum_{i=1}^N f_i M_i + \frac{0.5}{\sum_{i=1}^N \frac{f_i}{M_i}} \quad (4.5)$$

I exclude clay minerals from this calculation. Then, I mix the average grain with clay according to the shale volume derived from the elastic impedance analysis of seismic data using the method in Chapter 3. In Figure 4.6, the big yellow asterisk in the center is

the median value of all the data points. I adopt these median values as the representative grain shear and bulk moduli of the sandstone reservoir.

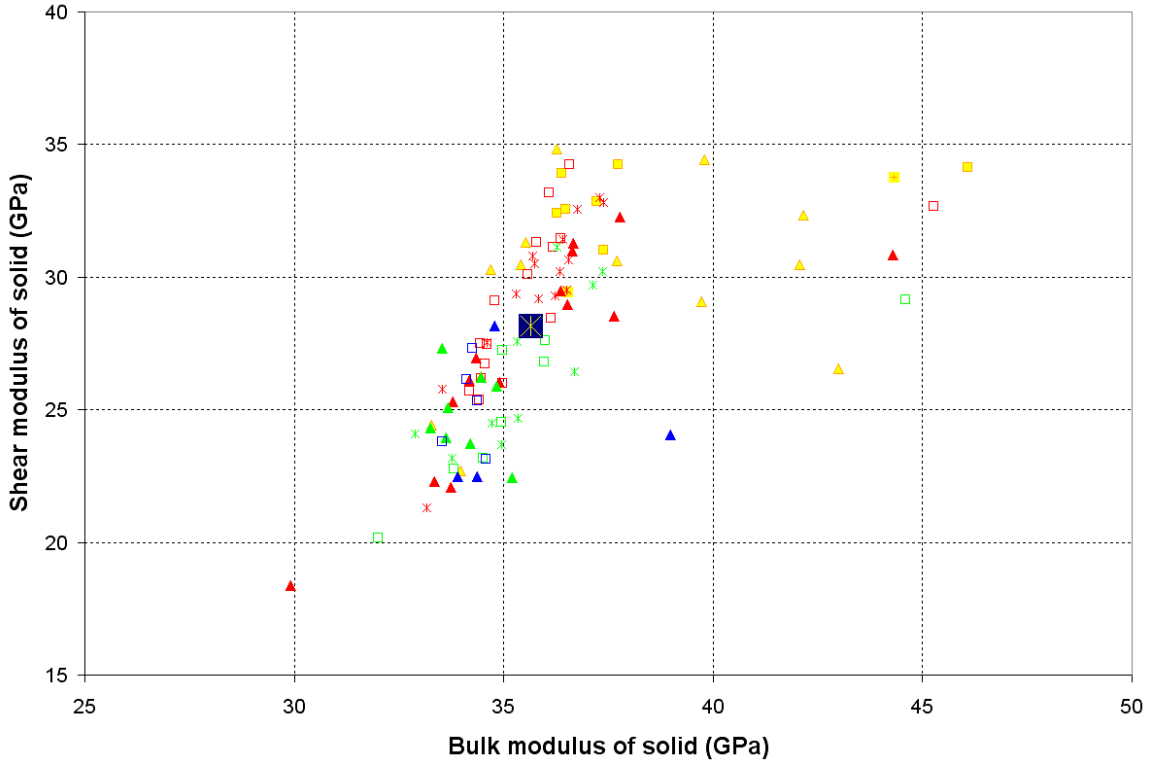


Figure 4.6: The crossplot of the calculated shear and bulk moduli of the sandstone in Figure 4.5. I use the Hill average for multi-mineral compositions. Clay is excluded from this calculation. Then, I use the shale volume from the elastic-impedance analysis to vary the solid-phase properties by mixing the representative properties of sandstone and clay, based on the shale volume. The color differences indicate different subunits in the reservoir. The shapes of the markers correspond to different wells.

## 4.6 Workflow to determine fluid saturation

At this point, I have prepared the necessary inputs including: (1)  $V_p$ ,  $V_s$ ,  $\rho$  and shale volume from the *EI* analysis; (2) the average properties of the solid fraction and the properties of fluid phase. Now, I apply a workflow as demonstrated in Figure 4.7. In the input parameter box at the top left of the figure, all parameters are determined using an

elastic impedance analysis, discussed in Chapter 3. In fact, I estimated all of these parameters twice, one for the 1997 vintage and one for the 2001 vintage. Then I averaged the rock-frame properties (shale volume, porosity, bulk density of water-saturated rock, bulk modulus of dry rock) from both vintages. The advantage of this coupling is to reduce the artifacts during the further analysis, as discussed in Johnston et al. (2003) and Gouveia et al. (2004). The subsequent analysis of fluid change has a common rock model using the consistent frame properties.

The representative properties of the solid phase in the top right box were discussed in the previous section. In addition, the properties of formation-water are calculated by the method of Batzle and Wang (1992), using laboratory measurements of the formation-water. I summarize the solid properties and the fluid properties in Table 4.1.

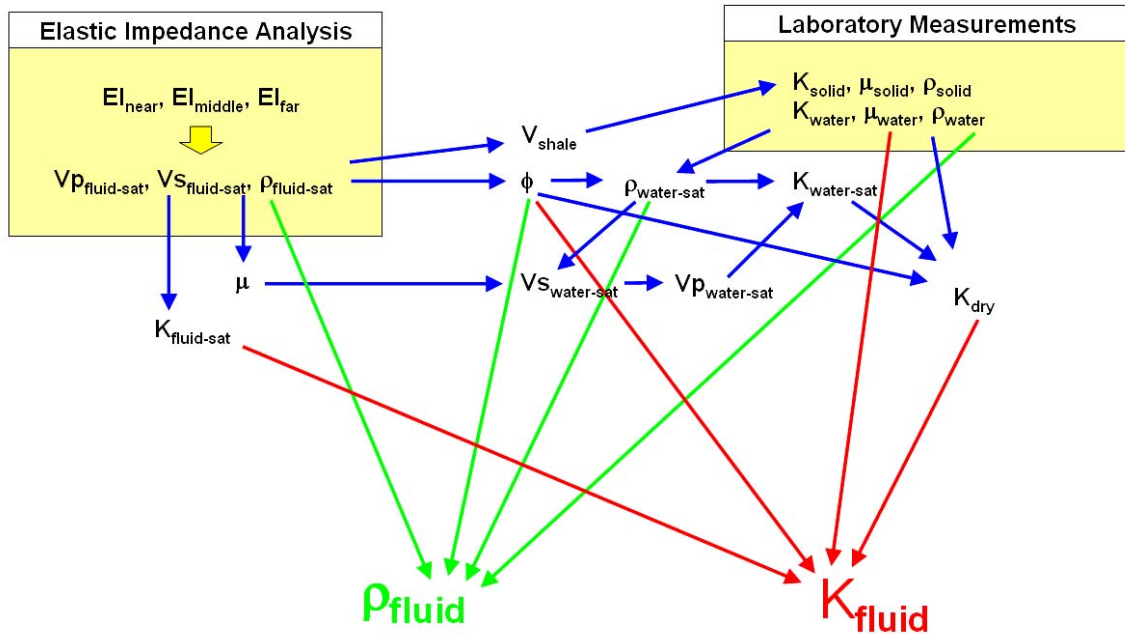


Figure 4.7: The workflow to derive the density and bulk modulus of in-situ-fluid. The input data at the top right is described in this paper. The sequence of computations to determine the final targets is explained step by step in this section. The input data in the top left box is discussed in Chapter 3.

Table 4.1: The parameters of the solids and fluids.

|                                      |                                      | Bulk modulus<br>(GPa) | Shear Modulus<br>(GPa) | Density<br>(g/cm <sup>3</sup> ) |
|--------------------------------------|--------------------------------------|-----------------------|------------------------|---------------------------------|
| Solid phase<br>(fraction=1- $\phi$ ) | Average grain<br>(fraction=1-Vshale) | 38.13                 | 34.93                  | 2.67                            |
|                                      | Clay<br>(fraction=Vshale)            | 23                    | 8                      | 2.58                            |
| Fluid phase<br>(fraction= $\phi$ )   | Formation_water                      | 2.7416                | 0                      | 1.0038                          |
|                                      | Oil                                  | 0.7637                | 0                      | 0.7136                          |
|                                      | Gas                                  | 0.1217                | 0                      | 0.2865                          |

\*Oil API 39.4°API, GOR 116.7, gas gravity 0.806, water salinity 31,000ppm, pore pressure 38MPa, reservoir temperature 90°C.

I describe the workflow step by step as follows:

1. I obtain the bulk modulus, shear modulus, bulk density and shale volume of the in-situ-fluid-saturated rock at every data point in the seismic cube from the result ( $V_p$ ,  $V_s$ ,  $\rho$ ) of the *EI* analysis as shown in the top left box of Figure 4.12.
2. I find porosity ( $\phi$ ) by a linear transform with bulk density ( $\rho$ ) as below:

$$\phi = -0.5401\rho + 1.4350. \quad (4.6)$$

This equation corresponds to the red line in Figure 4.8, which is the average trend of the target reservoir calculated from well-log data. Then using the estimated porosity, I derive a 100% formation-water-saturated bulk rock density using the properties in Table 4.1. For this step, since I employ an average trend in red in Figure 4.8, the points with higher water saturation on the cyan line side in the same figure are assigned lower porosity than actual. Likewise, the points with higher oil saturation on the green line side are assigned higher porosity than the actual data. The deviation from the actual porosity is summarized on the right in the Figure 4.8. The standard deviation

of the histogram is 6.9% (of the actual porosity): if porosity is 0.20, the deviation for this point is plus or minus 0.0138.

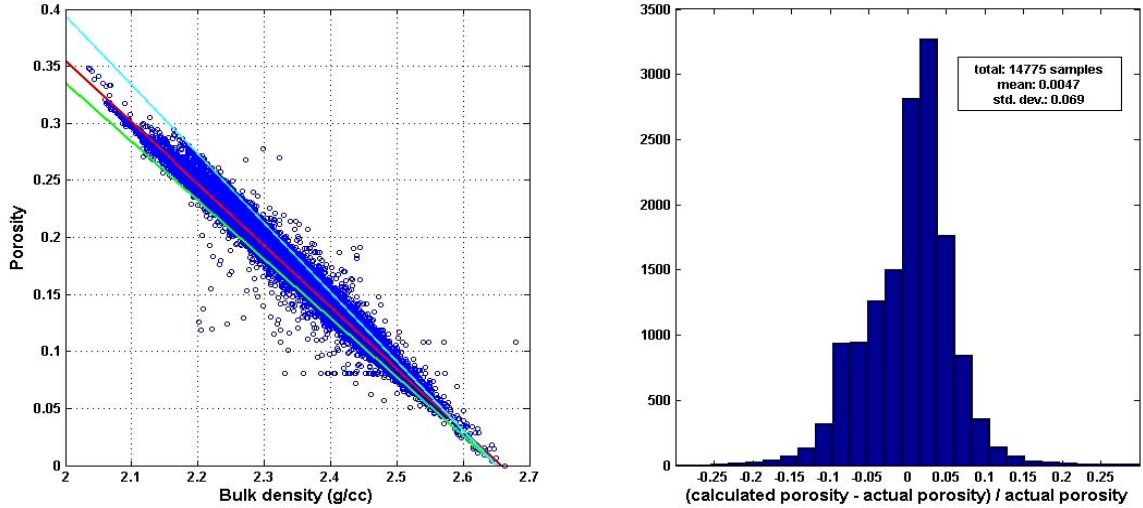


Figure 4.8: Average trend between porosity and bulk density from the well-log data of the target reservoir. The red line represents the employed linear regression. The cyan line corresponds to the trend for 100% water saturated condition and the green line corresponds to 100% oil saturated trend. The histogram on the right exhibits the estimation errors of porosity induced by an averaged trend.

3. I derive a 100% formation-water-saturated  $V_s$  by combining the 100% formation-water-saturated density and the rock shear modulus. Since shear modulus is less sensitive to the saturation fluid, I determine  $V_s$  first and transform it to  $V_p$  in the next step.
4. For simplicity, since I only need the relative difference in the internal fluid saturation, I use a linear relation between  $V_p$  and  $V_s$  for the 100% formation-water-saturated condition and compute  $V_p$  for 100% formation-water saturation. I find the following equation is a good regression for a well-log data from case study area:

$$V_s = 0.79V_p - 0.79. \quad (4.7)$$

Getting the proper  $V_p$  for full formation-water saturation depends very much on the  $V_p$ - $V_s$  relation. I explore the  $V_p$ - $V_s$  relations for reservoir rocks in Chapter 5.

5. I process the result to calculate a rock bulk modulus for the 100% formation-water-saturated condition.
6. Given the physical properties of the solid phase and the formation-water, as summarized in Table 4.1, I employ Gassmann's equation in Equation 4.8 to calculate the dry rock bulk modulus of at each seismic data location.

$$K_{dry} = \frac{K_{water-saturated} \left( \frac{\phi K_{solid}}{K_{water}} + 1 - \phi \right) - K_{solid}}{\frac{\phi K_{solid}}{K_{water}} + \frac{K_{water-saturated}}{K_{solid}} - 1 - \phi}, \quad (4.8)$$

where,

$K_{dry}$  is the bulk modulus of dry rock,

$K_{water-saturated}$  is the bulk modulus of formation-water-saturated rock,

$K_{solid}$  is the bulk modulus of the solid phase

(mixture of the average grain and clay)

$K_{water}$  is the bulk modulus of the formation-water

$\phi$  is porosity

7. I derive the bulk modulus of the in-situ fluid, using the rearranged Gassmann's relation given below:

$$K_{fluid} = \frac{\phi K_{solid} \left( \frac{K_{fluid-saturated}}{K_{solid} - K_{fluid-saturated}} - \frac{K_{dry}}{K_{solid} - K_{dry}} \right)}{1 + \phi \left( \frac{K_{fluid-saturated}}{K_{solid} - K_{fluid-saturated}} - \frac{K_{dry}}{K_{solid} - K_{dry}} \right)}, \quad (4.9)$$

where,

$K_{fluid}$  is the bulk modulus of the in-situ fluid

$K_{solid}$  is the bulk modulus of the solid phase

(mixture of average grain and clay)

$K_{fluid-saturated}$  is the bulk modulus of the in-situ-fluid-saturated rock

$K_{dry}$  is the bulk modulus of the dry rock

$\phi$  is the porosity .

8. On the other hand, it is a simple process to find the density of the in-situ fluid from the  $\rho_{fluid-saturated}$  (bulk density in the in-situ-fluid-saturated condition);  $\rho_{water-saturated}$  (the bulk density in the condition of 100% formation-water-saturated);  $\rho_{water}$  (the density of the formation water) and  $\phi$  (porosity) as follows:

$$\rho_{fluid} = \rho_{water} - \frac{\rho_{water-saturated} - \rho_{fluid-saturated}}{\phi}, \quad (4.10)$$

where,

$\rho_{fluid}$  is the bulk density of the in-situ fluid,

$\rho_{water}$  is the bulk density of the formation water,

$\rho_{water-saturated}$  is the bulk density of the formation-water-saturated rock,

$\rho_{fluid-saturated}$  is the bulk density of the in-situ-fluid-saturated rock,

$\phi$  is the porosity.

9. There are three possible fluids in the reservoir: namely, formation-water, crude oil and gas. The laboratory analysis of the crude oil supplies us with all the parameters to derive the properties of the oil and the segregated gas from the oil, using the method of Batzle and Wang (1992) in the reservoir condition.
10. Now, I can form simultaneous equations in terms of the saturations of these three fluids. First, I use Wood's equation (Wood, 1941) to demonstrate the relationship between the bulk moduli of the three fluids, assuming a homogeneous mixing scheme as below:

$$\frac{1}{K_{in-situ-fluid}} = \frac{S_{water}}{K_{water}} + \frac{S_{oil}}{K_{oil}} + \frac{S_{gas}}{K_{gas}} . \quad (4.11)$$

In this equation, “S” refers to the saturation of each fluid; “K” represents the bulk modulus of each fluid. Second, I equate the density of the in-situ fluid to the sum of each fluid as follows, where “ $\rho$ ” corresponds to the density of each fluid:

$$\rho_{in-situ-fluid} = S_{water} \rho_{water} + S_{oil} \rho_{oil} + S_{gas} \rho_{gas} . \quad (4.12)$$

Then, to balance the total saturation of the three fluids, I require

$$1 = S_{water} + S_{oil} + S_{gas} . \quad (4.13)$$

Here, I rearrange the above-mentioned relations into the matrix form given in Equation 4.14:

$$\begin{pmatrix} 1/K_{in-situ-fluid} \\ \rho_{in-situ-fluid} \\ 1 \end{pmatrix} = \begin{pmatrix} 1/K_{water} & 1/K_{oil} & 1/K_{gas} \\ \rho_{water} & \rho_{oil} & \rho_{gas} \\ 1 & 1 & 1 \end{pmatrix} \begin{pmatrix} S_{water} \\ S_{oil} \\ S_{gas} \end{pmatrix}. \quad (4.14)$$

I solve it to obtain the saturations of the three fluids using Equation 4.15:

$$\begin{pmatrix} 1/K_{water} & 1/K_{oil} & 1/K_{gas} \\ \rho_{water} & \rho_{oil} & \rho_{gas} \\ 1 & 1 & 1 \end{pmatrix}^{-1} \begin{pmatrix} 1/K_{in-situ-fluid} \\ \rho_{in-situ-fluid} \\ 1 \end{pmatrix} = \begin{pmatrix} S_{water} \\ S_{oil} \\ S_{gas} \end{pmatrix}. \quad (4.15)$$

11. Likewise, I solve the matrix form expressed in Equation 4.16:

$$\begin{pmatrix} K_{water} & K_{oil} & K_{gas} \\ \rho_{water} & \rho_{oil} & \rho_{gas} \\ 1 & 1 & 1 \end{pmatrix}^{-1} \begin{pmatrix} K_{in-situ-fluid} \\ \rho_{in-situ-fluid} \\ 1 \end{pmatrix} = \begin{pmatrix} S_{water} \\ S_{oil} \\ S_{gas} \end{pmatrix}. \quad (4.16)$$

Unlike Equation 4.15, this matrix form represents a patchy saturation of the three fluids. In other words, I assume heterogeneous distribution of three fluids due to spatial variation of relative permeability and wettability in this case.

12. Finally, comparing the outputs from Equations 4.15 and 4.16 to the results of well-log analysis at a well location, I determine the optimal weights to average the homogeneous saturation (Equation 4.15) and patchy saturation (Equation 4.16). Figure 4.9 demonstrates the result for the range of weighting factors. I calibrate the saturations extracted from the seismic data with the workflow just described, by comparing them with known saturation as a well. Eventually, I

adopt 0.5 as the weighting factor to compute the averaged saturation of three fluids in the case study.

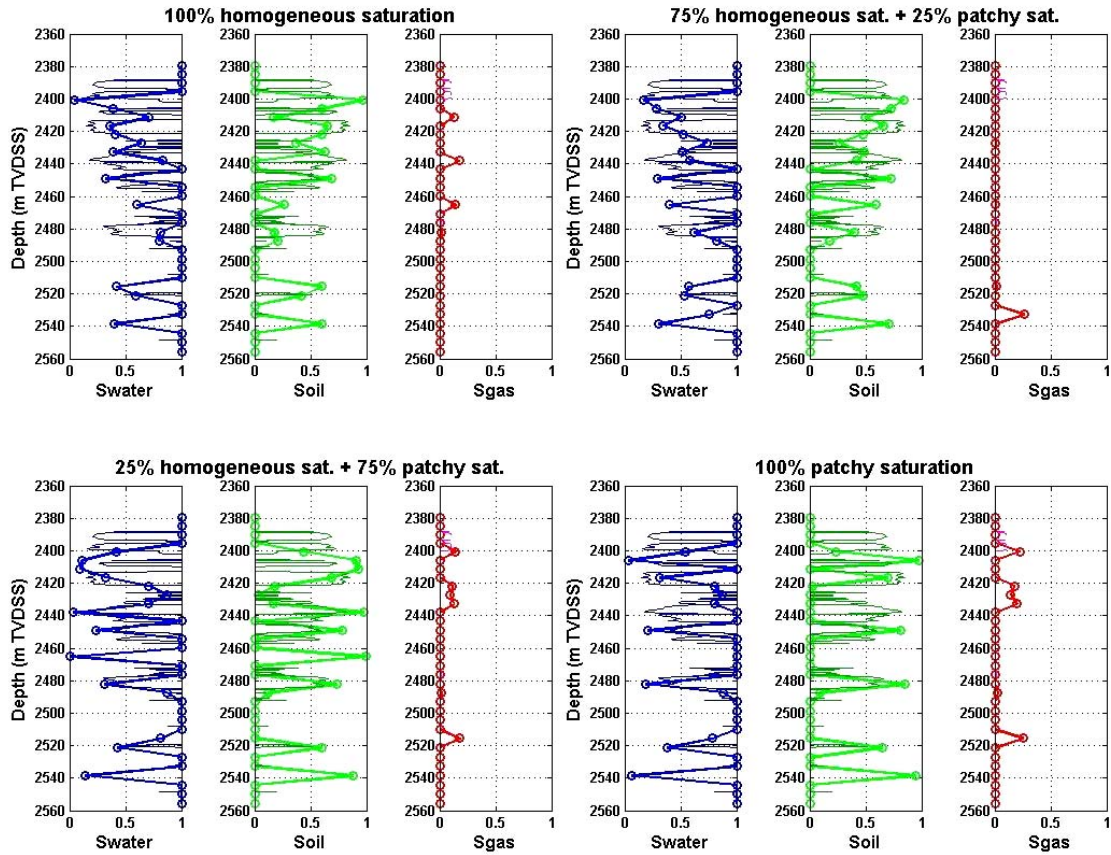


Figure 4.9: The calculated results of fluid saturation using different fractions of the saturation scale: homogeneous saturation represented in Equation 4.15 and patchy saturation given in Equation 4.16. For all columns, the thin lines represent the fluid saturation by well-log analysis, whereas the thick lines with open circles correspond to the results derived from seismic-data analysis.

Figure 4.10 shows the resultant fluid saturation from the seismic data analysis compared to the fluid saturation by well-log analysis. The erroneous spikes at 2465m and 2540m are induced by the skewed density input derived from miscalculations in the elastic-impedance analysis (Figure 4.13). In addition, a subtle problem is that because of the seismic resolution, the low water saturation at very top part of the reservoir is not

visible. However except for these portions, the overall result of the calculation of fluid saturation from seismic data demonstrates good agreement to the well-log analysis. The most points from the well-log analysis fall within 0.15 deviations of the seismic analysis result.

I adopt the fluid saturation from the seismic data for the portion of the reservoir with sandstone volume higher than 50% and for porosity higher than 10%. The purpose of these thresholds is to eliminate unreasonable saturations derived from the shaly sequence due to the mismatch between lithology and the averaged sandstone properties. Likewise, I dispose of the portion with very low porosity, where Gassmann's equations are extremely sensitive to the pore fluids, and fluid changes are not likely to occur.

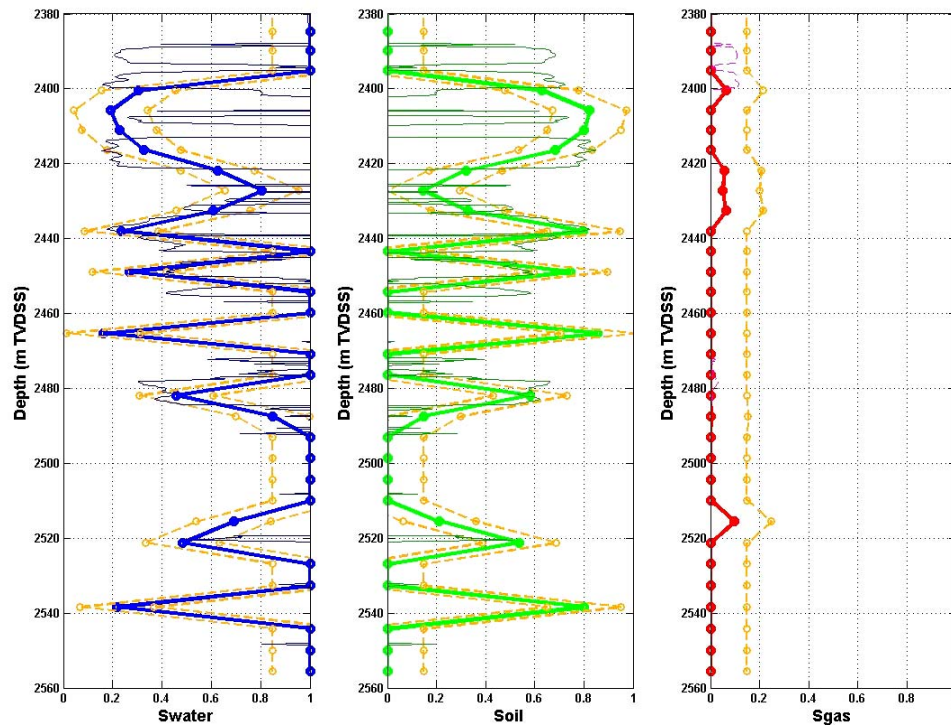


Figure 4.10: The resultant fluid saturation for Well A obtained by solving the simultaneous equations. For all columns, the thin lines represent the fluid saturation by well-log analysis, whereas the thick lines with open circles correspond to the results derived from seismic-data analysis. The dashed orange lines show 0.15 deviations from the seismically derived saturation. The erroneous spikes at 2465m and 2540m are induced by the skewed density input derived from the miscalculations in the elastic-impedance analysis.

## 4.7 Sensitivity analysis

Before applying the workflow to actual seismic data, I discuss the sensitivity analysis of the input parameters.

First, I generate a simple rock model with the average grain and fluid properties of the target field summarized in Table 4.2. Assuming the 100% water-saturated  $V_p$  and  $V_s$  are 3.0 km/sec and 1.58 km/sec, respectively, I calculate the exact values of  $V_p$ ,  $V_s$  and  $\rho$  for the fluid-saturation profile presented by the solid lines in Figure 4.11, using Gassmann's equation. Then, I employ  $V_p$ ,  $V_s$  and  $\rho$  as inputs for my workflow, with an altered parameter to retrieve the fluid saturation. This practice corresponds to the application of the workflow with a misestimated parameter, where the discrepancy between the resultant saturation and the initial model shows how sensitive the altered parameter is to the resultant saturation from the workflow.

Table 4.2: The parameters to generate a model for sensitivity analysis.

|                                  |                                 | Bulk modulus<br>(GPa) | Shear Modulus<br>(GPa) | Density<br>(g/cm <sup>3</sup> ) |
|----------------------------------|---------------------------------|-----------------------|------------------------|---------------------------------|
| Solid phase<br>(Total solid=0.8) | Average grain<br>(fraction=0.9) | 38.13                 | 34.93                  | 2.67                            |
|                                  | Clay<br>(fraction=0.1)          | 23                    | 8                      | 2.58                            |
|                                  | Quartz                          | 37                    | 44.73                  | 2.65                            |
| Fluid phase<br>(Porosity=0.2)    | Water                           | 2.7416                | 0                      | 1.0038                          |
|                                  | Oil                             | 0.7637                | 0                      | 0.7136                          |
|                                  | Gas                             | 0.1217                | 0                      | 0.2865                          |

### 4.7.1 Fluid saturation scale

The left three columns of Figure 4.11 compare the inversely calculated fluid saturation to the initial model. I assumed 100% patchy saturation for the initial model in this case. The triangles represent the saturation retrieved by my workflow with a 100% patchy saturation scheme in the inverse calculation. The circles show the result with 99% patchy saturation and the crosses show the result with 98% patchy saturation.

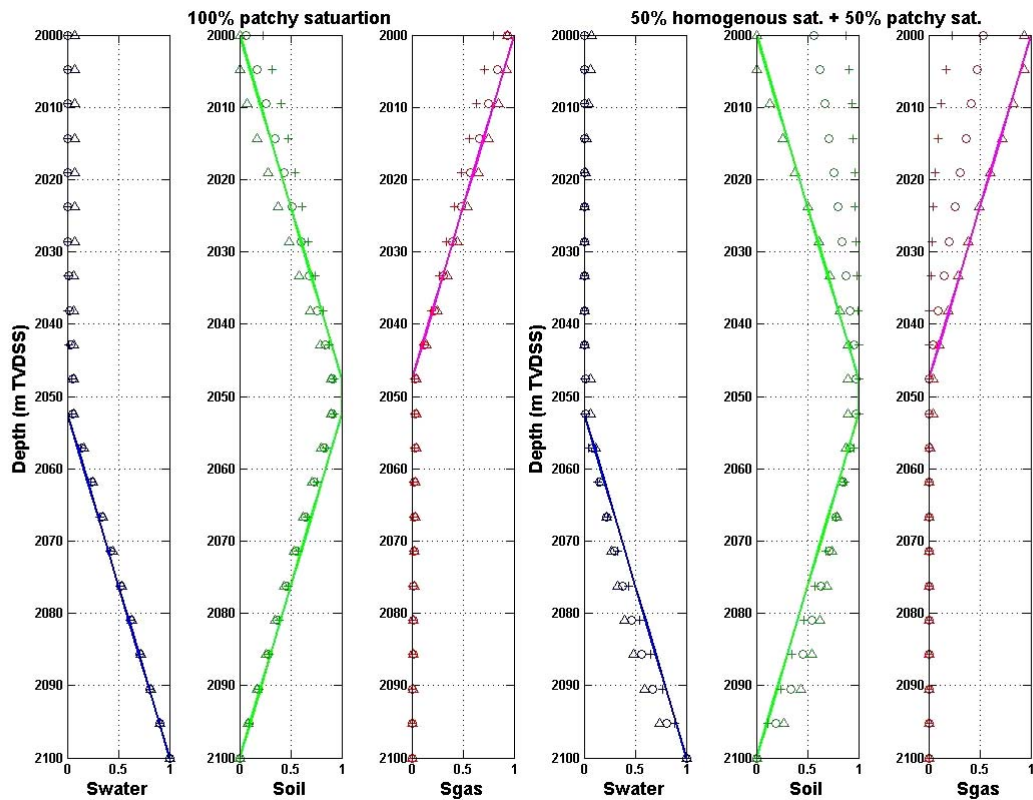


Figure 4.11: The sensitivity analysis of the fluid-saturation scale to the result of the workflow. The solid lines are the fluid saturation of the initial model. The left three columns represent the calculation results for the initial model of 100% patchy saturation. I used the following schemes of saturation scale in the inverse calculation: 100% patchy saturation for the triangles; 99% patchy saturation for the circles; 98% patchy saturation for the crosses. The right three columns show the calculation results for the initial model of the equally mixed saturation-scale schemes. I employed the following schemes in the inverse calculation: 100% patchy saturation for the triangles; 50% patchy saturation and 50% homogenous saturation for the circles; 100% homogenous saturation for the crosses.

Two important observations from these results are that (1) the exact fraction of the saturation scale in the inverse calculation does not give the best match to the initial model, and (2) all the calculation results demonstrate more errors in the portion of higher gas saturation. In this case, the circles match the best to the initial model.

In the right three columns in Figure 4.11, I show the calculation results of my workflow for the initial model of the equally mixed homogeneous saturation and patchy saturation. The triangles represent the calculation result with a 100% patchy saturation scheme in the inverse calculation; the circles correspond to the result with the equally mixed fluid saturation; the crosses represent the result with 100% homogeneous saturation. Again we recognize that the exact fraction of the saturation scale is not necessary to obtain the optimal result. In addition, the largest disagreement between the calculation result and the model is observed at the top of the sequence, where the gas saturation is the highest.

These disagreements are induced by the steps 10 and 11 discussed in section 4.6. Since the bulk modulus and density of gas are very small relative to those of liquids, the inverse matrix calculation is dominated by the gas terms, and the resultant saturation is distorted more where the gas saturation is higher. Furthermore, in the case of a mixed scheme of fluid saturation scales, we need to solve Equations 4.15 and 4.16 separately after dividing the total bulk modulus into the portions of homogeneous saturation and patchy saturation. However, in practice, we never know the fractions. Therefore, I am solving the saturation with one scheme for the total bulk modulus, and averaging the results afterwards. This method gives a good approximation, but it is difficult to obtain the exact saturation. The best way to obtain the optimal result with this workflow is to

calibrate the calculation result with the well-log analysis result first, for determining the weighting factor discussed in the step 12 in section 4.6.

For further discussions, I use the same initial model as the left three columns in Figure 4.11 and adopt the circles in those columns as the base case of the workflow.

#### **4.7.2 Velocity and bulk density**

Figure 4.12 shows the sensitivity analysis of velocity and bulk density. In the left three columns I present the result of velocity sensitivity, where the triangles are obtained from the inverse calculation with  $V_p$  and  $V_s$ , 5% lower than the initial model; the crosses show the calculation result with  $V_p$  and  $V_s$ , 5% higher than the model. In case of the lower velocity assumption, we observe higher errors near the bottom, where the workflow calculates some degree of oil saturation due to the lower-than-actual bulk moduli derived from the lower velocity. However, the saturation in the remaining portions stays almost the same, since the altered velocity cannot be compensated by the change in water saturation when the fractional oil saturation exceeds 0.5.

The influence of misestimated density on the resultant saturation is more severe. The right three columns in Figure 4.12 present the sensitivity analysis of density. I obtain the triangles using a 1% reduced density for the workflow; the crosses correspond to a 1% increased density. We observe that the deviation from the base case for the density sensitivity is much higher than that of the velocity sensitivity. Furthermore, the influence of the altered density is almost equal for the resultant saturation of oil and gas, but smaller for the water saturation. From the discussions above, we notice that the estimation of density is more important for calculating the appropriate fluid saturation,

and a 1% error in the density value induces a miscalculation of fluid saturation about 0.3. In addition, density is the most difficult property to determine from the seismic data. However, in practice, the density obtained from the elastic-impedance analysis is the average value of an interval, corresponding to the seismic wavelength. Therefore, I obtain a reasonable value as long as the density value stays in the range of the local perturbation of the corresponding well-log data.

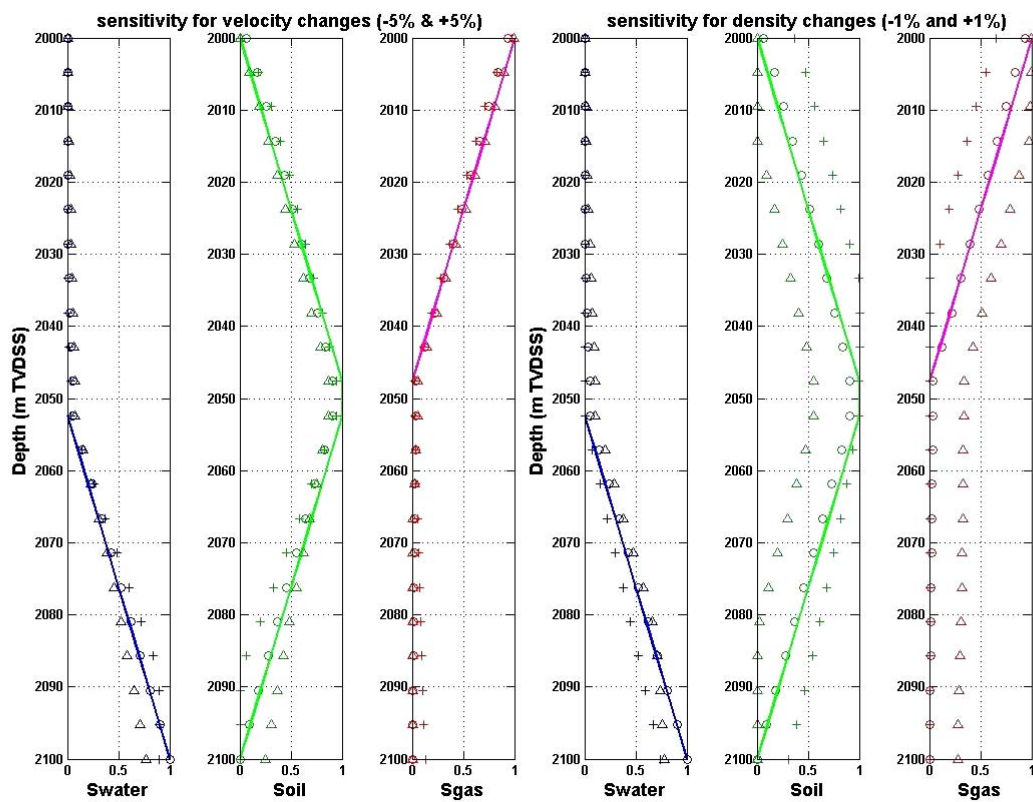


Figure 4.12: The analysis of sensitivity of the velocity and bulk density to the result of the workflow. The solid lines are the fluid saturation of the initial model. The left three columns show the sensitivity analysis for velocity. The circles represent the base case; the triangles present the resultant saturation calculated from the workflow with 5% lower  $V_p$  and  $V_s$  as inputs; the crosses represent the saturation calculated from the workflow with 5% higher  $V_p$  and  $V_s$ . The right three columns show the sensitivity analysis of density. The circles correspond to the base case; the triangles present the saturation calculated using the workflow with 1% lower density; the crosses represent the calculation result from the workflow with 1% higher density.

Figure 4.13 shows the  $V_p$ ,  $\rho$  and  $V_s$  from the elastic-impedance analysis discussed in Chapter 3. The estimated density in the dashed red line in the middle column is well controlled in the perturbation of the well log in the blue line, except at several depth points. The most prominent error is observed at 2500m, but this is a shaly portion that is 100% water-wet. Besides it, 2465m and 2540m exhibit higher deviation from the well log. We notice that the spiky miscalculations of the fluid saturation in Figure 4.10 at the same depth points are derived from the erroneous estimations of density.

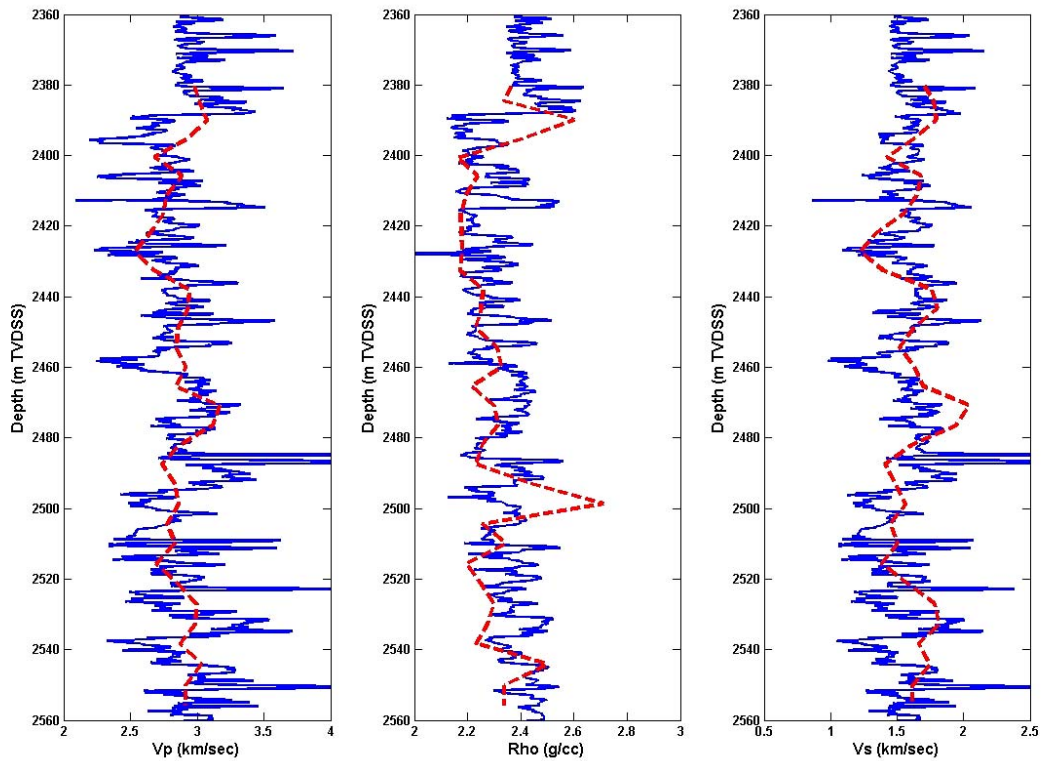


Figure 4.13: The estimated  $V_p$ ,  $\rho$  and  $V_s$  by the elastic-impedance analysis discussed in Chapter 3. The blue lines represent the actual well logs; the dashed red lines show the results of the seismic-data analysis. Note that most points on the red lines are within the local perturbations of the well logs.

### 4.7.3 Porosity and shale volume

Porosity and shale volume are determined from the calculations using the velocity and density derived from the elastic-impedance analysis. Thus, in general, the range of estimation errors for porosity and shale volume are slightly higher than that of the velocity and density themselves. Figure 4.14 shows the sensitivity analysis for porosity in the left half and for shale volume in the right half. The sensitivity analysis of porosity shows a result similar to the sensitivity analysis of density, but the deviation from the base case is about 1/6 of the result for density in Figure 4.12. In the case study in this chapter, I calculate porosity directly from density using

$$\phi = -0.5401\rho + 1.4350. \quad (4.17)$$

Therefore, when I underestimate the density, the corresponding porosity will be higher than the actual value. The effect of lower density is opposite to that of higher porosity on the saturation calculated by the workflow. This relation compensates the influence of the erroneous input of density. In the left three columns in Figure 4.14, the triangles represent the saturation calculated by the workflow with 3% smaller porosity; the crosses represent the calculation result from the workflow with 3% higher porosity.

The workflow is less sensitive to the misestimation of the shale volume, as shown in the right half of Figure 4.14. The triangles represent the result of the workflow assuming no clay, which is equivalent to a 100% reduction of the shale volume from the initial model (reduce from 0.1 to 0.) Likewise, the crosses are obtained from the workflow with a 100% increased shale volume from the initial model. Both cases demonstrate only small deviations from the base case. The result indicates that 100% errors in the estimation of shale volume result in only about 0.1 change in the resultant fluid saturation.

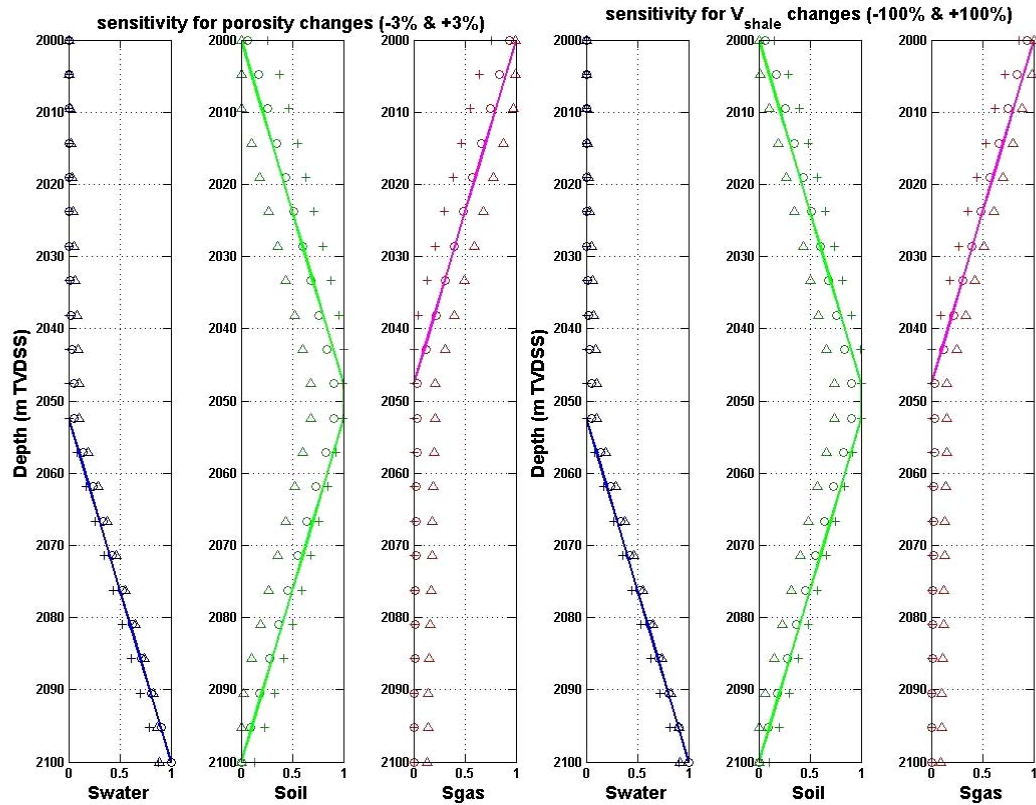


Figure 4.14: The analysis of porosity and shale-volume sensitivity to the result of the workflow. The left half shows the sensitivity analysis of porosity: the triangles are the result of 3% smaller porosity; the crosses are the result of 3% higher porosity. The right half shows the sensitivity analysis of shale volume: the triangles represent the result of 100% reduced shale volume; the crosses represent the result of 100% higher shale volume.

#### 4.7.4 Fluid and solid properties

The bulk moduli, shear moduli and densities of fluids and solids are determined based on the laboratory measurements. The left half of Figure 4.15 shows the sensitivity analysis of the fluid properties. I obtain the asterisks by rounding the fluid parameters in Table 4.2 to the first decimal point in the workflow. This precision is sufficient to derive the appropriate saturation as shown in Figure 4.15.

The right half of Figure 4.15 exhibits the sensitivity of the solid properties. The asterisks are derived from the workflow with the properties of quartz, instead using the

properties of the average mineral of the target reservoir. The maximum deviation from the initial model is about 0.16 at the bottom, where the formation is 100% water saturated. As shown in Figure 4.6, the properties of quartz is located out of the chart for this case-study dataset, therefore, the expected errors for most points in this chart are much smaller than this extreme case.

In addition, the triangles are obtained by the workflow using Castagna's regression between  $V_p$  and  $V_s$  as follows in step 4:

$$V_s=0.804V_p-0.856. \quad (4.18)$$

The water-saturated  $V_p$  and  $V_s$  of the initial model are determined following Han's regression as shown below:

$$V_s=0.79V_p-0.79. \quad (4.19)$$

Using other relations between  $V_p$  and  $V_s$  for the workflow has a similar effect to employing inappropriate solid properties. To avoid the occurrence of such errors, we need to determine the best relation between  $V_p$  and  $V_s$  from laboratory measurements and/or well-log data.

We need many kinds of input parameters to derive the fluid saturation of a reservoir from the seismic data. Each parameter shows different behaviors and degrees of sensitivity to the workflow. Thus, it is useful to calculate the saturation using several different schemes of input parameters. Nevertheless, since the combined effect of all parameters is difficult to estimate, matching the result to the well-log analysis is the most effective way to obtain the optimal calibrations of the input parameters.

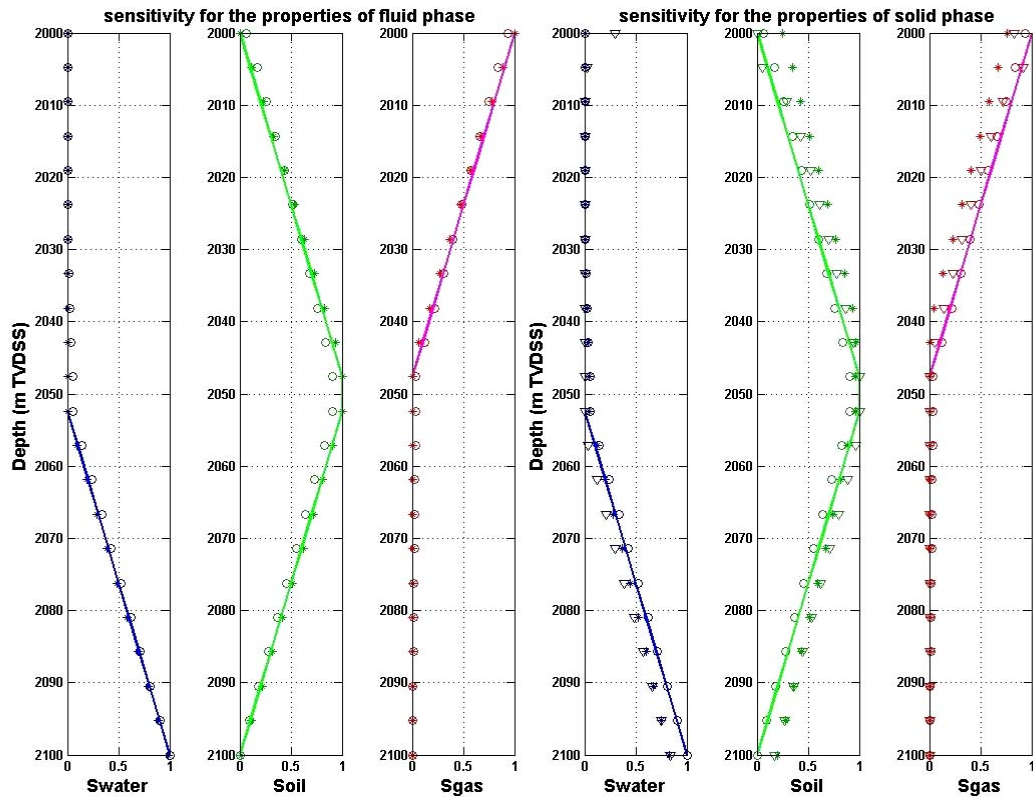


Figure 4.15: The sensitivity analysis of the fluid and solid properties to the result of the workflow. The left half shows the sensitivity analysis of fluid properties: the asterisks represent the fluid properties in Table 4.2 after rounding to the first decimal point in the workflow. The right half shows the sensitivity analysis of solid properties: the triangles represent the pure quartz assumption for the grains; the asterisks represent Castagna's regression of  $V_p$ - $V_s$  instead of using Han's regression.

For this matching process, optimizing the weighting factor for mixing the two fluid saturation scales, discussed in the step 12, is the most practical way to control the overall profile.

## 4.8 Implementation of the workflow on time-lapse seismic

I apply the workflow to a time-lapse seismic dataset from an actual producing oil field. The target reservoir is a blanket sandstone deposited under a braided-river environment in the early Jurassic. There are two vintages of seismic data available,

which were acquired in 1997 and 2001. Each set consists of three angle stacks, for which I used the elastic impedance to derive  $V_p$ ,  $V_s$ ,  $\rho$  and shale volume in Chapter 3.

First, I show a comparison of the time-lapse seismic data in Figure 4.16. The top section represents an east-west line from the 1997 data, and the bottom section corresponds to the same line from the 2001 data. The two data sets are processed in a sequence specifically designed to match the time-lapse seismic. The red line in the sections is the interpreted horizon of the near top reservoir, and the black trace indicates the sonic log of Well A, which is a vertical well drilled in this section.

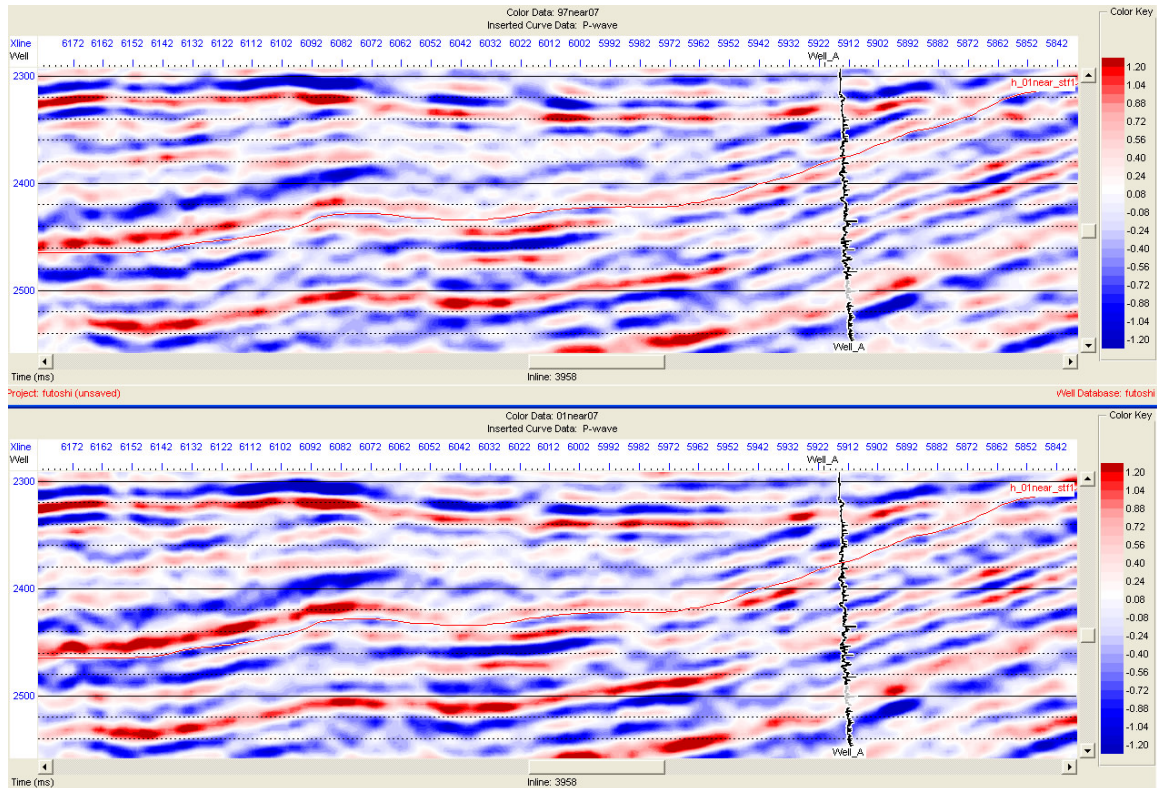


Figure 4.16: A comparison of the time-lapse seismic data for a case study. The thin red horizon represents the near top reservoir. The black trace indicates the sonic log of Well A. We observe a slight change in seismic amplitude along the horizon at the down flank, but it is impossible to quantitatively discuss the fluid displacement from the change.

Comparing two near-stack sections, we observe slight changes in amplitude in several portions, especially around the horizon at the down flank of the tilted structure. However, it is impossible to quantitatively evaluate the fluid displacement from the change in amplitude.

Another way to compare time-lapse seismic in terms of fluid displacement is to calculate the amplitude difference between the near stack and far stack. Since Poisson's ratio is a good indicator of the change in formation fluid, the amplitude difference often provides information of the fluid change. Figure 4.17 exhibits the comparison of the amplitude difference: the top section for 1997 and the bottom section for 2001.

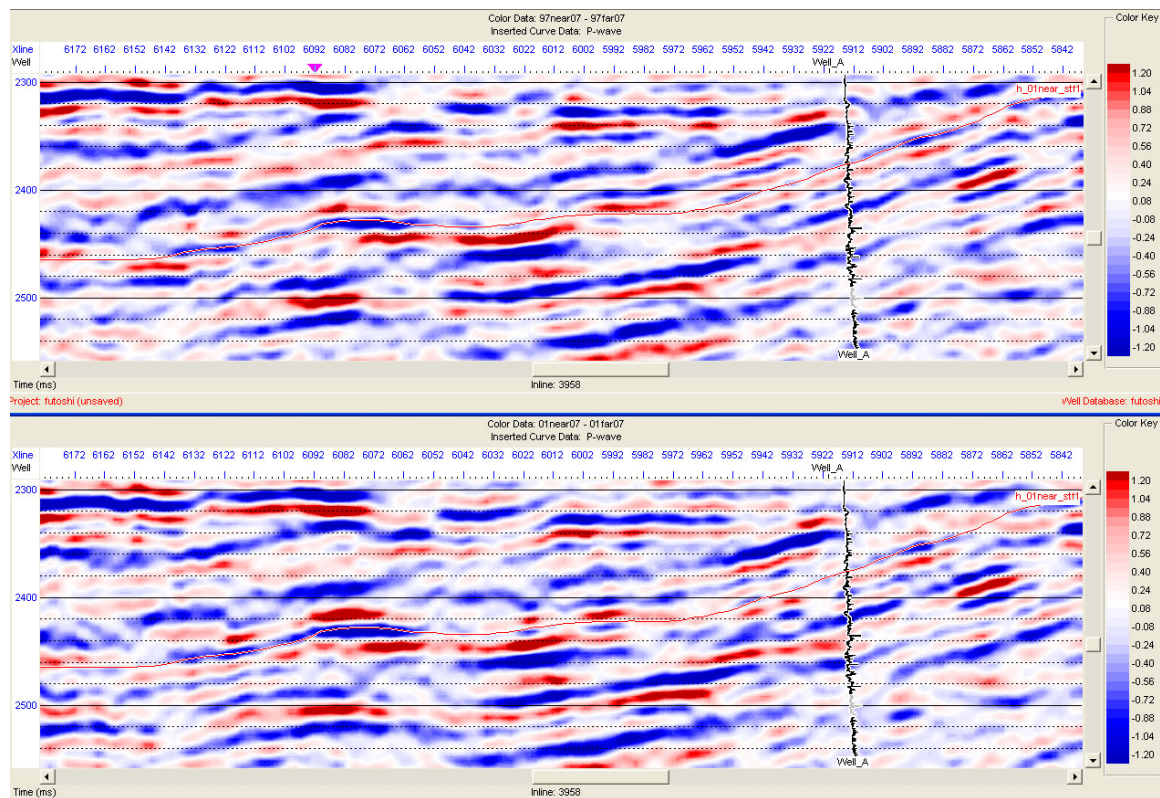


Figure 4.17: A comparison of the time-lapse seismic data in the amplitude difference between the near and far stacks. We observe a subtle change in the amplitude difference along the horizon at the down flank, but there is no way to discuss the fluid displacement quantitatively.

As in Figure 4.16, we observe subtle changes in the amplitude difference along the horizon at the down flank, but still cannot discuss the fluid displacement in a quantitative way.

Next, I show the oil saturation section derived from the angle stacks through my workflow. The top of Figure 4.18 represents the oil saturation section calculated from the seismic data acquired in 1997, and the bottom section is the section for the 2001 seismic data. I limit the calculation area within the reservoir so we only see the result inside the reservoir. Comparing the two sections, we now clearly recognize the fluid displacement. In the upper half for the down flank, there were several pockets of higher oil saturation in red in 1997.

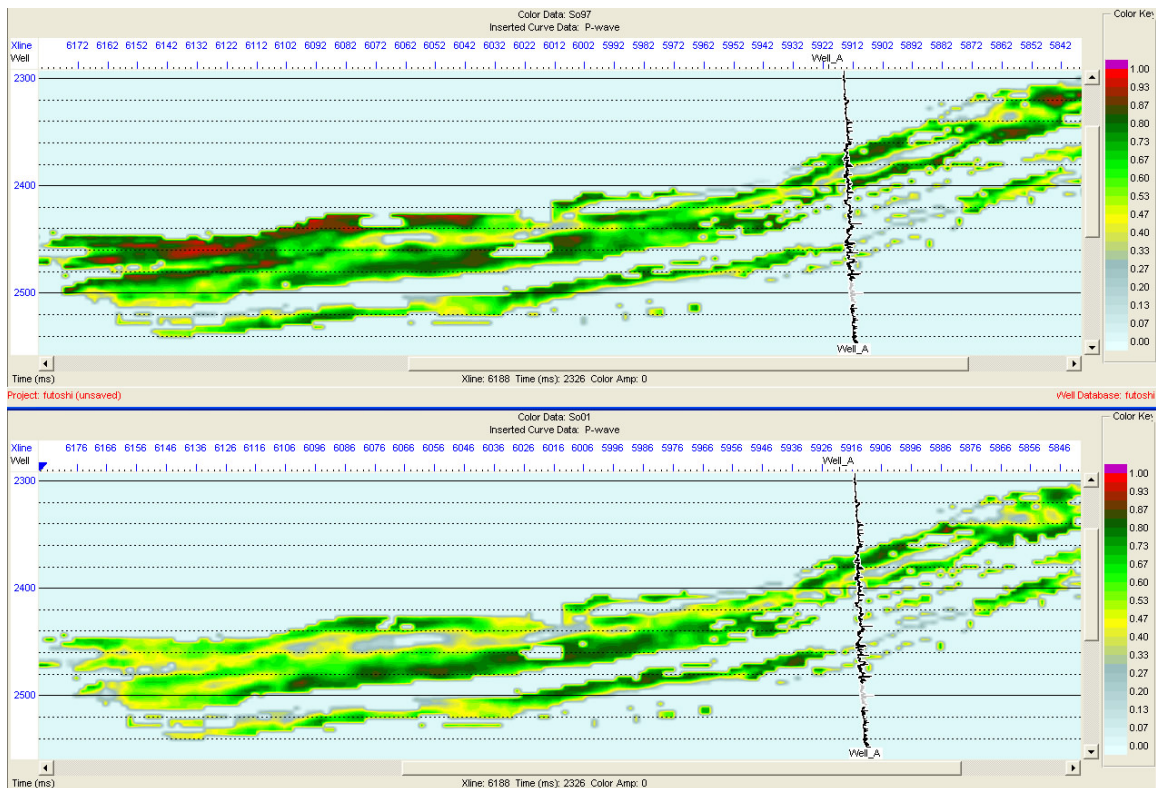


Figure 4.18: A comparison of the oil-saturation sections calculated from time-lapse seismic data: the top represents 1997; the bottom represents 2001. We observe (1) the clear reduction of oil saturation near the top reservoir at the down flank and (2) a big body of bypassed oil in green in the middle of the reservoir. The color code is fractional oil saturation calculated according to my workflow.

In contrast, all such higher oil saturation pockets have disappeared in the oil saturation section of 2001. The two sections explicitly demonstrate that (1) oil in the top subunit of the reservoir at the down flank was effectively produced in 4 years of production, and (2) a big body of high oil saturation, shown in green in the middle of the reservoir, remains as a bypassed oil accumulation, even in 2001. In addition, the flat bottom of the high oil saturation in a sand body ranging from crossline numbers 6046 to 6096 at 2440 msec corresponds to the flat spot in the seismic sections in Figure 4.17. This agreement proves the validity of the workflow.

Figures 4.19 and 4.20 show the saturation of gas and formation-water, respectively.

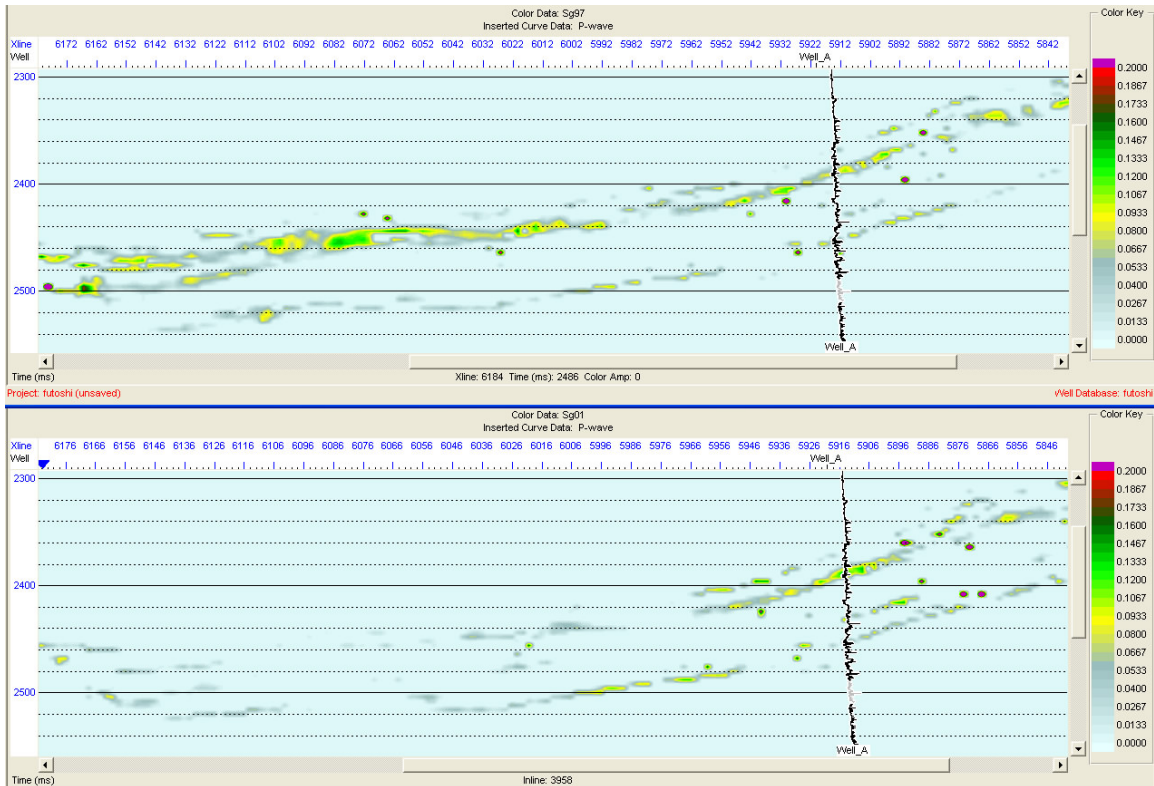


Figure 4.19: A comparison of the gas-saturation sections calculated from time-lapse seismic data: the top represents 1997; the bottom represents 2001. We observe the reduction of gas saturation near the top reservoir at the down flank. The color code is fractional gas saturation from 0 to 0.2.

In the both figures, the top section represents the analysis result of the 1997 seismic data and the bottom section corresponds to the result for the 2001 seismic data.

The highest gas saturation is less than 0.2 as shown in Figure 4.19, and the saturation in 2001 is smaller than that in 1997. This saturation reduction is obvious at the down flank, where the decrease in oil saturation is prominent as well.

The change in water saturation sections is the inverse image of the oil saturation. In Figure 4.20, I use the inverse color code of Figure 4.18, therefore the image is almost identical to Figure 4.18. Note that the spiky miscalculations discussed in Figure 4.10 appear as dots in the sections, due to the discontinuous nature of the errors.

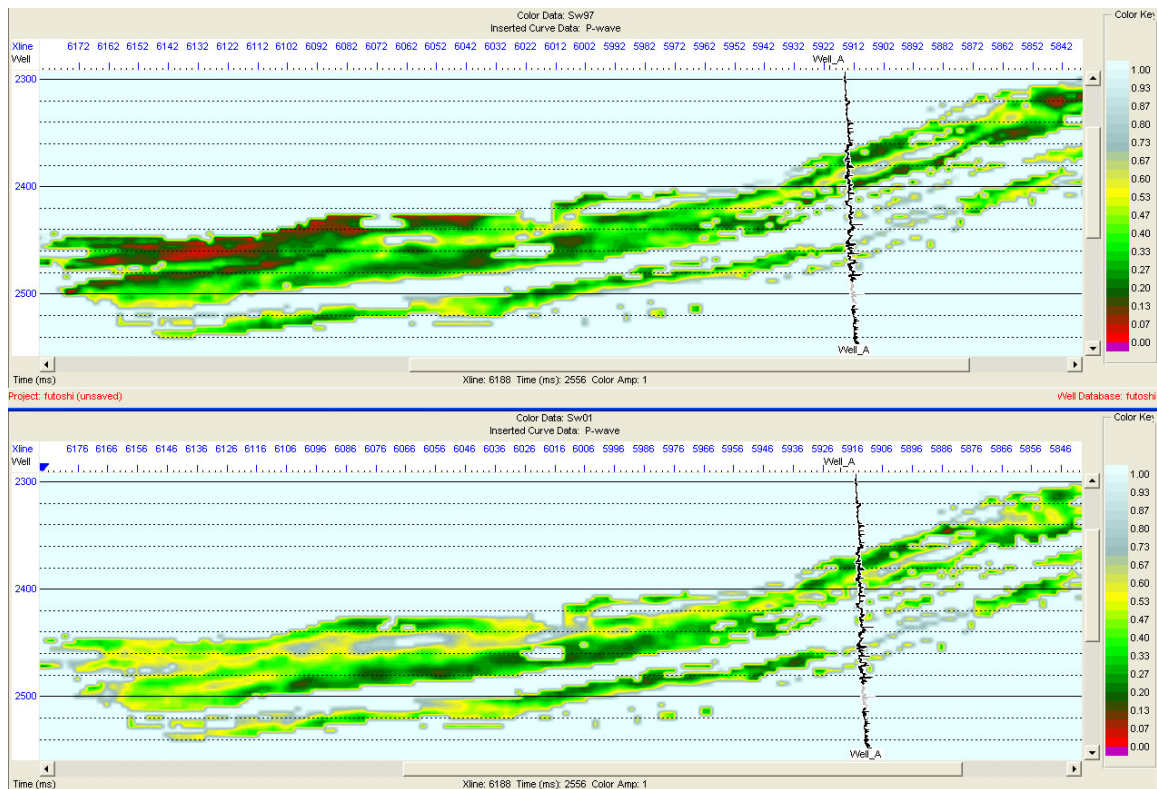


Figure 4.20: A comparison of the water-saturation sections calculated from time-lapse seismic data: the top represents 1997; the bottom represents 2001. The image is almost identical to Figure 4.18, since the gas saturation is almost negligible, and I use the inverse of the color code from Figure 4.18.

Finally, I apply the workflow to the whole volume of seismic data to calculate fluid saturation from the time-lapse seismic dataset, and display the results in a perspective view. Figures 4.21 and 4.22 show the oil saturation in 1997 and 2001, respectively. The limits of the color code range from 1.0 at 127 to 0 at -128, in fractional saturation. Some higher oil saturation bodies in red in the upper half of Figure 4.21 disappeared in Figure 4.22 after 4 years of oil production.

I display the gas saturation images from the time-lapse seismic data in Figures 4.23 and 4.24. Likewise, Figures 4.25 and 4.26 show the water saturation calculated from the time-lapse seismic. We can quantitatively detect the fluid saturation in a reservoir from the seismic data by applying the new workflow discussed in this chapter; a sequence of deterministic computations based on the known rock-physics theories.

An obvious question about the result is the reliability of the saturation derived from the time-lapse seismic data. When I compare the lower left portion of Figures 4.21 and 4.22, I observe the location shift of higher oil saturation in red near the compass. Similarly, patchy higher oil saturation portions in red around the center of Figures 4.21 and 4.22 are changing the locations. Moreover, in this area, overall oil saturation increases after 4 years production in contrast to the reduction of oil saturation in the west of the structure. The structure is a tilted fault block dipping towards northwest; therefore, it is possible to increase oil saturation in up-dip side, around the center of the figures. However, when we consider the uncertainty in the resultant saturation, plus or minus 0.15 as discussed in Figure 4.10, the oil saturation in the up-dip side can be unchanged and the reduction of oil saturation in the down flank may be more harsh: we need to aware of a possible slide scale up to plus or minus 0.15 in saturation for the result of the workflow.

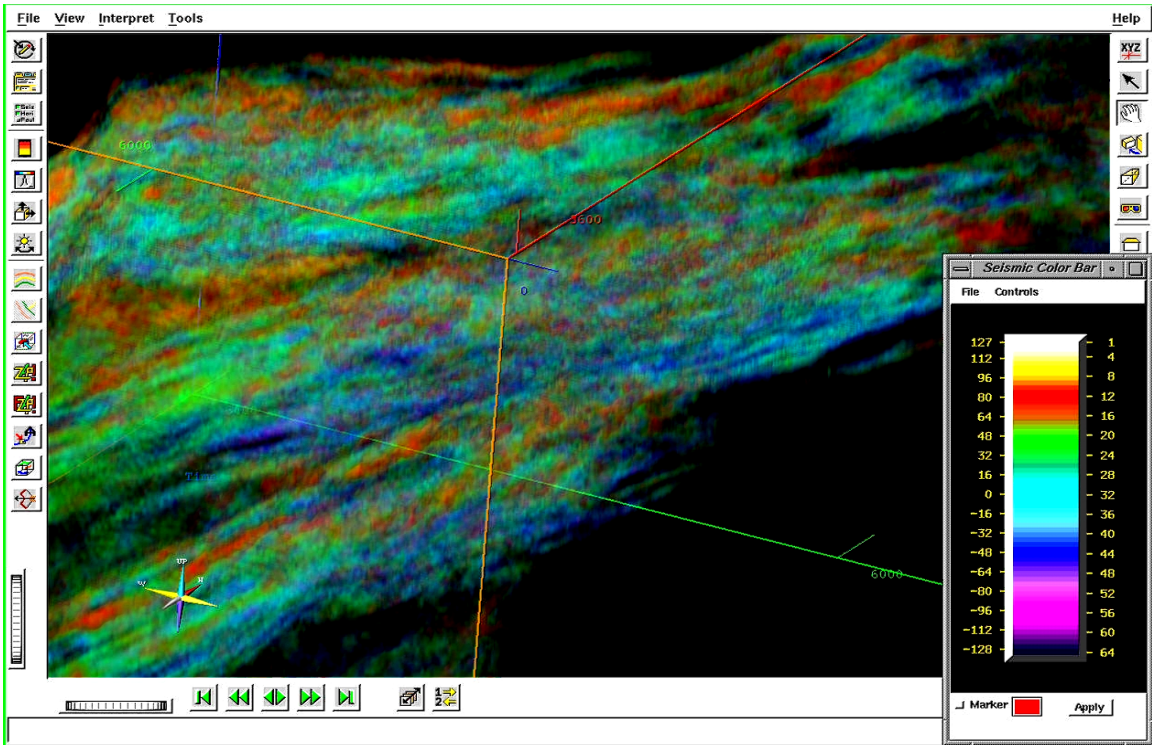


Figure 4.21: The distribution of oil saturation derived from the seismic data acquired in 1997. The color code is in fractional saturation from 1.0 at 127 to 0.0 at -128.

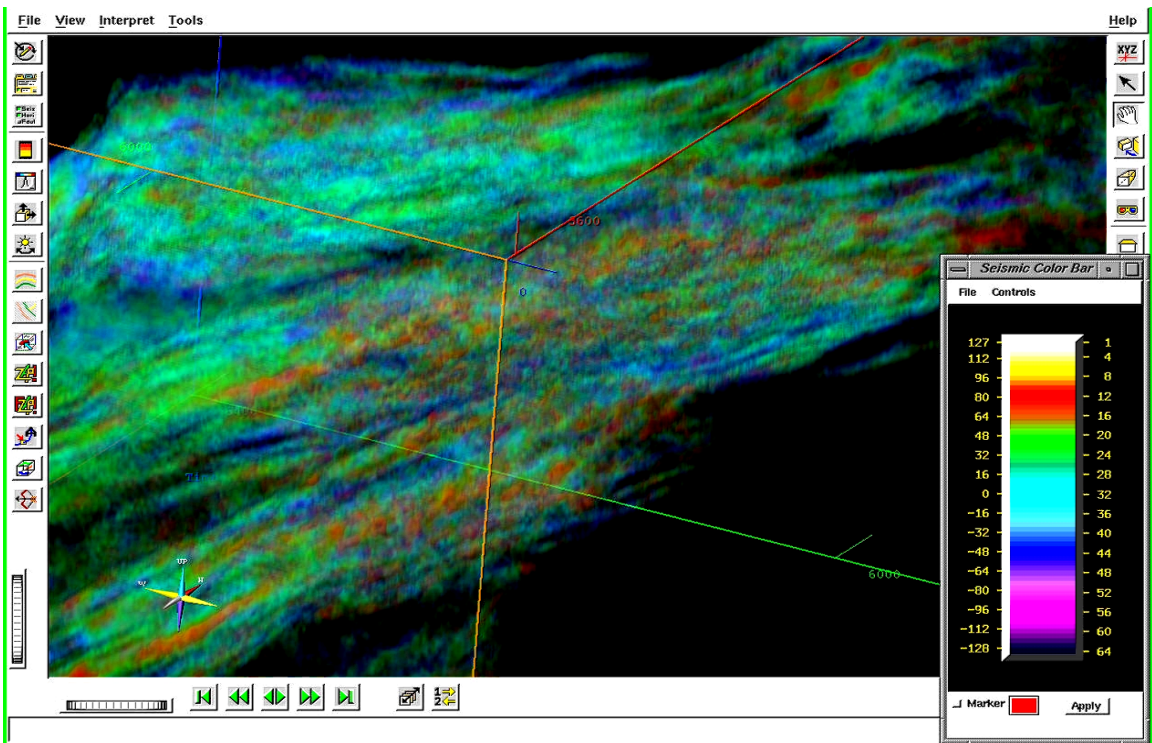


Figure 4.22: The distribution of oil saturation derived from the seismic data acquired in 2001. The color code is in fractional saturation from 1.0 at 127 to 0.0 at -128. Note that some higher-oil-saturation bodies in red in Figure 4.21 disappeared after 4 years of production.

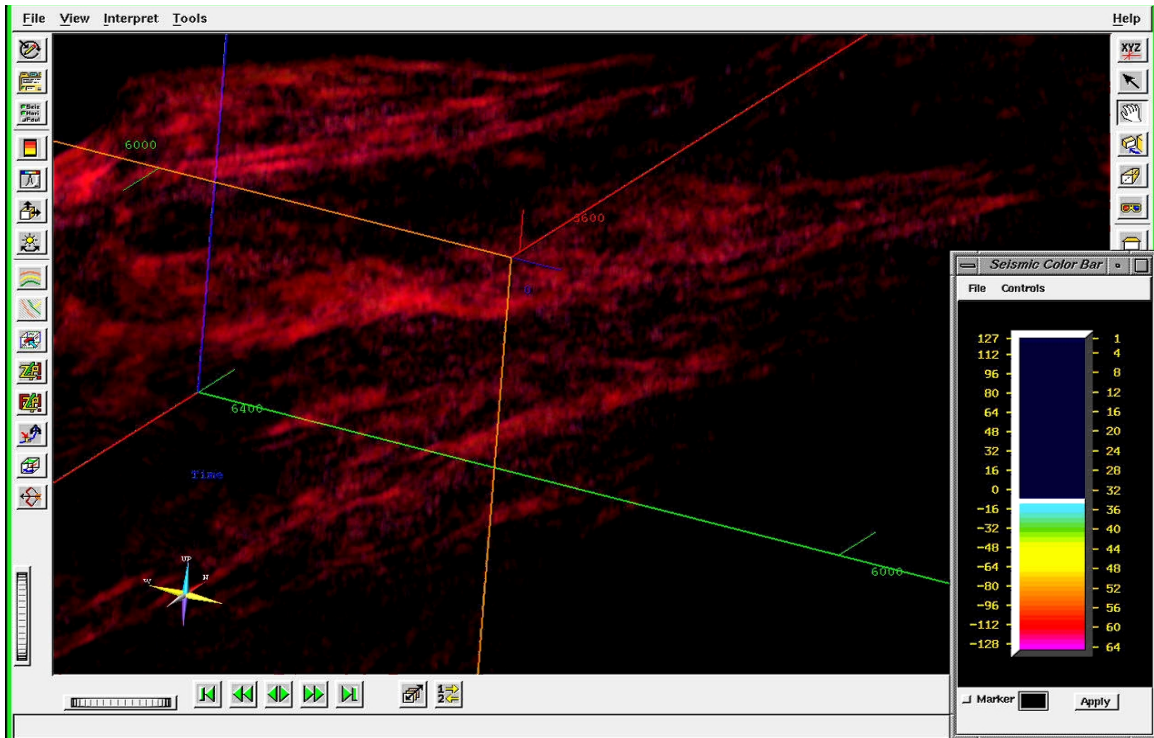


Figure 4.23: The distribution of gas saturation derived from the seismic data acquired in 1997. The color code is in fractional saturation from 1.0 at 127 to 0.0 at -128.

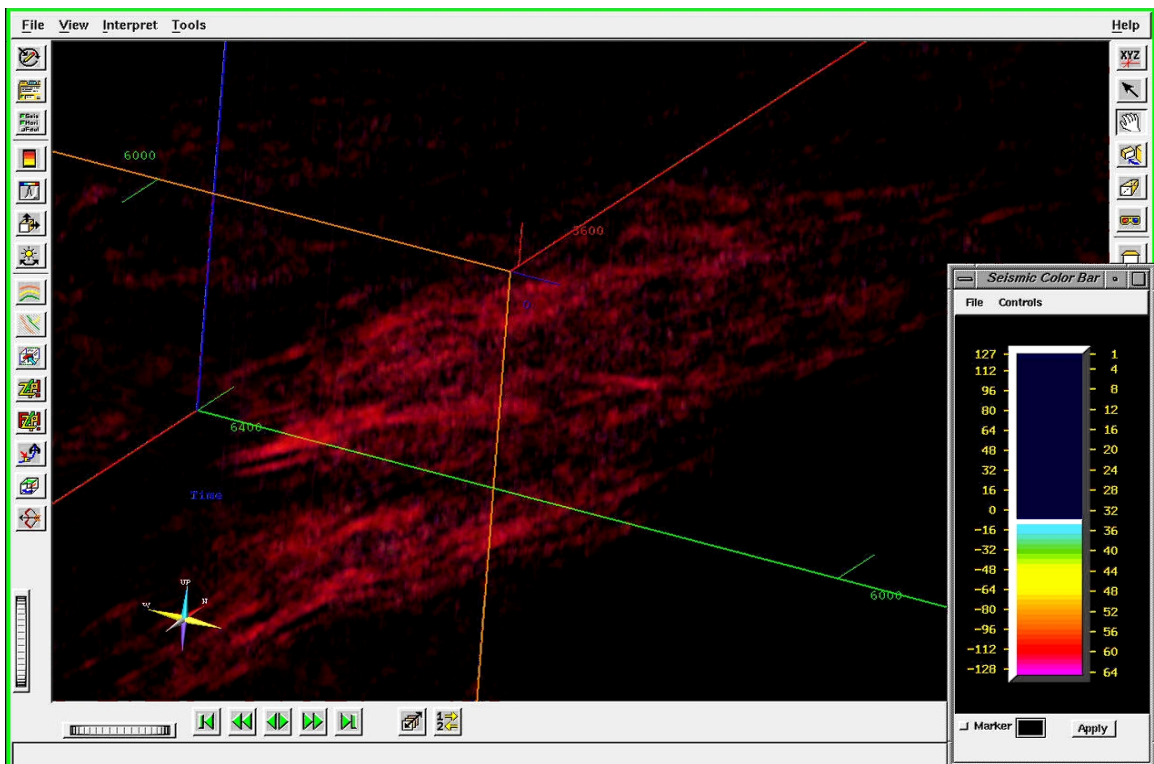


Figure 4.24: The distribution of gas saturation derived from the seismic data acquired in 2001. The color code is in fractional saturation from 1.0 at 127 to 0.0 at -128.

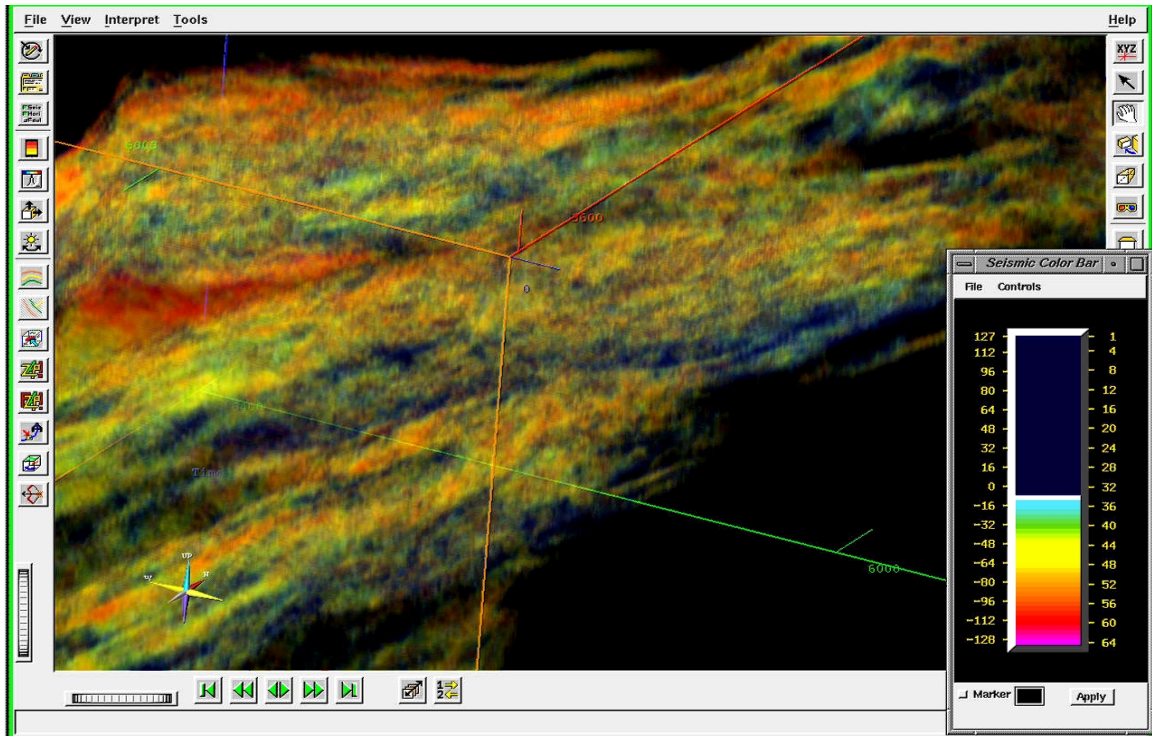


Figure 4.25: The distribution of water saturation derived from the seismic data acquired in 1997. The color code is in fractional saturation from 1.0 at 127 to 0.0 at -128.

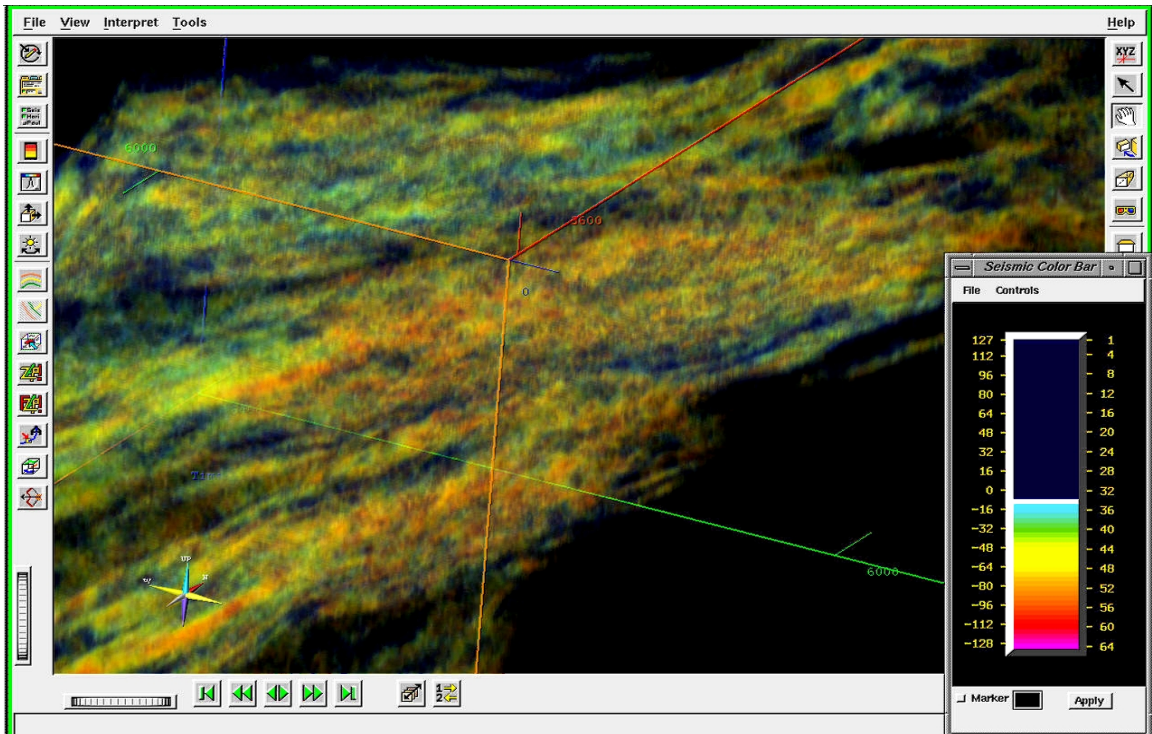


Figure 4.26: The distribution of water saturation derived from the seismic data acquired in 2001. The color code is in fractional saturation from 1.0 at 127 to 0.0 at -128.

## 4.9 Conclusions

Combining several rock-physics analytic methods and transforms, I have established a workflow to obtain the fluid saturation in a reservoir by processing seismic data.

First, the pressure change during oil production and the fluid saturation scale are considered. I use the output from the flow simulator of the field as input for the analyses of the pressure change and of the fluid saturation scale of the time-lapse seismic data. I conclude that the pressure has less than 1% effect on the velocity. Thus, I neglect the effect of pressure change in the case study. The fluid saturation scale is discussed in a method similar to Sengupta et al. (2003); I generate time-lapse well-log data for the control wells using the initial oil saturation as an oil accumulation indicator.

Next, I calculate the average moduli of sandstone grains for the reservoir using laboratory measurements. Then, I mix the properties of the average sand grain with a clay according to the shale volume derived from the elastic-impedance analysis discussed in Chapter 3. This process provides us the solid-phase properties for further analyses. Given the solid properties and the properties of the formation fluids measured in the laboratory, I demonstrate a deterministic workflow to calculate the bulk modulus and density of the in-situ fluid in the reservoir from the seismic data. The workflow is summarized in Figure 4.7.

Then I analyze the sensitivity of each input parameter. I find that the most sensitive parameter is bulk density, which is the most unstable output in the elastic-impedance analysis. The best way to optimize the result of the workflow is to use the weighting factor for mixing two different saturation scales to control the overall calculation result.

For this process, we need to find the optimal weighting factor that matches the seismic analysis result to the fluid saturation derived from well-log analysis at well locations.

Finally, I apply the workflow to the time-lapse seismic data of an offshore oil field. In the results, I show a clear image of the fluid displacement in the reservoir after 4 years of oil production and delineate a remaining oil body. However, the estimated values of the fluid saturation from the workflow are bearing the uncertainty ranging around plus or minus 0.15 in this case study. Such uncertainty range will expand when the rock-frame stiffness increases and the seismic data becomes more insensitive to the fluid in the reservoir.

I demonstrate that we can enhance the potential of rock-physics theories by carefully choosing the input data. For the analysis of time-lapse seismic, integrating the knowledge of geophysics, geology, and reservoir engineering very carefully is a key to obtain successful results.

## REFERENCES

- Al-Najjar, N., Doyen, P., Brevik, I., Kvamme, L. and Psaila, D., 1999, Stattjord field -- time-lapse seismic interpretation using a 4-D earth model. Expanded Abstracts, 69th Annual International Meeting, Society of Exploration Geophysicists, 1620-1623.
- Batzle, M., and Wang, Z., 1992, Seismic properties of pore fluids, *Geophysics*, **57**, 1396-1408.
- Gabriels, P. W., Horvei, N. A., Koster, J K., Onstein, A., Geo, A. and Staples, R., 1999, Time Lapse Seismic Monitoring of the Draugen Field. Expanded Abstracts, 69th Annual International Meeting, Society of Exploration Geophysicists, 2035-2037.
- Gassmann, F., 1951, Uber die elastizitat poroser medien. *Verteljahrsschrift der Naturforschenden Gesellschaft in Zurich*, **96**, 1-23.
- Gouveia, W. P., Johnston, D. H. and Solberg, A., 2004, Remarks on the estimation of time-lapse elastic properties: the case study for the Jotun field, Norway, Expanded Abstracts, 74th Annual International Meeting, Society of Exploration Geophysicists, 2212-2215
- Han, D-H., 1986, *Effects of Porosity and Clay Content on Acoustic Properties of Sandstones and Unconsolidated Sediments*. Ph.D. dissertation, Stanford University.
- Hill, R., 1952, The elastic behavior of a crystalline aggregate. *Proc. Phys. Soc. London Ser. A*, **65**, 349-354.
- Johnstad, S., Seymour, R., and Smith, P., 1995, Seismic reservoir monitoring over the Oseberg field during the period 1989-1992. *First Break*, **13**, May, 169-183.

- Johnston, D. H., Gouveia, W. P., Solberg, A. and Lauritzen, M., 2003, Integration of time-lapse seismic and production logging data: Jotun Field, Norway, Expanded Abstracts, 73rd Annual International Meeting, Society of Exploration Geophysicists, 1346-1349.
- Landro, M., 2001, Discrimination between pressure and fluid saturation changes from time-lapse seismic data. *Geophysics*, **66**, 836-844.
- Landro, M., 2002, Uncertainties in quantitative time-lapse seismic analysis. *Geophysical Prospecting*, **50**, 527-538.
- Landro, M., Veire, H. H., Duffaut K. and Al-Najjar, N., 2003, Discrimination between pressure and fluid saturation changes from marine multicomponent time-lapse seismic data. *Geophysics*, **68**, 1592-1599.
- Lumley, D., Meadows, M., Cole, S. and Adams, D., 2003, Estimation of reservoir pressure and saturations by crossplot inversion of 4D seismic attributes. 73rd Annual International Meeting, Society of Exploration Geophysicists, 1513-1516.
- Lumley, D., 2004, Business and technology challenges for 4D seismic reservoir monitoring. *The Leading Edge*, **23**, 1166-1168.
- Rutledal, H., Helgesen, J. and Buran, H., 2003, 4D elastic inversion helps locate in-fill wells at Oseberg field. *First Break*, **21**, 39-43.
- Sengupta, M., Mavko, G. and Mukerji, T., 2003, Quantifying subresolution saturation scales from time-lapse seismic data: A reservoir monitoring case study. *Geophysics*, **68**, 803-814.

- Smith, P., Berg, J., Eidsvig, S., Magnus, I. and Verhelst, F., 2001, 4-D Seismic in a complex fluvial reservoir: The Snorre feasibility study. *The Leading Edge*, **20**, 270-277.
- Sonneland, L., Veire, H. H., Raymond, B., Signer, C., Pedersen, L., Ryan, S., and Sayers, C., 1997, Seismic reservoir monitoring on Gullfaks. *The Leading Edge*, **16**, 1247-1252.
- Tsuneyama, F., and Mavko, G., 2005, Rock-physics-bounds-constrained elastic-impedance analysis for sand body detection, Stanford Rock Physics and Borehole Physics Annual Meeting, A8.
- Veire, H. H., Raymond, S. B., Signer, C., Tennebo, P. O. and Sonneland, L., 1998, Estimation of reservoir fluid volume through 4-D seismic analysis on Gullfaks. Expanded Abstracts, 68th Annual. International Meeting: Society of Exploration Geophysicists, 27-30
- Watts, G., Jizba, D., Gawith, D., and Gutteridge, P., 1996, Reservoir monitoring of the Magnus field through 4-D time-lapse seismic analysis. *Petroleum Geoscience*, **2**, 361-372.
- Wood, A. B., 1941, *A Textbook of Sound*. G. Bell and Sons.

# Chapter 5

## Exploring $V_p$ - $V_s$ relations: Approach from effective medium theories

### 5.1 Abstract

Several empirical relations between  $V_p$  and  $V_s$  have been proposed for the lithologies of oil and gas reservoirs. Although recent technology supplies us an improved sonic log tool to measure  $V_s$  as well as  $V_p$ , often the  $V_s$  measurement is distorted due to the very sensitive nature of S-waves to borehole conditions. In addition, the difficulty of picking the first breaks of S-waves often makes the quality of the  $V_s$  log insufficient for seismic analysis. On the other hand, the demand for  $V_s$  information is expanding since the  $V_p/V_s$  ratio (or Poisson's ratio calculated from the  $V_p/V_s$  ratio) is key to characterizing subsurface lithology and/or estimating the formation fluids in the reservoir, by analyzing the AVO response of the seismic data.

In Chapter 5, I present a theoretical approach for understanding rock  $V_p$ - $V_s$  relations using the Hashin-Shtrikman bounds and effective-medium theories. To find the bounds of the  $V_p/V_s$  ratio, I adopt the upper and lower Hashin-Shtrikman bounds of the mixture of a rock and brine. For any mixture, the upper Hashin-Shtrikman bound corresponds to the lowest  $V_p/V_s$  bound and the lower Hashin-Shtrikman bound is equivalent to the highest  $V_p/V_s$  bound.

Then, I compare the  $V_p$ - $V_s$  relations calculated by a model with tubular pores by Mavko (1980) and a self-consistent inclusion model of spheroid pores by Berryman (1995). I explore the  $V_p$ - $V_s$  relations of the computed results in the crossplot domain among  $V_p$ ,  $V_s$  and porosity. The  $V_p$ - $V_s$  trend of sandstone is represented better by the model with tubular pores.

I discuss that the location in the crossplots is an indicator of the pore shape. I show that a modified Reuss bound provides a good approximation of the  $V_p$ - $V_s$  relation of a rock comprised of grains, and that the upper Hashin-Shtrikman bound resembles Castagna's trend for carbonates.

## **5.2 Introduction**

The most widely used empirical  $V_p$ - $V_s$  relations have been published by Castagna *et al.* (1993), for rock types including sandstone, mudrock, limestone and dolomite. In general, Castagna's regressions provide us reasonable results in terms of calculating  $V_s$  from the measured  $V_p$  in most practical cases. Xu and White (1995) demonstrated a method to determine the  $V_p$ - $V_s$  relation of shaly sandstone by mixing two inclusion

models with different aspect ratios, which represent the sandstone and shale portions. Jørstad *et al.* (1999) compared the method by Xu and White (1995) to linear regressions using a dataset from the North Sea. They concluded that the inclusion models need to be calibrated well by well, whereas the simple regression tuned to the target wells provide good prediction of  $V_s$  from the measured  $V_p$  in their data. However, there is no systematic explanation why a linear regression works well in most cases.

One way to discuss the  $V_p$ - $V_s$  relation is by deriving velocities using an effective-medium theory. As quoted in Mavko *et al.* (1998), the best bounds, defined as giving the narrowest possible range in the velocity-porosity plane without specifying anything about the geometries of constituents, are the Hashin-Shtrikman bounds. These bounds give us the upper and lower limits of the data distribution for bulk and shear moduli as a function of the volume fractions of mixing materials. I adopt the Hashin-Shtrikman bounds to explore  $V_p$ - $V_s$  relations for rock-fluid mixtures.

### **5.3 The Hashin-Shtrikman Bounds**

The Hashin-Shtrikman bounds represent a geometrically defined mixture of two materials, which are allocated outside and inside of concentric spheres. The spheres are in various sizes so that the visual image of the upper bound is randomly sized spherical pores in a chunk of rock. The lower bound can be visualized as variously sized spheres suspended in another material. However, since the lower bound is identical to the Reuss bound when the shear modulus of one of the two materials is 0, the lower bound can be considered as horizontally stacked layers of the two materials.

The upper (+) and lower (-) Hashin-Shtrikman bounds are given by the following:

$$\begin{aligned}
 K^{\pm} &= K_1 + \frac{f_2}{\frac{1}{(K_2 - K_1)} + f_1 \left( K_1 + \frac{4}{3} \mu_1 \right)}, \\
 \mu^{\pm} &= \mu_1 + \frac{f_2}{\frac{1}{(\mu_2 - \mu_1)} + \frac{2f_1(K_1 + 2\mu_1)}{5\mu_1 \left( K_1 + \frac{4}{3} \mu_1 \right)}}.
 \end{aligned}
 \tag{5.1}$$

where

$K_1$  is the bulk modulus of material 1,  
 $K_2$  is the bulk modulus of material 2,  
 $\mu_1$  is the shear modulus of material 1,  
 $\mu_2$  is the shear modulus of material 2,  
 $f_1$  is the volume fraction of material 1,  
 $f_2$  is the volume fraction of material 2.

In addition, I calculate the density of a mixture of the two materials as follows:

$$\rho_{bulk} = f_1 \rho_1 + f_2 \rho_2.
 \tag{5.2}$$

Then, I compute  $V_p$ ,  $V_s$ , porosity (=volume fraction of a fluid) and density for the Hashin-Shtrikman bounds of a mixture.

Now, I calculate the upper and lower Hashin-Shtrikman bounds for brine-saturated sandstone. But the shear modulus of brine is 0; thus, I obtain 0 for the shear modulus of the mixture. This means  $V_s$  is 0 for the lower bound, except for the 100% solid point. To obtain a practical limit of the lowest  $V_s$ , I investigate the laboratory measurement of loose sand by Zimmer (2004). He measured the  $V_s$  for brine-saturated Galveston beach sand at critical porosity of 0.4336 under a confining pressure of 0.1 MPa and obtained  $V_s \approx 0.2$  Km/sec. I employ this velocity as a realistic lowest  $V_s$  at critical porosity and calculate the equivalent shear modulus,  $\mu = 0.09$  GPa. Then, to obtain  $V_p = 1.5$  Km/sec at the critical

porosity, the bulk modulus is determined to be  $K=4.3575$  GPa. For future discussions, I assume the critical porosity to be 0.4. Table 5.1 summarizes the parameters used to calculate the Hashin-Shtrikman bounds for sandstone and shale.

Table 5.1: Summary of the parameters used to calculate the Hashin-Shtrikman bounds of sandstone.

| Material                            | Bulk modulus (GPa) | Shear modulus (GPa) | Density (g/cm <sup>3</sup> )                      |
|-------------------------------------|--------------------|---------------------|---|
| quartz                              | 37                 | 44.73               | 2.65  |
| clay                                | 23                 | 8                   | 2.58  |
| brine                               | 2.7416             | 0                   | 1.0038  |
| mixture at critical porosity (=0.4) | 4.3575             | 0.09                | $0.6\rho_{\text{solid}} + 0.4\rho_{\text{brine}}$ |

Figure 5.1 presents the resultant bounds in the  $V_p$ -porosity plane on the left and the  $V_s$ -porosity plane on the right. The solid lines represent the upper Hashin-Shtrikman bound and the dashed lines represent the lower Hashin-Shtrikman bound. All bounds in following figures are displayed with this convention. Then, I convert all the bounds into the  $V_p$ - $V_s$  plane as shown in Figure 5.2, where we observe the upper Hashin-Shtrikman bounds and the lower Hashin-Shtrikman bounds. Note that the upper Hashin-Shtrikman bound corresponds to the *lower*  $V_p/V_s$  bound, and vice versa. The black lines indicate two constant values for  $V_p/V_s$ : the dashed line corresponds to 1.5 and the solid line represents 2.0. Comparing the bounds to these  $V_p/V_s$  lines, we recognize that the upper Hashin-Shtrikman bound is the lowest  $V_p/V_s$  bound and the lower Hashin-Shtrikman bound is the highest  $V_p/V_s$  bound for any mixtures. I plot the regression line by Castagna et al. (1993) for brine-saturated sandstones in the yellow circles in Figure 5.2.

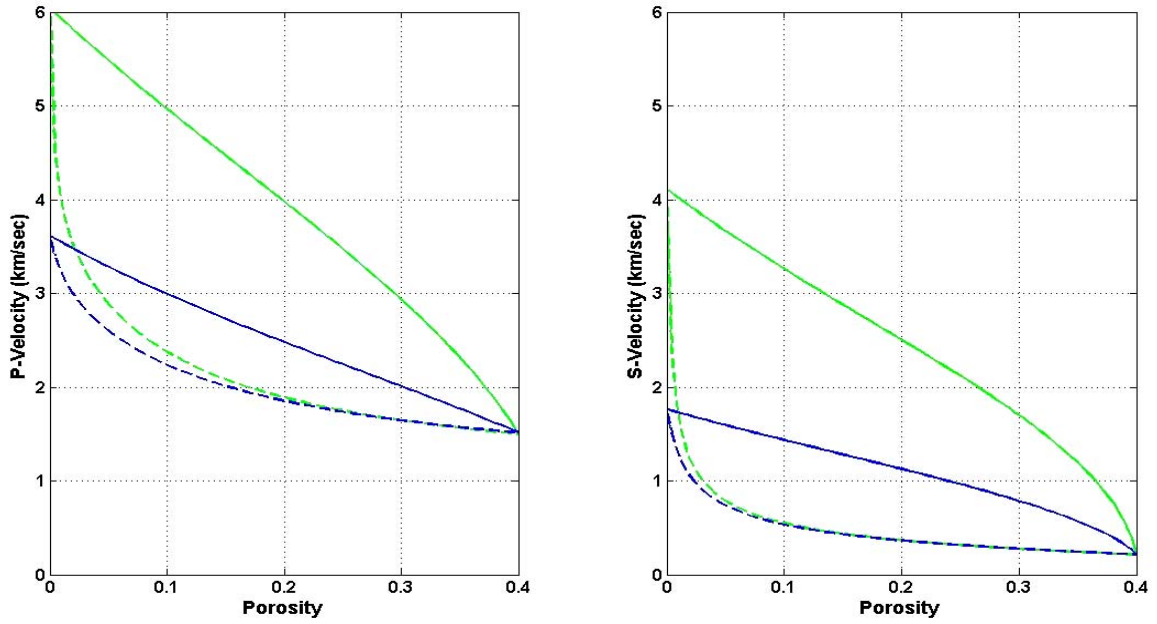


Figure 5.1: The upper and lower Hashin-Shtrikman bounds in the  $V_p$ -porosity plane on the left and the same bounds in the  $V_s$ -porosity plane on the right. The green lines represent a quartz-brine mixture, and the blue lines correspond to a clay-brine mixture. The solid lines correspond to the upper Hashin-Shtrikman bounds and the dashed lines correspond to the lower Hashin-Shtrikman bound.

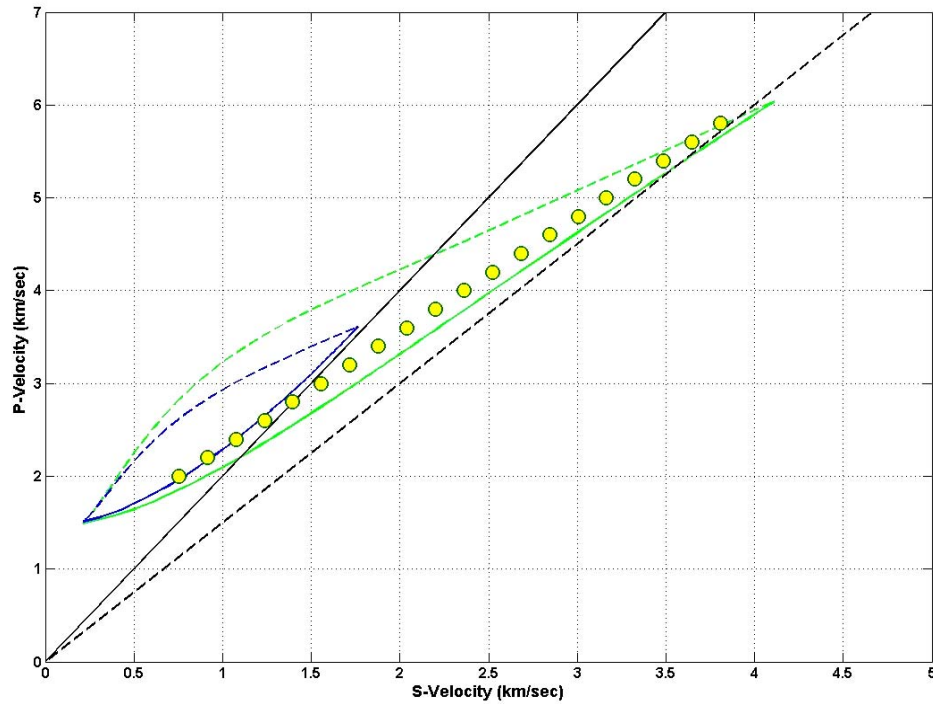


Figure 5.2: The upper and lower Hashin-Shtrikman bounds in  $V_p$ - $V_s$  plane. The green and blue lines are equivalent to those in Figure 5.1. The black lines indicate constant  $V_p/V_s$ : the dashed line is  $V_p/V_s=1.5$ ; the solid line corresponds to  $V_p/V_s=2$ . The yellow circles represent the regression line for brine-saturated sandstones by Castagna *et al.* (1993). Note that Castagna's regression is located between the solid green line and the solid blue line.

Castagna's empirical regression locates in between the upper Hashin-Shtrikman bound for quartz-brine mixture and the upper Hashin-Shtrikman bound of a clay-brine mixture. The intuitive interpretation of this result is that the regression line by Castagna represents intermediate trends between the upper Hashin-Shtrikman bounds for quartz-brine and clay-brine mixtures in both the  $V_p$ -porosity and  $V_s$ -porosity planes, therefore the resultant  $V_p$ - $V_s$  trend also falls between those end members in the  $V_p$ - $V_s$  plane. In general, most sandstones fall between the upper Hashin-Shtrikman bounds of quartz-brine and clay-brine mixtures. Castagna's regression is one of the best averaged  $V_p$ - $V_s$  trends for brine-saturated, quartz-dominated sandstones.

## **5.4 $V_p$ - $V_s$ relation of sandstone**

### **5.4.1 Stiff-sand and soft-sand models**

I have demonstrated the correlation of the locations for the Hashin-Shtrikman bounds in the velocity-porosity plane and in the  $V_p$ - $V_s$  plane. Next, I explore the relation of data locations in the two planes for the soft-sand model and the stiff-sand models introduced by Dvorkin and Nur (1996). They theoretically derived these effective-medium models, based on the contact stiffness of a sphere pack, which are derived from the Hertz-Mindlin model. The soft-sand model is given in a form of a modified lower Hashin-Shtrikman bound as follows:

$$\begin{aligned}
K_{dry} &= \frac{1}{\left[ \frac{\phi / \phi_{critical}}{K_{HM} + 4\mu_{HM} / 3} + \frac{1 - \phi / \phi_{critical}}{K_{solid} + 4\mu_{HM} / 3} \right]} - 4\mu_{HM} / 3, \\
\mu_{dry} &= \frac{1}{\left[ \frac{\phi / \phi_{critical}}{\mu_{HM} + z} + \frac{1 - \phi / \phi_{critical}}{\mu_{solid} + z} \right]} - z, \\
z &= \frac{\mu_{HM}}{6} \left( \frac{9K_{HM} + 8\mu_{HM}}{K_{HM} + 2\mu_{HM}} \right), \\
K_{HM} &= \left[ \frac{n^2(1 - \phi_{critical})^2 \mu_{solid}^2}{18\pi^2(1 - \nu_{solid})^2} P \right]^{\frac{1}{3}}, \\
\mu_{HM} &= \frac{(2Fd + 3) - (Fd + 3)\nu_{solid}}{5Fd(2 - \nu_{solid})} \left[ \frac{3n^2(1 - \phi_{critical})^2 \mu_{solid}^2}{2\pi^2(1 - \nu_{solid})^2} P \right]^{\frac{1}{3}},
\end{aligned} \tag{5.3}$$

where

$K$  is the bulk modulus,

$\mu$  is the shear modulus,

$\phi$  is the volume fraction of porosity,

$\nu$  is the Poisson's ratio,

$n$  is the coordination number, the number of average contacts per grain,

$P$  is the differential pressure in MPa,

$Fd$  is the fudge factor to control shear contact stiffness,  $> 1$  to reduce the stiffness.

The stiff-sand model is a modified upper Hashin-Shtrikman bound, expressed below:

$$\begin{aligned}
K_{dry} &= \frac{1}{\left[ \frac{\phi / \phi_{critical}}{K_{HM} + 4\mu_{solid} / 3} + \frac{1 - \phi / \phi_{critical}}{K_{solid} + 4\mu_{solid} / 3} \right]} - 4\mu_{solid} / 3, \\
\mu_{dry} &= \frac{1}{\left[ \frac{\phi / \phi_{critical}}{\mu_{HM} + z} + \frac{1 - \phi / \phi_{critical}}{\mu_{solid} + z} \right]} - z, \\
z &= \frac{\mu_{solid}}{6} \left( \frac{9K_{solid} + 8\mu_{solid}}{K_{solid} + 2\mu_{solid}} \right),
\end{aligned} \tag{5.4}$$

where  $K_{HM}$  and  $\mu_{HM}$  are the same as in Equation 5.3.

Employing the resultant bulk modulus and shear modulus of a dry rock from Equations 5.3 and 5.4, I calculate the brine-saturated  $Vp$  and  $Vs$  as a function of porosity, using Gassmann's equation. Figure 5.3 exhibit a series of soft and stiff sandstone models. I used 0.1 MPa as a confining pressure and 6 for a coordination number in the calculations. In addition, to fit the results within the Hashin-Shtrikman bounds, I applied a porosity-dependent velocity scale as detailed below:

$$scaled\_velocity = (1 - 0.3\phi / \phi_{critical})velocity, \quad \text{where } \phi < \phi_{critical}. \tag{5.5}$$

This velocity scale reduces  $Vp$  and  $Vs$  rapidly as porosity increases, but keeps  $Vp/Vs$  ratio of the model trends since I apply exactly the same scale to both  $Vp$  and  $Vs$ .

In Figure 5.3, the dashed magenta lines represent the stiff-sand models with a fudge factor (defined in Equation 5.3) of 1.0; the dashed cyan lines indicate the soft-sand model with the same fudge factor. Next, I change the fudge factor to 0.2, and obtain the red solid lines, which represent the stiff-sand model; the black lines show the soft-sand model with this fudge factor. For each different setting, I vary the solid-phase composition from 100% quartz to 100% clay with 20% exchange steps in this two-mineral system.

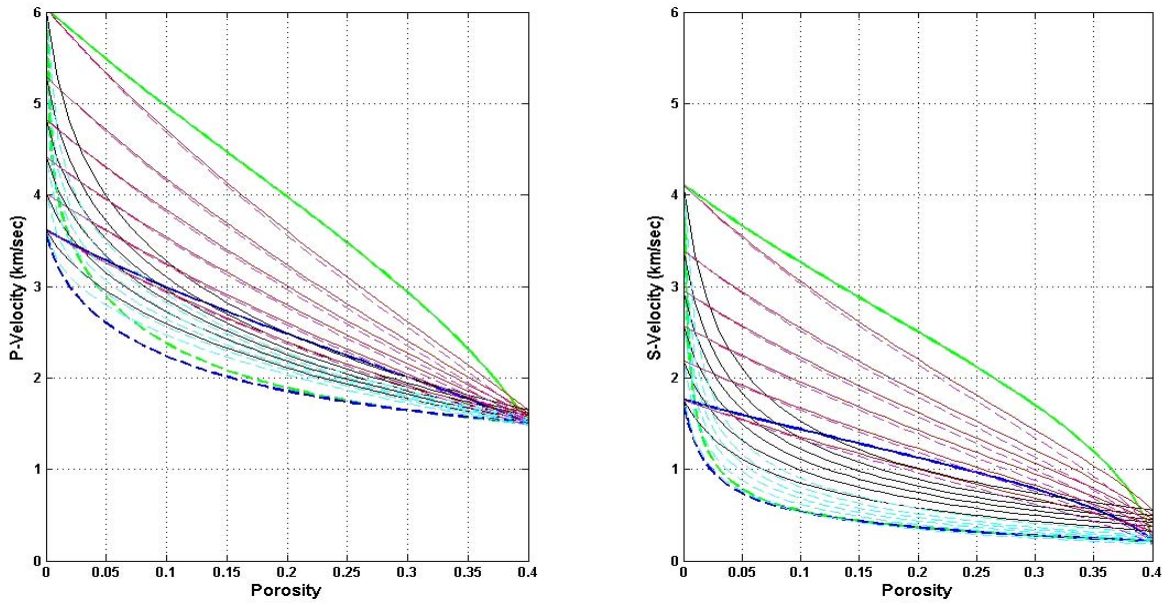


Figure 5.3: Stiff-sand models in the solid red lines and the dashed magenta lines; soft-sand models in the solid black lines and the dashed cyan lines, based on the Hertz-Mindlin contact stiffness. The red solid lines and the black solid lines are calculated with a fudge factor=0.2, whereas the dashed magenta lines and the cyan lines are calculated with a fudge factor=1. Each set has five lines, ranging from 100% quartz at the top to 100% clay at the bottom. I applied a porosity-dependent velocity scale.

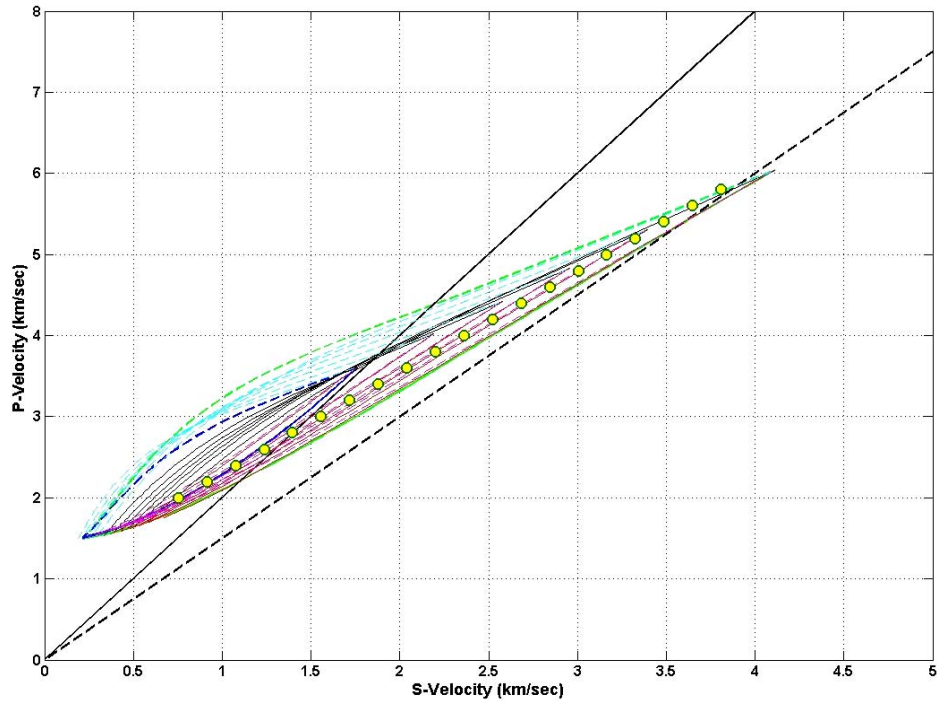


Figure 5.4:  $V_p$ - $V_s$  plot of the stiff-sand and soft-sand models in Figure 5.3. The black lines indicate constant  $V_p/V_s$ : the dashed line for  $V_p/V_s=1.5$  and the solid line for  $V_p/V_s=2$ . The yellow circles represent the regression line for brine-saturated sandstones by Castagna *et al.* (1993).

Consequently, there are five lines for each setting. These lines range from pure quartz at the top to pure clay at the bottom in the figure.

Next, I transform all the lines into the  $V_p$ - $V_s$  plane as shown in Figure 5.4. Comparing this chart to the previous figure, we recognize that if a trend locates close to the upper Hashin-Shtrikman bound in the  $V_p$ -porosity plane, the trend will be situated near the upper Hashin-Shtrikman bound in the  $V_p$ - $V_s$  plane as well. I interpret this result in relation to the pore shape. For any fixed porosity, a higher  $V_p$  close to the upper Hashin-Shtrikman bound means that the pore shape is almost spherical, which is the stiffest pore shape of a mixture. This pore shape gives us the lowest  $V_p/V_s$  ratio for the mixture due to its high  $V_s$  value. In contrast, the lower Hashin-Shtrikman bound is coincident with the Reuss bound, when the shear modulus for one material of a mixture is 0. This fact indicates that very low  $V_p$  near the bounds, a rock texture is described by a scheme of a horizontal stack of two materials. Approaching the Reuss scheme of a mixture of solid and fluid,  $V_s$  reduces rapidly toward 0. As a result,  $V_p/V_s$  increases toward the maximum value at the lower bound of the mixture.

From the discussions above, we recognize that location relative to the Hashin-Shtrikman bounds is a good tool to investigate  $V_p$ - $V_s$  relations of a rock. Since most sandstones fall between the upper Hashin-Shtrikman bound of a quartz-brine mixture and the upper bound of a clay-brine mixture, I evaluate a general trend of sandstone using the upper Hashin-Shtrikman bound.

I gradually vary the constituents of the solid phase from 100% quartz to 100% clay in 10% exchange steps. Next, I employ Hill's average to calculate the elastic moduli of a dry rock, and I brine-saturate the rock using Gassmann's equation. I adopt the same rock

properties as in Table 5.1. Eventually, I calculate the upper Hashin-Shtrikman bounds for the mixtures with the solids of the different volume fractions and brine.

Figure 5.5 displays the result of this practice. The data are color-coded by the calculated  $V_p/V_s$  ratio. As we expect given the previous discussions, the data clearly show that the higher our  $V_p$  is, due to the higher quartz content, the lower  $V_p/V_s$  ratio we obtain at a fixed porosity. Note that when I take a fixed  $V_p$ , the  $V_p/V_s$  ratio reduces as it approaches the upper Hashin-Shtrikman bound at the highest porosity allowed for the mixture. In this sense,  $V_s$  is not a function only of  $V_p$ , but is influenced by porosity as well. Having  $V_p$ ,  $V_s$ , porosity and clay volume for all the points, I plot the same data in the  $V_p$ - $V_s$  plane, color-coded by porosity as shown in Figure 5.6. I regress all the points to derive the linear equation of  $V_s$  as a function of  $V_p$  and I get the following relation:

$$V_s = 0.7937V_p - 0.7890. \quad (5.6)$$

This result remarkably resembles Han's regression (1986), which is based on ultrasonic laboratory measurements:

$$V_s = 0.7936V_p - 0.7868. \quad (5.7)$$

Both equations cross validate each other. Furthermore, these regressions are virtually equivalent to the regression by Castagna *et al.* (1993) below:

$$V_s = 0.8042V_p - 0.8559. \quad (5.8)$$

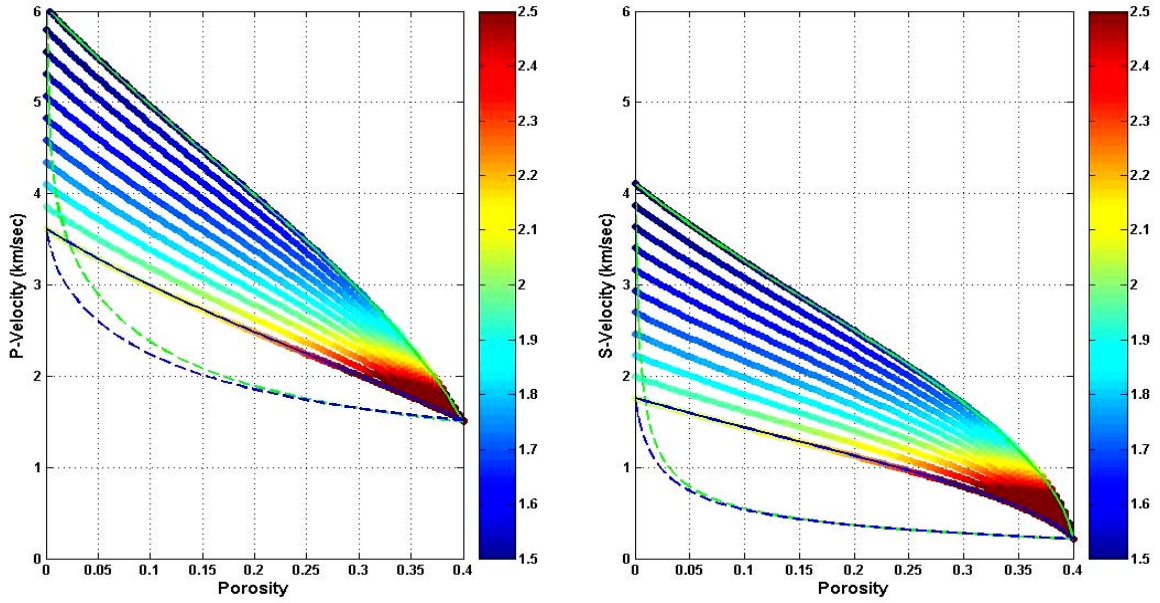


Figure 5.5: The calculation results of the upper Hashin-Shtrikman bound for the mixtures with different quartz contents. I use Hill's average to calculate the dry-rock elastic moduli, ranging from 100% quartz to 100% clay in 10% intervals. All data are brine-saturated using Gassmann's equation.

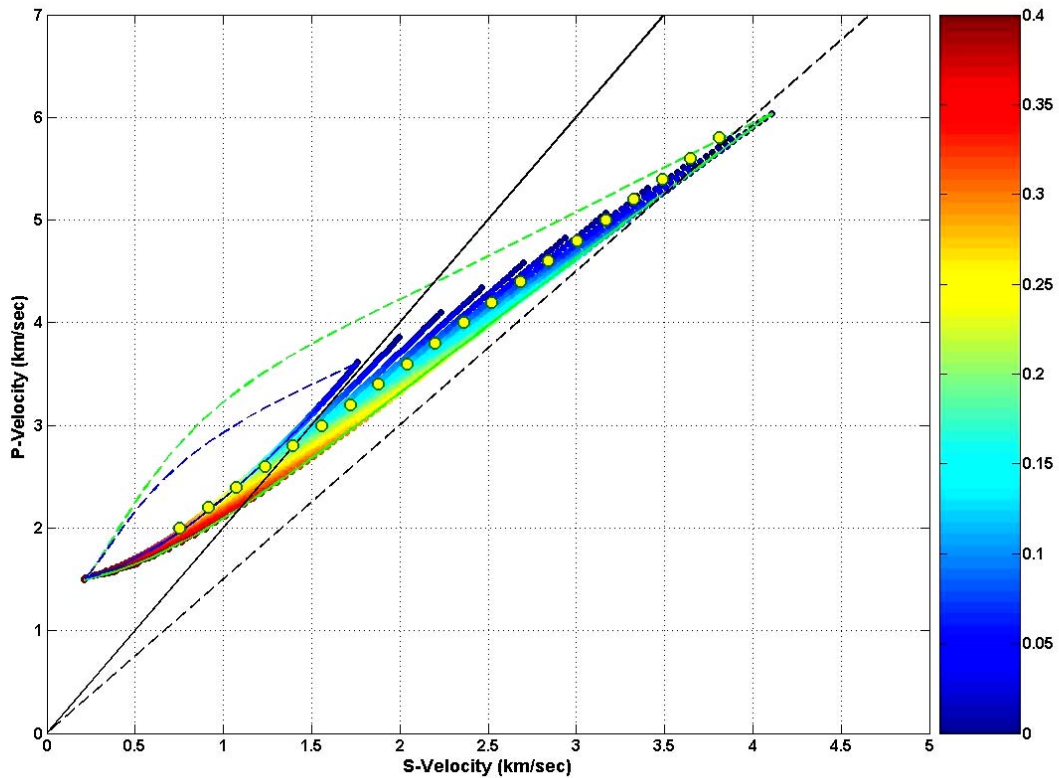


Figure 5.6:  $V_p$ - $V_s$  plot of the data in Figure 5.5, color-coded by porosity. Note that I adopt critical porosity at 0.4. We recognize iso-porosity trends.

### 5.4.2 Effective elastic moduli of a rock with tubular pores

Mavko (1980) discussed the effective elastic moduli of a crystalline rock with randomly oriented tubular melts along the mineral junctions. When a volume fraction of the melts is large, this situation is similar to a rock comprised of grains with connecting tubular pores. I adopt the two models with the extreme shapes of the cross section of each tube. The shapes are calculated in the  $x$ - $y$  plane by the following equations using  $\varepsilon=0$  and  $\varepsilon=\infty$ :

$$\begin{aligned} x &= R\left(\cos \theta + \frac{1}{2 + \varepsilon} \cos 2\theta\right), \\ y &= R\left(-\sin \theta + \frac{1}{2 + \varepsilon} \sin 2\theta\right), \end{aligned} \quad (5.9)$$

where,  $R$  is a constant and the  $\theta$  varies from 0 to  $2\pi$ . The shape for  $\varepsilon=0$  is a three-sided hypotrochoid, whereas the shape for  $\varepsilon=\infty$  is a perfect circle. Then the effective moduli of a dry rock for  $\varepsilon=0$  are expressed as below:

$$\begin{aligned} \frac{1}{K_{dry}} &= \frac{1}{K_{solid}} + \frac{\phi}{K_{solid}} \left[ \frac{13 - 4\nu_{solid} - 8\nu_{solid}^2}{3(1 - 2\nu_{solid})} \right], \\ \frac{1}{\mu_{dry}} &= \frac{1}{\mu_{solid}} + \frac{2\phi}{\mu_{solid}} \left[ \frac{40 - 26\nu_{solid}}{15} \right], \end{aligned} \quad (5.10)$$

where

$K$  is the bulk modulus,

$\mu$  is the shear modulus,

$\phi$  is the volume fraction of porosity (=volume fraction of melt),

$\nu$  is the Poisson's ratio.

However, the formulation above is not self-consistent, consequently the resultant moduli are high all way down to 100% porosity. Assuming that the moduli of a dry rock

are close to the moduli of the solid, we can derive a pseudo-self-consistent version of the equations for the lower porosity range (personal communication with Dr. Mavko.) For the derivation, first we replace the solid modulus in the second term on the right side with the modulus of the dry rock and we get

$$\begin{aligned}\frac{1}{K_{dry}} &= \frac{1}{K_{solid}} + \frac{\phi}{K_{dry}} \left[ \frac{13 - 4\nu_{solid} - 8\nu_{solid}^2}{3(1 - 2\nu_{solid})} \right], \\ \frac{1}{\mu_{dry}} &= \frac{1}{\mu_{solid}} + \frac{2\phi}{\mu_{dry}} \left[ \frac{40 - 26\nu_{solid}}{15} \right].\end{aligned}\tag{5.11}$$

Next, we move the term to the left side and rearrange the equations to obtain the expressions below:

$$\begin{aligned}K_{dry} &= K_{solid} \left( 1 - \phi \left[ \frac{13 - 4\nu_{solid} - 8\nu_{solid}^2}{3(1 - 2\nu_{solid})} \right] \right), \\ \mu_{dry} &= \mu_{solid} \left( 1 - \phi \left[ \frac{40 - 26\nu_{solid}}{15} \right] \right).\end{aligned}\tag{5.12}$$

Using the calculated moduli of a dry rock made of 100% quartz, I compute the velocity of the rock in a brine-saturated condition using Gasmann's equation. Figure 5.7 shows the results in the  $V_p$ -porosity and  $V_s$ -porosity planes. The red circles represent a rock with tubular pores which have circular cross section; the purple triangles represent a rock with tubular pores for which the cross section of the tubes is a three-sided hypotrochoid. The trend curves in the planes are similar to the lower Hashin-Shtrikman bounds.

Figure 5.8 shows the same data in the  $V_p$ - $V_s$  plane. The trend of the red circles is very close to Castagna's regression for sandstone in the yellow circles. This result suggests that the general trend of sandstone is represented well by the tubular pore model with circular cross sections.

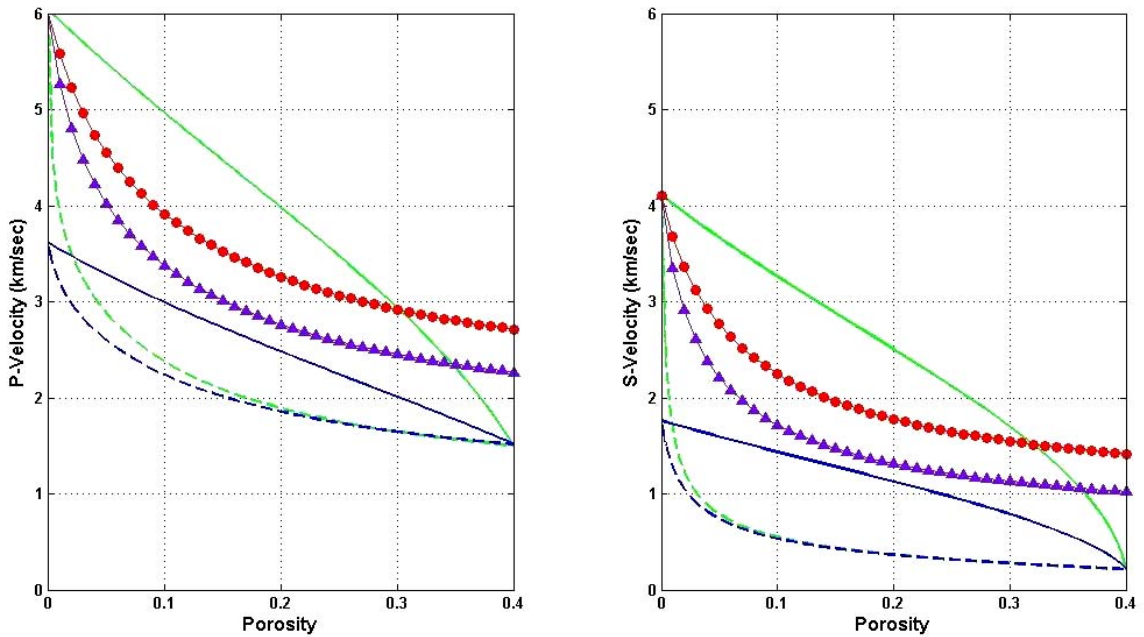


Figure 5.7: The trends of a rock with tubular pores by a modified Mavko's equation in the velocity-porosity plane. The red circles represents that the cross section of tubes with perfectly circular cross sections, and the purple triangles represents tubes with three-sided hypotrochoid cross sections.

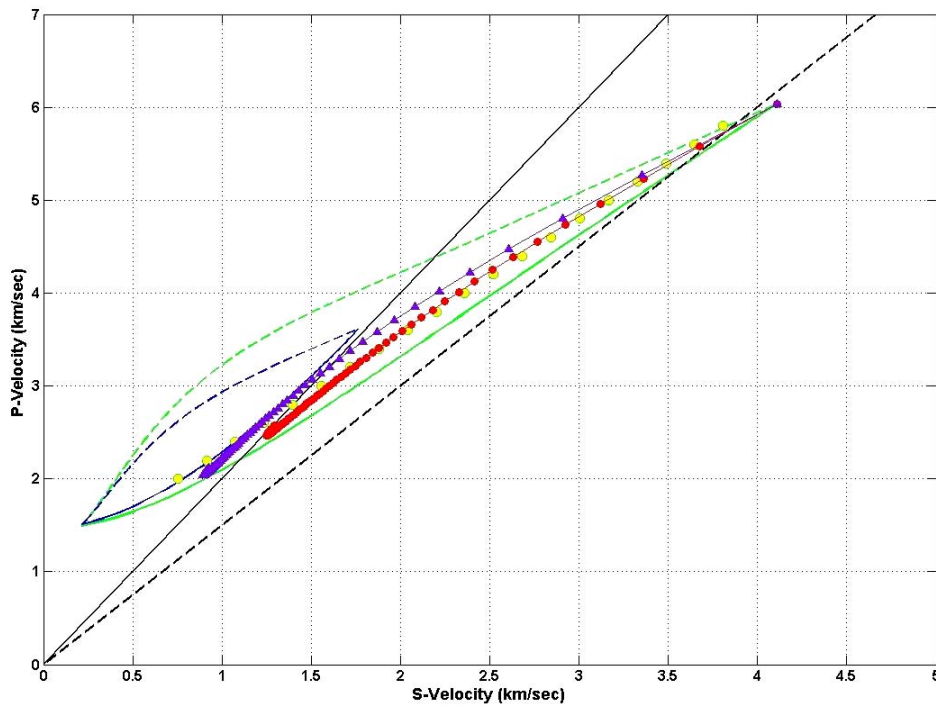


Figure 5.8: The trends of a rock with tubular pores by a modified Mavko's equation in the  $V_p$ - $V_s$  plane. The red circles represent tubes with perfectly circular cross sections, and the purple triangles represent tubes with three-sided hypotrochoid cross sections. Note that the trend of the red circles is very close to Castagna's regression for sandstone in the yellow circles.

### 5.4.3 Self-consistent inclusion model of spheroid pores

Kuster and Toksöz (1974) derived expressions for the effective moduli of a mixture consisting of a host rock and inclusion materials as follows:

$$\begin{aligned} (K_{KT}^* - K_m) \frac{(K_m - 4\mu_m/3)}{(K_{KT}^* + 4\mu_m/3)} &= \sum_{i=1}^N x_i (K_i - K_m) P^{mi}, \\ (\mu_{KT}^* - \mu_m) \frac{(\mu_m + \zeta_m)}{(\mu_{KT}^* + \zeta_m)} &= \sum_{i=1}^N x_i (\mu_i - \mu_m) Q^{mi}, \\ \zeta_m &= \frac{\mu_m (9K_m + 8\mu_m)}{6(K_m + 2\mu_m)}, \end{aligned} \quad (5.13)$$

where

$K_{KT}^*$  is the effective bulk modulus of the mixture,

$K_m$  is the bulk modulus of the host rock,

$\mu_{KT}^*$  is the effective shear modulus of the mixture,

$\mu_m$  is the shear modulus of the host rock,

$x_i$  is the volume fraction of the  $i$ th inclusion,

$K_i$  is the bulk modulus of the  $i$ th inclusion,

$\mu_i$  is the shear modulus of the  $i$ th inclusion.

The coefficient  $P^{mi}$  and  $Q^{mi}$  are the scalars calculated by the aspect ratio of pores ( $\alpha$ =length of short semi-axis/length of long semi-axis; less than 1 for oblate spheroids) and the properties of the constituents. I describe the calculation sequence for a two phase mixture below:

$$\begin{aligned} P^{mi} &= \frac{3F_1}{F_2}, \\ Q^{mi} &= \frac{2}{F_3} + \frac{1}{F_4} + \frac{F_4 F_5 + F_6 F_7 - F_8 F_9}{F_2 F_4}, \end{aligned} \quad (5.14)$$

where,

$$\begin{aligned}
F_1 &= 1 + A \left[ \frac{3}{2}(m+n) - R \left( \frac{3}{2}m + \frac{5}{2}n - \frac{4}{3} \right) \right], \\
F_2 &= 1 + A \left[ 1 + \frac{3}{2}(m+n) - \frac{R}{2}(3m+5n) \right] + B(3-4R) \\
&\quad + \frac{A}{2}(A+3B)(3-4R) \left[ m+n - R(m-n+2n^2) \right], \\
F_3 &= 1 + A \left[ 1 - \left( m + \frac{3n}{2} \right) + R(m+n) \right], \\
F_4 &= 1 + \frac{A}{4} \left[ m + 3n - R(m-n) \right], \\
F_5 &= A \left[ -m + R \left( m + n - \frac{4}{3} \right) \right] + Bn(3-4R), \\
F_6 &= 1 + A \left[ 1 + m - R(m+n) \right] + B(1-n)(3-4R), \\
F_7 &= 2 + \frac{A}{4} \left[ 3m + 9n - R(3m+5n) \right] + Bn(3-4R), \\
F_8 &= A \left[ 1 - 2R + \frac{m}{2}(R-1) + \frac{n}{2}(5R-3) \right] + B(1-n)(3-4R), \\
F_9 &= A \left[ m(R-1) - Rn \right] + Bn(3-4R),
\end{aligned}$$

and

$$\begin{aligned}
A &= \frac{\mu_i}{\mu_m} - 1, \\
B &= \frac{1}{3} \left( \frac{K_i}{K_m} - \frac{\mu_i}{\mu_m} \right), \\
R &= \frac{3\mu_m}{3K_m + 4\mu_m}, \\
m &= \frac{\alpha^2}{1-\alpha^2} (3n-2), \\
n &= \frac{\alpha}{(1-\alpha^2)^{3/2}} \left[ \cos^{-1} \alpha - \alpha(1-\alpha^{1/2}) \right].
\end{aligned}$$

Berryman (1995) introduced a way to derive a self-consistent approximation of the elastic moduli of the inclusion model by the iterative calculation that follows:

$$\begin{aligned}\sum_{i=1}^N x_i (K_i - K_{SC}^*) P^{*mi} &= 0, \\ \sum_{i=1}^N x_i (\mu_i - \mu_{SC}^*) Q^{*mi} &= 0,\end{aligned}\tag{5.15}$$

where

$K_{SC}^*$  is the self-consistent effective bulk modulus of the mixture,

$\mu_{SC}^*$  is the self-consistent effective shear modulus of the mixture.

The scalars  $P^{*mi}$  and  $Q^{*mi}$  are calculated by Equation 5.14, using the bulk and shear moduli of a tentative result in the iterative computation, and updated in the each iteration step. I set the program to terminate computation when the difference of two consecutive calculation results is less than  $10^{-6}$  times the solid modulus.

I use the properties of quartz and brine in Table 5.1 to calculate the velocity trends for a rock whose pores have aspect ratios of 0.001, 0.01, 0.03, 0.06, 0.1, 0.2, and 1.0. Figure 5.9 shows the calculation results in the red lines. Likewise, Figure 5.10 shows the same data in the  $Vp$ - $Vs$  plane. Although the trends in the velocity-porosity plane are clearly separated, the trends corresponding to the  $\alpha$  higher than 0.06 are located very close to each other in the  $Vp$ - $Vs$  plane. Furthermore, none of the trends in the red lines resembles Castagna's regression, shown in the yellow circles. This result indicates that the self-consistent model of the spheroid inclusions with fixed aspect ratio is not appropriate to predict the  $Vp$ - $Vs$  trend of sandstone. According to the result of Xu and White (1995), the original inclusion model by Kuster and Toksöz (1974) works well to describe the trend of sandstone and shale. To estimate  $Vp$ - $Vs$  relation of sandstone, the original inclusion theory is much more effective than a self-consistent version of the model, when we assume a fixed aspect ratio.

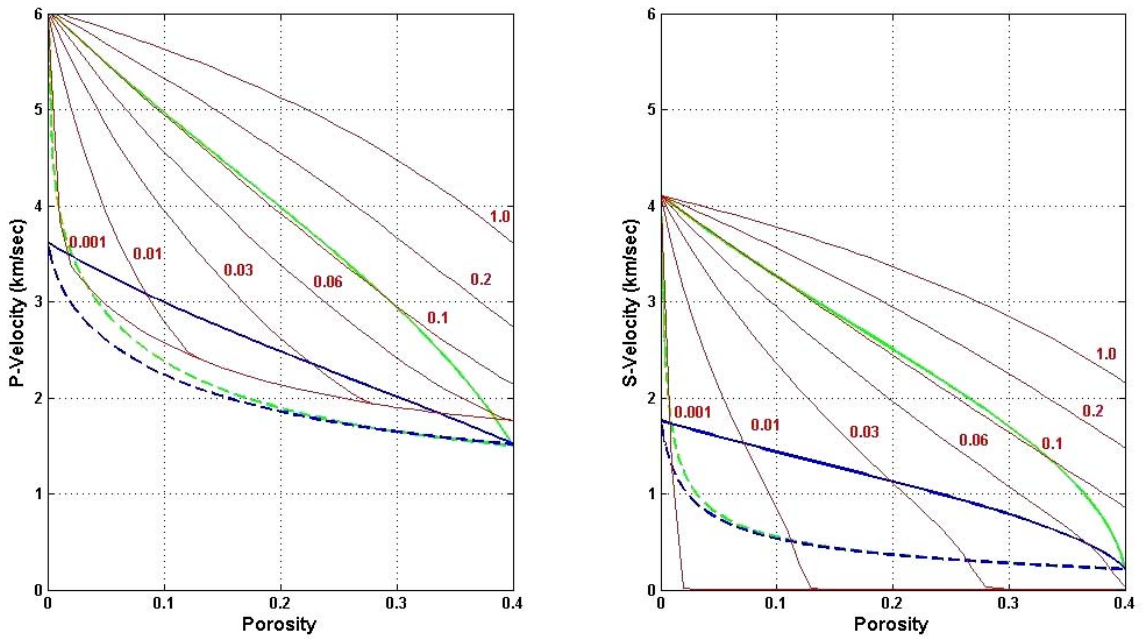


Figure 5.9: The calculation results of a self-consistent inclusion model in the red lines. The numbers indicate the aspect ratios of the pores used in the calculation.

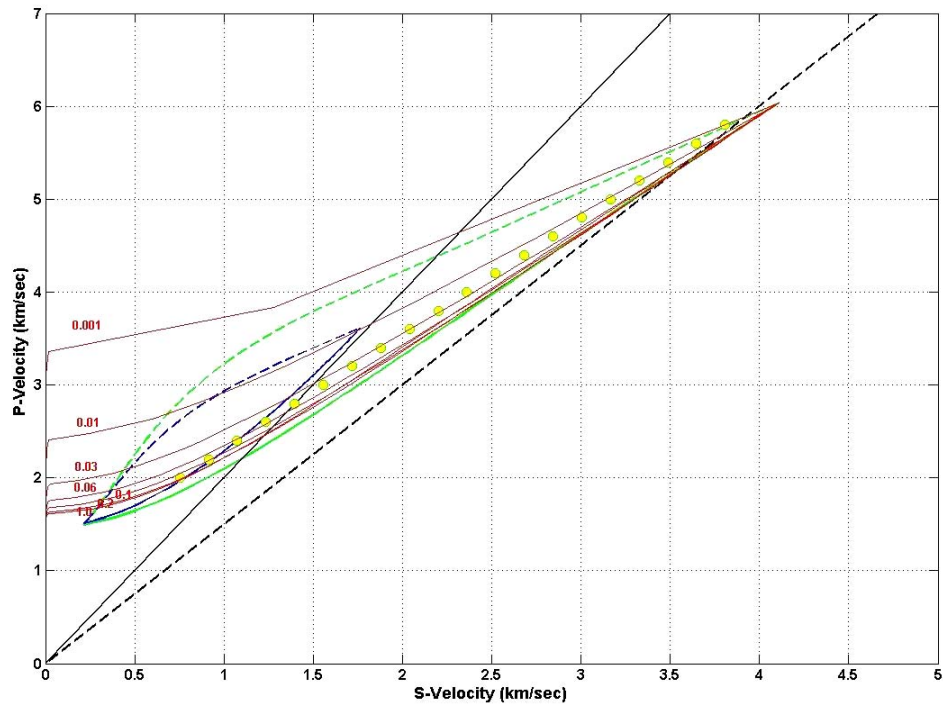


Figure 5.10: The same data as in Figure 5.9 in the  $V_p$ - $V_s$  plane. Note that relative position to the Hashin-Shtrikman bounds correlates to that in Figure 5.9. However, the trends of  $\alpha$  higher than 0.06 are not separable in the  $V_p$ - $V_s$  plane.

#### 5.4.4 Comparison of the theoretical trends with laboratory measurements

To observe the validity of the effective moduli derived from theoretical models, I plot the results of the tubular-pore model and the inclusion model with the laboratory measurement by Han (1986). Figure 5.11 shows the model trends and the measurement with a confining pressure of 5MPa in the velocity-porosity plane. The laboratory data are color-coded by the shale volume. I expand the Hashin-Shtrikman bounds in green and blue to a critical porosity of 0.6 instead of 0.4 in this figure. The black solid line corresponds to the red circles in Figure 5.7 and the black dashed line represents the purple triangles in Figure 5.7. Comparing the two charts in Figure 5.11, we notice that the data locations relative to the model trends are very consistent in both charts.

As shown in Figure 5.12, the data locations relative to the model trends are more scattered in the  $V_p$ - $V_s$  plane. Yet, we recognize the samples of higher shale volume in reddish colors are plotted between the dashed and solid black lines in both Figures 5.11 and 5.14. A similar constraint cannot be obtained from the trend of the inclusion model.

It seems that the trends with curves similar to the lower Hashin-Shtrikman bound, which is equivalent to the Reuss bound, provide us a better control of  $V_p$ - $V_s$  relations of sandstone.

Figures 5.13 and 5.14 display the same panels for Han's data with a confining pressure of 40MPa. I expected a better correlation of the relative locations for the data to the model trends. However, the result is almost the same as the dataset at 5MPa. Moreover, in case of 40MPa, the reddish points tend to show higher velocity than the solid black line in Figure 5.13, although the data stay between the two black lines in Figure 5.14. This suggests that we need to modify the model for a higher pressure.

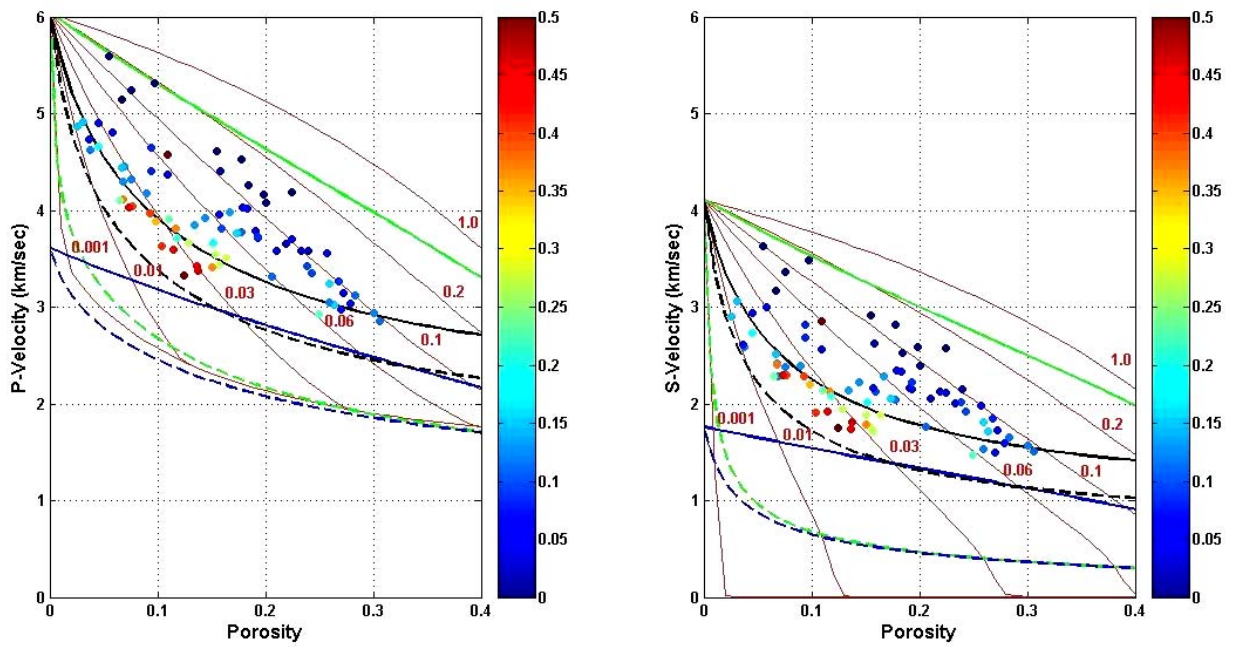


Figure 5.11: Comparison of the trends from effective-medium models with the laboratory measurement by Han (1986) with a confining pressure of 5MPa. The measurement data are color-coded by the shale volume.

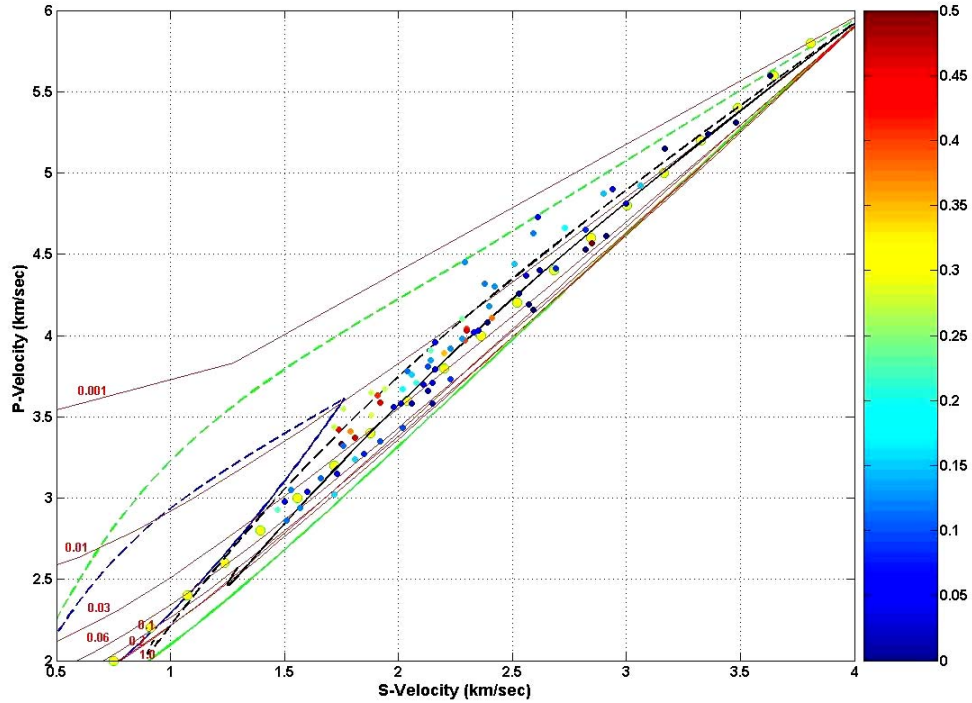


Figure 5.12: The same data as in Figure 5.11 in the  $V_p$ - $V_s$  plane. Note that the data in reddish colors are located in between the solid and dashed black lines, as in Figure 5.11.

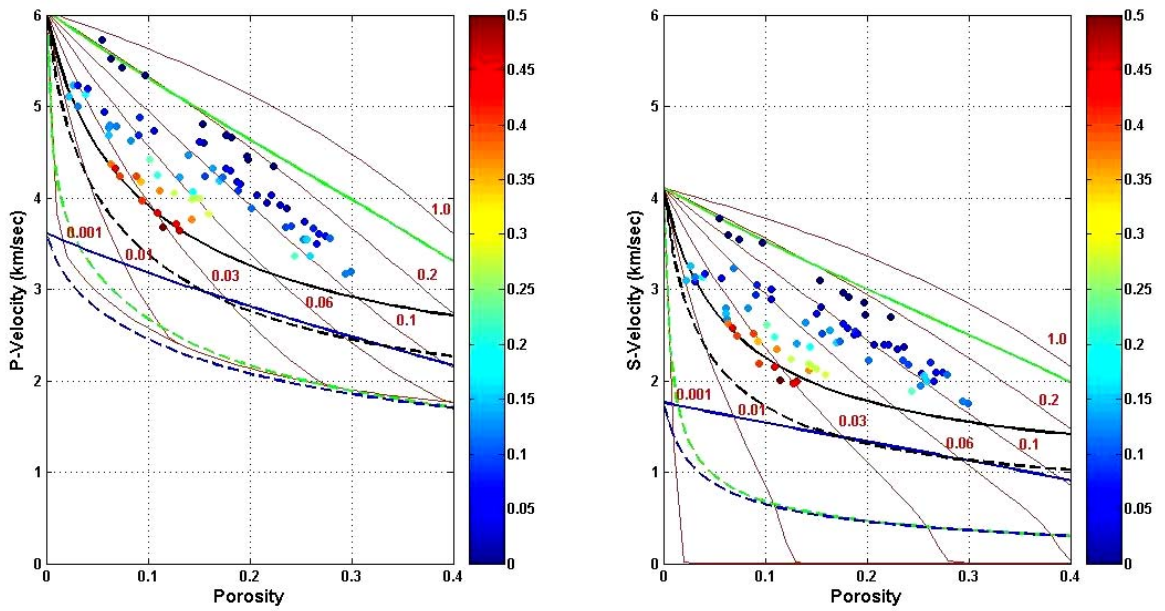


Figure 5.13: Comparison of the trends from effective medium models with the laboratory measurement by Han (1986) at a confining pressure of 40MPa. The measurement data are color-coded by the shale volume.

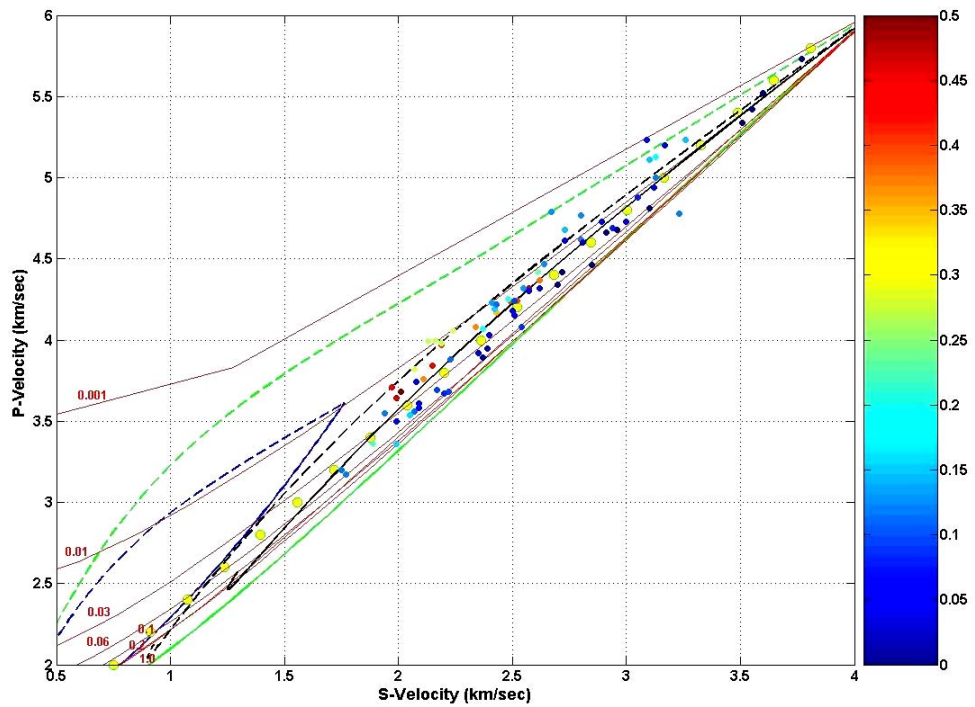


Figure 5.14: The same data as in Figure 5.11 in the  $V_p$ - $V_s$  plane. Note that the data in reddish colors are located between the solid and dashed black lines, although the data exhibit velocities around the solid black line in Figure 5.13.

#### 5.4.5 Modified Reuss bound

Since the trend similar to the lower Hashin-Shtrikman bound seems to represent well the  $V_p$ - $V_s$  relation of sandstone. I generate a series of modified Reuss bounds to compare with the laboratory data. In this practice, I adopt the upper Hashin-Shtrikman bound calculated with the properties in Table 5.1. Then, I stretch it in the porosity axis to the maximum porosity at 1. Therefore, the  $V_p$  and  $V_s$  at 100% porosity point are 1.5 km/sec and 0.2 km/sec, respectively. Next, I extract  $V_p$  and  $V_s$  at the porosity points 0.95, 0.90, 0.85, 0.80, 0.75, 0.70, 0.64, and 0.60 on the upper Hashin-Shtrikman bound. Employing the recorded velocities, I calculate the modified Reuss bounds between the quartz-mineral point and each extracted porosity point.

Figure 5.15 shows the modified Reuss bound in red with Han's data: the solid circles represent the data at 5MPa confining pressure; the open circles represent the data at 40MPa confining pressure; both sets are color-coded by the shale volume.

First, most samples are located within the range of the red lines, the top red line corresponding to the modified Reuss bound at 0.6 porosity, and the bottom red line corresponding to the porosity point at 0.95. Second, in both charts, the sample locations relative to the modified Reuss bounds are very consistent.

Furthermore, the same bounds in the  $V_p$ - $V_s$  plane exhibit similarly good locations relative to the samples, considering small measurement errors, as shown in Figure 5.16. I demonstrate the consistency of the locations among the three crossplot planes, when we determine the appropriate properties of the end points for the bounds.

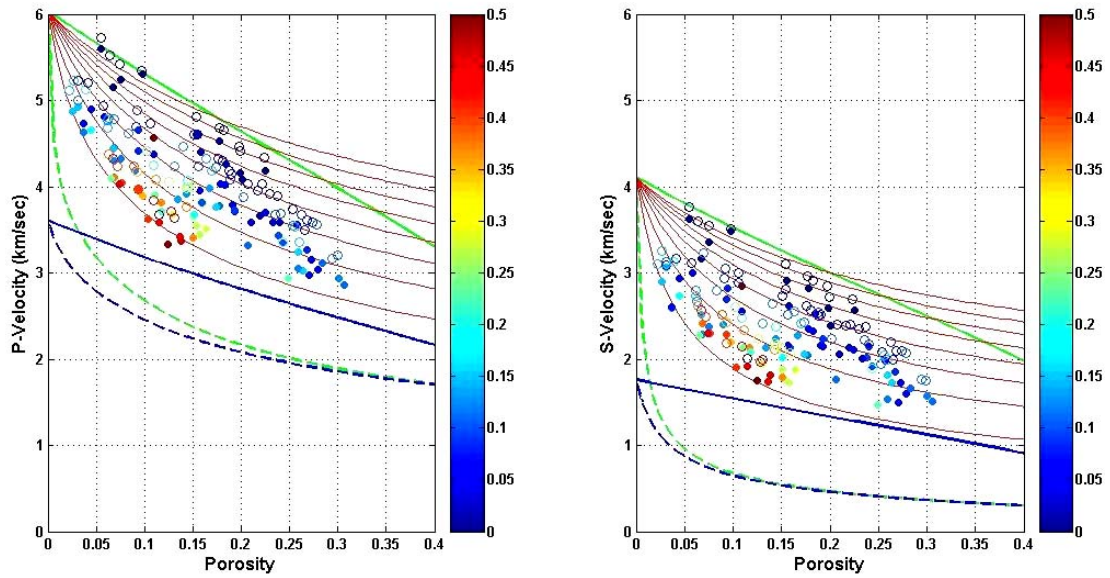


Figure 5.15: Comparison of the trends of modified Reuss bounds with the laboratory measurement by Han (1986): the solid circles represent the data at 5MPa confining pressure; the open circles are for 40MPa. The measurement data are color-coded by the shale volume.

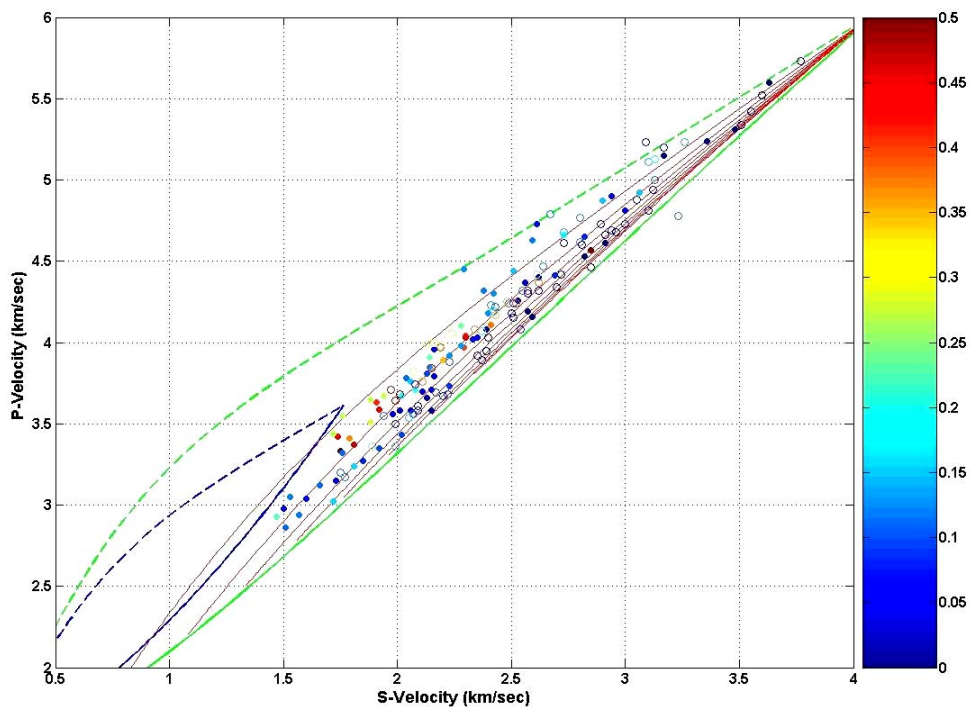


Figure 5.16: The same data as in Figure 5.15 in the  $V_p$ - $V_s$  plane. Note that the locations of measurement data relative to the modified Reuss bounds are consistent with the relative locations in Figure 5.15 for most of the data. The measurement data are color-coded by the shale volume.

Note that since the location in the  $V_p$ - $V_s$  plane is independent of porosity, the selection of the end points of the bounds in the velocity-porosity plane is critically important for comparing with measurement data. We obtain exactly the same locations in the  $V_p$ - $V_s$  plane, as long as the shapes of the bounds in the velocity-porosity planes stay constant, even if the porosity range violates the reasonable limit of the mixture. Furthermore, we have to be careful about the effect of saturation fluid. Any fluid more compressible than brine pulls down the model trends toward the lower Hashin-Shtrikman bound in the velocity-porosity plane. On the other hand, in the same case, the model trends will move toward the upper Hashin-Shtrikman bound in the  $V_p$ - $V_s$  plane because  $V_p$  is more reduced than  $V_s$ .

Figure 5.17 compares the modified Reuss bounds with Castagna's regressions for sandstone in the yellow circles and the mudrock line in the cyan circles. The purple asterisks show Han's regression for sandstone from Equation 5.7.

As I discussed above, most sandstone is in the range of the red lines. Therefore, both Castagna's regression and Han's regression are appropriate linear averages for sandstone as shown in Figure 5.17. Moreover, the location of the mudrock line agrees with the location of the shaly sandstone data in reddish colors in Figure 5.16. These consistencies of my findings about the data locations in the three crossplot planes with the known  $V_p$ - $V_s$  relations prove the validity of my approach.

We recognize the stiffness of the pore, or the shape of pore, is a key factor controlling the location in the velocity-porosity plane, so it controls the  $V_p$ - $V_s$  relation. The stiffest pore shape, a sphere, gives us the upper Hashin-Shtrikman bound, which is equivalent to the lowest  $V_p/V_s$  trend in the  $V_p$ - $V_s$  plane. For any sandstone, an inter-granular pore

shape mimicking randomly oriented tubes exhibits a velocity trend between the upper and lower Hashin-Shtrikman bounds. Moreover, the distribution is limited inside the range between the red lines in Figures 5.15 and 5.16. Therefore, a linear regression can represent well an averaged  $V_p$ - $V_s$  relation for sandstone and shaly sand. When samples consist of the higher shale volume, the regression line will move towards the top red line in Figure 5.17, according to the trend location in the velocity-porosity plane. By contrast, when samples have been highly cemented, we need to move the regression line down closer to the bottom red line in Figure 5.17.

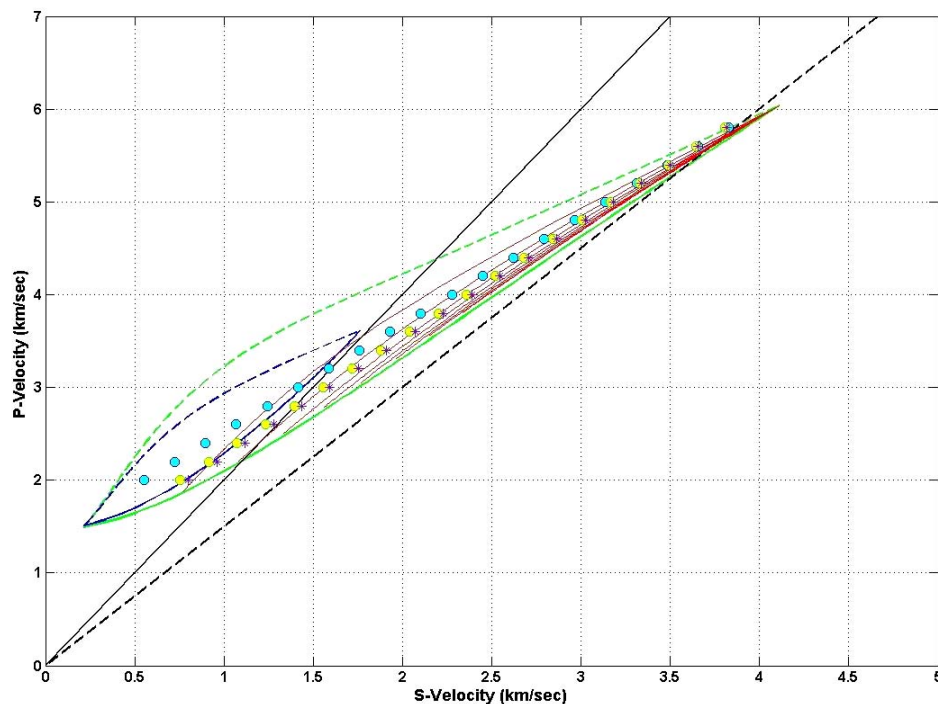


Figure 5.17: Comparison of the modified Reuss bounds in red with known  $V_p$ - $V_s$  relations. The yellow circles represent Castagna's regression for sandstone; the cyan circles represent Castagna's mudrock trend; the purple asterisks correspond to Han's regression for sandstone.

## 5.5 $V_p$ - $V_s$ relation of carbonates

I expand the stiffness assumption at the critical porosity point in Table 5.1 to carbonates as well. Figure 5.18 shows the upper and lower Hashin-Shtrikman bounds for a limestone-brine mixture in red and a dolomite-brine mixture in purple. Table 5.2 summarizes the properties of calcite (mineral to compose limestone) and dolomite. In general, carbonates do not display obvious grains, except grainstone facies of limestone. Instead, the rock frame is rigidly connected as a matrix-supported scheme of the internal texture. Consequently, the pore shape of carbonates is closer to a sphere or a fat ellipsoid with a lower aspect ratio. Considering this stiff nature of pores in carbonates, I anticipate the actual samples to fall in the area very close to the upper Hashin-Shtrikman bounds of the carbonate-brine mixture.

Table 5.2: Summary of the parameters used to calculate the Hashin-Shtrikman bounds of carbonates.

| Mineral  | Bulk modulus (GPa) | Shear modulus (GPa) | Density ( $\text{g/cm}^3$ ) |
|----------|--------------------|---------------------|-----------------------------|
| calcite  | 70.76              | 30.34               | 2.71                        |
| dolomite | 80.23              | 48.77               | 2.87                        |

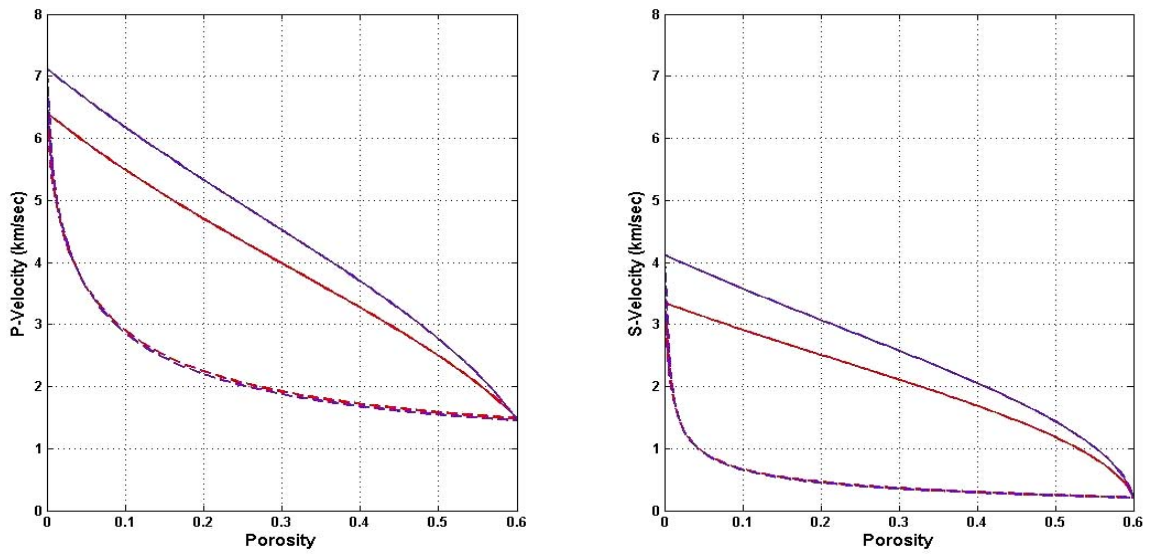


Figure 5.18: The upper and lower Hashin-Shtrikman bounds of carbonates in the  $V_p$ -porosity plane on the left and the same bounds in the  $V_s$ -porosity plane on the right. The red lines represent a limestone-brine mixture and the purple lines a dolomite-brine mixture. The solid lines indicate the upper Hashin-Shtrikman bounds and the dashed lines correspond to the lower Hashin-Shtrikman bounds.

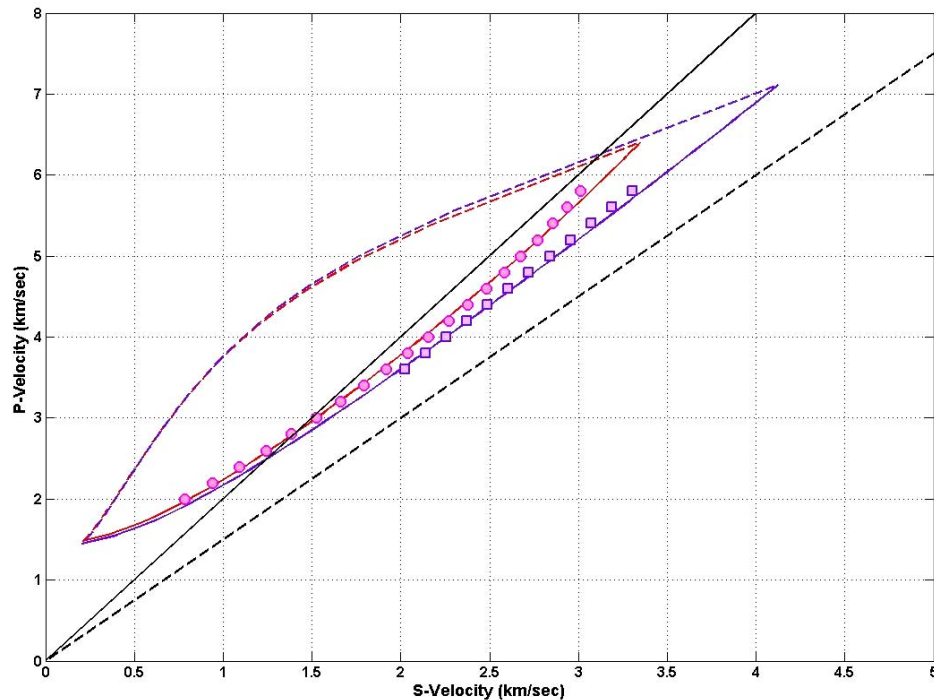


Figure 5.19: The upper and lower Hashin-Shtrikman bounds of carbonate-brine mixtures in the  $V_p$ - $V_s$  plane. The red lines represent a limestone-brine mixture and the purple lines a dolomite-brine mixture. The red circles and purple squares represent Castagna's regressions for these lithologies. Note that Castagna's regressions agree with the upper Hashin-Shtrikman bound for the lithology.

Figure 5.19 shows the  $V_p$ - $V_s$  plots of the upper and lower Hashin-Shtrikman bounds of the limestone and dolomite in Figure 5.18. The red circles represent Castagna's polynomial regression for limestone given in Equation 5.16, and the purple squares represent Castagna's linear regression for dolomite in the  $V_p$  range higher than 3.5 km/sec.

$$V_s = -0.05508V_p^2 + 1.01677V_p - 1.03049. \quad (5.16)$$

Applying polynomial regression to the upper Hashin-Shtrikman bound of a limestone-brine mixture, I obtain the expression below:

$$V_s = -0.0412V_p^2 + 0.9202V_p - 0.8888. \quad (5.17)$$

The result is very close to Castagna's regression. Both equations cross-validate each other.

Castagna *et al.* (1993) found that the empirical regression of a dolomite-brine mixture is a linear line for the higher velocities, but the data in the lower velocity range were not available for the regression. Therefore, the  $V_p$ - $V_s$  relation of brine-saturated dolomite in lower velocity range remains undefined. Based on the calculated data of the upper Hashin-Shtrikman bound of the mixture, I derive a polynomial regression similar to that of limestone, shown below:

$$V_s = -0.023V_p^2 + 0.8452V_p - 0.7609. \quad (5.18)$$

The result coincides with the solid purple line in Figure 5.19, and the line agrees very well with Castagna's regression in the higher velocity range. In the higher velocity range,

the  $V_p$ - $V_s$  relation of dolomite-brine mixture seems to fit a linear trend, because the  $V_p/V_s$  ratio of dolomite is smaller than that of calcite. However, the trend will curve in the low velocity range, similar to the trend for limestone. The degree of the curvature for the upper Hashin-Shtrikman bound in the  $V_p$ - $V_s$  plane is controlled by the  $V_p/V_s$  ratio of the mineral point; where the mineral point exhibits a  $V_p/V_s$  ratio closer to 1, the upper bound becomes straight.

Tsuneyama *et al.* (2003) demonstrated a new trend for limestone, which represents grainstone facies defined as grain supported, and limy mud lacking limestone, having almost a sphere-pack internal texture. Figure 5.20 presents the grainstone trend as a dotted red line with the well log data scattered over the chart in the blue dots. In the microscope photo at the bottom of Figure 5.20, we observe that the grainstone has a texture similar to sandstone, where the dominant pore shape is an inter-granular type. In contrast, general limestone in the top photo of Figure 5.20 exhibits a pore shape like an isolated hole.

Now, it is clear that the red dotted trend in Figure 5.20 corresponds to the trend of the red circles in Figure 5.8, which represents a solid-fluid mixture in a form of sphere-pack. This trend of a sphere-pack form seems almost straight in the  $V_p$ - $V_s$  plane for any minerals, due to the character of the deviation from the upper Hashin-Shtrikman bound for the mixture.

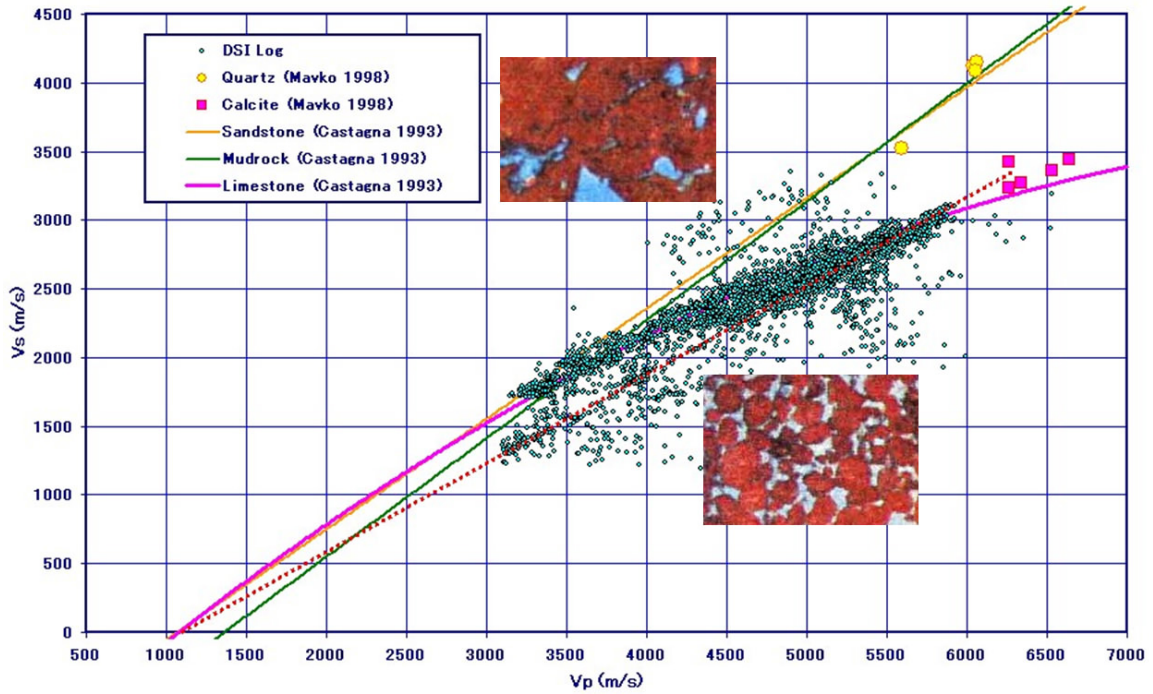


Figure 5.20: A trend of the  $V_p$ - $V_s$  relation for grainstone facies of limestone (dotted red line). The photo on the lower right shows the grainstone; the photo on the left above shows typical limestone. Note that the axes are the reverse of the convention in previous figures.

## 5.6 Conclusions

I discussed a method to investigate  $V_p$ - $V_s$  relations using the Hashin-Shtrikman bounds and several effective-medium theories of solid-fluid mixtures. The comparison of the location of the model trends in the velocity-porosity plane with that in the  $V_p$ - $V_s$  plane is a key idea to interpret the location as an indicator of the rock texture.

The linear regressions for sandstone by Castagna *et al.* (1993) and Han (1986) were compared with the results of the theoretical approach. The results cross-validated each other, since all equations are virtually identical in the  $V_p$ - $V_s$  plane.

I investigated the trend curves of several effective-medium theories in the crossplot planes. The general trend of sandstone is represented well by the modified Mavko's equation (Equation 5.12) for the tubular-pore model. The self-consistent inclusion model

by Berryman (1995) is not appropriate to predict the  $V_p$ - $V_s$  trend of sandstone when we fix the aspect ratio of pores. The original inclusion model by Kuster and Toksöz (1974) is better for investigating the  $V_p$ - $V_s$  relation in case of a fixed aspect ratio. A modified Reuss bound seemed best for finding an appropriate trend of the relations among  $V_p$ ,  $V_s$  and porosity.

A key factor controlling the location in the velocity-porosity plane is the stiffness of pore, or the shape of pore. Therefore, it controls the  $V_p$ - $V_s$  relation as well. The stiffest pore shape, a sphere, gives us the upper Hashin-Shtrikman bound, which is equivalent to the lowest  $V_p/V_s$  trend in the  $V_p$ - $V_s$  plane. Likewise, the softest pore shape, a flat film, gives us the lower Hashin-Shtrikman bound or the Reuss bound, which is equivalent to the highest  $V_p/V_s$  trend. For sandstone, an inter-granular pore shape mimicked by randomly oriented tubes exhibits the general  $V_p$ - $V_s$  trend very well.

In contrast, carbonates have pores more like isolated spheres in well bounded matrix. Therefore, the trend in the velocity-porosity and  $V_p$ - $V_s$  planes are identical to the upper Hashin-Shtrikman bound. The bound has curved nature in the  $V_p$ - $V_s$  plane. This is why the general  $V_p$ - $V_s$  relation of limestone is approximated best by a polynomial expression. The trend for dolomite was found to exhibit a character similar to the trend of limestone. I introduced a polynomial equation for a dolomite-brine mixture to extend Castagna's regression into the range of lower velocity, which the empirical regression did not cover due to insufficient data in that range. In relation to the dominant pore shape, I explained the linear trend for the grainstone facies of limestone, demonstrated in Tsuneyama *et al.* (2003).

The approach discussed in this chapter is applicable for a mixture of two arbitrarily selected materials, where fluid is not necessarily brine. Given appropriate parameters for a particular reservoir rock, we can investigate the  $V_p$ - $V_s$  relation to obtain the optimal method to estimate  $V_s$  from the measured  $V_p$  and porosity. Furthermore, we can use the crossplots for diagnosing the reliability of the  $V_s$  measurement.

For a long time,  $V_p$ - $V_s$  relations have relied almost exclusively on several empirical relationships. This chapter presented theoretical assessments for the validity of several known regressions. I discussed how we should consider modifying the known relations depending on the character of the pores in the target rock.

Since the approach is closely related to the pore shapes in a rock, further studies in this direction may lead to a way to determine permeability from the measured velocity and porosity.

## REFERENCES

- Berryman, J.G., 1995, Mixture theories for rock properties, in “*Handbook of Physical Constants*”, T.J. Ahrens, eds. American Geophysical Union, Washington D.C., 205-228.
- Castagna, J., Batzle, M. and Kan, T., 1993, Rock Physics – The link between rock properties and AVO response, in “*Offset Dependent Reflectivity – Theory and Practice of AVO Analysis*”, J.P. Castagna and M. Backus, eds. Investigations in Geophysics, No. 8, Society of Exploration Geophysicists, Tulsa, Oklahoma, 135-171.
- Dvorkin, J. and Nur, A., 1996, Elasticity of high-porosity sandstones: Theory for two North Sea datasets. *Geophysics*, **61**, 1363-1370.
- Han, D–H., 1986, *Effects of Porosity and Clay Content on Acoustic Properties of Sandstones and Unconsolidated Sediments*. Ph.D. dissertation, Stanford University.
- Hashin, Z. and Shtrikman, S., 1963, A variational approach to the theory of elastic behavior of multiphase materials, *Journal of Mechanics and Physics Solids*, **11**, 127-140.
- Jørstad, A., Mukerji, T. and Mavko, G., 1999, Model-based shear-wave velocity estimation versus empirical regressions. *Geophysical Prospecting*, **47**, 785-797.
- Kuster, G.T. and Toksöz, M.N., 1974, Velocity and attenuation of seismic waves in two phase media: Part 1: Theoretical formulation, *Geophysics*, **39**, 587-606.
- Mavko, G., 1980, Velocity and attenuation in partially molten rocks, *Journal of Geophysical Research*, **85**, 5173-5189.
- Mavko, G., Mukerji, T. and Dvorkin, J., 1998, *The Rock Physics Handbook, Tools for Seismic Analysis in Porous Media*, Cambridge University Press.

- Tsuneyama, F., Takahashi, I., Nishida, A. and Okamura, H., 2003, Vp/Vs ratio as a rock frame indicator for a carbonate reservoir. *First Break*, **21**, 53-58
- Xu, S. and White, R.E., 1995, A new velocity model for clay-sand mixtures. *Geophysical Prospecting*, **43**, 91-118.
- Zimmerman, R.W., 1986, Compressibility of two-dimensional cavities of various shapes: *Journal of Applied Mechanics*, Transactions of American Society of Mechanical Engineers, 53, 500-504.
- Zimmerman, R.W., 1991, *Compressibility of Sandstones*, Elsevier, New York, 173 pp.

## Appendix A      Matlab code for the grid preparation of velocity-anisotropy estimation

```

%%%%% preparation of input %%%%%
phi=linspace(0,0.4,401);
phi=phi';
one=ones(1,451);
grid_phi_vp=phi*one;
grid_phi_vp=grid_phi_vp';
one=ones(1,351);
grid_phi_vs=phi*one;
grid_phi_vs=grid_phi_vs';
vp0=linspace(1.5,6,451);
vp0=vp0';
vp0=-1*(sort(-1*vp0));
one=ones(1,401);
grid_vp0=vp0*one;
vs0=linspace(0.5,4.0,351);
vs0=vs0';
vs0=-1*(sort(-1*vs0));
grid_vs0=vs0*one;
clear phi one vp0 vs0

%%%%% generate grid for epsilon %%%%%
eps_A=2.65.*(grid_vp0.^2)-1.65.*(grid_phi_vp).*(grid_vp0.^2);
eps_a=(35.525+2.3095.*eps_A.*grid_phi_vp)./(-2.3095);
eps_b=- (37.403+35.525.*eps_A.*grid_phi_vp-
        eps_A.*grid_phi_vp+eps_A)./(-2.3095);
eps_c=(37.403.*eps_A.*grid_phi_vp)./(-2.3095);
eps_p=eps_b-((eps_a.^2)./3);
eps_q=2.*((eps_a.^3)./27)-(eps_a.*eps_b)./3+eps_c;
eps_m=(-eps_q./2+sqrt((eps_q.^2)./4-(eps_p.^3)./27)).^(1/3);
eps_n=-1.*((abs(-eps_q./2-sqrt((eps_q.^2)./4-
        (eps_p.^3)./27))).^(1/3));
eps_m2=(-(eps_m+eps_n)-eps_a./3);
eps_m1=-2.3095.*eps_m2.^2+35.525.*eps_m2-37.403;
grid_eps=(-1.0428.*eps_m2+3.621).*(eps_m2<3.2048)+(-
        0.0809.*eps_m2+0.5383).*(eps_m2<5.9924).*(eps_m2>=3.20
        48)+(-0.0152.*eps_m2+0.1446).*(eps_m2>=5.9924);
grid_eps=grid_eps.*(grid_eps>=0);
clear eps_A eps_a eps_b eps_c eps_p eps_q eps_m eps_n eps_m2
        eps_m1

%%%%% generate grid for gamma %%%%%
gam_A=2.65.*(grid_vs0.^2)-1.65.*grid_phi_vs.*(grid_vs0.^2);
gam_a=(24.278+5.6031.*gam_A.*grid_phi_vs)./(-5.6031);
gam_b=(18.778-24.278.*gam_A.*grid_phi_vs+gam_A.*grid_phi_vs-
        gam_A)./(-5.6031);
gam_c=(-18.778.*gam_A.*grid_phi_vs)./(-5.6031);
gam_p=gam_b-((gam_a.^2)./3);

```

```

gam_q=2.*((gam_a.^3)./27)-(gam_a.*gam_b)./3+gam_c;
gam_m=(-gam_q./2+sqrt((gam_q.^2)./4-(gam_p.^3)./27)).^(1/3);
gam_n=-1.*((abs(-gam_q./2-sqrt((gam_q.^2)./4-
(gam_p.^3)./27))).^(1/3));
gam_m2=(-(gam_m+gam_n)-gam_a./3);
gam_m1=-5.6031.*gam_m2.^2+24.278.*gam_m2+18.778;
grid_gam=(-0.0316.*gam_m2+0.0944).*(gam_m2>=1.8711)+(-
0.1286.*gam_m2+0.2759).*(1.8711>gam_m2).*(gam_m2>=0.85
49)+(-1.3598.*gam_m2+1.3284).*(gam_m2<0.8549);
grid_gam=grid_gam.*(grid_gam>=0);
clear gam_A gam_a gam_b gam_c gam_p gam_q gam_m gam_n gam_m2
gam_m1

```

## Appendix B      Matlab code for the estimation of velocity anisotropy

```
tail=length(input_logs(:,1));
for n=1:1:tail;
vp=input_Vp_brine(n,1)*(input_Vp_brine(n,1)>=1.5)+6*(input_Vp_brine(n,1)<1.5);    %% low velocity<1.5 to 6
theta=input_deviation_angle(n,1);
phi=round(1000*input_porosity(n,1))/1000;    %% set decimal point
i0=phi*1000+1;
vp_theta=grid_vp0(:,i0).*(1+grid_eps(:,i0).*(sin(pi*theta/180)^4));
vp=vp*(min(vp_theta)<=vp)+min(vp_theta)*(min(vp_theta)>vp);
i1=find(vp_theta(:,1)<=vp);
i2=i1(1,:);
output_eps(n,1)=grid_eps(i2,i0);
output_Vp_brine0(n,1)=(vp)./(1+output_eps(n,1).*(sin(pi*theta/180)^4));
end

%%%%% edit this code to estimate gamma, or use a linear relation
%%%%% between epsilon and gamma
```

## Appendix C      HRS code for elastic-impedance analysis constrained by rock-physics bounds

```

/##### unit conversion m/sec*g/cc -> km/sec*g/cc #####/
y1=log(EI97near/1000);
y2=log(EI97mid/1000);
y3=log(EI97far/1000);
/##### least squares linear fit #####/
x1=0.024471741;
x2=0.066987298;
x3=0.15900082;
B=x1^2+x2^2+x3^2;
C=y1+y2+y3;
D=x1*y1+x2*y2+x3*y3;
a=(3*D-C*(x1+x2+x3))/(3*B-(x1+x2+x3)^2);
b=(B*C-D*(x1+x2+x3))/(3*B-(x1+x2+x3)^2);
EIIn1=exp(a*x1+b);
EIIm1=exp(a*x2+b);
EIFI1=exp(a*x3+b);
/##### apply rock-physics bounds #####/
EIFI2=(EIFI1-(0.8077*EIIn1+0.15))*((0.689*EIIn1+1.8466)-
(0.8077*EIIn1+0.6415))/((0.689*EIIn1+2.6)-
(0.8077*EIIn1+0.15))+((0.8077*EIIn1+0.6415);
EIIn2=(EIIn1-(EIFI1-2.6)/0.689)*((EIFI1-0.6415)/0.8077-(EIFI1-
1.8466)/0.689)/((EIFI1-0.15)/0.8077-(EIFI1-
2.6)/0.689)+(EIFI1-1.8466)/0.689;
dEIIn=EIIn1-EIIn2;
dEIFI=EIFI1-EIFI2;
X=(dEIIn*(dEIFI^2))/(dEIIn^2+dEIFI^2);
Y=((dEIIn^2)*dEIFI)/(dEIIn^2+dEIFI^2);
EIIn3=EIIn1-X;
EIFI3=EIFI1-Y;
EIIm3=(EIFI3-(0.8077*EIIn3+0.6415))*((0.8934*EIIn3+0.6030)-
(0.9267*EIIn3+0.2414))/((0.689*EIIn3+1.8466)-
(0.8077*EIIn3+0.6415))+((0.9267*EIIn3+0.2414);
/##### solve inverse matrix equation & final scaling #####/
Vp=0.95*(exp(133.8317*log(EIIn3)-
195.6696*log(EIIm3)+61.8380*log(EIFI3)));
Vs=0.95*(exp(151.2873*log(EIIn3)-
216.6207*log(EIIm3)+64.8335*log(EIFI3)));
Rho=1.05*(exp(-132.0151*log(EIIn3)+194.7416*log(EIIm3)-
61.7266*log(EIFI3)));
/##### compute shale volume #####/
Vpg=4.0;
b1=3-Vpg*2.5;
b2=2.6-Vpg*2.1;
Vsho=(b2-(Vp-Vpg*Rho))/(b2-b1);
sc1=0;
sc2=0.6;
Vsh97=1-(sc2-Vsho)/(sc2-sc1);
Vsh97;

```

## Appendix D      HRS code for the computation of fluid saturation: (1) calculation of common rock-frame properties

```

/*#####*/
/*#          #*/
/*# Computation for 1997 #*/
/*#          #*/
/*#####*/
/*=====*/
/* Compute elastic moduli and porosity */
/*=====*/
Vshm=0.5*(Vsh97vp+Vsh01vp);
Gsat97=Vs97*Vs97*Rho97;
Gdry97=Gsat97;
Ksat97=Vp97*Vp97*Rho97-4/3*Gsat97;
Phi97=-0.5401*Rho97+1.4350;
/*=====*/
/* Porosity cut-off, indicator1 & indicator2 */
/*=====*/
Low_por=0.001;
indicator1 = Phi97;
indicator2 = Phi97;
index=0;
while( index < numsamples(Phi97))
{
    if(Phi97[index] < Low_por)
    {
        indicator1[index] = 0;
        indicator2[index] = 0.001;
    }
    else
        indicator1[index] = 1;
        indicator2[index] = 0;
    index = index +1;
}
Phi97=Phi97*indicator1+indicator2;
/*=====*/
/* Water-saturated rock consists of average solid */
/*=====*/
Rho97ww=(1-Phi97)*(2.67*(1-Vshm)+2.58*Vshm)+Phi97*1.0038;
Vs97ww=sqrt(Gsat97/Rho97ww);
Vp97ww=Vs97ww/0.79+1;
Ksat97ww=Vp97ww*Vp97ww*Rho97ww-4/3*Gsat97;
Kmnrl=0.5*((1-Vshm)*38.13+Vshm*23)+0.5*(1/((1-
    Vshm)/38.13+Vshm/23));
/*=====*/
/* Compute the bulk modulus and density of in-situ fluid */
/*=====*/
Kdry97=Kmnrl*(1-(1-Phi97)*Ksat97ww/Kmnrl-
    Phi97*Ksat97ww/2.7416)/(1+Phi97-Phi97*Kmnrl/2.7416-
    Ksat97ww/Kmnrl);

```

```

/*#####*/
/*#           #*/
/*# Computation for 2001 #*/
/*#           #*/
/*#####*/
/*=====*/
/* Compute elastic moduli and porosity */
/*=====*/
Gsat01=Vs01*Vs01*Rho01;
Gdry01=Gsat01;
Ksat01=Vp01*Vp01*Rho01-4/3*Gsat01;
Phi01=-0.5401*Rho01+1.4350;
/*=====*/
/* Porosity cut-off, indicator1 & indicator2 */
/*=====*/
Low_por=0.001;
indicator1 = Phi01;
indicator2 = Phi01;
index=0;
while( index < numsamples(Phi01))
{
    if(Phi01[index] < Low_por)
    {
        indicator1[index] = 0;
        indicator2[index] = 0.001;
    }
    else
        indicator1[index] = 1;
        indicator2[index] = 0;
    index = index +1;
}
Phi01=Phi01*indicator1+indicator2;
/*=====*/
/* Water-saturated rock consists of average solid */
/*=====*/
Rho01ww=(1-Phi01)*(2.67*(1-Vshm)+2.58*Vshm)+Phi01*1.0038;
Vs01ww=sqrt(Gsat01/Rho01ww);
Vp01ww=Vs01ww/0.79+1;
Ksat01ww=Vp01ww*Vp01ww*Rho01ww-4/3*Gsat01;
Kmnrl=0.5*((1-Vshm)*38.13+Vshm*23)+0.5*(1/((1-
    Vshm)/38.13+Vshm/23));
/*=====*/
/* Compute the bulk modulus and density of in-situ fluid */
/*=====*/
Kdry01=Kmnrl*(1-(1-Phi01)*Ksat01ww/Kmnrl-
    Phi01*Ksat01ww/2.7416)/(1+Phi01-Phi01*Kmnrl/2.7416-
    Ksat01ww/Kmnrl);
/*#####*/
/*#           #*/
/*# Computation for common rock frame #*/
/*#           #*/
/*#####*/

```

```
Phim=0.5*(Phi97+Phi01);  
Rhomww=0.5*(Rho97ww+Rho01ww);  
Kdrym=0.5*(Kdry97+Kdry01);  
/*=====*/  
/* output selection */  
/*=====*/  
Rhomww;
```

## Appendix E      HRS code for the computation of fluid saturation: (2) calculation of fluid saturation

```

/*=====*/
/* Compute K and density of in-situ fluid */
/*=====*/
Gsat97=Vs97*Vs97*Rho97;
Ksat97=Vp97*Vp97*Rho97-4/3*Gsat97;
Kmnrl=0.5*((1-Vshm)*38.13+Vshm*23)+0.5*(1/((1-
Vshm)/38.13+Vshm/23));
Kf97=Phim*Kmnrl*(Ksat97/(Kmnrl-Ksat97)-Kdrym/(Kmnrl-
Kdrym))/(1+Phim*(Ksat97/(Kmnrl-Ksat97)-Kdrym/(Kmnrl-Kdrym)));
Rhof97=1.0038-(Rhomww-Rho97)/Phim;
Kf97rcp=1/Kf97;
/*=====*/
/* Solve inverse matrix for fluids saturation */
/*=====*/
Sw97h=0.2668*Kf97rcp+4.3142*Rhof97-3.4279;
So97h=-0.4480*Kf97rcp-4.9043*Rhof97+5.0863;
Sg97h=0.1813*Kf97rcp+0.5900*Rhof97-0.6584;
Sw97a=0.6486*Kf97-0.9750*Rhof97+0.2004;
So97a=-1.0894*Kf97+3.9789*Rhof97-1.0074;
Sg97a=0.4407*Kf97-3.0039*Rhof97+1.8070;
/*=====*/
/* Mix saturation-scale hw: weight for fine-mixture */
/*=====*/
hw=0.5;
Sw97=hw*Sw97h+(1-hw)*Sw97a;
So97=hw*So97h+(1-hw)*So97a;
Sg97=hw*Sg97h+(1-hw)*Sg97a;
/*=====*/
/* Cut-off for Sfluid (-2<=Sfluid<=2) */
/*=====*/
/*****/
/* Sw */
/*****/
Low_Sw=-2;
High_Sw=2;
indicatorSw = Sw97h;
index=0;
while( index < numsamples(Sw97h) )
{
  if( Sw97h[index] >= Low_Sw &&
      Sw97h[index] <= High_Sw &&
      Sw97a[index] >= Low_Sw &&
      Sw97a[index] <= High_Sw )
  {
    indicatorSw[index] = 1;
  }
  else
    indicatorSw[index] = 0;
}

```

```

index = index +1;
}
Sw97=indicatorSw*Sw97+(1-indicatorSw);
/*****/
/* So */
/*****/
Low_So=-2;
High_So=2;
indicatorSo = So97h;
index=0;
while( index < numsamples(So97h) )
{
  if( So97h[index] >= Low_So &&
      So97h[index] <= High_So &&
      So97a[index] >= Low_So &&
      So97a[index] <= High_So )
    {
      indicatorSo[index] = 1;
    }
  else
    indicatorSo[index] = 0;
  index = index +1;
}
So97=indicatorSo*So97;
/*****/
/* Sg */
/*****/
Low_Sg=-2;
High_Sg=2;
indicatorSg = Sg97h;
index=0;
while( index < numsamples(Sg97h) )
{
  if( Sg97h[index] >= Low_Sg &&
      Sg97h[index] <= High_Sg &&
      Sg97a[index] >= Low_Sg &&
      Sg97a[index] <= High_Sg )
    {
      indicatorSg[index] = 1;
    }
  else
    indicatorSg[index] = 0;
  index = index +1;
}
Sg97=indicatorSg*Sg97;
/*=====*/
/* Cut-off (Negative values of Porosity & Shale volume), */
/*          indicator3 */
/*=====*/
Low_Rhof=0;
Low_Kf=0;
Low_Phi=0.1;

```

```

Up_Vshm=0.5;
indicator3 = Sw97;
index = 0;
while( index < numsamples(Sw97) )
{
  if( Rhof97[index] > Low_Rhof &&
      Kf97[index] > Low_Kf &&
      Phim[index] >= Low_Phi &&
      Vshm[index] < Up_Vshm )
    {
      indicator3[index] = 1;
    }
  else
    indicator3[index] = 0;
  index = index +1;
}
Sw97=indicator3*Sw97+(1-indicator3);
So97=indicator3*So97;
Sg97=indicator3*Sg97;
/*=====*/
/* Cut-off negative Sw, indicator4 */
/*=====*/
Low_Sw=0;
indicator4 = Sw97;
index = 0;
while( index < numsamples(Sw97) )
{
  if( Sw97[index] < Low_Sw )
    {
      indicator4[index] = 0;
    }
  else
    indicator4[index] = 1;
  index = index +1;
}
Sw97=indicator4*Sw97+(1-indicator4);
/*=====*/
/* Cut-off negative So, indicator5 */
/*=====*/
Low_So=0;
indicator5 = So97;
index = 0;
while( index < numsamples(So97) )
{
  if( So97[index] < Low_So )
    {
      indicator5[index] = 0;
    }
  else
    indicator5[index] = 1;
  index = index +1;
}

```

```

So97=indicator5*So97;
/*=====*/
/* Cut-off negative Sg, indicator6 */
/*=====*/
Low_Sg=0;
indicator6 = Sg97;
index = 0;
while( index < numsamples(Sg97) )
{
  if( Sg97[index] < Low_Sg )
  {
    indicator6[index] = 0;
  }
  else
    indicator6[index] = 1;
  index = index +1;
}
Sg97=indicator6*Sg97;
/*=====*/
/* Balance fluids saturation */
/*=====*/
Sw97=Sw97/(Sw97+So97+Sg97);
So97=So97/(Sw97+So97+Sg97);
Sg97=Sg97/(Sw97+So97+Sg97);
/*=====*/
/* Output selection */
/*=====*/
So97;

```